NASA TN D-55

TECHNICAL NOTE

D-55

WIND-TUNNEL INVESTIGATION OF LONGITUDINAL AERODYNAMIC CHARACTERISTICS OF THREE PROPELLER-DRIVEN VTOL CONFIGURATIONS IN THE TRANSITION SPEED RANGE, INCLUDING EFFECTS OF GROUND PROXIMITY

By Richard E. Kuhn and William C. Hayes, Jr.

Langley Research Center
Langley Field, Va.

NATIONAL AERONAUTICS AND SPACE ADMINISTRATION

WASHINGTON February 1960

NATIONAL AERONAUTICS AND SPACE ADMINISTRATION

TECHNICAL NOTE D-55

WIND-TUNNEL INVESTIGATION OF LONGITUDINAL AERODYNAMIC CHARACTERISTICS OF THREE PROPELLER-DRIVEN VTOL CONFIGURATIONS IN THE TRANSITION SPEED RANGE, INCLUDING EFFECTS OF GROUND PROXIMITY

By Richard E. Kuhn and William C. Hayes, Jr.

SUMMARY

An investigation has been made in the 17-foot test section of the Langley 300-MPH 7- by 10-foot tunnel to determine the longitudinal aerodynamic characteristics of tilt-wing, deflected-slipstream, and combination tilt-wing—deflected-slipstream VTOL configurations in the transition speed range.

The results of this investigation are in general agreement with prior related investigations in that although the tilt-wing configuration requires the least power in hovering, the combination tilt-wing—deflected-slipstream configuration has relatively low power requirements throughout the transition speed range. In addition, the longitudinal trim problems of the combination configuration can be handled easily by use of a rearward location of the wing pivot and by properly programing the flap deflection angle with wing tilt angle.

The power requirements for the combination configuration in the region of ground effect are only slightly larger than those for the tilt-wing configuration at the lower speeds and are lower than the requirements for the tilt-wing configuration at speeds above about 30 knots. The power requirements for the deflected-slipstream configuration are greatly increased in the region of ground effect. The extension of a leading-edge slat had little value except in the case of the deflected-slipstream configuration at high flap deflection. An appendix describing the 17-foot test section of the Langley 300-MPH 7- by 10-foot tunnel in which the model was tested is included.

INTRODUCTION

An investigation of the aerodynamic characteristics of wing-propeller configurations that may be applicable to aircraft designed for vertical

take-off and landing (VTOL) or short take-off and landing (STOL) is being conducted at the Langley Research Center of the National Aeronautics and Space Administration. The results of this work have generally indicated that a combination of the tilt-wing and deflected-slipstream configurations may have several advantages over a configuration employing either tilt wings or deflected slipstream alone. Reference 1, for instance, indicates that the trim problem of the tilt wing can be alleviated by adding a trailing-edge flap, the deflection of which could be programed so that the diving moment arising from the flap deflection would cancel the thrust-induced nose-up pitching moment during transition flight. In addition, reference 2 indicates that the flap is beneficial in reducing the stall and, therefore, the power requirements in the transition or low-speed range. These factors, plus the thrust recovery factor - that is, the ratio of lift produced to thrust input obtainable with only a moderate amount of slipstream deflection - indicate the desirability of further investigation of the combination configuration.

Inasmuch as the foregoing observations have been made from results obtained from various models having generally different physical characteristics, the present investigation was undertaken to obtain, with one model, a comparison of the tilt-wing, the deflected-slipstream, and the combination tilt-wing—deflected-slipstream configurations.

The effects of ground proximity have, in general, been investigated only for the hovering condition (zero forward speed). Very little data on the effects of ground proximity on the performance in the transition speed range are available. A large part of the present investigation has, therefore, been devoted to this problem.

The flow in the region of possible horizontal-tail locations was surveyed by measuring the floating angle of freely floating downwash vanes and from total-pressure tubes in the vane leading edges which measured the dynamic pressure of the flow. The characteristics of this model at zero forward speed have been presented in reference 3.

SYMBOLS

When a wing operates in the slipstream of large-diameter propellers, large forces and moments can be produced at low or zero forward speed. Coefficients based on the free-stream dynamic pressure approach infinity and thus become meaningless. Therefore, it seems appropriate to base the coefficients on the dynamic pressure in the propeller slipstream; in the present paper, coefficients so based are indicated by the use of the subscript s. The relationship between the propeller thrust and the dynamic pressure in the slipstream is discussed in reference 4.

Conventional coefficients based on the free stream can be obtained by dividing by $(1 - C_{T,s})$; for example, $C_L = C_{L,s}/(1 - C_{T,s})$.

The positive sense of forces, moments, and angles is shown in figure 1. The pitching-moment coefficients are presented with reference to the wing quarter-chord line. Forces and moments obtained for the propeller alone are based on wing geometric characteristics and are referred to the intersection of the plane of rotation of the propeller and the propeller shaft.

b propeller blade chord, ft

$C_{D,o}$ profile drag coefficient

C_L lift coefficient based on free airstream, $\frac{L}{q_0 \frac{S}{2}}$

$C_{L,s}$ lift coefficient based on slipstream, $\frac{L}{q_s \frac{S}{2}}$

$C_{L,t}$ lift coefficient of horizontal tail, $\frac{\text{Horizontal-tail lift}}{qS_t}$

$C_{m,p,s}$ pitching-moment coefficient of propeller, $\frac{M_{Y,p}}{q_s \bar{c} \frac{S}{2}}$

$C_{m,s}$ pitching-moment coefficient, $\frac{M_Y}{q_s \bar{c} \frac{S}{2}}$

$C_{N,p,s}$ normal-force coefficient of propeller, $\frac{F_{N,p}}{q_s \frac{S}{2}}$

C_P power coefficient, $\frac{P}{\rho n^3 D^5}$

C_T thrust coefficient, $\frac{T}{\rho n^2 D^4}$

$C_{T,s}$ thrust coefficient or nominal value of thrust coefficient (taken as the average value at low angles of attack), $\frac{T}{q_s \frac{\pi}{4} D^2}$

$C_{X,s}$	longitudinal-force coefficient, $\frac{F_X}{q_s \frac{S}{2}}$
$\bar{c}$	wing chord, ft
D	propeller diameter, ft
F	resultant force, lb
$F_{N,p}$	propeller normal force, lb
F_X	longitudinal force, lb
h	distance from ground board to wing quarter-chord line, ft
h'	propeller blade thickness, ft
L	lift, lb
M_Y	pitching moment, ft-lb
$M_{Y,p}$	propeller pitching moment, ft-lb
n	propeller rotational speed, rps
P	propeller shaft power per propeller, $2\pi nQ$, ft-lb/sec
p	static pressure at downwash vanes, lb/sq ft
p^0	average total pressure across span of survey vane, lb/sq ft
Q	propeller shaft torque, ft-lb
q	free-stream dynamic pressure, $\frac{\rho V^2}{2}$, lb/sq ft
q_{cl}	dynamic pressure at tunnel center line, lb/sq ft
q_s	slipstream dynamic pressure, $q + \frac{T}{\frac{\pi}{4}D^2}$, lb/sq ft
q_t	average dynamic pressure across semispan of tail, lb/sq ft

R	radius of propeller, ft
r	radius at any propeller blade section, ft
S	twice area of semispan wing, sq ft
S_t	horizontal tail area, sq ft
T	measured propeller thrust per propeller, lb
V	free-stream velocity, ft/sec
x	wing coordinate measured from leading edge (fig. 2)
x_I	wing coordinate of surface between retracted slat and wing upper surface, measured from leading edge (fig. 2)
y_l	wing lower-surface coordinate, measured from chord plane (fig. 2)
y_u	wing upper-surface coordinate, measured from chord plane (fig. 2)
y_I	wing coordinate of surface between retracted slat and wing upper surface, measured from wing chord plane (fig. 2)
z	distance of downwash vanes from tunnel center line, ft (fig. 1)
α	angle of attack, deg
γ	climb angle, deg
$\delta_{f,F}$	Fowler flap deflection, deg
$\delta_{f,S}$	sliding-flap deflection, deg
δ_t	horizontal-tail deflection, deg
δ_{slat}	leading-edge slat deflection, deg
ϵ	angle of downwash, deg
ρ	mass density of air, slugs/cu ft
σ	angle of sidewash in 17-foot test section, deg

MODEL AND APPARATUS

Drawings and a photograph of the semispan model with a table of geometric characteristics are presented in figures 2 to 4. The wing was constructed on a steel spar which held the two motor nacelles, the wooden blocks which formed the wing contour, and the brackets which held the sliding flap in position.

The sliding flap rotated about a point 1.25 inches below the chord line at the 41-percent-chord station. The sliding ramp radius was 20 percent of the wing chord and was made tangent to the upper surface of the wing. The rear flap, which was a Fowler flap, had a Clark Y airfoil section and a chord length equal to 40 percent of the wing chord. When the Fowler flap was deflected, the leading edge was located so that a slot gap of $0.015\bar{c}$ was maintained. The sliding flap had deflections of 0°, 30°, and 50°, and the Fowler flap was either retracted or was deflected 30°, 50°, or 60°.

The three-blade propellers (blade form curves presented in fig. 5) were made of balsa covered with glass cloth and were driven by water-cooled variable-frequency electric motors operated in parallel from one variable-frequency power supply, which kept the motor speeds matched within 10 rpm. The speed of rotation of each propeller was determined by a stroboscopic indicator which received the output frequency of small alternators connected to each motor shaft. Both propellers rotated in a clockwise direction when viewed from the rear, so as to oppose the direction of flow of the wing-tip vortex. During the tests, the speed of rotation was maintained at approximately 5,800 rpm which corresponds to a propeller-tip Mach number of 0.54.

The motor of the inboard propeller was mounted inside the aluminum-alloy nacelle by means of strain-gage beams (as shown in ref. 4) so that the propeller thrust, torque, normal force, and pitching moment could be measured. The total lift, longitudinal force, and pitching moment were measured by a three-component strain-gage balance mounted below the tunnel floor.

The angularity of the flow in the vicinity of a horizontal tail was measured by means of five free-floating downwash vanes which were pivoted about vertical axes approximately two inches forward of each vane leading edge. The vanes were located in a straight line across the tunnel approximately 3 wing-chord lengths behind the wing and about 1 wing-chord length apart (figs. 1 and 4). The center vane (when undeflected) was located on the tunnel center line in the plane of the wing chord at an angle of attack of 0°. The angle at which the vane floated was measured by a slide wire unit and automatically recorded on a chart potentiometer.

The average dynamic pressure over the span of each vane was obtained from a series of six equally spaced total-pressure tubes which projected from the leading edge of each vane to a line coincident with the pivot axis of the vane. An average total pressure p^0 was obtained for each vane by connecting the six total-pressure tubes to a small plenum chamber with pieces of 0.03-inch-diameter tubing of equal length. Calibration indicated that the plenum-chamber pressure was within a few percent of the average pressure applied to the total-pressure tubes; therefore, corrections were not considered necessary. The average total pressure was connected to a strain-gage pressure cell, and the readings thus obtained were also printed on a chart potentiometer.

The average dynamic-pressure ratio over the span was then obtained from the relation

$$\frac{q_t}{q_s} = \frac{p^0 - p}{q_s}$$

where the static pressure p at the vane was obtained from the tunnel calibration.

TESTS AND CORRECTIONS

The investigation reported in reference 5 indicated that an increased ratio of tunnel size to model size is necessary for deflected-slipstream or tilt-wing configurations in order to avoid large unknown tunnel-wall effects. As a result, a 17-foot test section was constructed in the large end of the Langley 300-MPH 7- by 10-foot tunnel, upstream of the regular test section. The arrangement and calibration of this test section are presented in the appendix to this paper.

Corrections to the free-stream velocity due to blockage and slipstream contraction were estimated and found to be negligible. The jet-boundary corrections applied to the angle of attack and the longitudinal force were estimated for a square test section by a method similar to that of reference 6. Inasmuch as these corrections depend on the circulation about the wing, it was necessary to subtract the direct thrust contribution to lift before applying them. The following relations were used:

$$\alpha = \alpha_{measured} + 0.143C_{L,1}$$

$$C_{X,s} = C_{X,s,measured} - 0.0025(C_{L,1})^2(1 - C_{T,s})$$

where $C_{L,l}$ is the increment of lift coefficient that is approximately proportional to the circulation and is obtained by subtracting the direct thrust contribution as follows:

$$C_{L,l} = \frac{C_{L,s} - C_{T,s} \frac{2\left(\frac{\pi}{4} D^2\right)}{S} \frac{F}{T} \sin(\theta + \alpha)}{1 - C_{T,s}}$$

where θ and $\frac{F}{T}$ are the turning angle and thrust recovery factor obtained at zero forward speed (ref. 3). In general these corrections were found to be small; however, they were applied.

The tests were made at a combination of free-stream dynamic pressures and propeller thrusts selected to maintain a dynamic pressure of approximately 8 lb/sq ft in the slipstream. The tests with propeller off and propeller free (windmilling) were run at a free-stream dynamic pressure of 8 lb/sq ft. The thrust of the inboard propeller was held constant throughout the angle-of-attack range. The selected thrust could be maintained on both propellers at zero angle of attack by appropriate adjustment in the propeller blade angles; however, because of the spanwise variation in flow conditions, the thrust of the outboard propeller varied slightly from the initial value at angles of attack other than zero.

In order to minimize test time, operating conditions were chosen so that only two blade-angle settings were required. A blade angle of about 8° was used at the higher thrust coefficients while a blade angle of about 16° was used for the lower thrust coefficients.

The Reynolds number in the slipstream, based on a mean aerodynamic chord of 1.20 feet, was 0.63×10^6.

PRESENTATION OF RESULTS

The results of the investigation are presented in the following order:

The results of the flow-angularity and dynamic-pressure surveys behind the model (in the vicinity of a horizontal tail) are included as the last part of figures 9 to 19, 21, 23, and 25. The position of the vane pivot point remains fixed with respect to the model, and the vane height parameter $z/\bar{c}$ is measured with respect to a plane containing the wing quarter-chord line and the relative wind. Thus, for angles of attack other than zero, the wing incidence and the airplane angle of attack must be used in calculating the effective horizontal-tail position ($z/\bar{c}$) to be used in entering the data figures to determine flow angularity and dynamic pressure.

DISCUSSION

The discussion of the data is divided into two main parts. The first part is a general discussion in which the more significant results are pointed out. The second part demonstrates the application of the data to the estimation of the performance of a hypothetical airplane. The three configurations considered are the tilt-wing, the combination tilt-wing—deflected-slipstream, and the deflected-slipstream.

The variations of lift and pitching-moment coefficients with longitudinal-force coefficient included in figures 7 to 31 are of particular interest in assessing the aerodynamic characteristics of a given configuration. Positive values of $C_{X,s}$ indicate accelerating or climbing flight, whereas negative values of $C_{X,s}$ indicate decelerating or descending flight. A value of zero for $C_{X,s}$ indicates that drag is exactly balanced by a component of thrust and that a condition of steady level flight exists. The angle of steady climb or descent is defined as $\gamma = \tan^{-1} \frac{C_{X,s}}{C_{L,s}}$. The pitching-moment coefficient for level flight at a particular thrust coefficient or at any climb or glide angle may be read directly at the appropriate value of $C_{X,s}$. The values of thrust coefficient listed in the figure keys are nominal, and typical variations of the actual values with angle of attack are shown in figures 6(a) and 9(c).

General Discussion

The basic data for the propeller alone and for the wing alone are presented in figures 6 and 7, respectively. The expected high lift coefficients and large negative pitching moments resulting from the extension of the Fowler flap are shown in figure 7(a).

Effect of slat position.- The results of the investigation reported in reference 5 indicated that a leading-edge slat would be effective in delaying wing stall to higher angles of attack. Therefore, the initial phase of the present investigation was the determination of the effectiveness of a 30-percent-chord slat at three different positions with respect to the wing (fig. 3). These results are shown in figure 8 and, in general, indicate that the highest position investigated gave the highest maximum lift coefficients and extended the high lift condition well into the deceleration or approach range of $C_{X,s}$ values. However, these results are restricted to a thrust coefficient of 0.90 and large flap deflection angles ($\delta_{f,S} = 50^\circ$; $\delta_{f,F} = 50^\circ$). Subsequent tests at

other flap deflection angles and thrust coefficients indicated that the slat was useful only with the combination of high thrust coefficients and high flap deflection angles. Comparisons of slat-on and slat-off data presented in figure 31 indicate that at lower flap deflection angles the slat slightly reduced both the lift and the longitudinal force except at the highest angles of attack. This result was not realized while the tests were in progress, and most of the data presented herein were obtained with the slat extended in the high position.

Effect of flap deflection.- The basic data showing the effect of thrust coefficient for various flap deflection angles (slat extended) are presented in figures 9 to 14, and a comparison of the effects of flap deflection at given thrust coefficients is presented in figure 26. The lift coefficients attainable for steady level flight $\left(C_{X,s} = 0\right)$ with the flaps retracted (tilt-wing configuration) and with a thrust coefficient of 0.60 are relatively low because of wing stall (fig. 26(a)). In addition, nose-up moments (about the wing quarter chord) are encountered as a result of both the low position of the thrust line and the direct propeller pitching moments which are as indicated in figure 9(b) and in reference 4. Deflection of the Fowler flap only to 50° (combination tilt-wing—deflected-slipstream configuration) appreciably increases the lift for steady level flight $\left(C_{X,s} = 0\right)$ and also produces a large diving moment (fig. 26(a)). The losses in lift and longitudinal force when both flaps are set at large angles $\left(\delta_{f,S} = 50°;\ \delta_{f,F} = 30°\right)$ are not of significance at this thrust coefficient $\left(C_{T,s} = 0.60\right)$ since these high flap deflection angles are not likely to be used because of the large negative angles of attack $(\alpha \approx -34°)$ necessary for steady level flight at this thrust coefficient.

At a thrust coefficient of 1.00 (fig. 26(d)) the forward speed is zero and for $C_{X,s} = 0$ the data represent hovering conditions. As may be expected for this condition, the tilt-wing configuration (flaps retracted) exhibits the highest lift coefficients. The losses involved in the process of deflecting the slipstream are responsible for the progressively lower lift coefficients obtained at a thrust coefficient of 1.00 $\left(\text{at } C_{X,s} = 0\right)$ as the flaps are deflected to larger angles. At the intermediate thrust coefficients $\left(C_{T,s} = 0.90 \text{ and } 0.95\right)$, the effects of the turning losses and wing stall are both present (figs. 26(b) and 26(c)).

Effect of ground proximity.- The basic data obtained with the ground board installed at two distances below the model are presented in figures 18 to 24 and comparisons of the data with and without the ground board installed are presented in figures 27 to 30. In general, the proximity of the ground caused premature stall and loss of lift. The

tilt-wing configuration ($\delta_{f,S} = 0^\circ$; $\delta_{f,F} = 0^\circ$) was least affected by the ground (fig. 27), probably because with the flaps retracted the wing was stalled out of the region of ground effect. The losses in lift were most severe for the larger flap deflection angles (figs. 29 and 30). Visual observation revealed flow separation on the flaps and a vortex-type flow between the wing and the ground similar to that experienced with jet-flap configurations (ref. 7). It is felt that both phenomena contribute to the lift loss in the region of ground effect.

Flow in the region of the horizontal tail.- Some indication of the dynamic pressure and the downwash angle of the flow in the region of the horizontal tail can be gained from the data obtained from the downwash vanes and presented as the last part of figures 9 to 19, 21, 23, and 25. The level of the free-stream dynamic pressure is indicated on the dynamic-pressure-ratio plots by a dashed line. Data points below this line indicate a deficiency of dynamic pressure or a wake. The wake from the wing is indicated, for instance, in figure 9(e) by the low values of q_t/q_s at $z/\bar{c} = 0$ in the plot for windmilling propeller. Similarly the propeller slipstream is indicated by values of q_t/q_s much higher than the free-stream level for the thrust coefficients of 0.30, 0.60, and 0.90. Although it is not possible to determine accurately the gradient of dynamic pressure with height of the horizontal tail when only five vanes are used, it appears that there are steep gradients present which would produce rapidly changing pitching moments with changing airplane attitude.

The downwash angles became rather large at the highest thrust coefficients; however, these angles are associated with relatively low levels of dynamic pressure as long as the region of the slipstream is avoided. In general, the results indicate that in order to avoid an erratic pitching-moment contribution from the horizontal tail, as high a location as possible is desirable.

Estimated Performance of a Hypothetical Airplane

The performance of a hypothetical airplane was calculated by the method of reference 4. The test model was assumed to be a 1/4-scale semispan wing of the hypothetical airplane shown in figure 32, which has an assumed gross weight of 3,600 pounds. The three configurations considered were the tilt-wing, the combination tilt-wing—deflected-slipstream ($\delta_{f,S} = 0^\circ$; $\delta_{f,F} = 50^\circ$), and the deflected-slipstream for which a sliding-flap deflection of 50° and a Fowler flap deflection of 30° were assumed in the very low speed range ($V = 0$ to $V \approx 15$ knots) until an angle of attack of 0° was reached. Above 15 knots a programed retraction of the flaps was assumed until the transition flight was complete at an angle of attack of 0°.

When the airplane is considered as a tilt-wing configuration, the wing pivot point lies on the wing chord plane at the 60-percent-chord point. As the wing is pivoted from the position for hovering to the position for cruise, the weight of the wing, propellers, and engines or power train shifts forward. The percentage of total aircraft weight to be shifted and the associated center-of-gravity shift may, of course, vary considerably depending on the designer's choice of power systems, location of fuel cells, and so forth. For this analysis it is assumed that these parts weigh 1,600 pounds, and the associated center of gravity is located so that the center of gravity of the entire airplane in the cruise condition is 10 inches below the quarter-chord point of the wing chord. The location of the center of gravity for the cruise and for the hovering condition is shown in the following sketch:

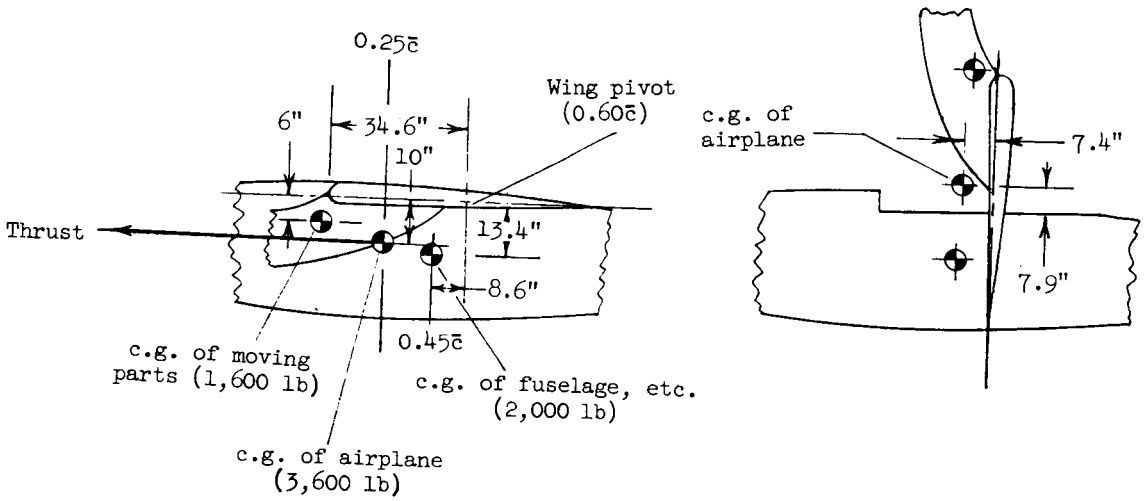

Cruise Condition

Hovering Condition

The change in center-of-gravity location due to flap deflection is considered negligible.

The horizontal tail is an all-movable surface having a plan form and longitudinal location corresponding to that of the downwash vanes used in the investigation. The T-tail configuration was chosen after a preliminary evaluation of the flow-angularity and dynamic-pressure surveys indicated that in lower positions the horizontal tail would be subject to nonlinear variations of flow angularity and dynamic pressure which would produce erratic pitching moments.

Effect of flap deflection.- The effects of flap deflection on attitude, thrust, and the power required for operation out of the region of ground effect are presented in figures 33 to 35. The leading-edge slat is extended and set at 0° deflection. In the hovering condition (V = 0 knots), the tilt-wing configuration ($\delta_{f,S} = 0°$; $\delta_{f,F} = 0°$) requires least thrust (fig. 33). As the flaps are progressively deflected and the angle of attack decreased, the thrust required to hover increases because of the thrust loss inherent in the turning process. As the airplane moves into forward flight, the thrust required for the flapped configurations decreases rapidly and at speeds of between 10 and 15 knots becomes less than that for the tilt-wing configuration. This condition results from the fact that the stall of the tilt-wing configuration is not adequately controlled by the leading-edge slat. The combination tilt-wing—deflected-slipstream configuration ($\delta_{f,S} = 0°$; $\delta_{f,F} = 50°$) presents thrust requirements which are only about 10 percent higher than those of the tilt-wing configuration in the hovering condition and which decrease rapidly in transition flight. At speeds above approximately 5 knots, the thrust requirements are lower for the combination configuration than for the other two configurations investigated.

The complete level-flight power curves (V = 0 to V = 300 knots) are presented for these configurations in figure 34, and the power curves for climb and approach are presented in figure 35. The tilt-wing configuration shows the smallest variation of power required for climb at 10° and approach at 10° throughout the flight speed range considered (V = 0 to V ≈ 40 knots). The reason for this is that the lift coefficients available with the flapped configurations generally increase as the airplane goes from the level-flight condition ($C_{X,s} = 0$) to the approach condition ($C_{X,s} < 0$), whereas the lift coefficients available with the tilt-wing configuration remain nearly constant from the climb through level flight to the approach condition. The maximum values of lift coefficient for the flapped configurations are reached at values of $C_{X,s}$ which correspond to angles of approach larger than 10°; however, these maximum values were followed by such large reductions that a very rapid increase in power would be required.

Effect of ground proximity.- The effects of ground proximity on the aerodynamic characteristics are presented in figures 27 to 30, and the

effects on the level-flight power requirements are presented in figure 36. The effects of ground proximity were most severe on the deflected-slipstream configuration, both in hovering and in the transition speed range. The tilt-wing configuration was least affected by the proximity of the ground, partly because the wing was stalled out of the region of ground effect. Although data for the tilt-wing configuration hovering in the region of ground effect were not obtained, experience indicates that the ground effect would be negligible or to some extent favorable. Although the power requirements for the combination configuration in the region of ground effect are slightly larger than those for the tilt-wing configuration at lower speeds, they are lower at speeds above about 30 knots.

L
5
1
0

Effect of slat.- The effect of a leading-edge slat on the power required for a flight is presented for the three configurations in figure 37. The deflected-slipstream configuration shows some reduction in power requirements, particularly in the approach condition, when the slat is extended; however, the combination configuration is generally penalized by the addition of a slat. Although no data were obtained for the tilt-wing configuration with the slat retracted, reference 8 indicates that some benefits may be derived in the form of reduced power requirements in the transition speed range.

Longitudinal trim.- Figure 38 presents the variation of the moment which the horizontal tail could provide for trimming purposes with forward speed. These moments were computed by using the results of the dynamic-pressure surveys and assuming a tail lift coefficient of $C_{L,t} = 1.0$. The horizontal-tail incidence settings required to obtain these moments were estimated from the flow-angularity surveys in the vicinity of the horizontal tail and a tail angle of attack of 15° (required for a lift coefficient of 1.0) with respect to the local flow. The variation of the untrimmed pitching moment of each configuration with forward speed is presented in figure 39. The variation of this moment due to the movement of the airplane center of gravity with wing tilt has been considered in the computation. In addition, the envelope of the trimming moment available from the horizontal tail (from fig. 38) is presented, and from these curves it is seen that forward speeds above 40 knots are necessary before the horizontal tail can provide the necessary trim. Forward speeds of 30 knots would be required even if a horizontal-tail lift coefficient of 2.0 could be realized. It would, of course, be possible to minimize the untrimmed moments in hovering flight by proper location of the airplane center of gravity.

Consideration of the magnitudes of the pitching moment for the tilt-wing and the combination configuration shown in figure 39 indicates that intermediate Fowler flap deflections $\left(0^{\circ} < \delta_{f,F} < 50^{\circ}\right)$ would provide levels of pitching moment between those shown. Therefore, proper programing of wing tilt and Fowler flap deflection would provide negligible,

or at least easily controlled, pitching-moment variations throughout the transition speed range, as is also shown in reference 1.

Trim is only part of the problem, however. Past experience has indicated that in order to provide sufficient pitch control for hovering and transition flight, a moment of about 3,000 ft-lb would be required. Therefore it must be concluded that the horizontal tail would be ineffective for either trim or control below forward speeds of approximately 30 knots.

In view of the foregoing discussion, required horizontal-tail incidence settings appear to be moderate (fig. 38). Although the basic data from the flow-angularity surveys indicate downwash angles of 50° and higher for some conditions, these angles are accompanied by low dynamic-pressure ratios and occur at very low forward speeds (high thrust coefficients) and are, therefore, not significant. It may be seen from figure 38 that for the tilt-wing configuration at a velocity of 16 knots, a tail incidence of 45° is required for the realization of a lift coefficient of 1.0. The dynamic-pressure ratio at this speed is so low, however, that the moment which can be produced is negligible; thus it appears that tail incidence settings above about 30° are unnecessary.

L
5
1
0

CONCLUDING REMARKS

In general, the results of this comparative investigation support the previous conclusions regarding these configurations, that is, the power requirements for hovering are lowest for the tilt-wing configuration, whereas at the intermediate and higher speeds of transition flight the power requirements of the flapped configurations are lowest. These observations indicate that the combination tilt-wing—deflected-slipstream configuration is a good configuration in that it has relatively low power requirements throughout the entire transition flight range. In addition, the longitudinal trim problems of this combination configuration can be handled easily by use of a rearward location of the wing pivot and by properly programing the wing tilt angle and flap deflections with forward speed in transition.

The results also indicate that the power requirements for the deflected-slipstream configuration are greatly increased in the region of ground effect and that the power requirements for the tilt-wing configuration are least affected by the ground, probably because the wing is stalled and appreciable power is required out of the region of ground effect. The power requirements for the combination configuration in the region of ground effect are only slightly larger than those for the tilt-wing configuration at the lower speeds and are lower than those for the

tilt-wing configuration at speeds above about 30 knots. This aspect is particularly significant in the consideration of short-take-off-and-landing (STOL) aircraft.

The leading-edge slat appeared to be of little value except to the deflected-slipstream configuration with the flaps at large deflections.

Langley Research Center,
National Aeronautics and Space Administration,
Langley Field, Va., October 21, 1959.

APPENDIX

CHARACTERISTICS OF THE 17-FOOT TEST SECTION

The results of the investigation in the 7- by 10-foot test section reported in reference 5 indicated the need for a much larger wind-tunnel test section or much smaller models in order to avoid significant tunnel-wall effects. In general, these effects resulted in premature separation on the model. Errors could be determined at static-thrust conditions by comparison of static-thrust characteristics obtained in the 7- by 10-foot tunnel test section with those obtained in a large room. It is fairly certain that similar effects are also present to an unknown extent at forward-speed conditions. Inasmuch as there is no known way to correct for these effects, it appeared that reliable data could be obtained only through the use of a larger test section since construction of smaller models with the necessary moving parts (deflectable flaps, tiltable wings, powered propellers, etc.) and associated instrumentation would soon prove prohibitive in cost. In addition, references 4 and 5 indicated difficulty in controlling tunnel airspeeds in the range of low velocities (high thrust coefficients) which were necessary to simulate the transition speed range. The lower Reynolds numbers associated with smaller models were also undesirable. Reference 9 presents some information on the 17-foot test section and some comparisons between data obtained in the 7- by 10-foot test section and the 17-foot test section.

Figure 40 presents a plan view of the 17-foot test section. In spite of the fairly long settling chamber upstream of this test section, difficulties were encountered in the development of sufficiently uniform velocity distributions. Initial development tests in a 1/10-scale model tunnel revealed a pronounced velocity gradient in the streamwise direction at the tunnel center line, which was probably caused by the influence of the low static pressures in the smaller downstream test section. It was therefore necessary to increase the divergence of the sidewalls to a greater extent than would be required for boundary-layer buildup alone. Subsequent tunnel calibration showed that satisfactory flow distribution had been obtained. The tunnel calibration was in excellent agreement with the pilot-model calibration.

The dynamic-pressure distribution in the vertical plane at the tunnel center line is presented in figure 41. The reduction in dyanmic pressure near the floor at downstream locations is a direct result of the large divergence required to obtain the flat center-line distribution shown.

The curvature at the entrance to the 17-foot test section was greater than that normally desired in entrance design but was necessary because

of the close proximity of the turning vanes as shown in figure 40. This abrupt entrance produced a velocity peak on the curved surface as indicated by the one open contour line $q/q_{cl} = 0.98$ in the lower upstream part of figure 41. The boundary layer was not seriously disturbed by the slightly adverse pressure gradient behind this peak as shown by the boundary-layer profiles presented in figure 42.

The dynamic pressure at the center line of the 17-foot test section is determined from the instrumentation normally used in the 7- by 10-foot test section, by means of the relation

$$q_{cl} = 0.0705Q'$$

where Q' is the manometer reading for the 7- by 10-foot section. The constant, 0.0705, includes manometer calibration factors.

Alinement-angle tests with a 7-foot-span calibration wing indicate a 0.25° upflow angle at the tunnel center line at a position 8.5 feet above the tunnel floor and a 0.75° upflow angle at a position 3 feet above the tunnel floor. A survey of crossflow in the vertical plane at the tunnel center line was made with hemispherical angularity probes and is presented in figure 43. The alinement angle for any semispan wing will be a weighted average of the angularity distribution over the span of the wing. Tests with a 5-foot-semispan calibration wing indicated a crossflow angle of 1.25° from right to left when facing upstream (fig. 43).

Surveys of flow in vertical planes 4 feet on either side of the center line yielded almost identical dynamic-pressure distributions, angularity distributions, and boundary-layer profiles. Therefore, the region available for testing is at least 8 feet wide and 12 feet long at the tunnel center line. It is somewhat shorter for floor-mounted models because of the reduced dynamic pressures in the downstream region.

Inasmuch as these pressure gradients were predicted by the pilot-tunnel tests, the model support system was designed to be movable along the tunnel center line to any test position desired. The center of the turntable can be located anywhere between stations 2.5 and 10.5, as indicated in figure 40.

Two types of model support systems are available; each uses strain-gage-balance installations. For complete models a strut support system which may be lowered to the proximity of the floor for tests of ground effect is provided. In addition, semispan models may be mounted on a 3-component strain-gage balance located directly beneath the tunnel floor.

REFERENCES

1. Newsom, William A., Jr.: Effect of Propeller Location and Flap Deflection on the Aerodynamic Characteristics of a Wing-Propeller Combination for Angles of Attack From 0° to 80°. NACA TN 3917, 1957.

2. Kuhn, Richard E.: Take-Off and Landing Distance and Power Requirements of Propeller-Driven STOL Airplanes. Preprint No. 690, S.M.F. Pub. Fund Preprint, Inst. Aero. Sci., Inc., Jan. 1957.

3. Hayes, William C., Jr., Kuhn, Richard E., and Sherman, Irving R.: Effects of Propeller Position and Overlap on Slipstream Deflection Characteristics of a Wing-Propeller Configuration Equipped With a Sliding and Fowler Flap. NACA TN 4404, 1958.

4. Kuhn, Richard E., and Draper, John W.: Investigation of the Aerodynamic Characteristics of a Model Wing-Propeller Combination and of the Wing and Propeller Separately at Angles of Attack up to 90°. NACA Rep. 1263, 1956. (Supersedes NACA TN 3304 by Draper and Kuhn.)

5. Kuhn, Richard E., and Hayes, William C., Jr.: Wind-Tunnel Investigation of Effect of Propeller Slipstreams on Aerodynamic Characteristics of a Wing Equipped With a 50-Percent-Chord Sliding Flap and a 30-Percent-Chord Slotted Flap. NACA TN 3918, 1957.

6. Gillis, Clarence L., Polhamus, Edward C., and Gray, Joseph L., Jr.: Charts for Determining Jet-Boundary Corrections for Complete Models in 7- by 10-Foot Closed Rectangular Wind Tunnels. NACA WR L-123, 1945. (Formerly NACA ARR L5G31.)

7. Lowry, John G., Riebe, John M., and Campbell, John P.: The Jet-Augmented Flap. Preprint No. 715, S.M.F. Fund Paper, Inst. Aero. Sci., Jan. 1957.

8. Taylor, Robert T.: Wind-Tunnel Investigation of Effect of Ratio of Wing Chord to Propeller Diameter with Addition of Slats on the Aerodynamic Characteristics of Tilt-Wing VTOL Configurations in the Transition Speed Range. NASA TN D-17, 1959.

9. Kuhn, Richard E., and Naeseth, Rodger L.: Tunnel-Wall Effects Associated With VTOL-STOL Model Testing. Presented to Wind Tunnel and Model Testing Panel of AGARD (Brussels, Belgium), Mar. 2-5, 1959.

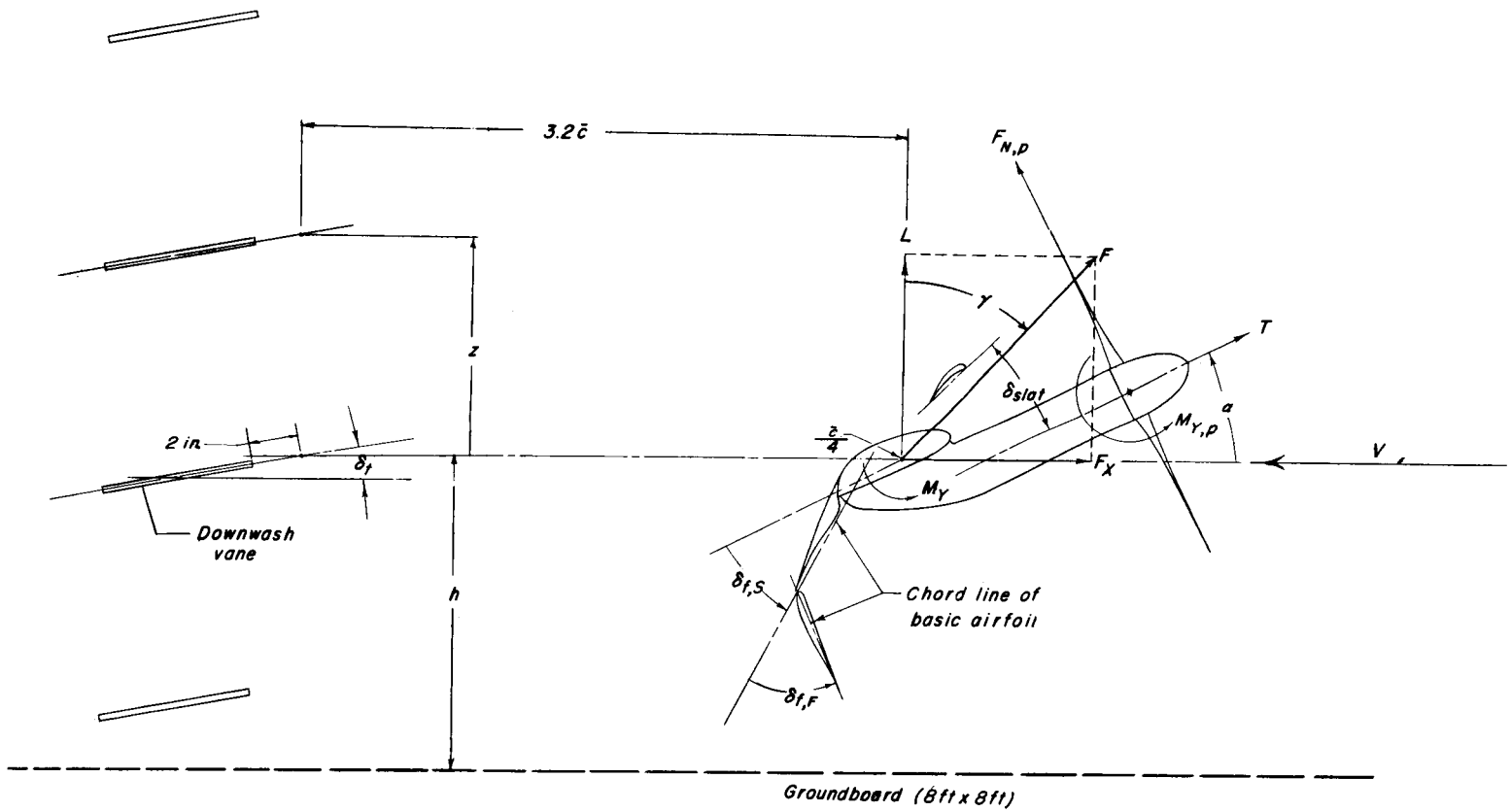

Figure 1.- Positive sense of forces, moments, and angles.

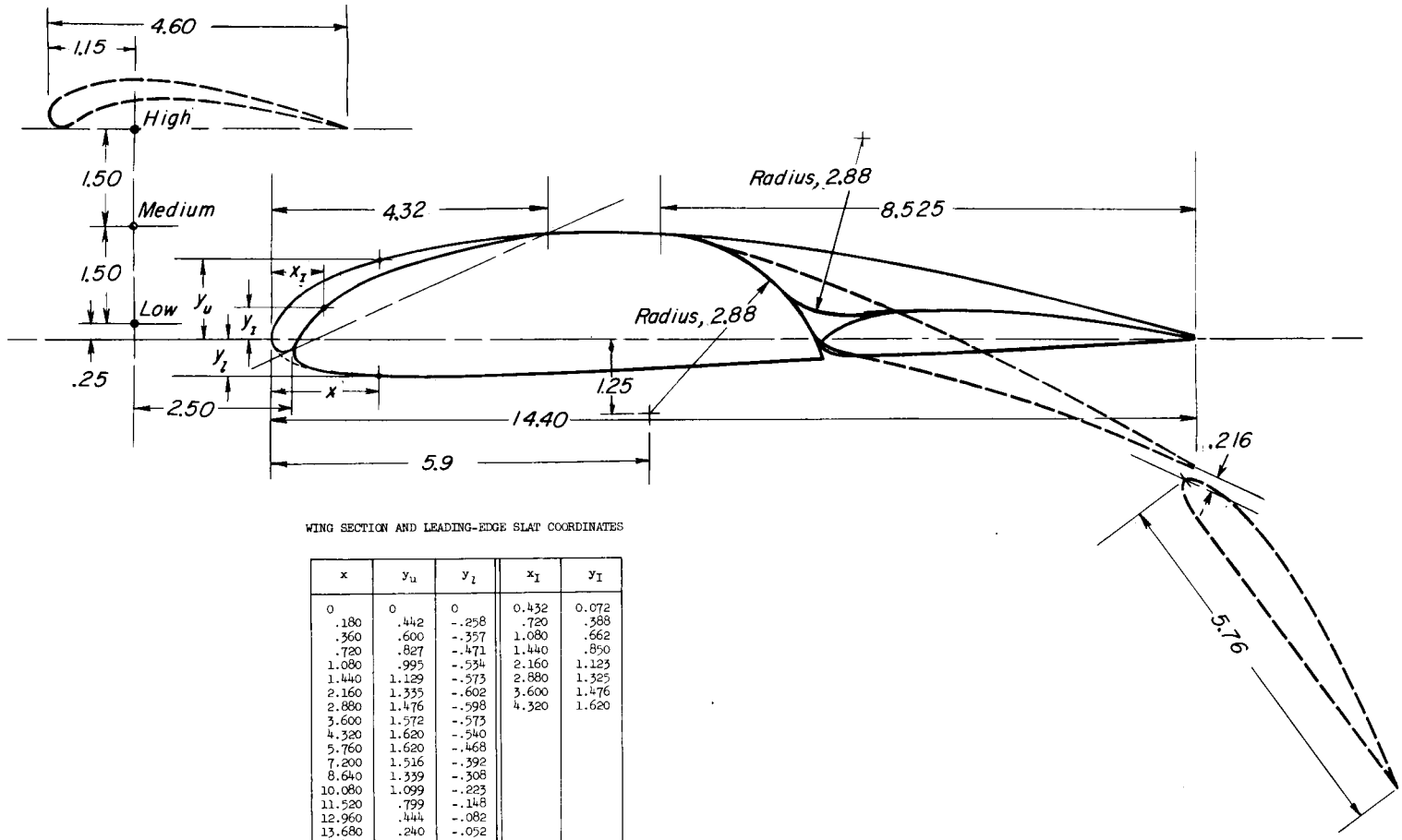

WING SECTION AND LEADING-EDGE SLAT COORDINATES

x	y_u	y_l	x_I	y_I
0	0	0	0.432	0.072
.180	.442	-.258	.720	.388
.360	.600	-.357	1.080	.662
.720	.827	-.471	1.440	.850
1.080	.995	-.534	2.160	1.123
1.440	1.129	-.573	2.880	1.325
2.160	1.335	-.602	3.600	1.476
2.880	1.476	-.598	4.320	1.620
3.600	1.572	-.573		
4.320	1.620	-.540		
5.760	1.620	-.468		
7.200	1.516	-.392		
8.640	1.339	-.308		
10.080	1.099	-.223		
11.520	.799	-.148		
12.960	.444	-.082		
13.680	.240	-.052		
14.400	.023	-.023		
Leading-edge radius = 0.357				

Figure 2.- Geometric characteristics of wing section. All dimensions are in inches.

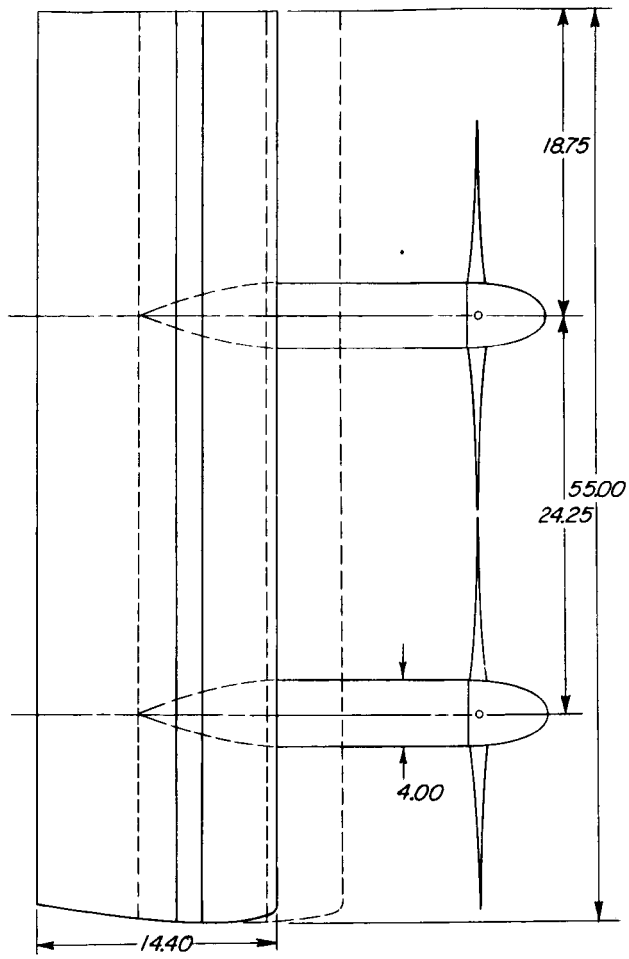

Geometric Characteristics

Wing:		
Area, sq ft		5.48
Semispan, ft		4.58
Chord, ft		1.20
Airfoil section	NACA	4415
Aspect ratio, full span		7.66
Propellers:		
Diameter, ft		2.00
Nacelle diameter, ft		.033
Number of blades (each)		3

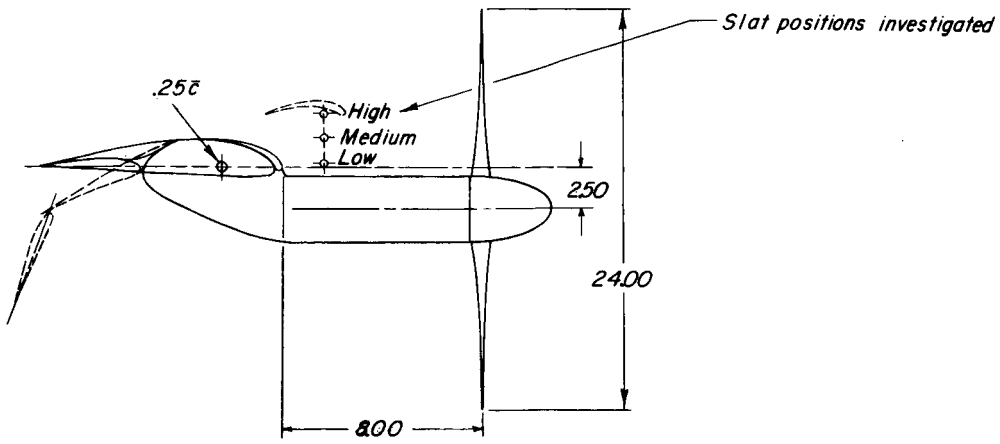

Figure 3.- Drawing of model. All dimensions are in inches.

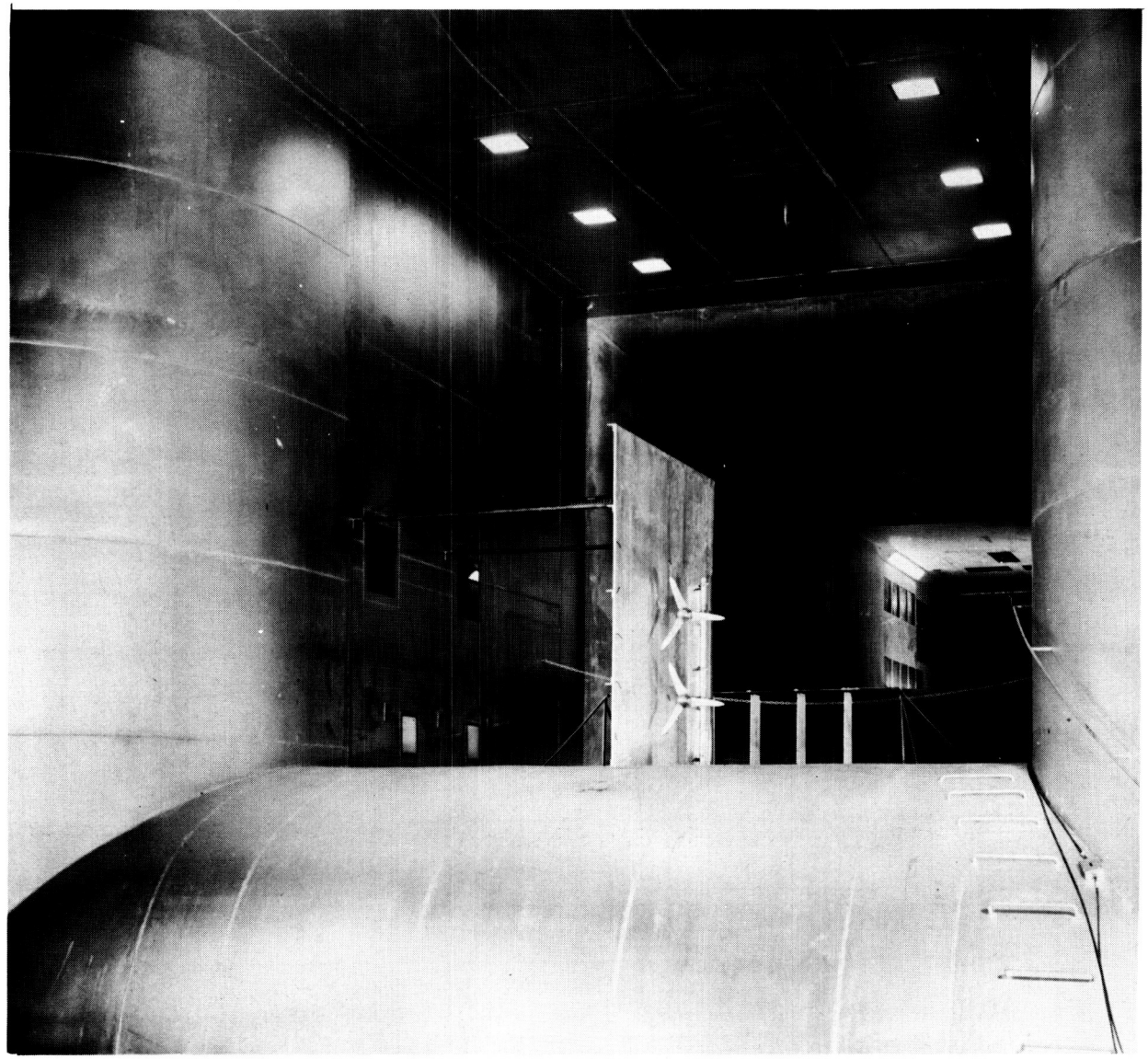

L-57-1192

Figure 4.- Photograph of model in 17-foot test section with ground board installed.

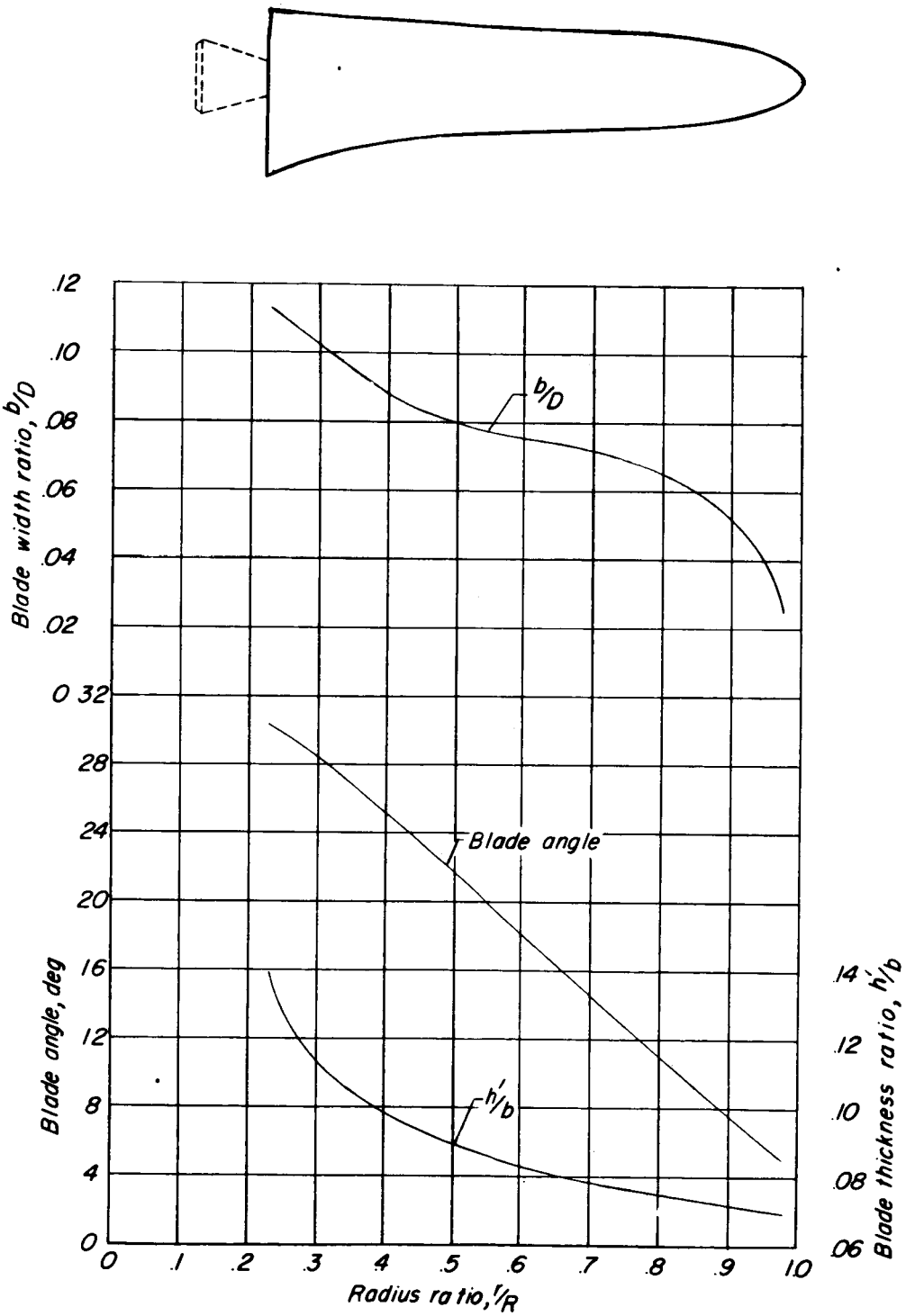

Figure 5.- Propeller blade form curves.

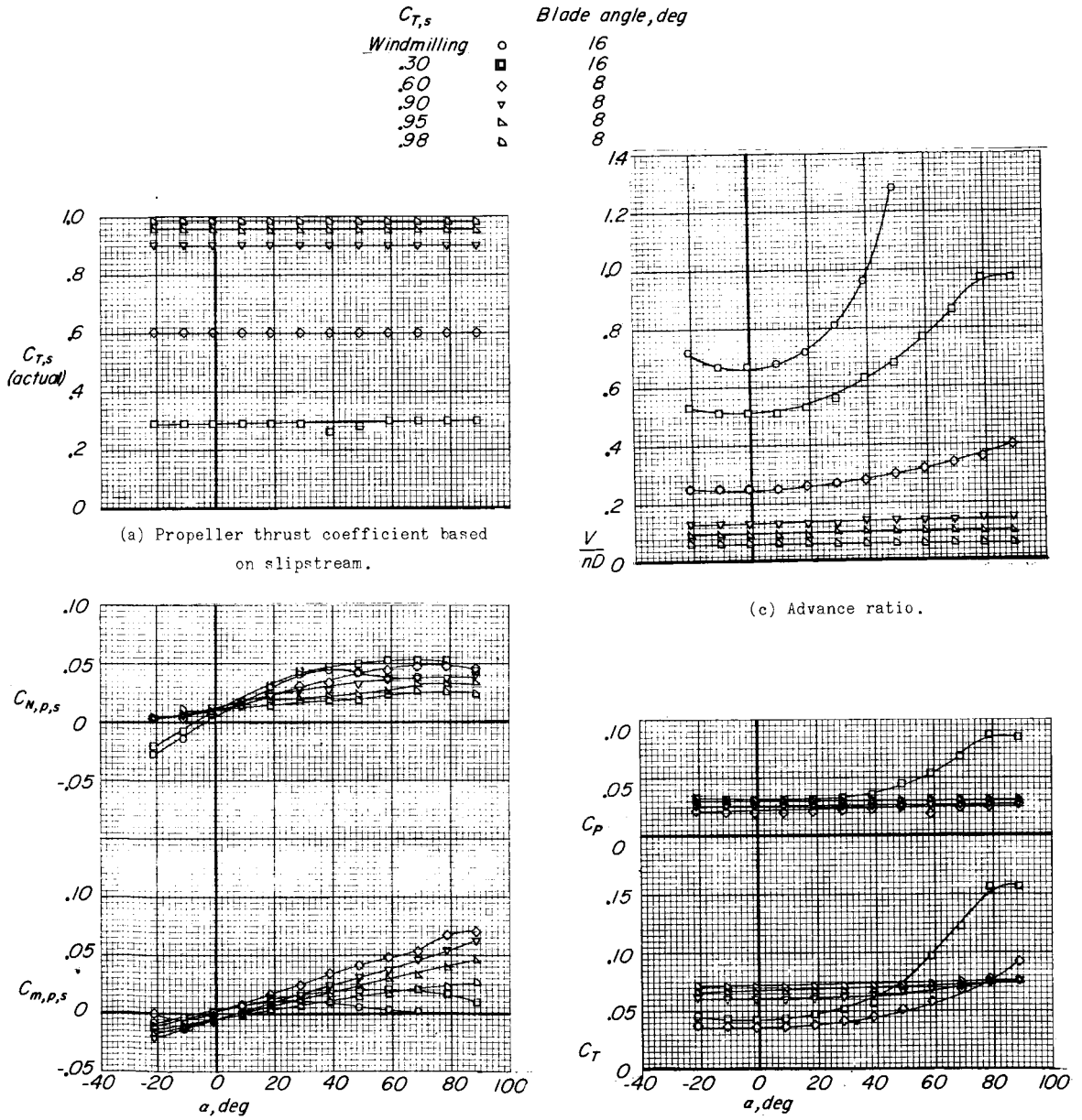

(a) Propeller thrust coefficient based on slipstream.

(b) Propeller normal-force and pitching-moment coefficients.

(c) Advance ratio.

(d) Propeller thrust and power coefficients.

Figure 6.- Propeller characteristics; wing removed.

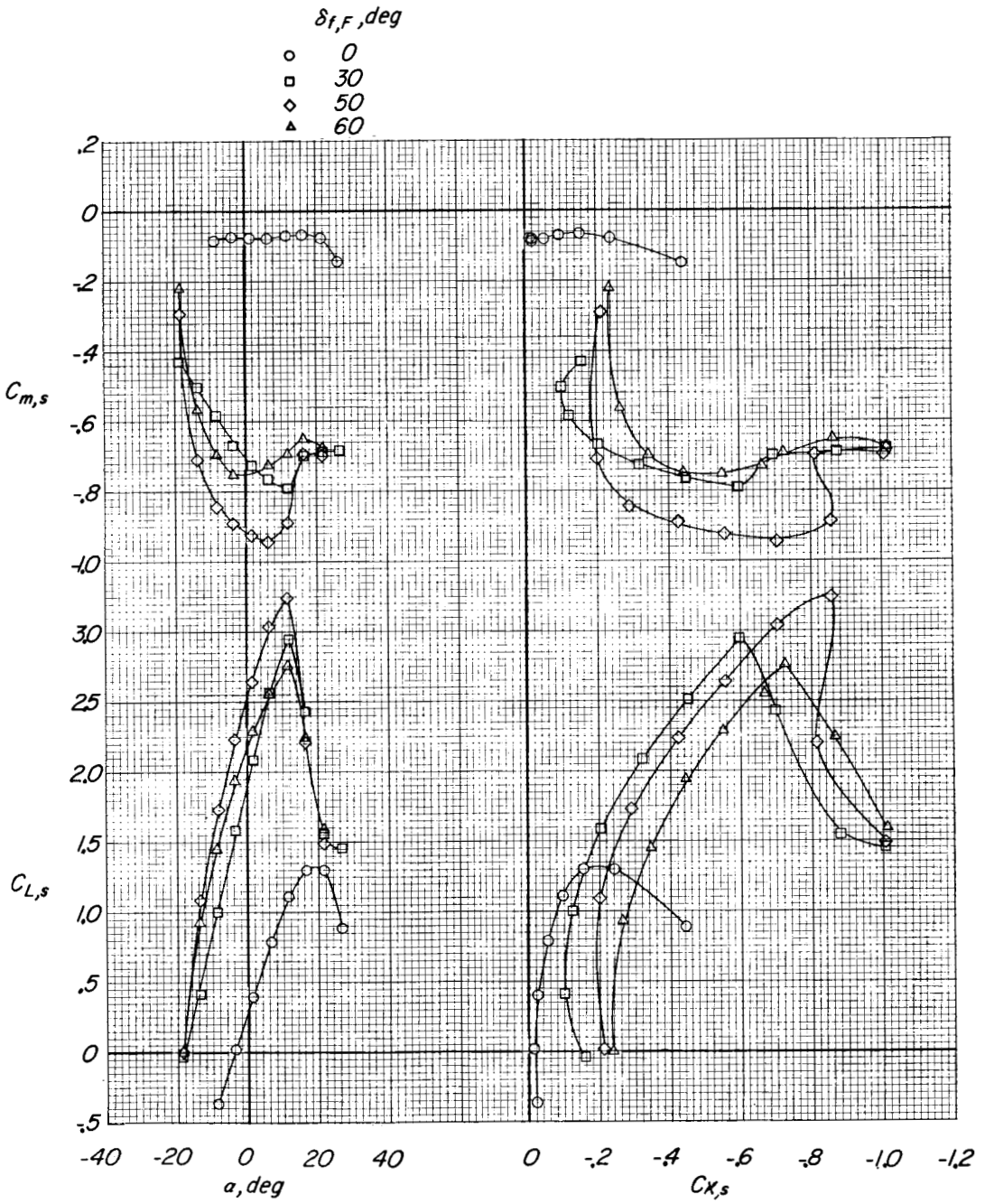

(a) $\delta_{f,S} = 0^{\circ}$.

Figure 7.- Aerodynamic characteristics of wing alone out of region of ground effect. Propellers off; slat retracted.

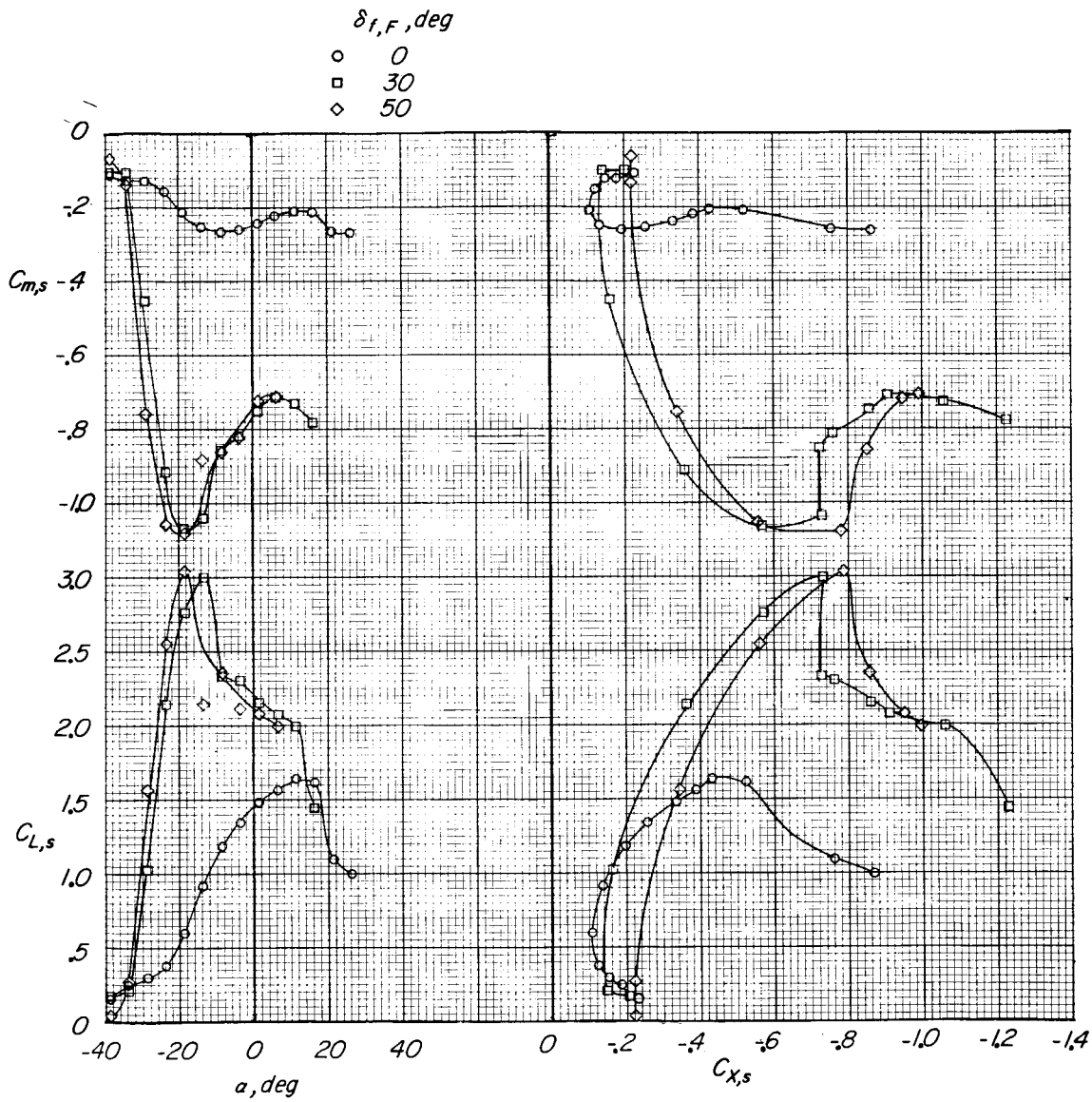

(b) $\delta_{f,S} = 30^{\circ}$.

Figure 7.- Continued.

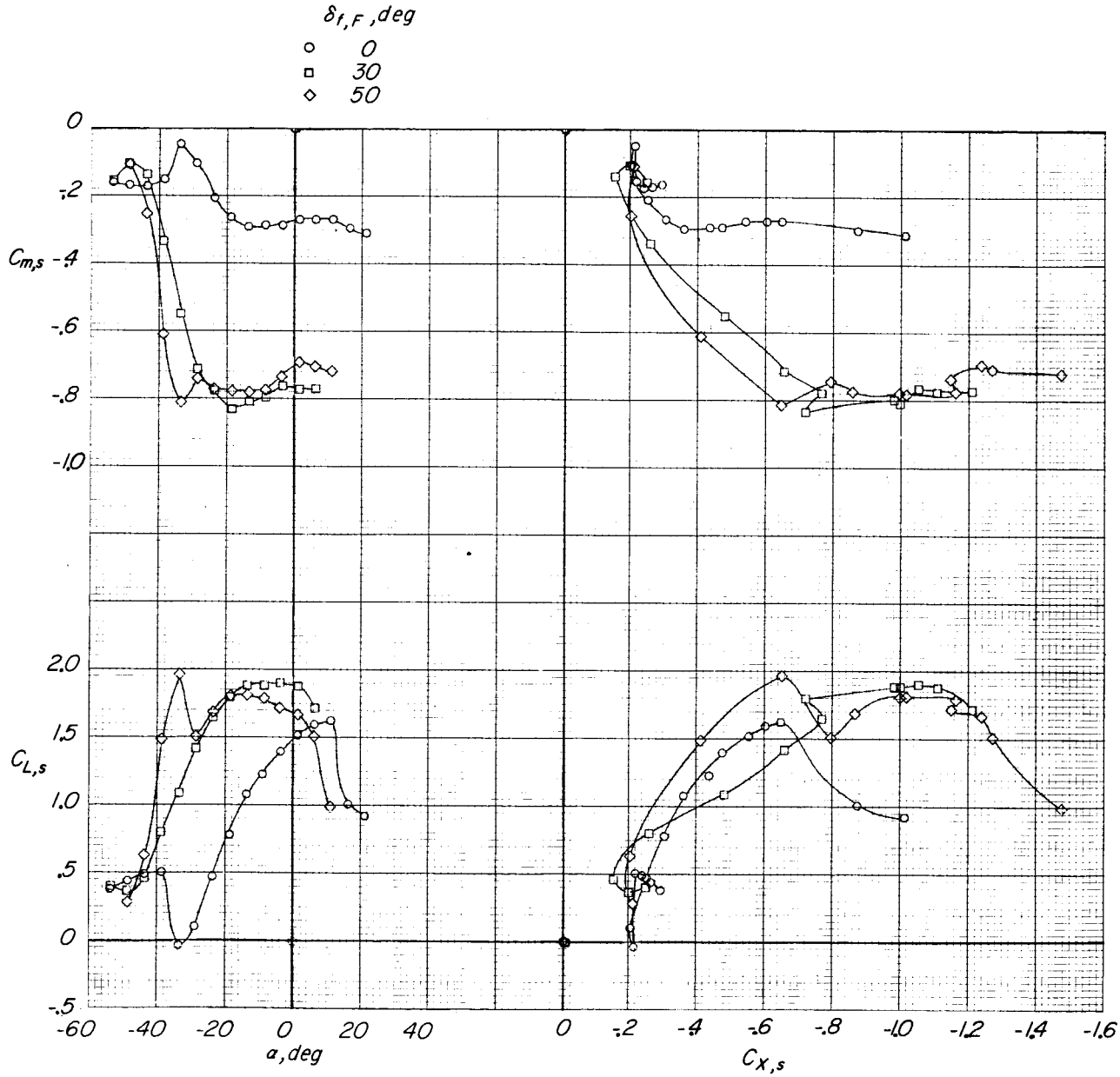

(c) $\delta_{f,S} = 50^{\circ}$.

Figure 7.- Concluded.

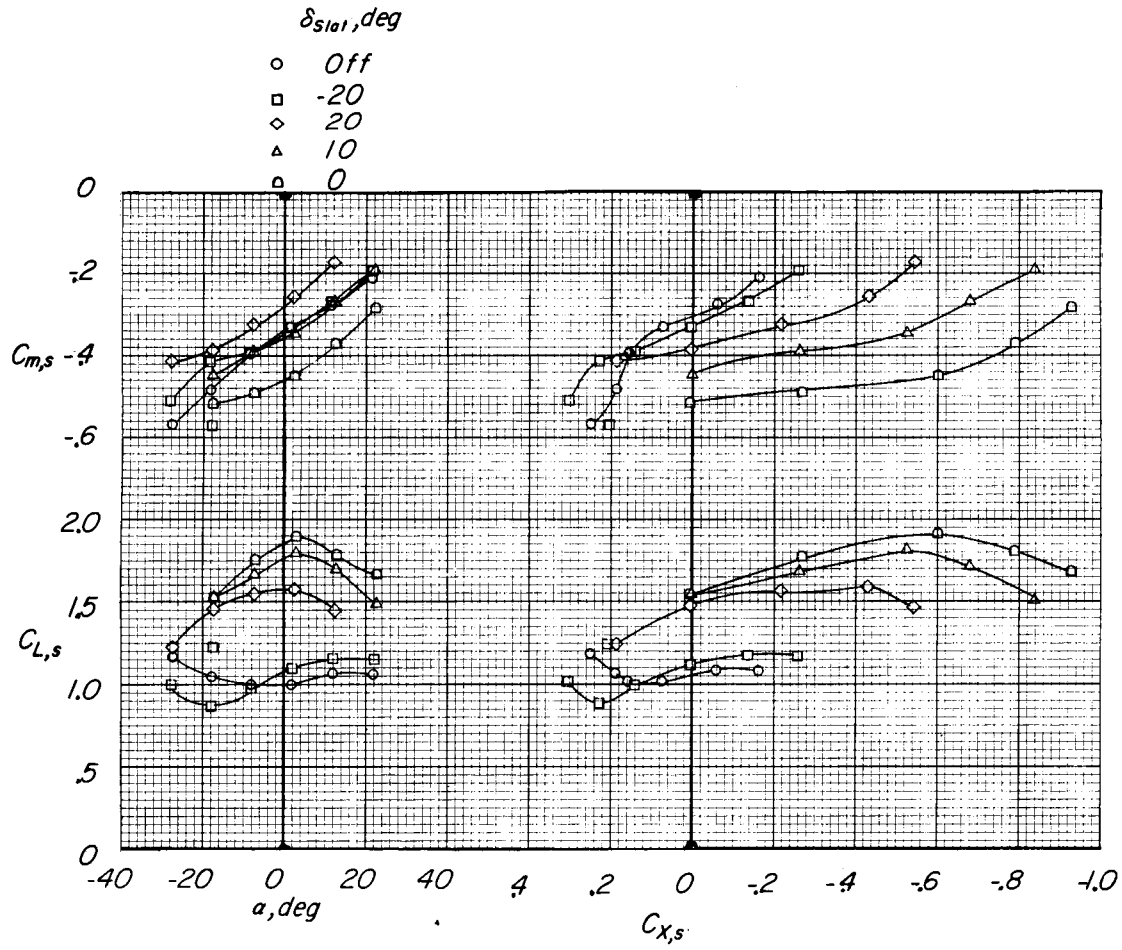

(a) Slat in high position.

Figure 8.- Effect of slat position and deflection on longitudinal aerodynamic characteristics of model. $C_{T,s} = 0.90$; $\delta_{f,S} = 50^{\circ}$; $\delta_{f,F} = 50^{\circ}$.

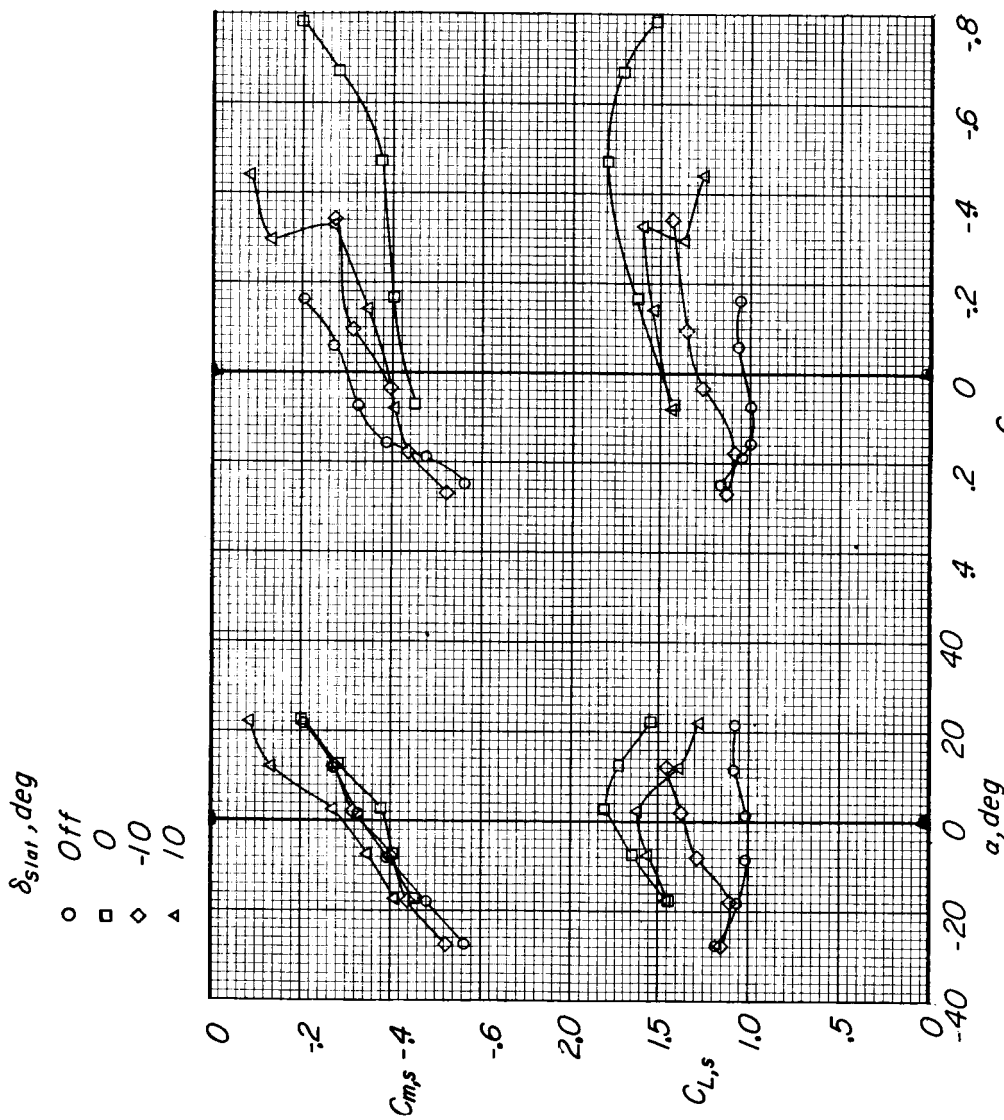

(b) Slat in middle position.

Figure 8.- Continued.

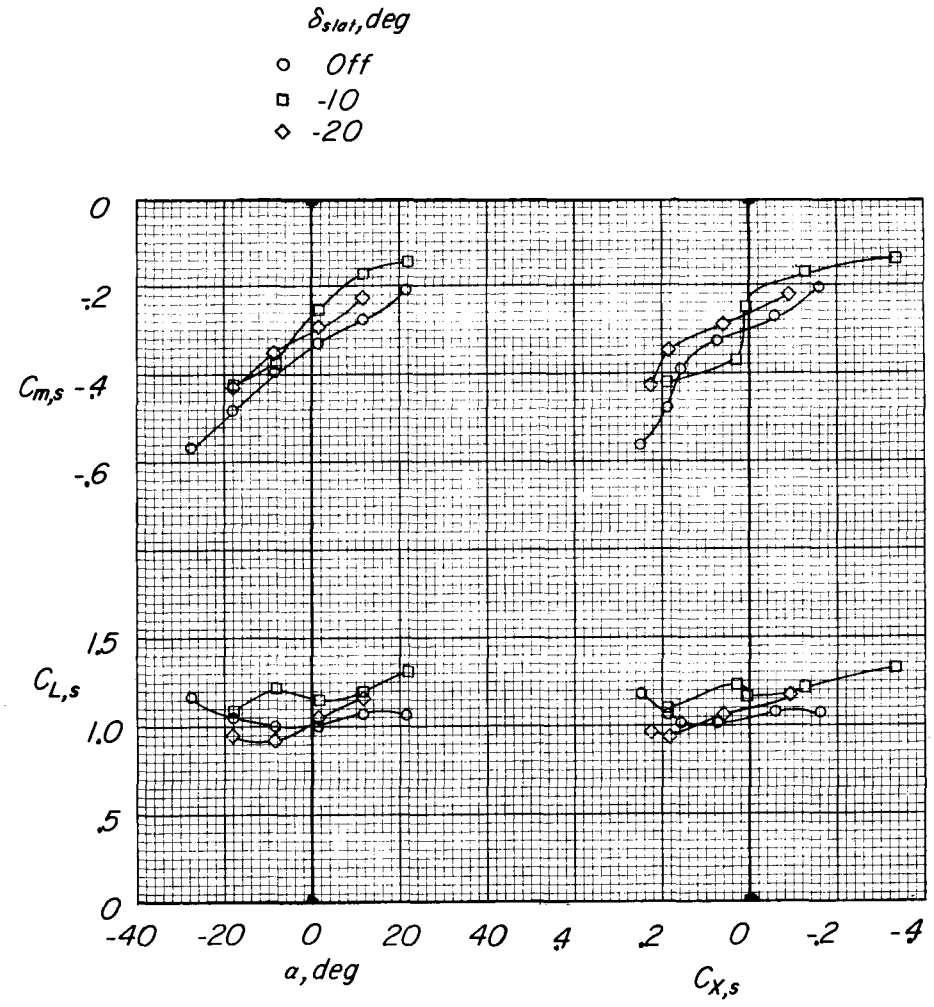

(c) Slat in low position.

Figure 8.- Concluded.

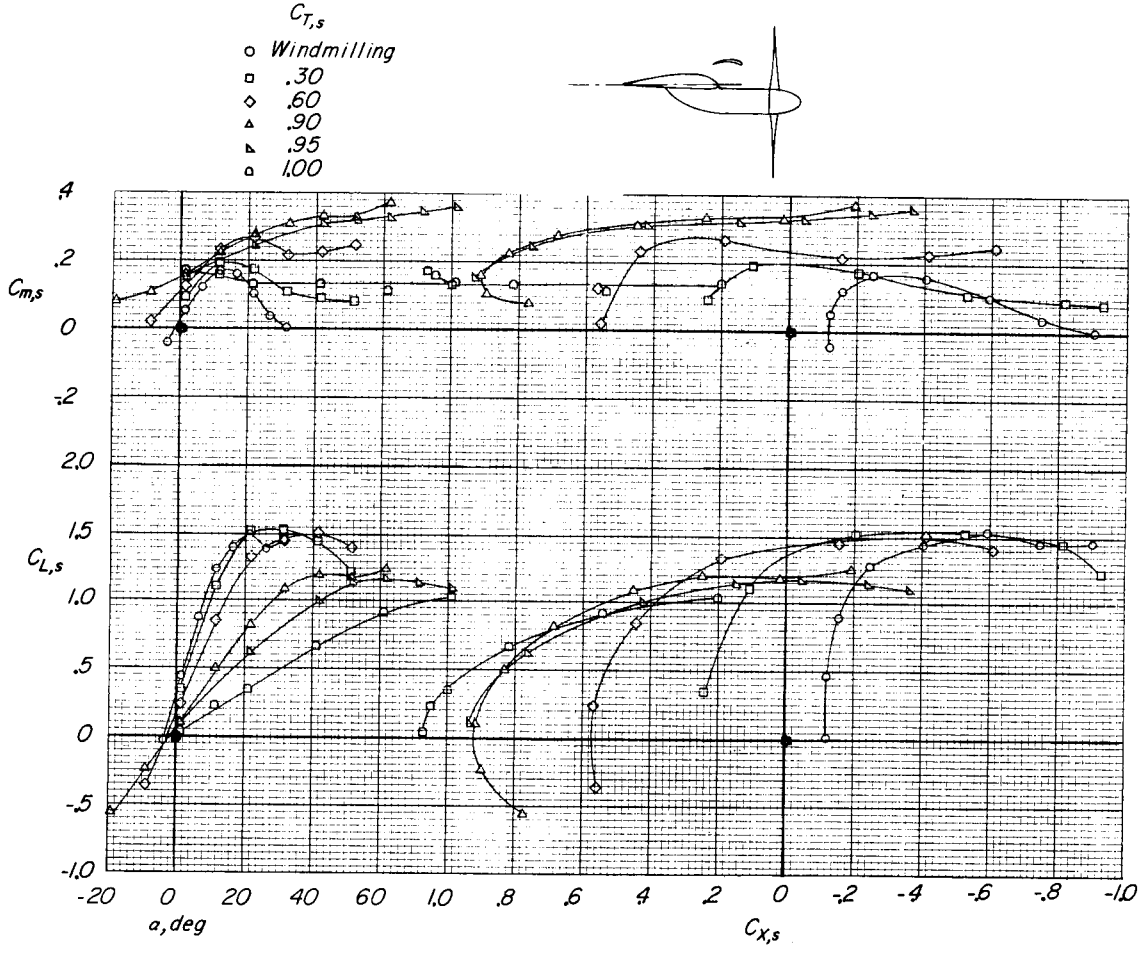

(a) Complete-model data.

Figure 9.- Aerodynamic characteristics of the model out of the region of ground effect. Tilt-wing configuration ($\delta_{f,S} = 0^{\circ}$; $\delta_{f,F} = 0^{\circ}$); slat in high position; $\delta_{slat} = 0^{\circ}$.

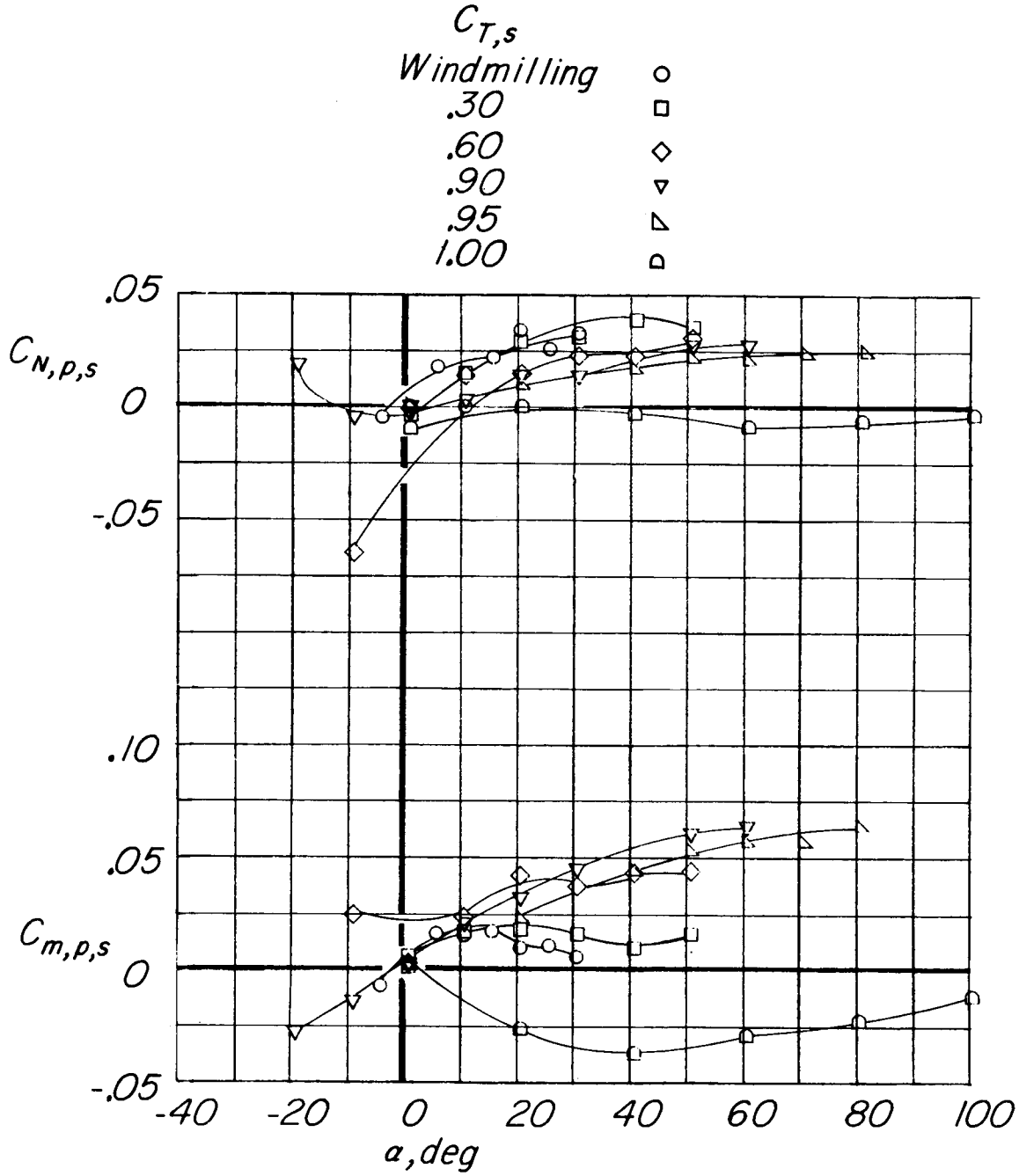

(b) Propeller normal-force and pitching-moment coefficients. Inboard propeller.

Figure 9.- Continued.

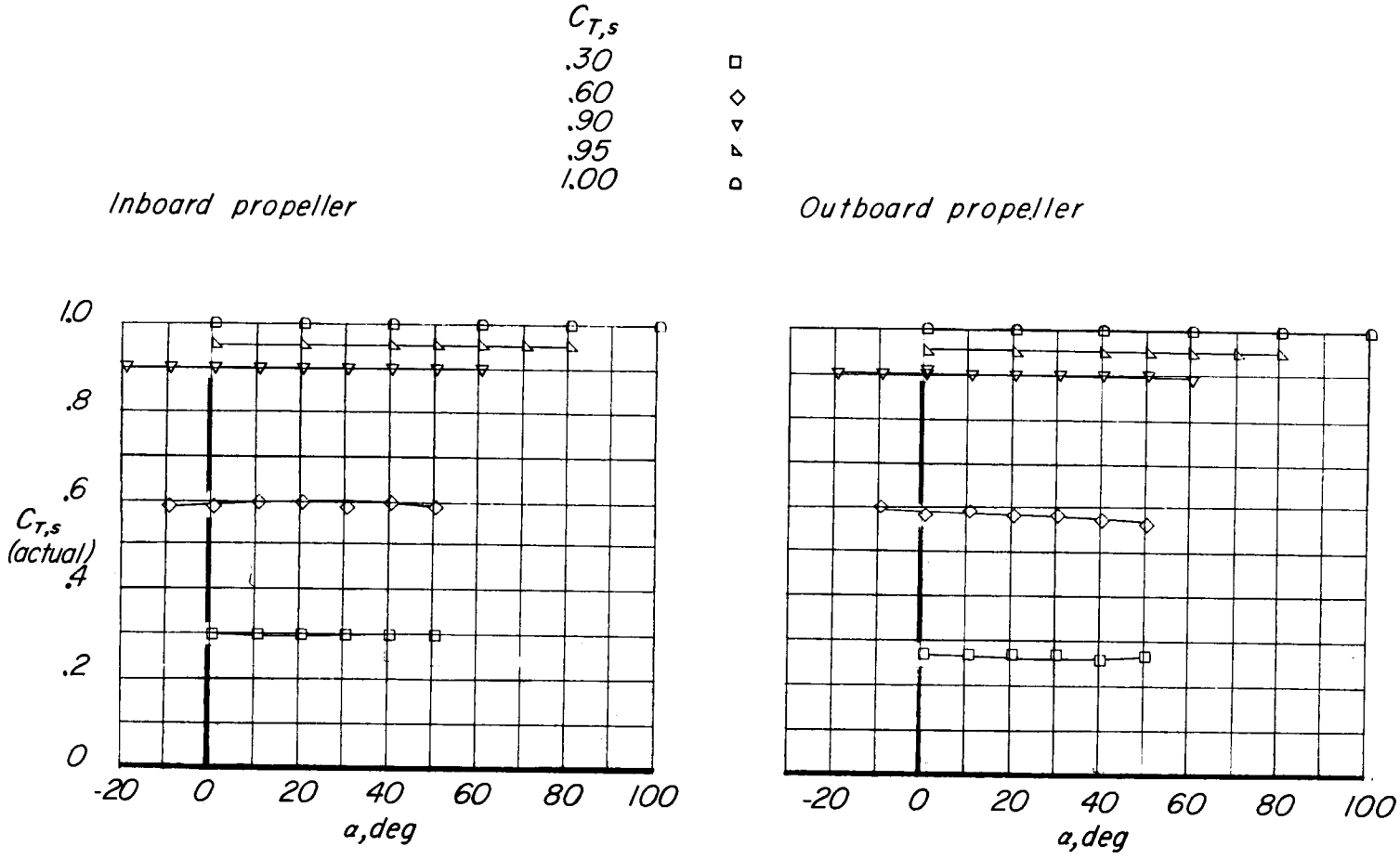

(c) Propeller thrust coefficient based on slipstream.

Figure 9.- Continued.

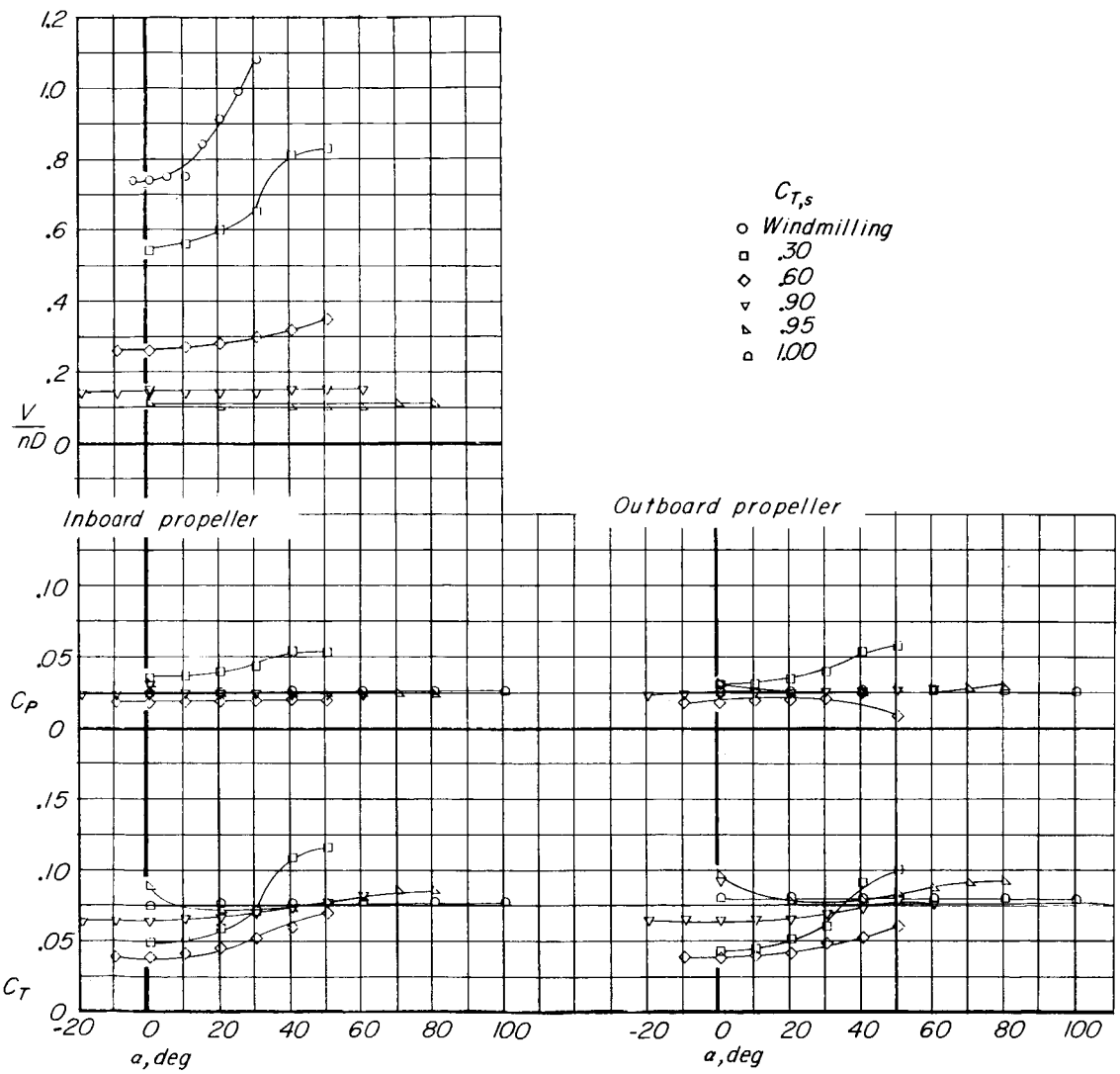

(d) Propeller thrust and power coefficients and advance ratio.

Figure 9.- Continued.

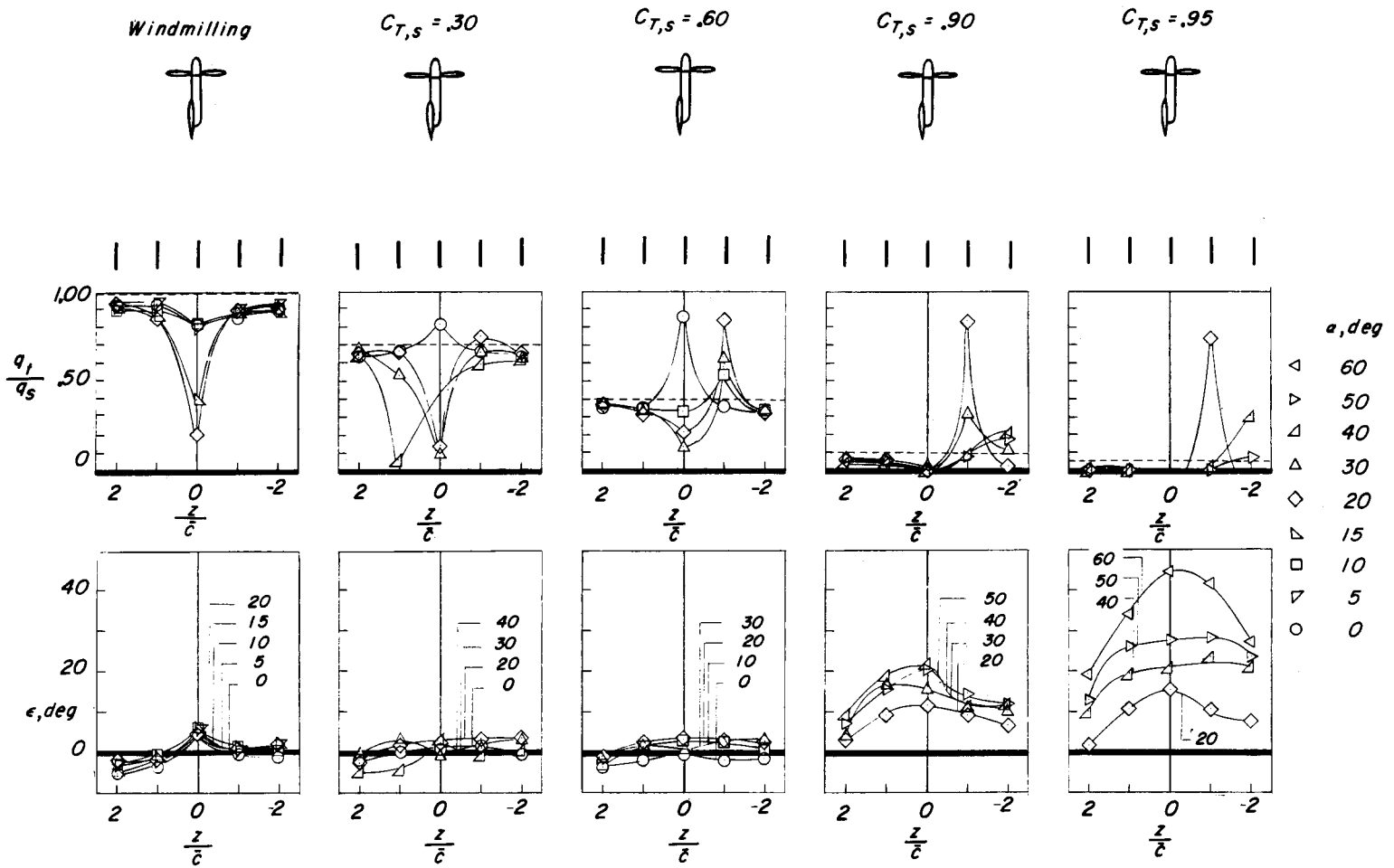

(e) Downwash and dynamic-pressure surveys. Dashed lines indicate level of free-stream dynamic pressure.

Figure 9.- Concluded.

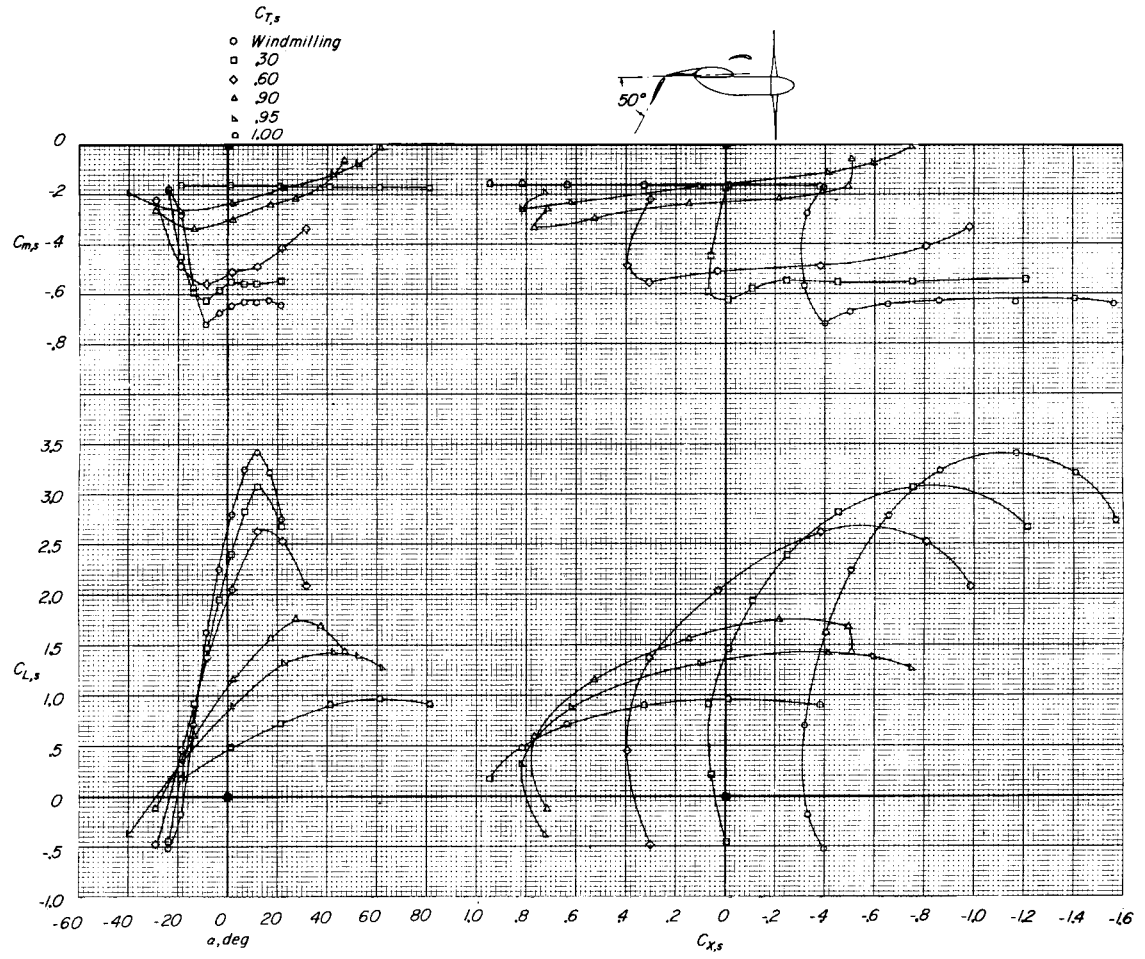

(a) Complete-model data.

Figure 10.- Aerodynamic characteristics of model out of region of ground effect. Combination configuration ($\delta_{f,S} = 0^{\circ}$; $\delta_{f,F} = 50^{\circ}$); slat in high position; $\delta_{slat} = 0^{\circ}$.

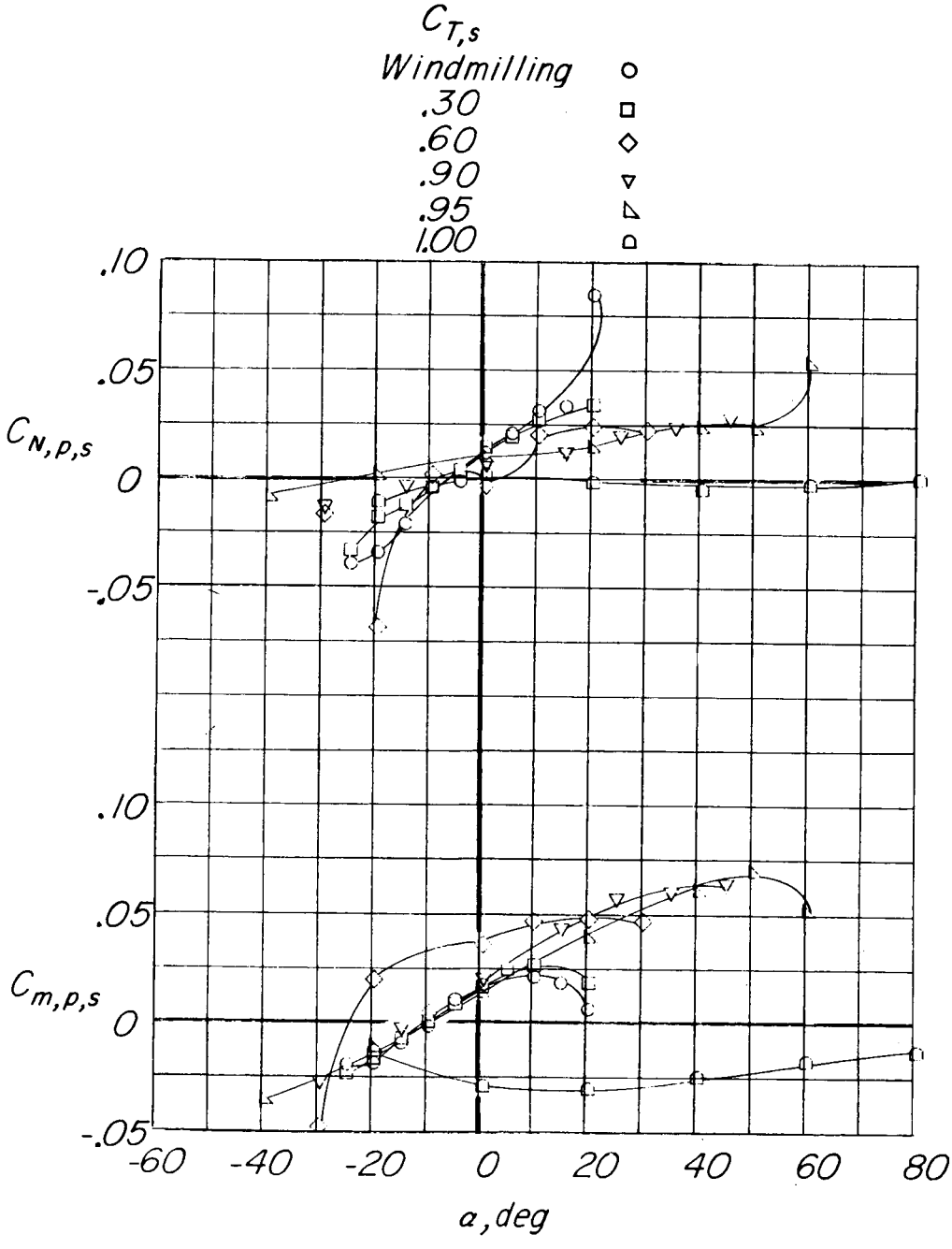

(b) Propeller normal-force and pitching-moment coefficients. Inboard propeller.

Figure 10.- Continued.

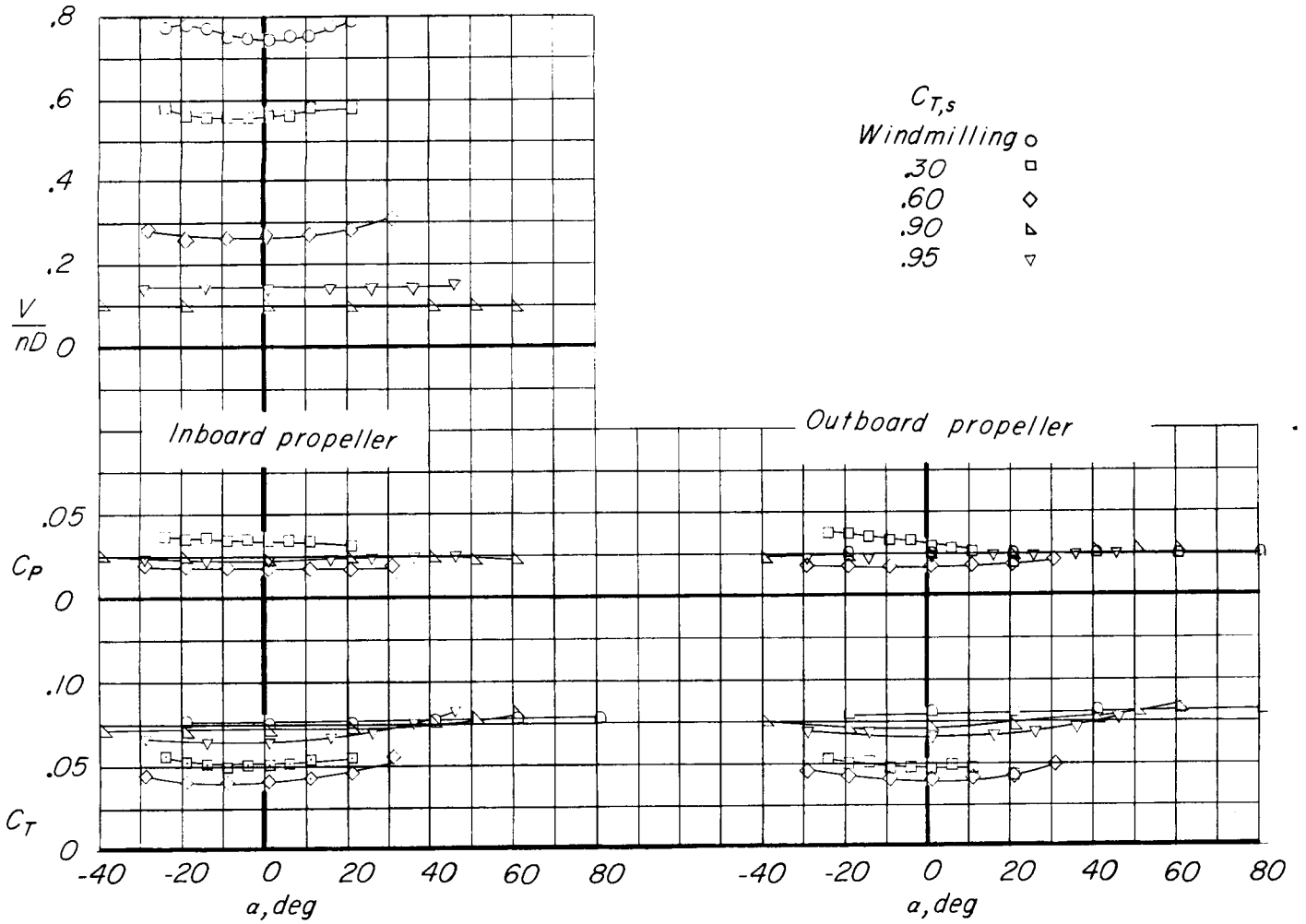

(c) Propeller thrust and power coefficients and advance ratio.

Figure 10.- Continued.

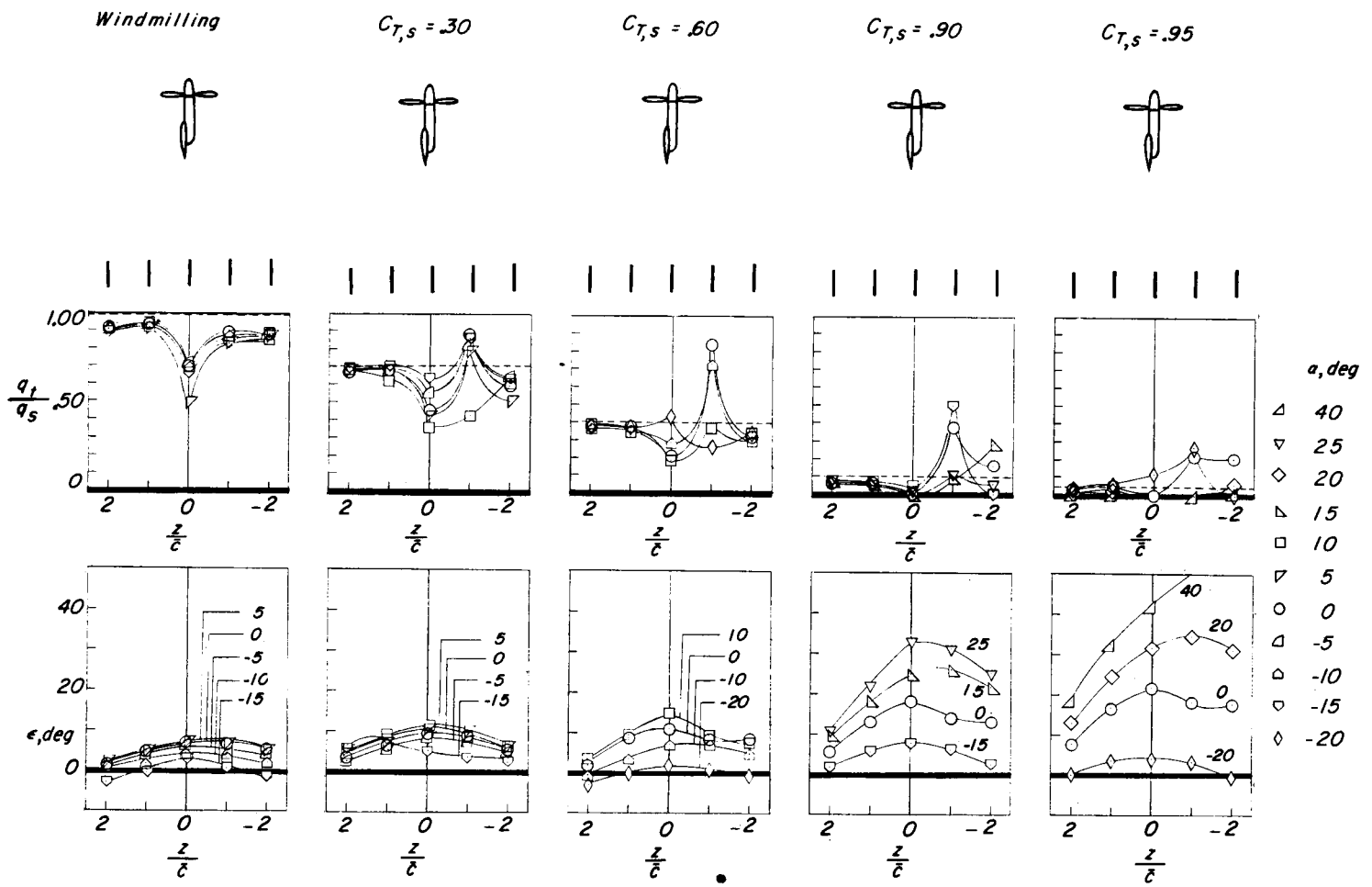

(d) Downwash and dynamic-pressure surveys. Dashed lines indicate level of free-stream dynamic pressure.

Figure 10.- Concluded.

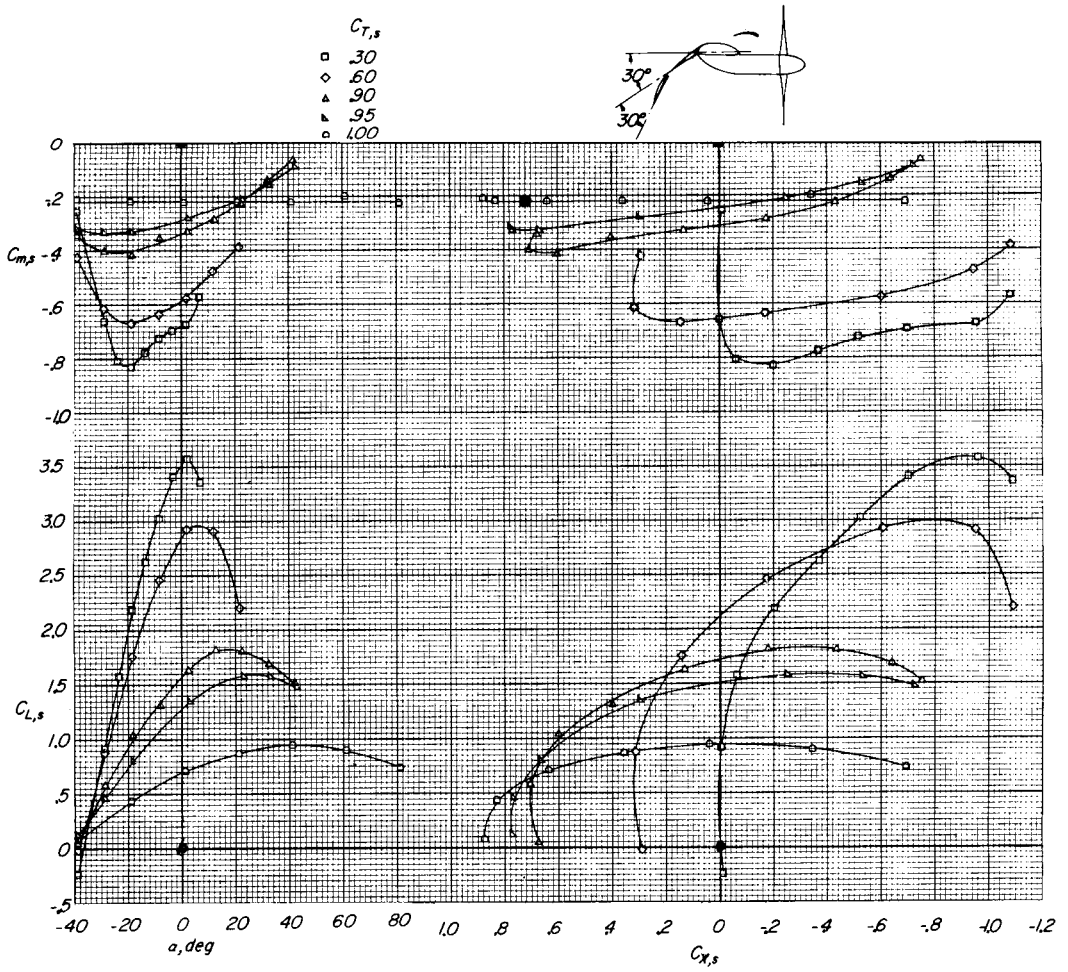

(a) Complete-model data.

Figure 11.- Aerodynamic characteristics of model out of region of ground effect. Deflected-slipstream configuration ($\delta_{f,S} = 30^\circ$; $\delta_{f,F} = 30^\circ$); slat in high position; $\delta_{slat} = 0^\circ$.

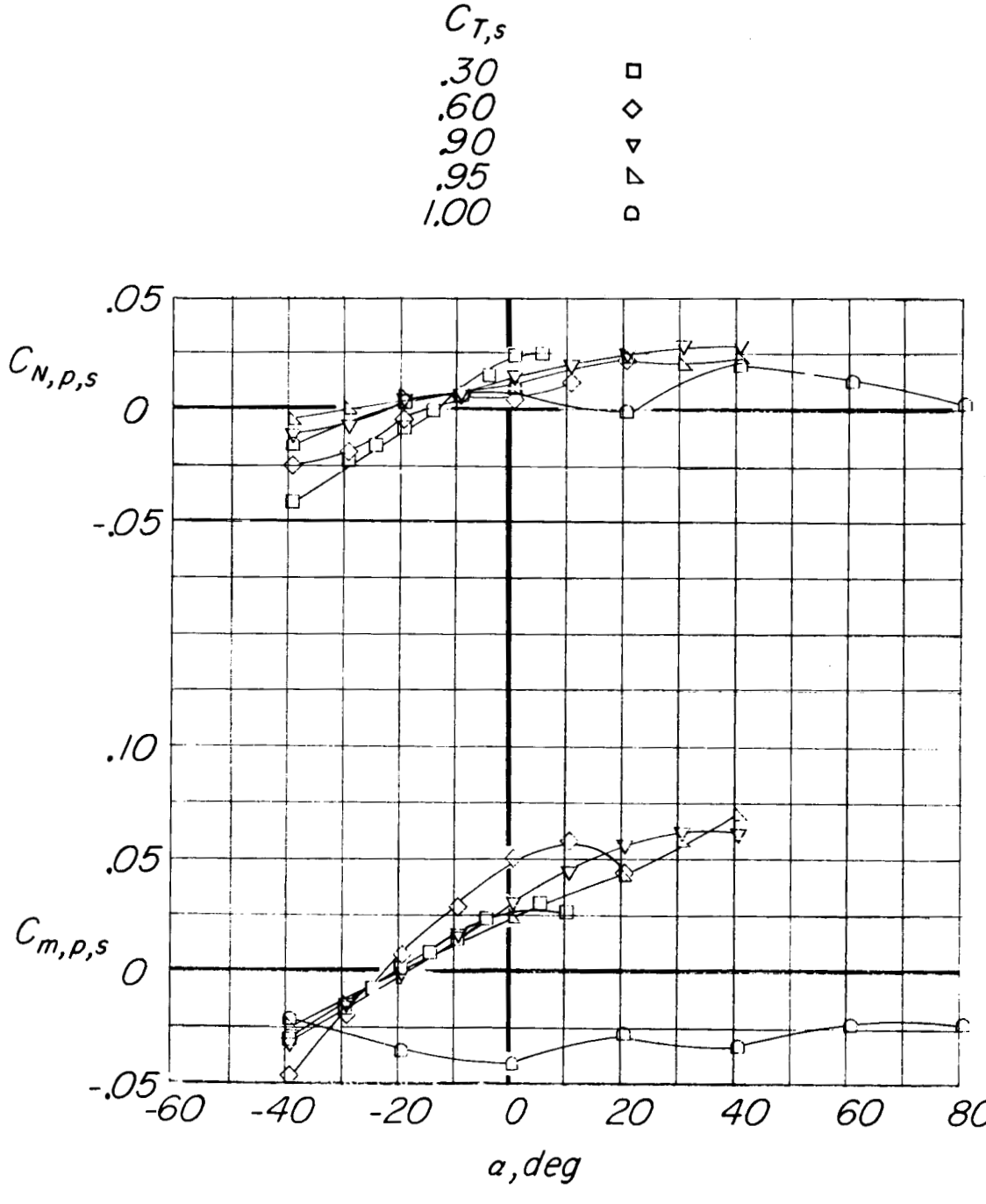

(b) Propeller normal-force and pitching-moment coefficients. Inboard propeller.

Figure 11.- Continued.

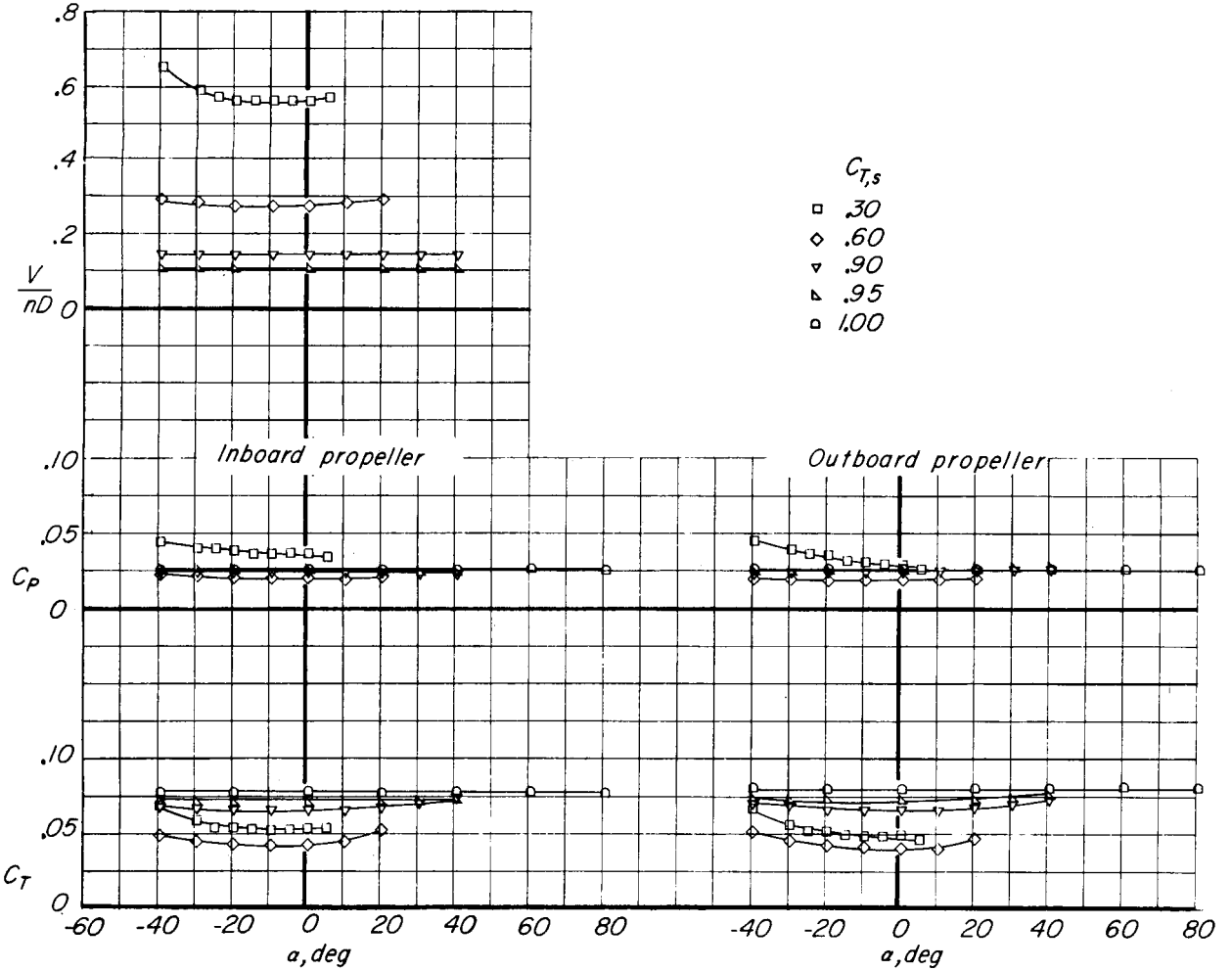

(c) Propeller thrust and power coefficients and advance ratio.

Figure 11.- Continued.

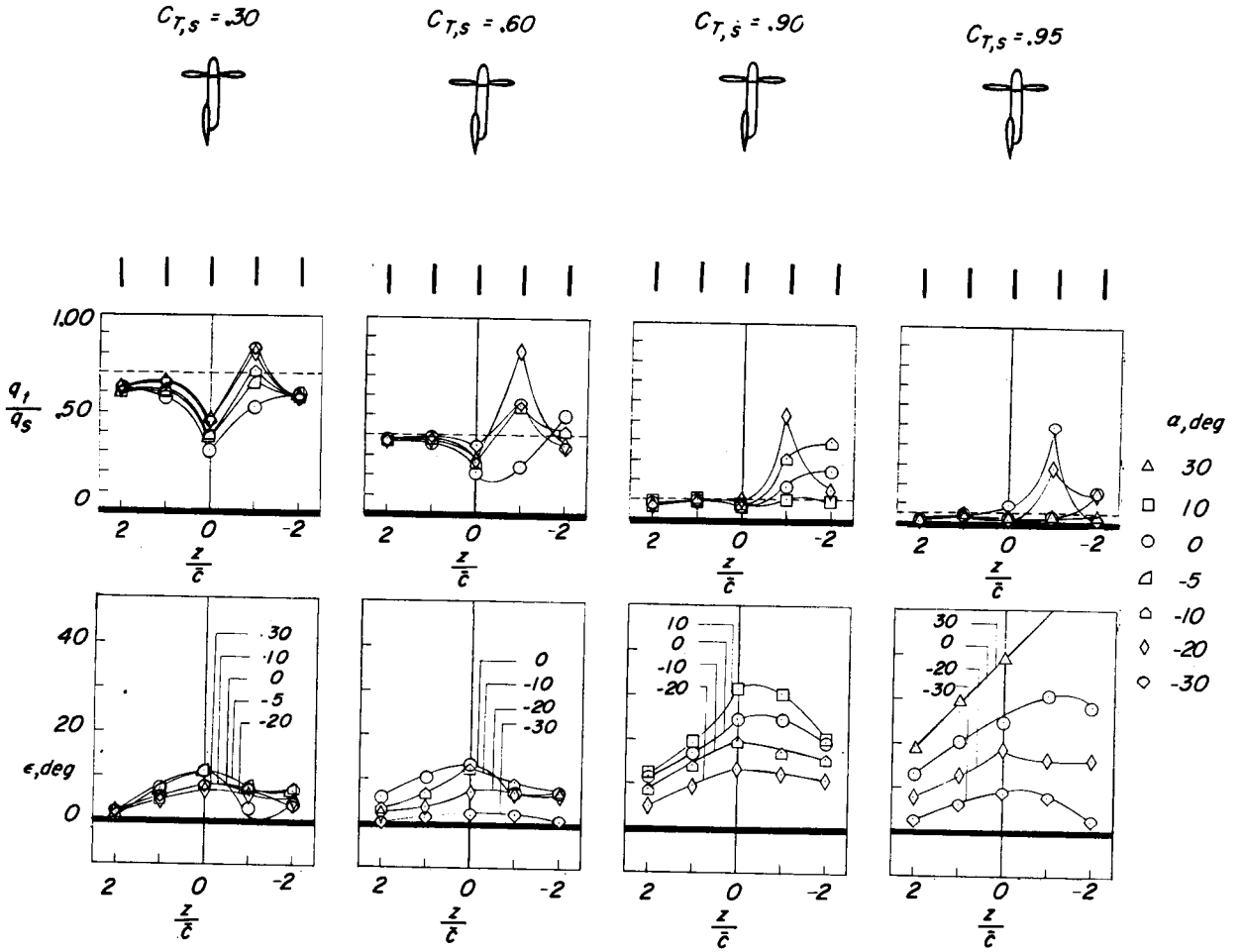

(d) Downwash and dynamic-pressure surveys. Dashed lines indicate level of free-stream dynamic pressure.

Figure 11.- Concluded.

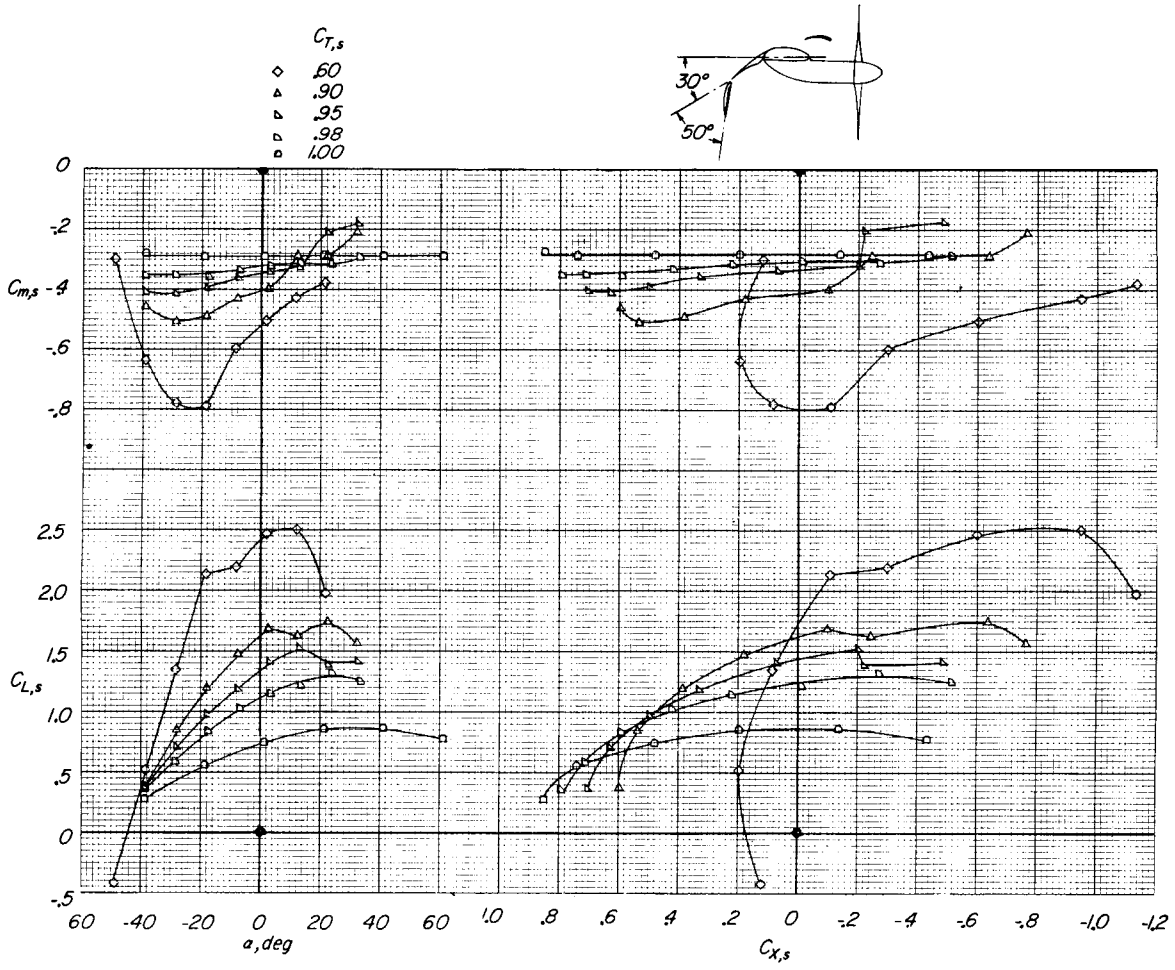

(a) Complete-model data.

Figure 12.- Aerodynamic characteristics of model out of region of ground effect. Deflected-slipstream configuration ($\delta_{f,S} = 30^\circ$; $\delta_{f,F} = 50^\circ$); slat in high position; $\delta_{slat} = 0^\circ$.

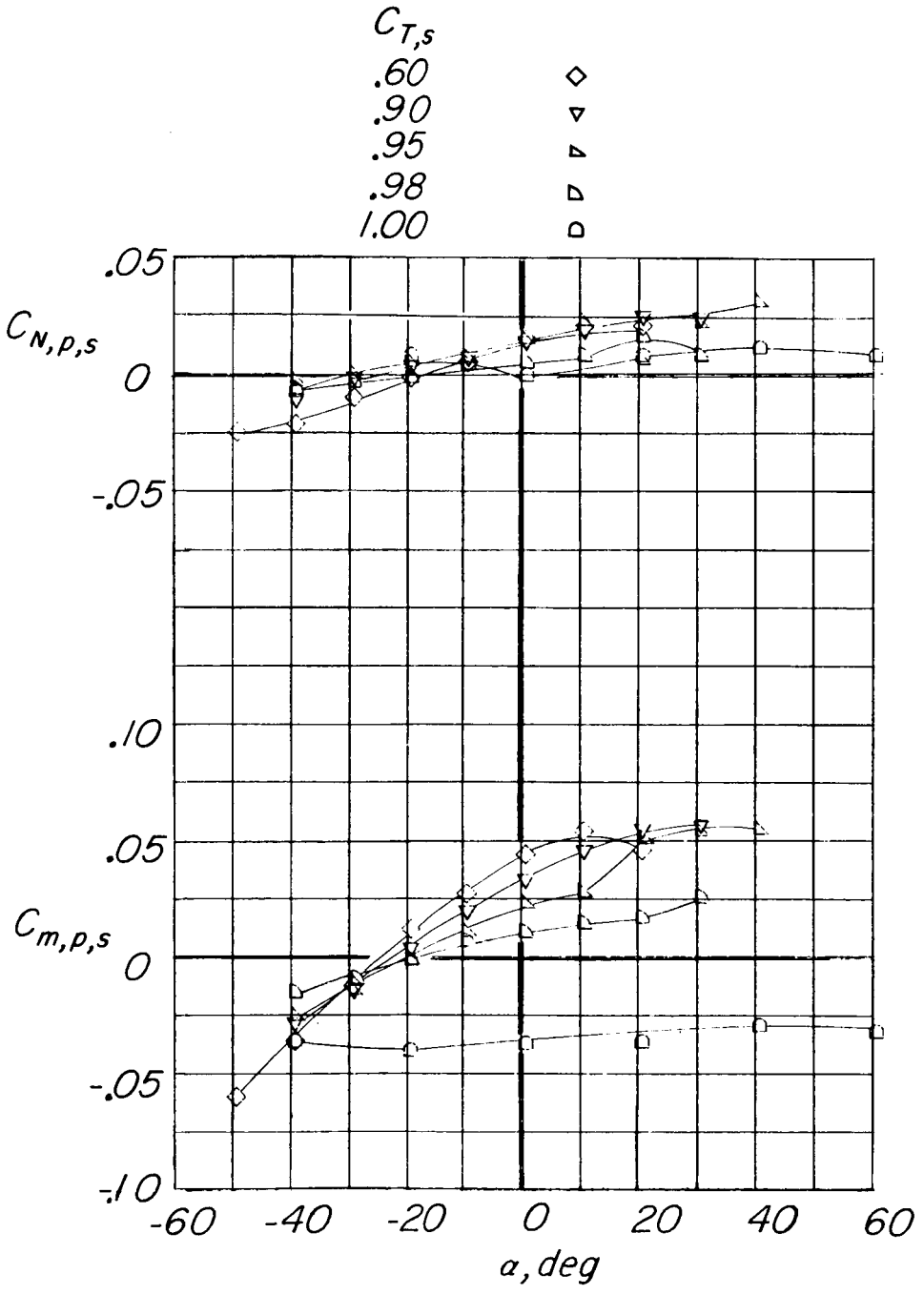

(b) Propeller normal-force and pitching-moment coefficients. Inboard propeller.

Figure 12.- Continued.

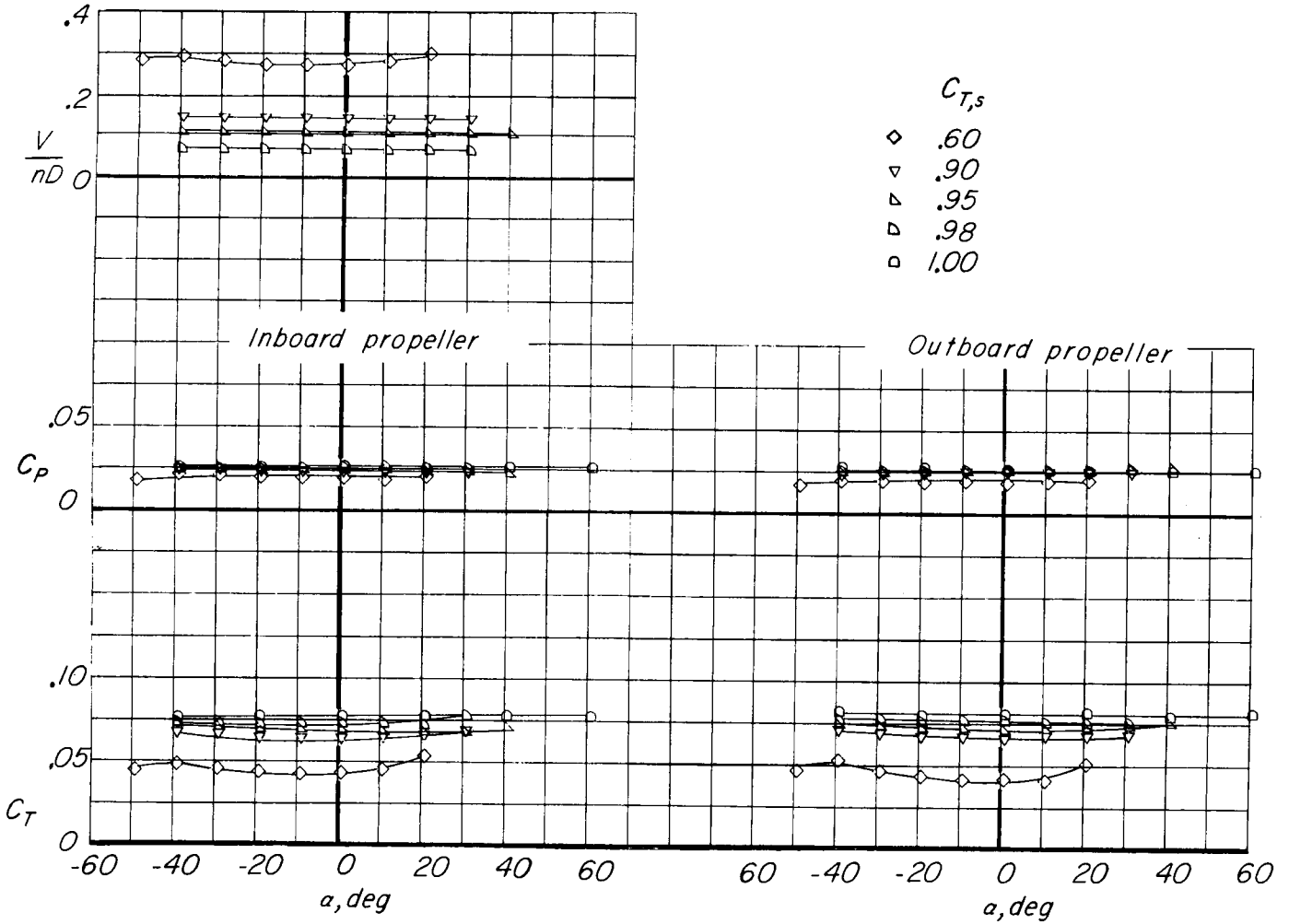

(c) Propeller thrust and power coefficients and advance ratio.

Figure 12.- Continued.

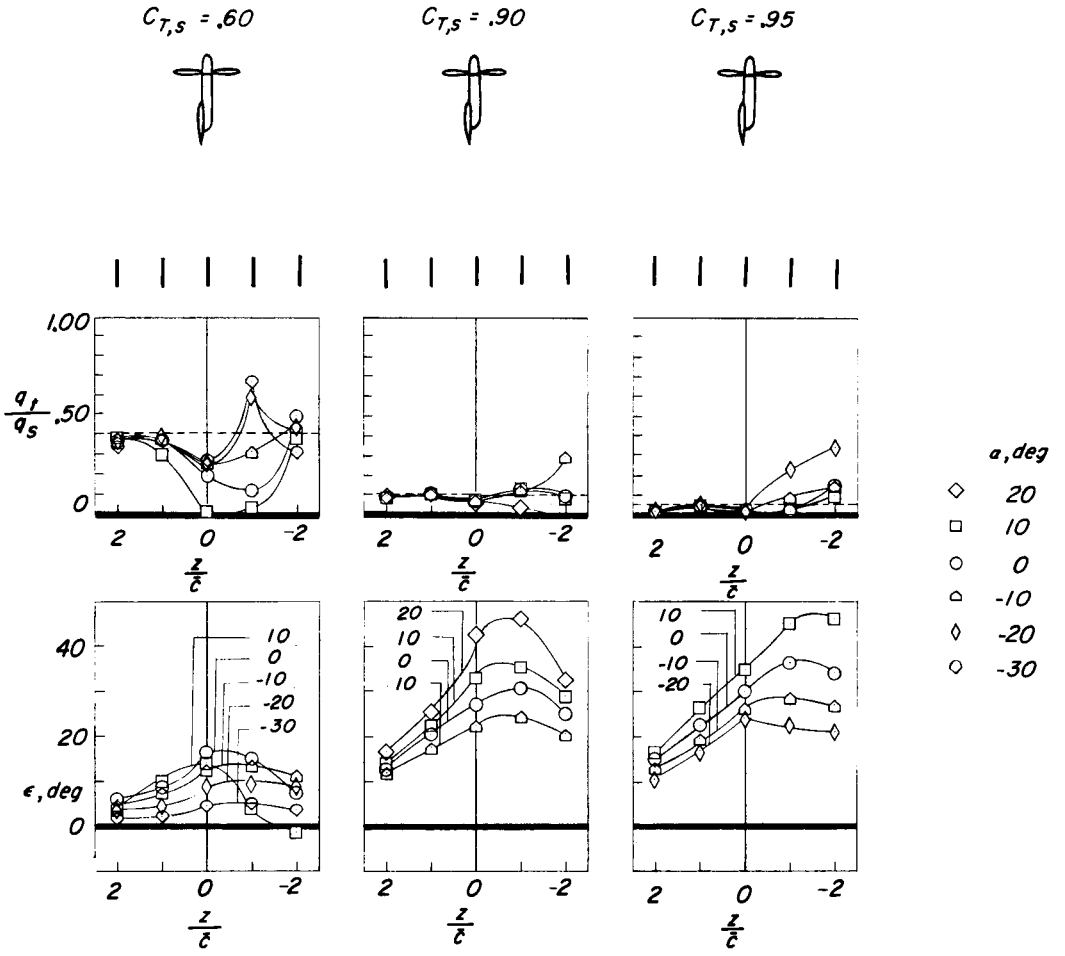

(d) Downwash and dynamic-pressure surveys. Dashed lines indicate level of free-stream dynamic pressure.

Figure 12.- Concluded.

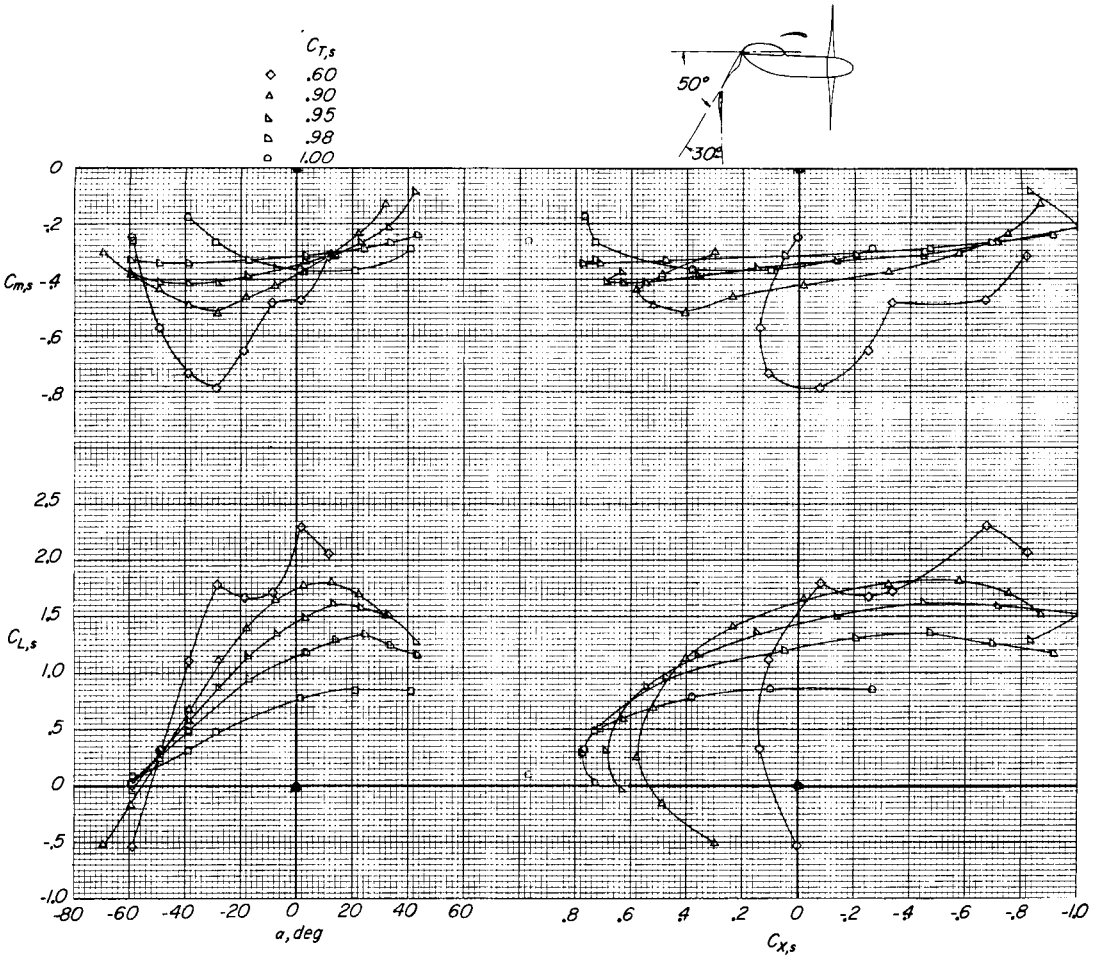

(a) Complete-model data.

Figure 13.- Aerodynamic characteristics of model out of region of ground effect. Deflected-slipstream configuration $\left(\delta_{f,S} = 50^{\circ};\ \delta_{f,F} = 30^{\circ}\right)$; slat in high position; $\delta_{slat} = 0^{\circ}$.

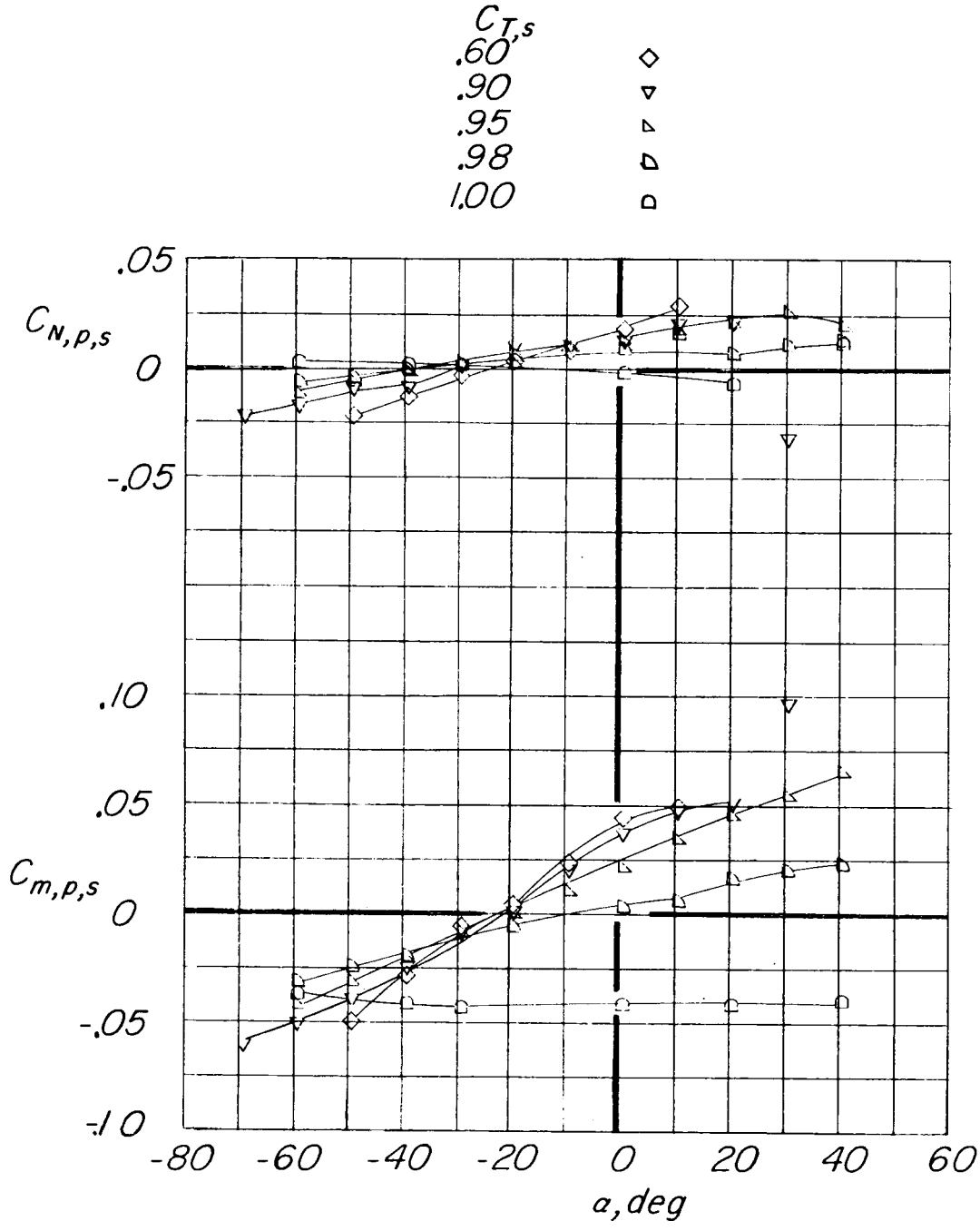

(b) Propeller normal-force and pitching-moment coefficients. Inboard propeller.

Figure 13.- Continued.

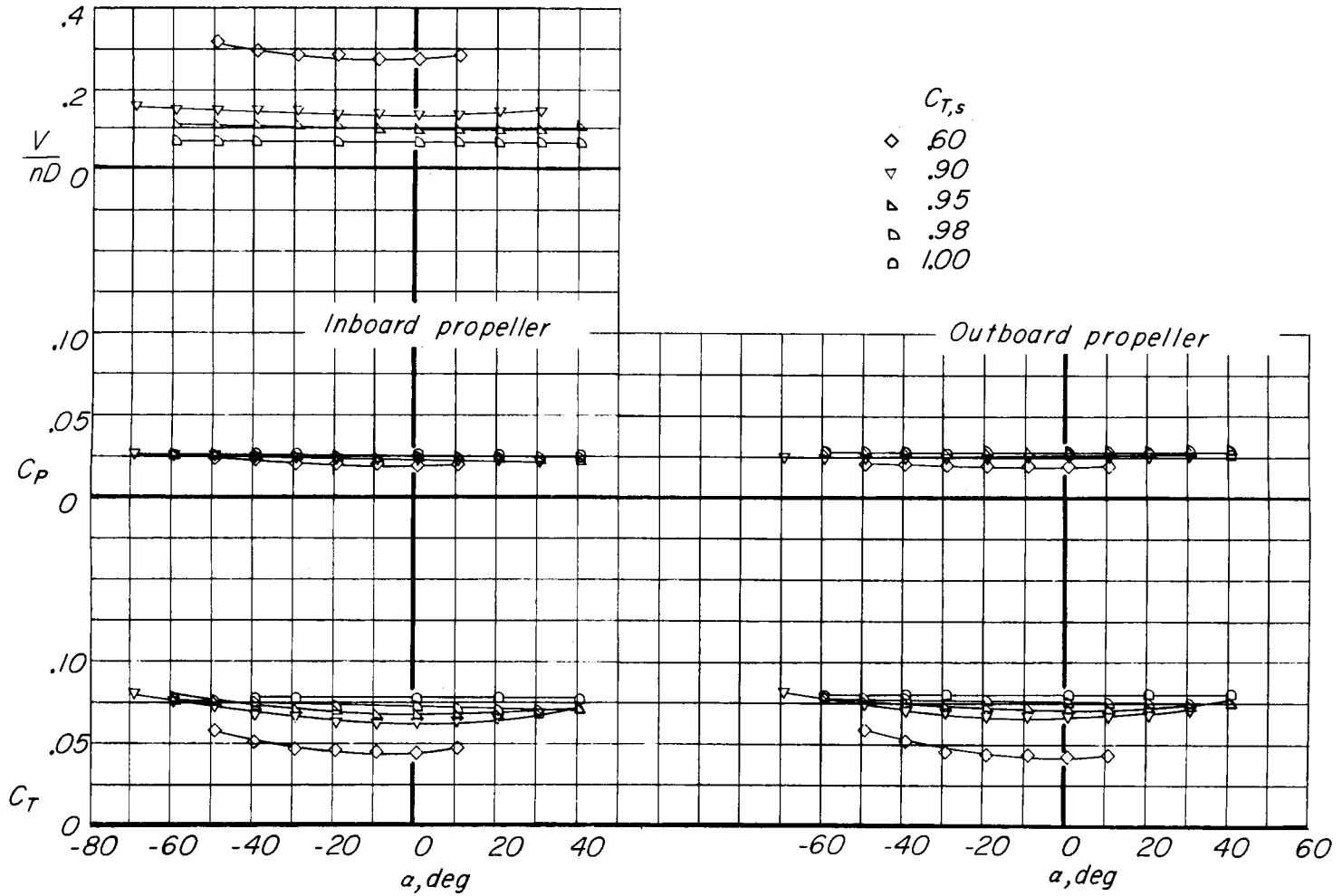

(c) Propeller thrust and power coefficients and advance ratio.

Figure 13.- Continued.

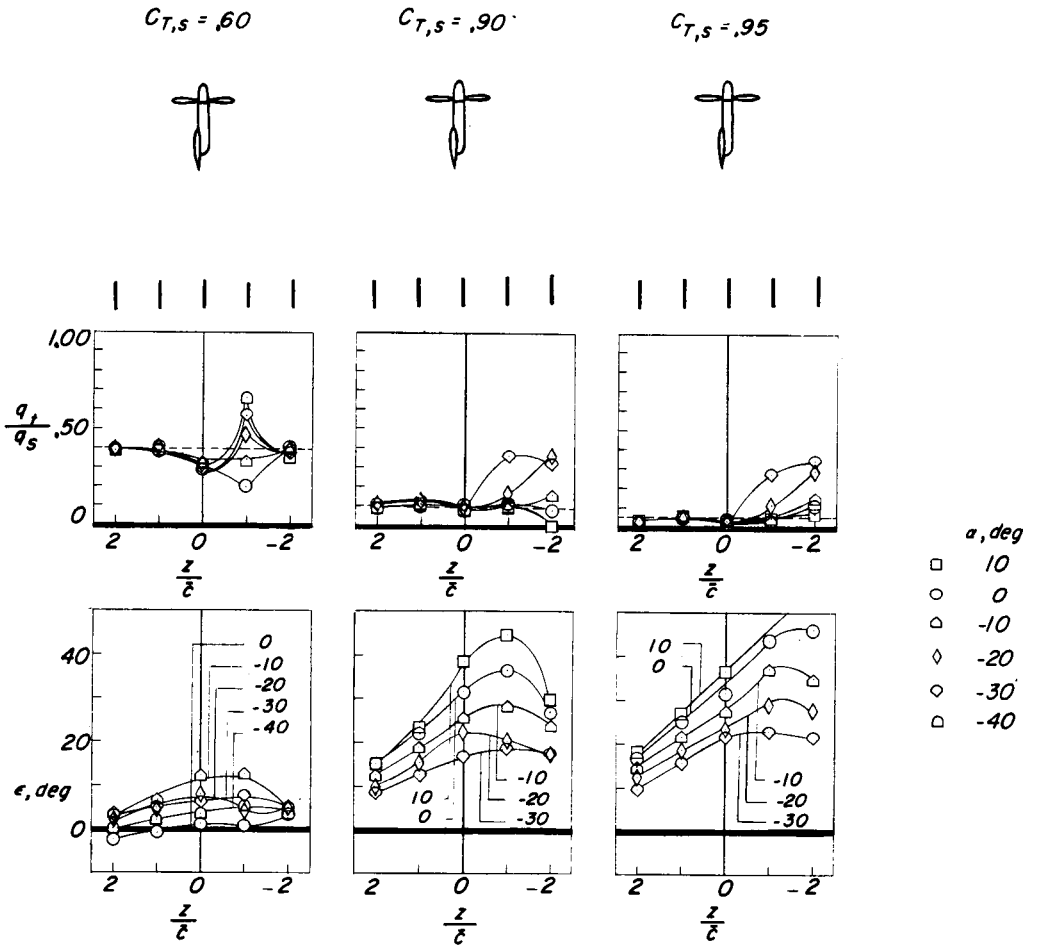

(d) Downwash and dynamic-pressure surveys. Dashed lines indicate level of free-stream dynamic pressure.

Figure 13.- Concluded.

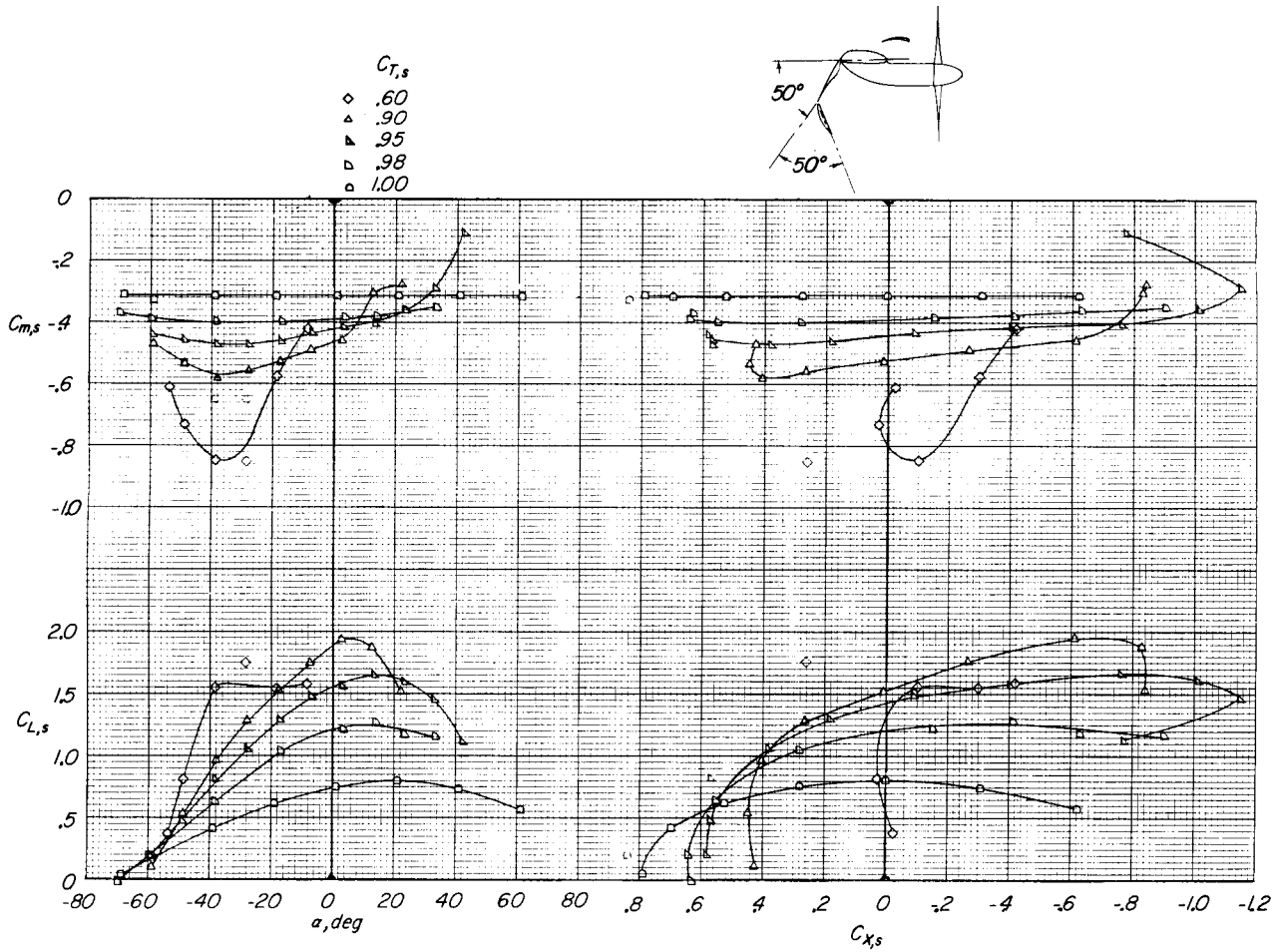

(a) Complete-model data.

Figure 14.- Aerodynamic characteristics of model out of region of ground effect. Deflected-slipstream configuration ($\delta_{f,S} = 50^{\circ}$; $\delta_{f,F} = 50^{\circ}$); slat in high position; $\delta_{slat} = 0^{\circ}$.

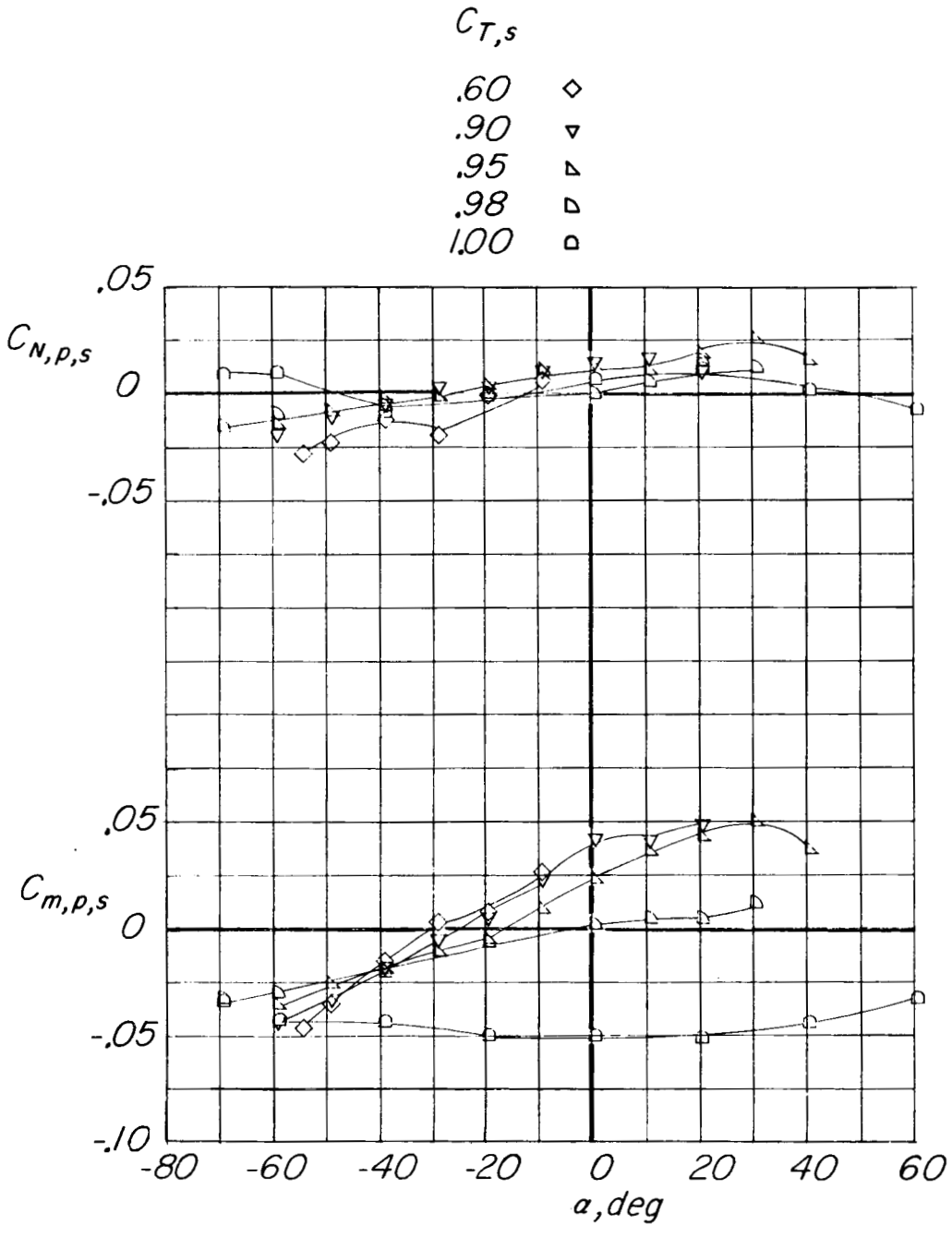

(b) Propeller normal-force and pitching-moment coefficients. Inboard propeller.

Figure 14.- Continued.

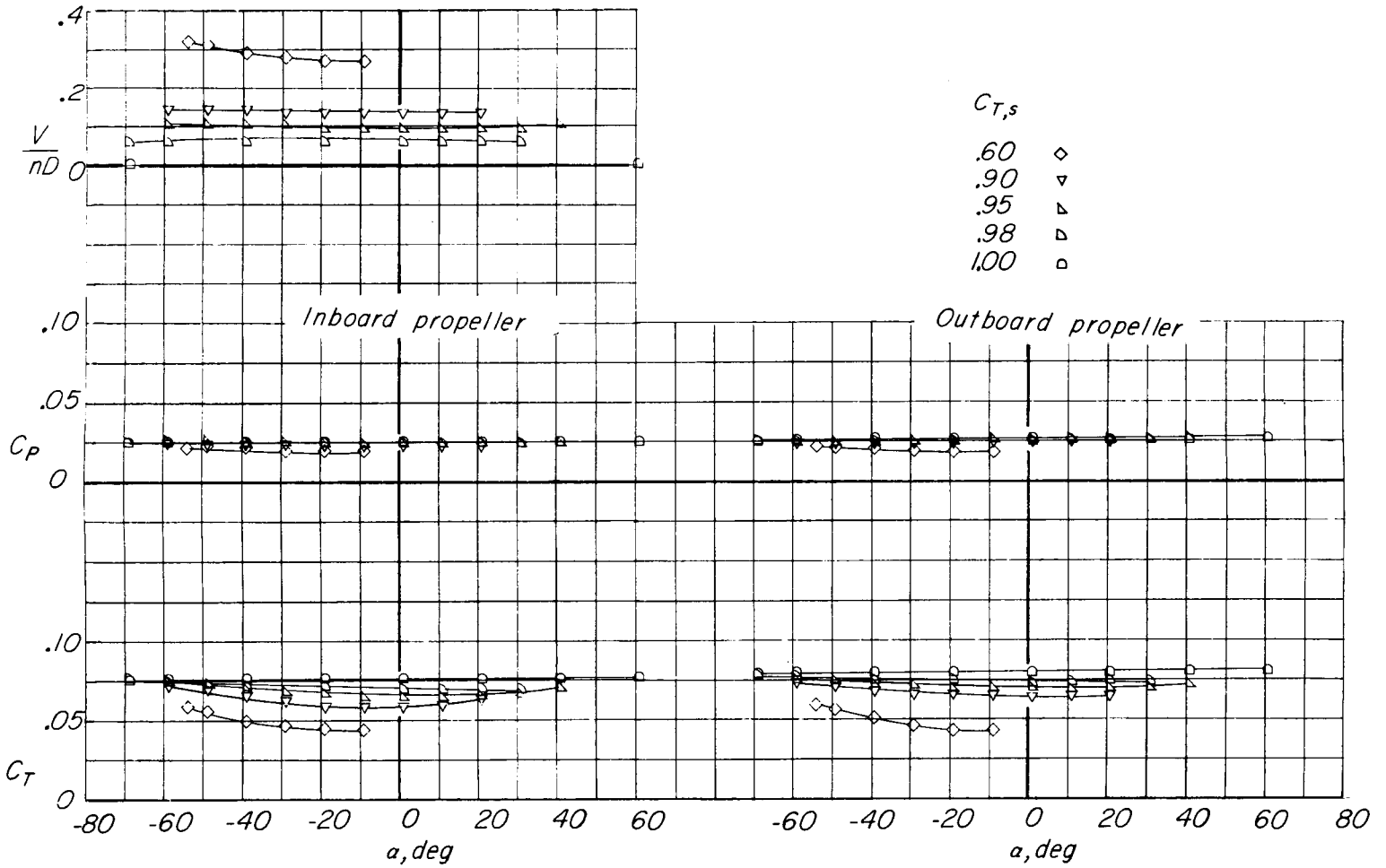

(c) Propeller thrust and power coefficients and advance ratio.

Figure 14.- Continued.

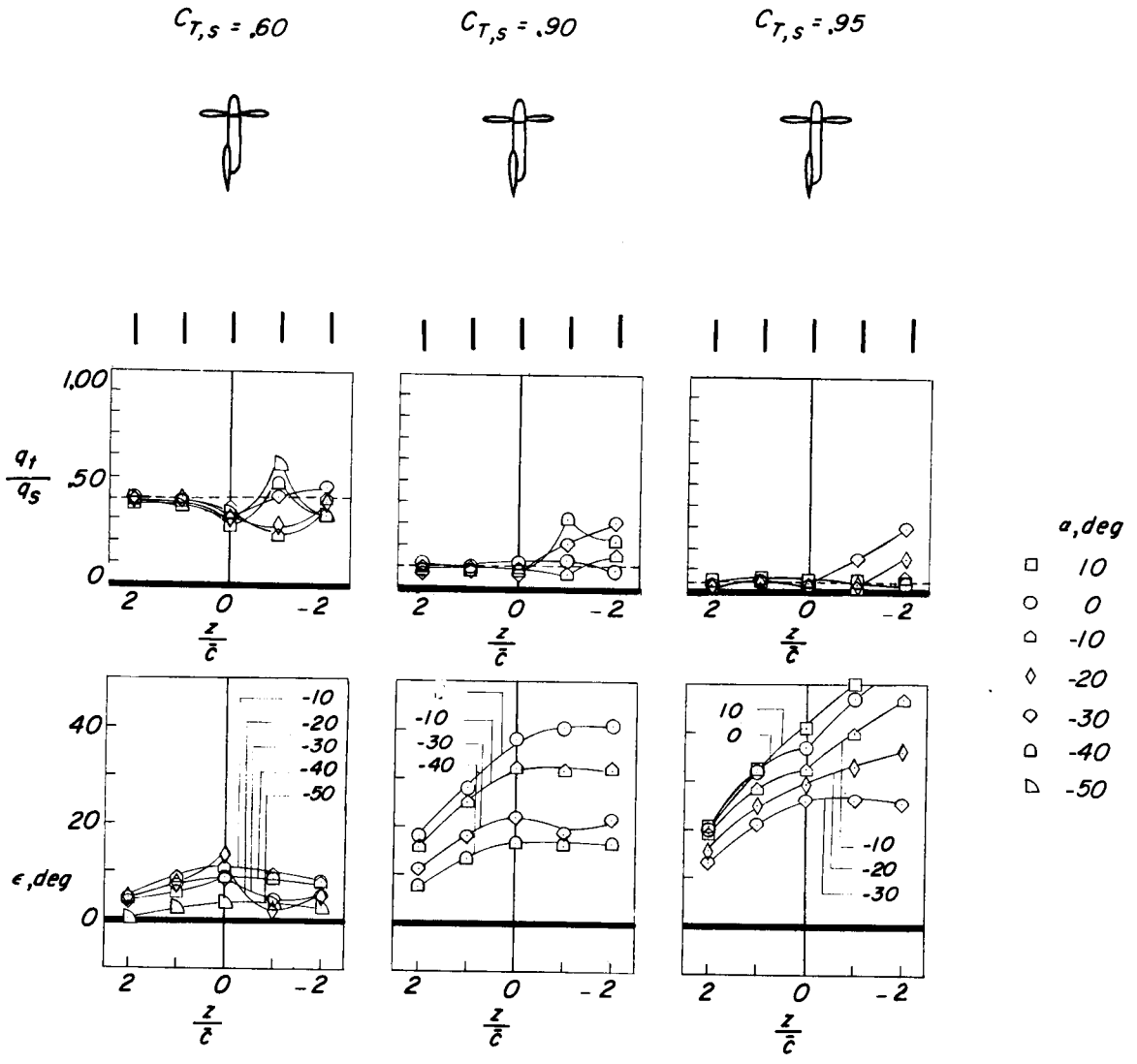

(d) Downwash and dynamic-pressure surveys. Dashed lines indicate level of free-stream dynamic pressure.

Figure 14.- Concluded.

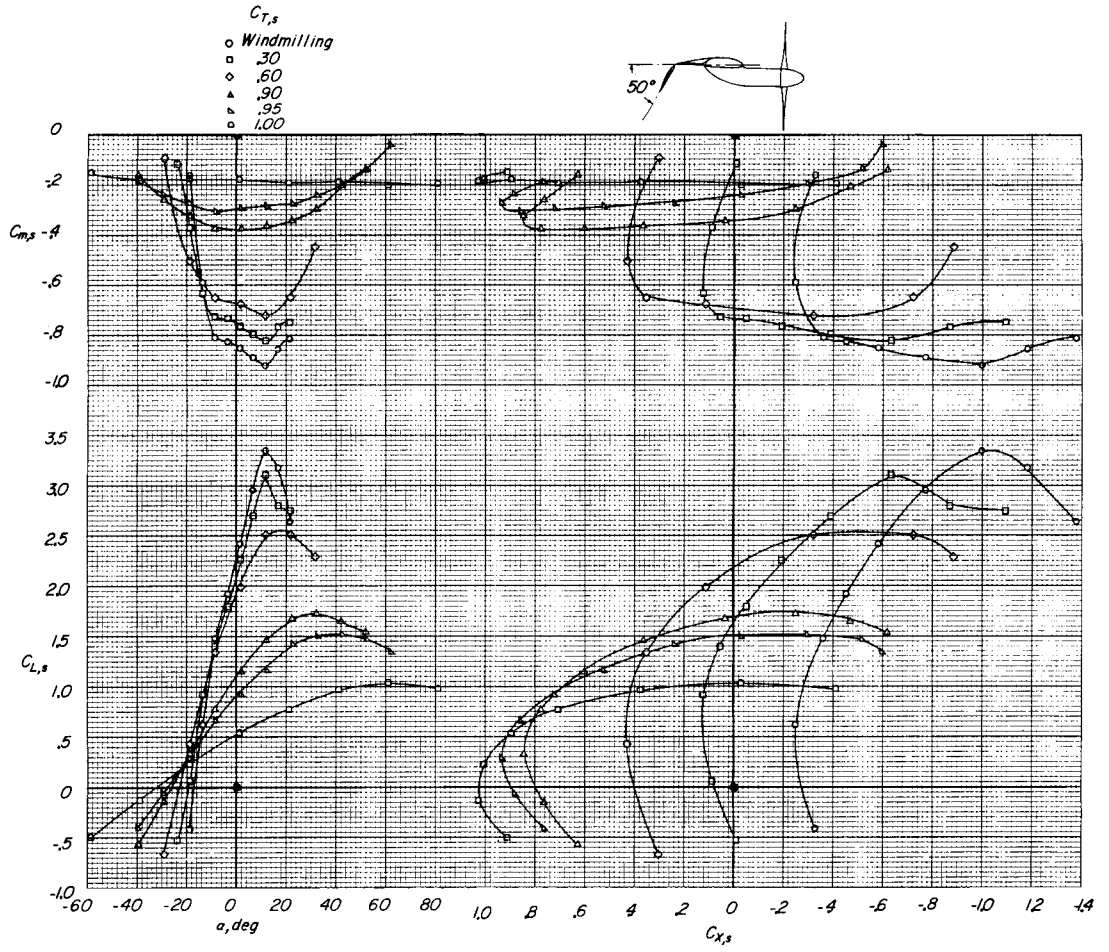

(a) Complete-model data.

Figure 15.- Aerodynamic characteristics of model out of region of ground effect. Combination configuration ($\delta_{f,S} = 0°$; $\delta_{f,F} = 50°$); slat retracted.

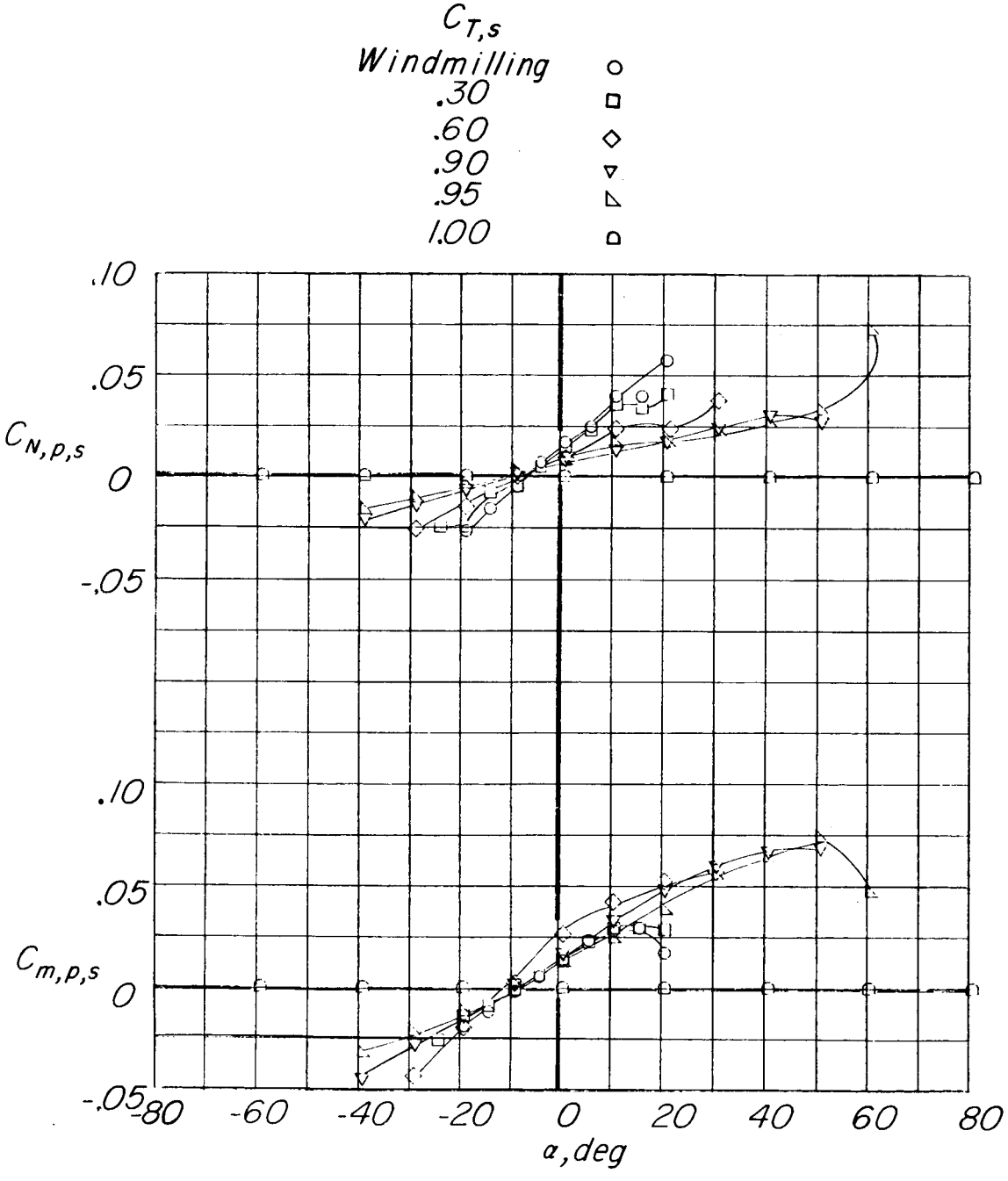

(b) Propeller normal-force and pitching-moment coefficients. Inboard propeller.

Figure 15.- Continued.

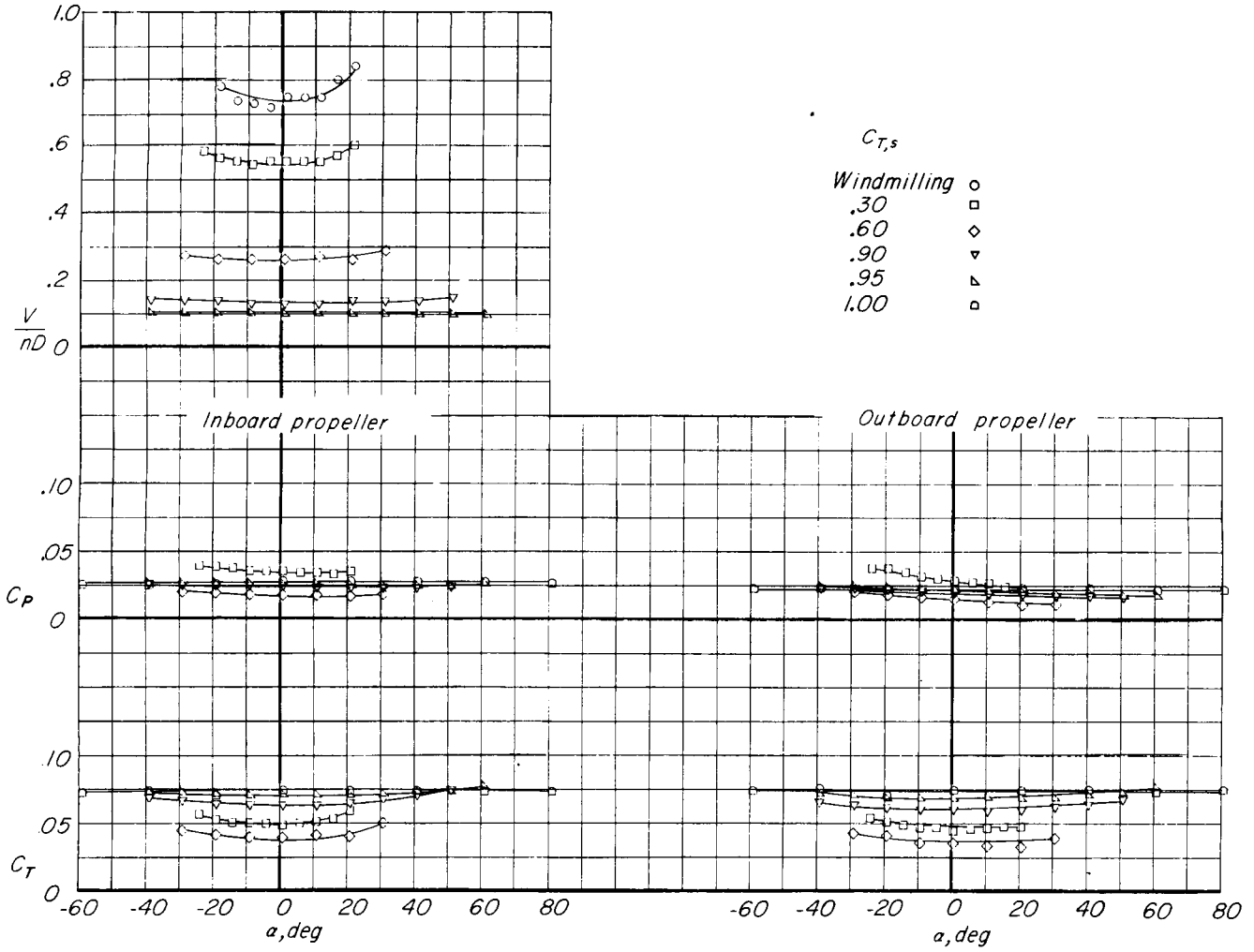

(c) Propeller thrust and power coefficients and advance ratio.

Figure 15.- Continued.

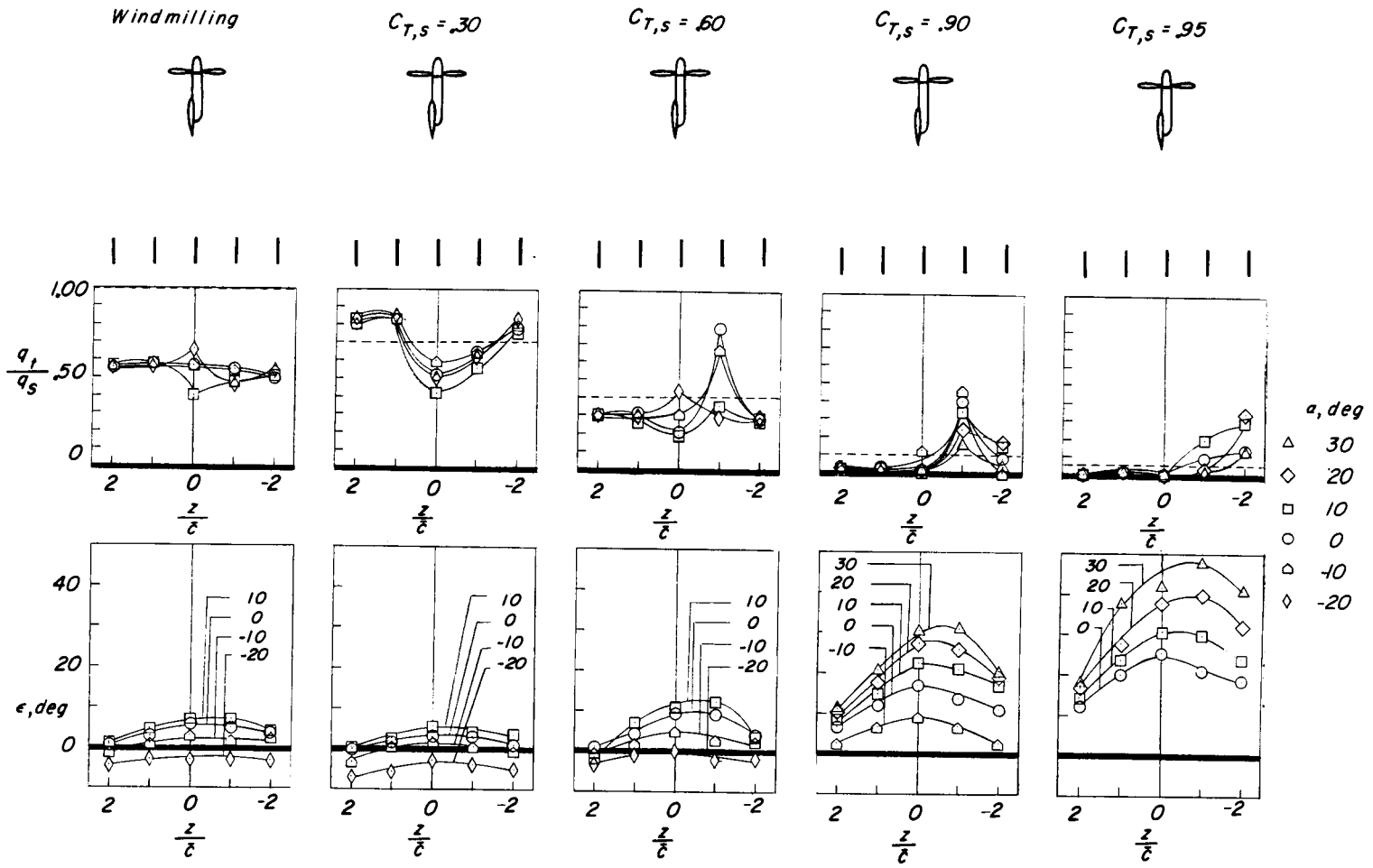

(d) Downwash and dynamic-pressure surveys. Dashed lines indicate level of free-stream dynamic pressure.

Figure 15.- Concluded.

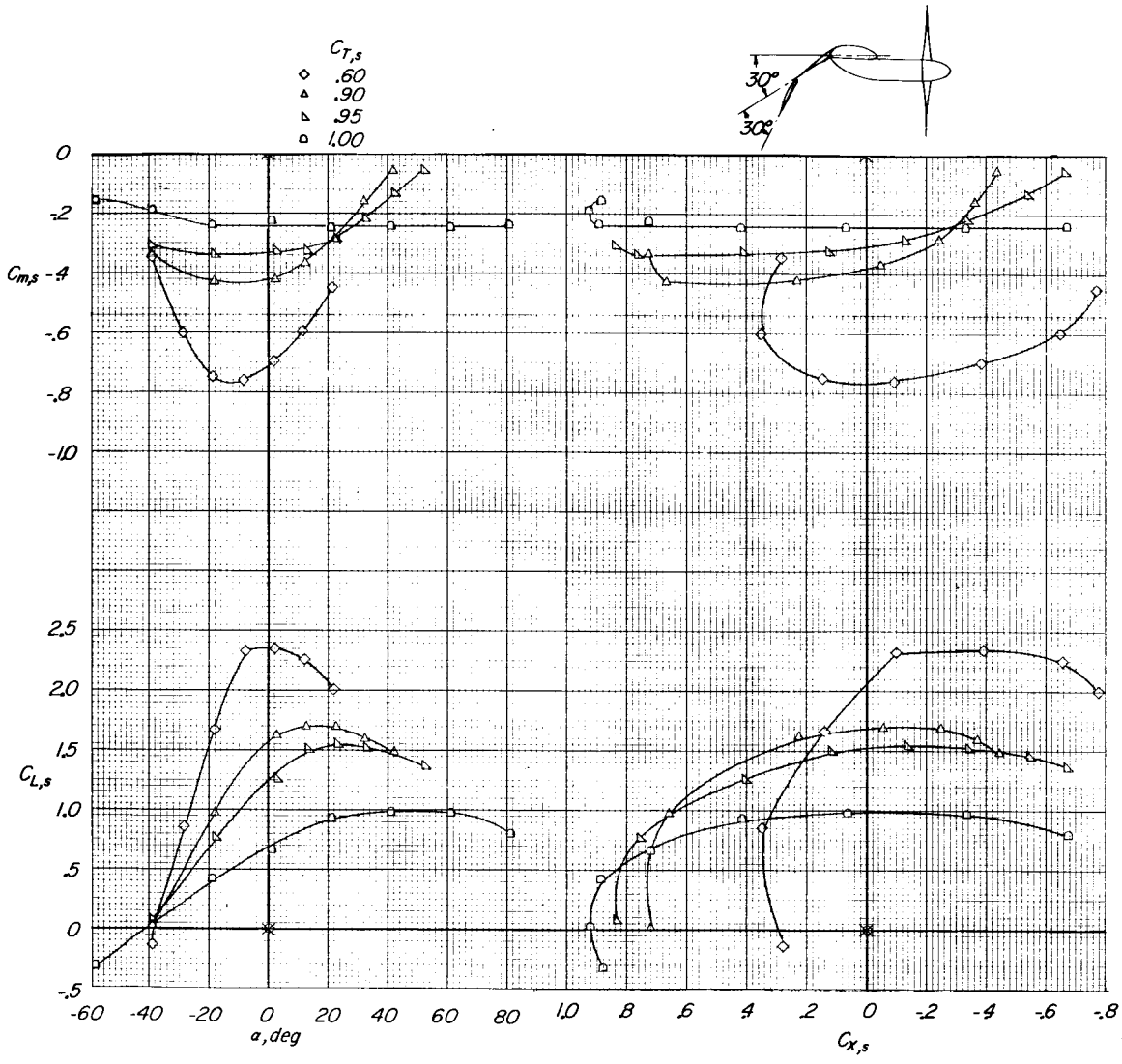

(a) Complete-model data.

Figure 16.- Aerodynamic characteristics of model out of region of ground effect. Deflected-slipstream configuration ($\delta_{f,S} = 30^\circ$; $\delta_{f,F} = 30^\circ$); slat retracted.

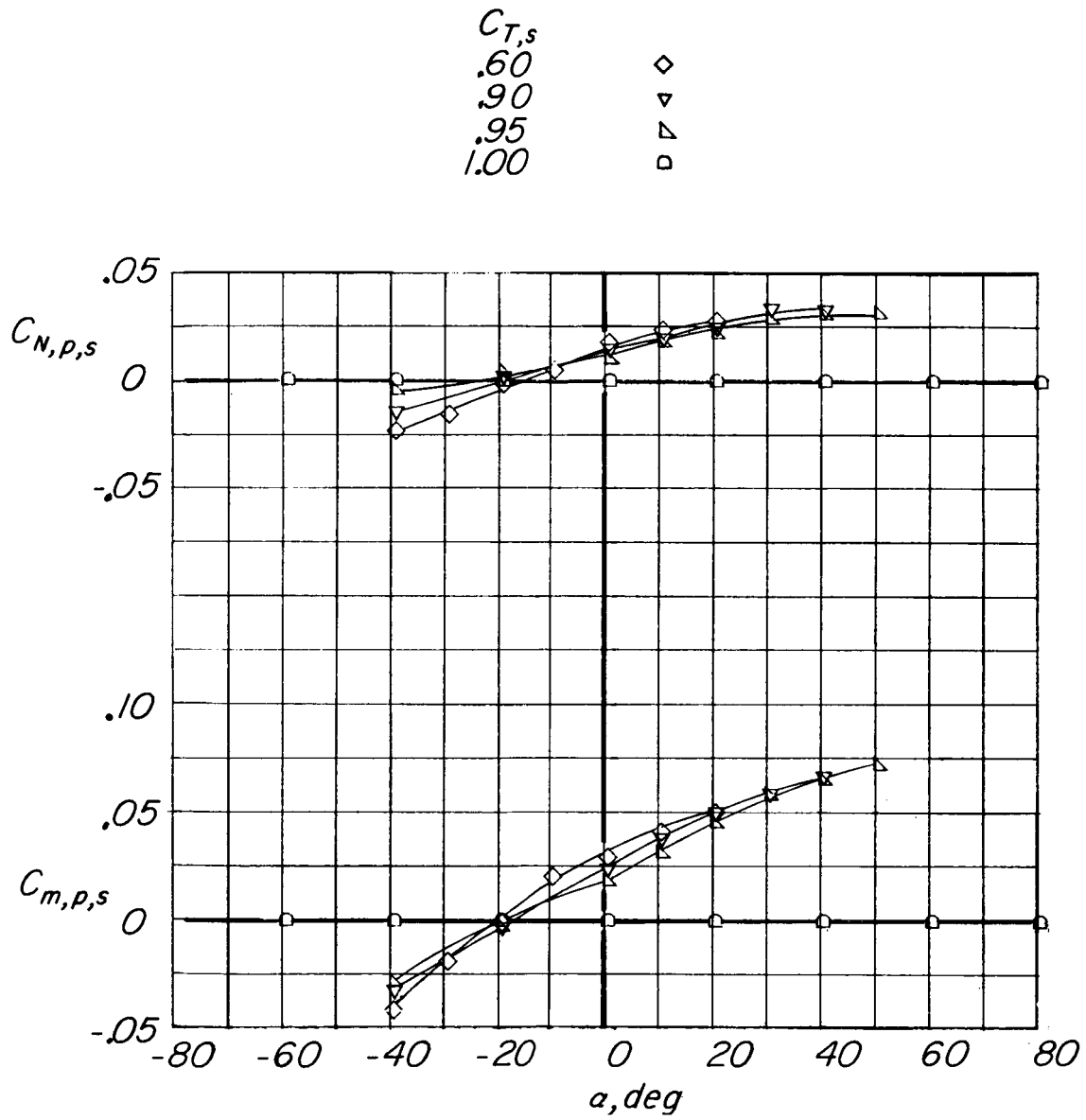

(b) Propeller normal-force and pitching-moment coefficients. Inboard propeller.

Figure 16.- Continued.

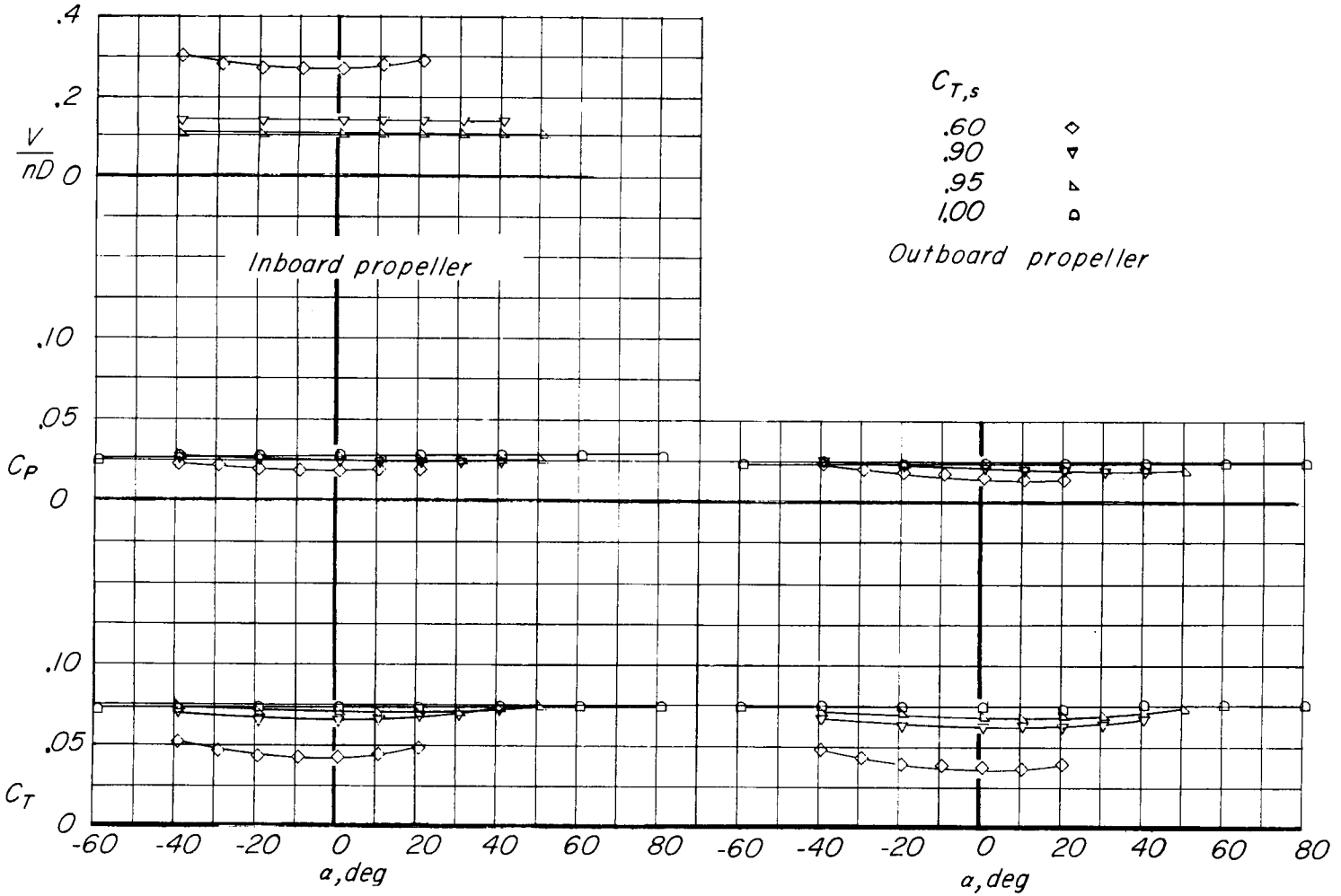

(c) Propeller thrust and power coefficients and advance ratio.

Figure 16.- Continued.

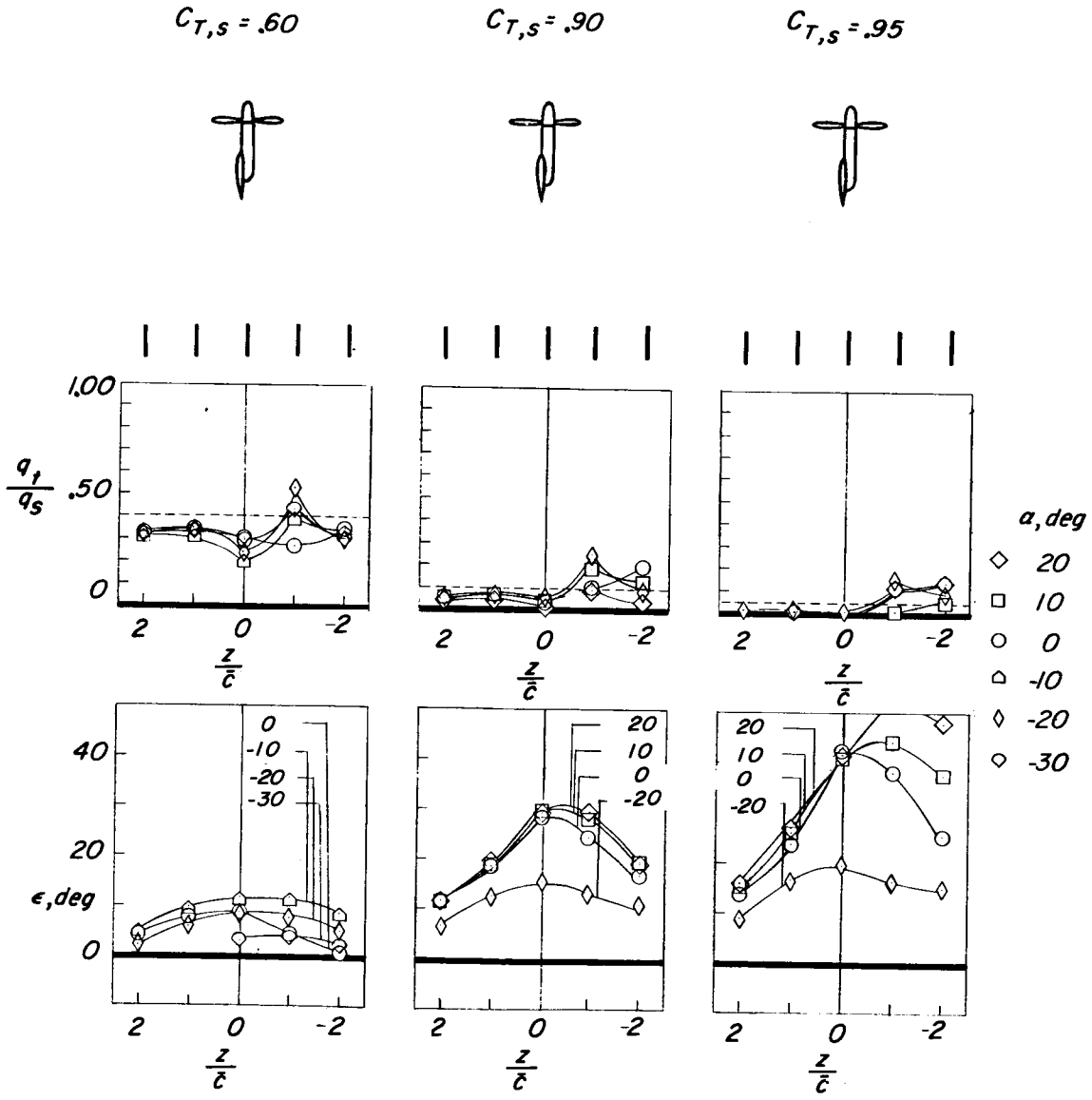

(d) Downwash and dynamic-pressure surveys. Dashed lines indicate level of free-stream dynamic pressure.

Figure 16.- Concluded.

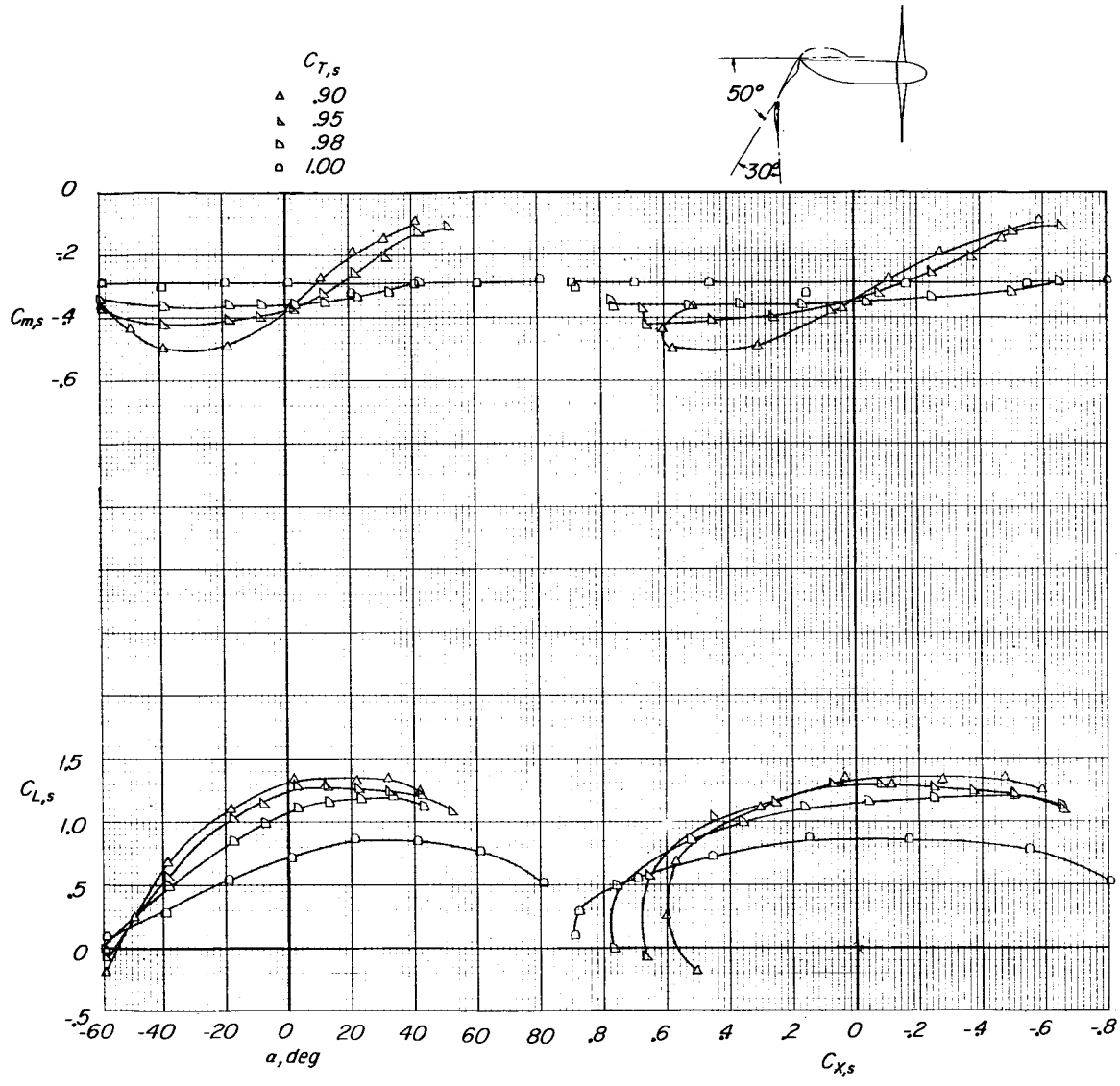

(a) Complete-model data.

Figure 17.- Aerodynamic characteristics of model out of region of ground effect. Deflected-slipstream configuration ($\delta_{f,S} = 50°$; $\delta_{f,F} = 30°$); slat retracted.

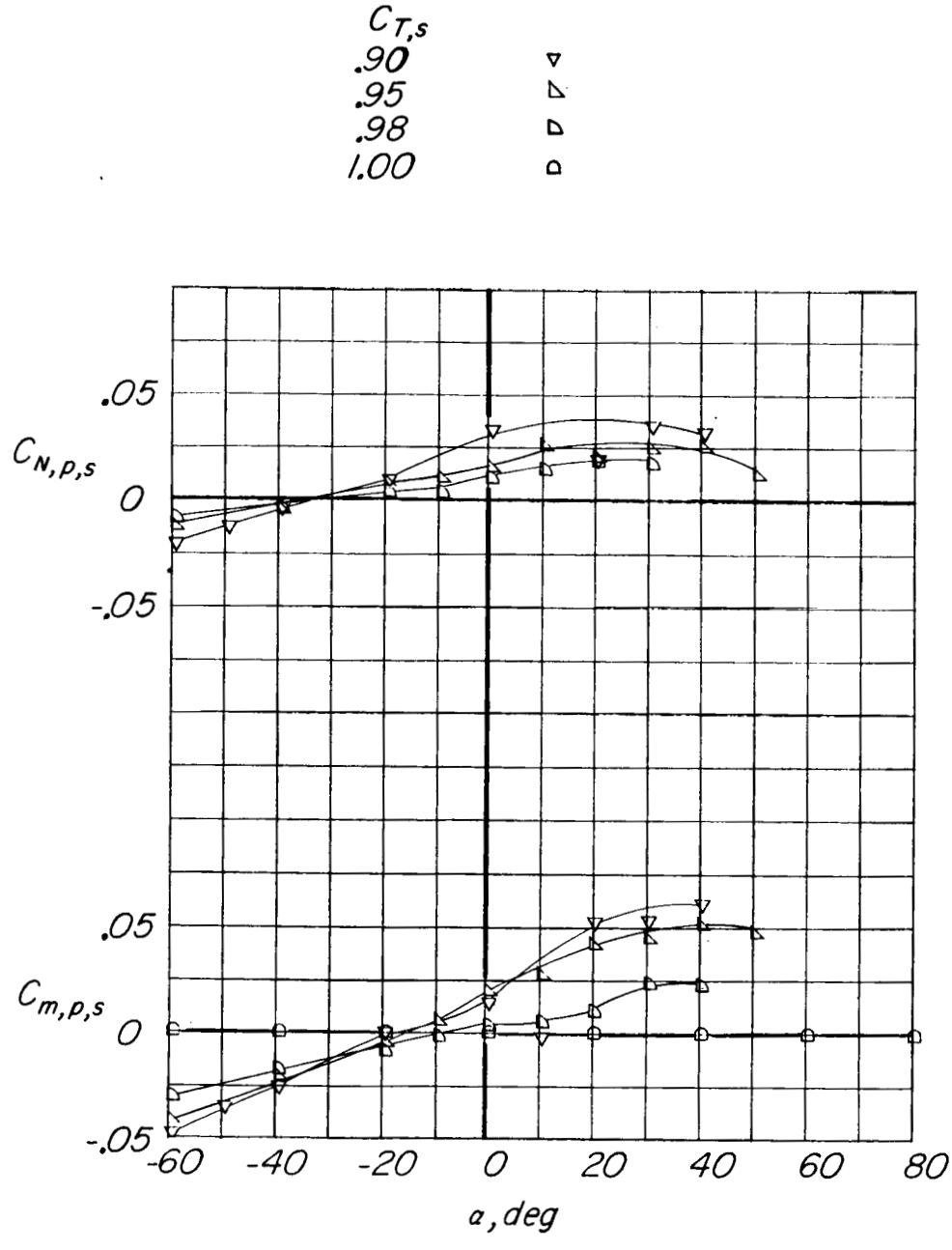

(b) Propeller normal-force and pitching-moment coefficients. Inboard propeller.

Figure 17.- Continued.

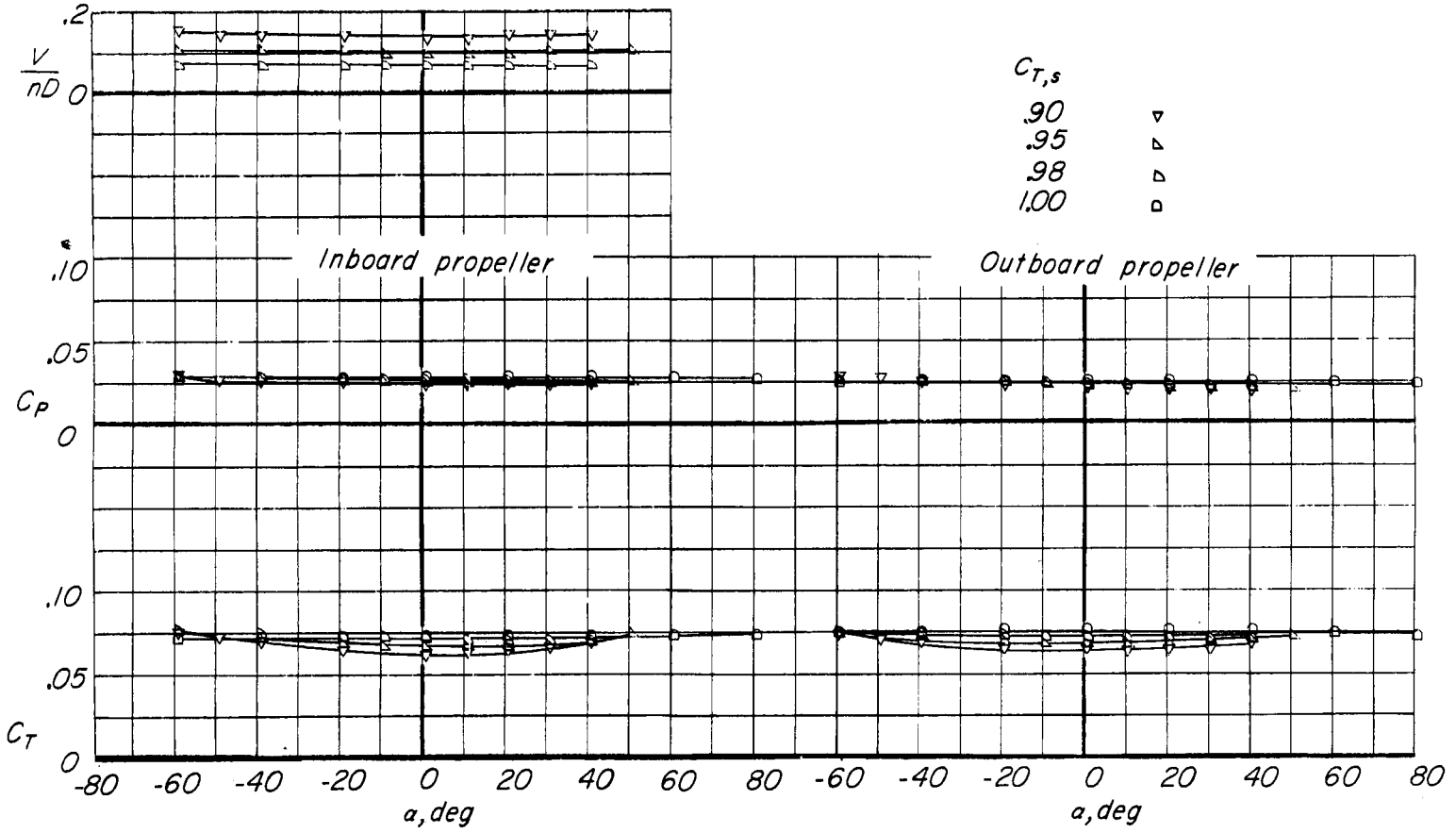

(c) Propeller thrust and power coefficients and advance ratio.

Figure 17.- Continued.

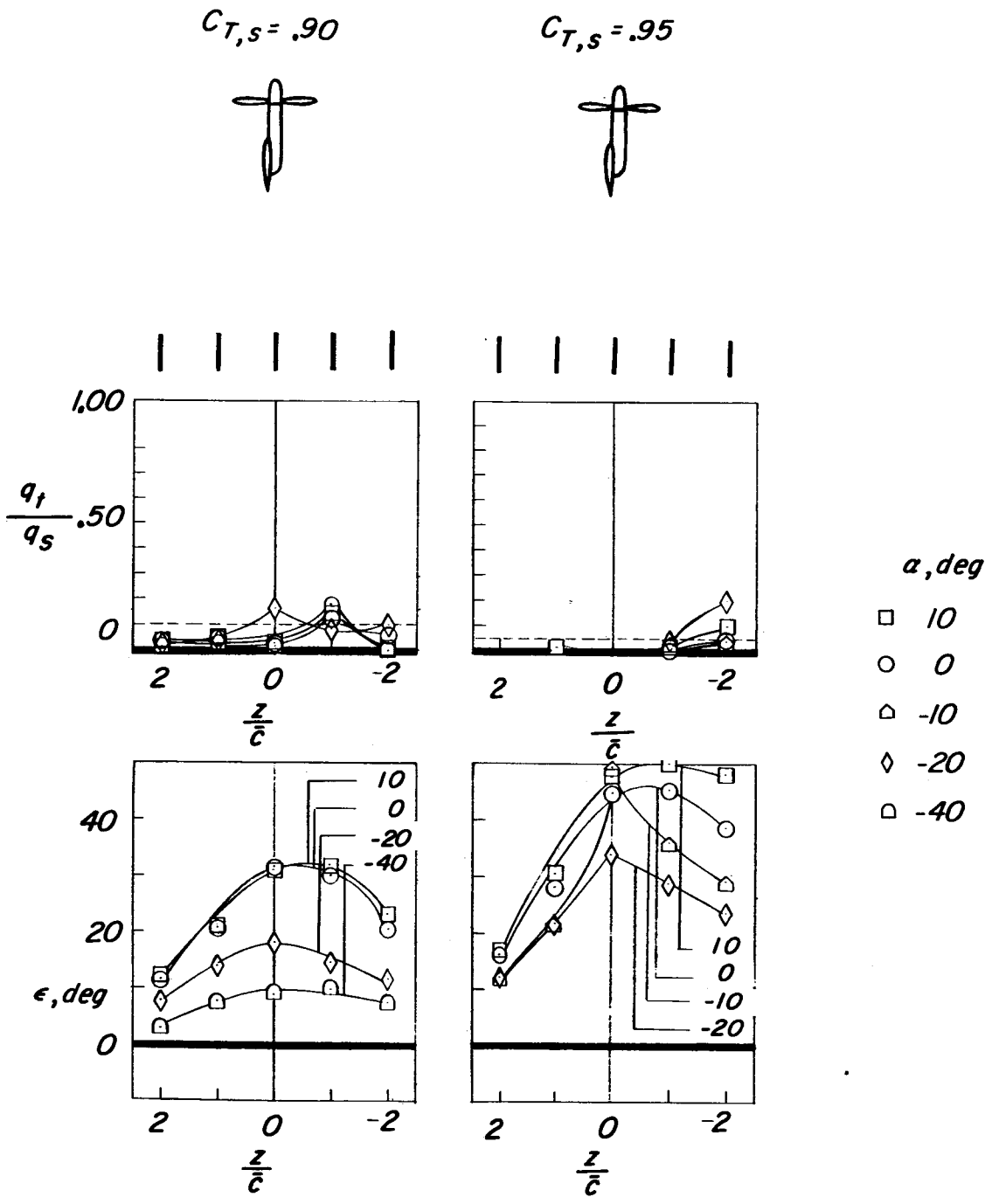

(d) Downwash and dynamic-pressure surveys. Dashed lines indicate level of free-stream dynamic pressure.

Figure 17.- Concluded.

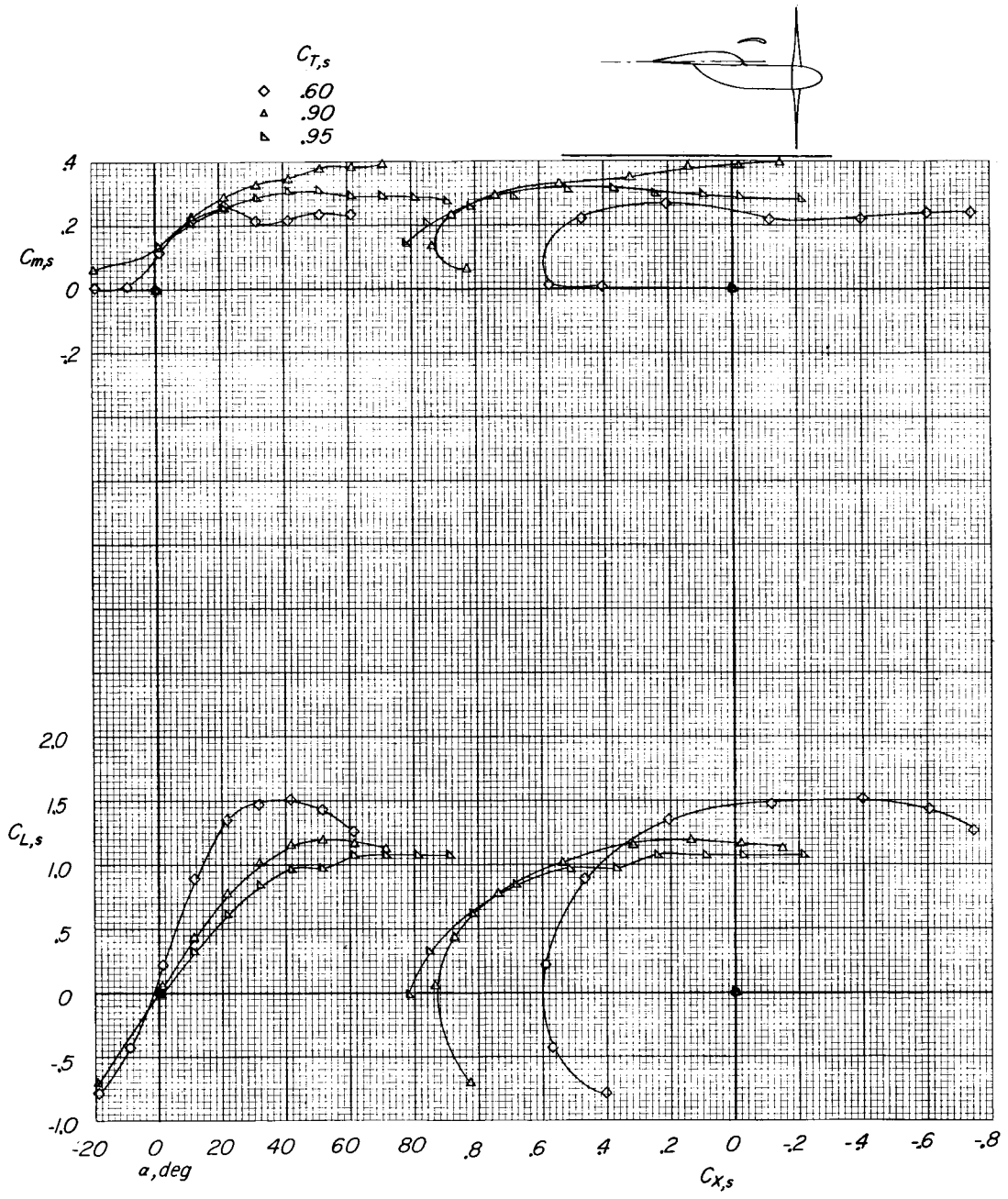

(a) Complete-model data.

Figure 18.- Aerodynamic characteristics of model in region of ground effect. Tilt-wing configuration ($\delta_{f,S} = 0^{\circ}$; $\delta_{f,F} = 0^{\circ}$); slat in high position; $\delta_{slat} = 0^{\circ}$; h/D = 0.81.

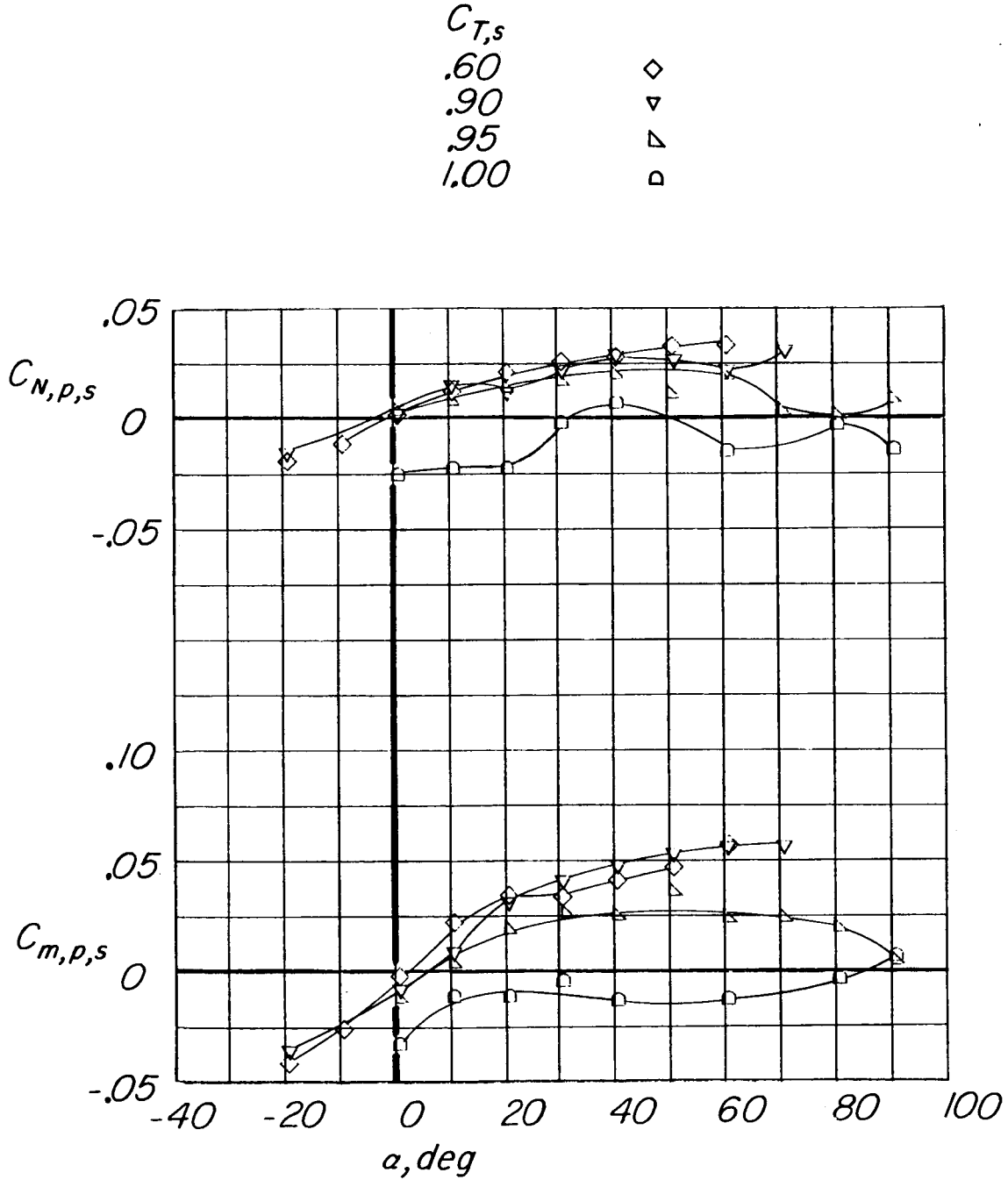

(b) Propeller normal-force and pitching-moment coefficients.

Figure 18.- Continued.

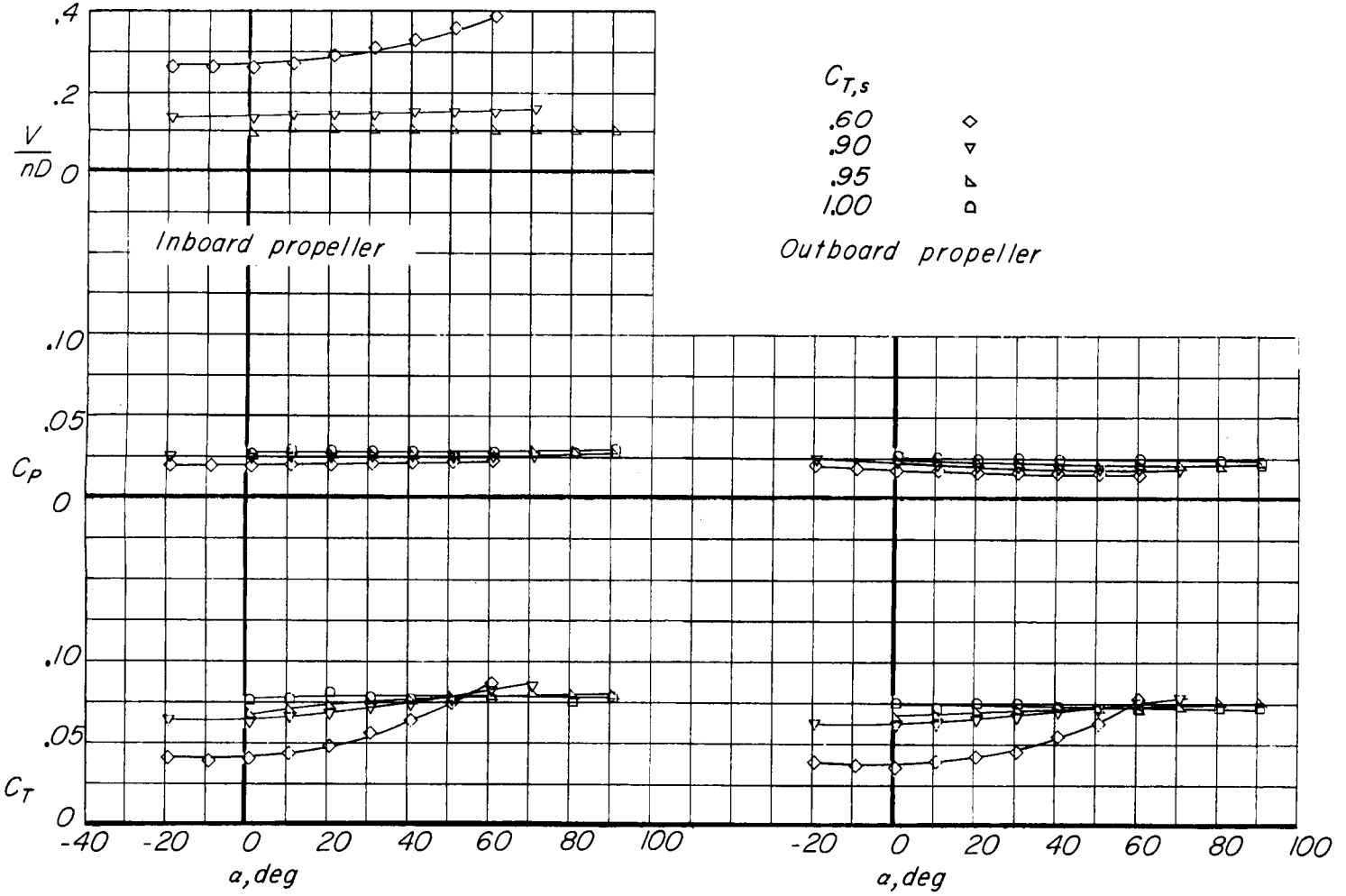

(c) Propeller thrust and power coefficients and advance ratio.

Figure 18.- Continued.

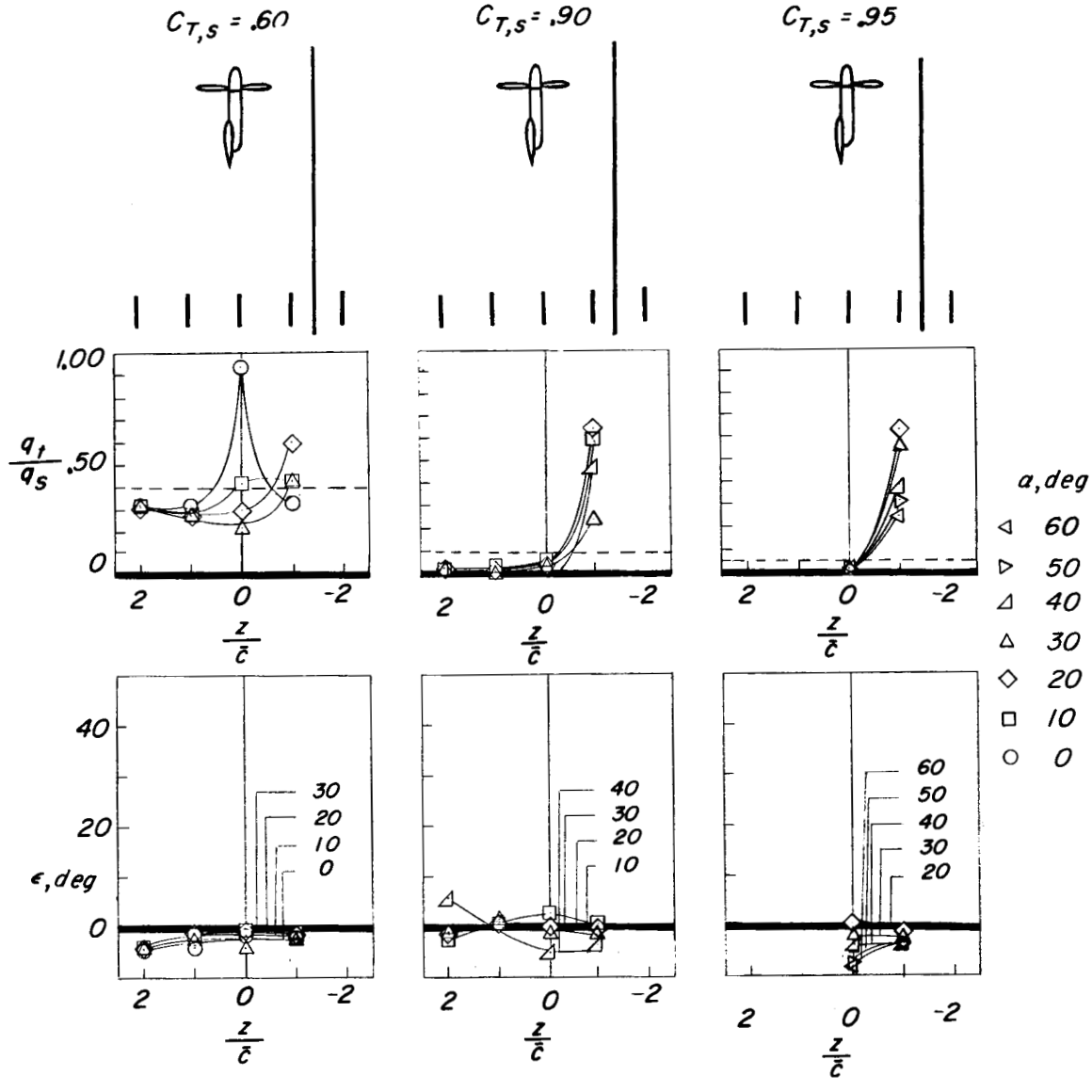

(d) Downwash and dynamic-pressure surveys. Dashed lines indicate level of free-stream dynamic pressure.

Figure 18.- Concluded.

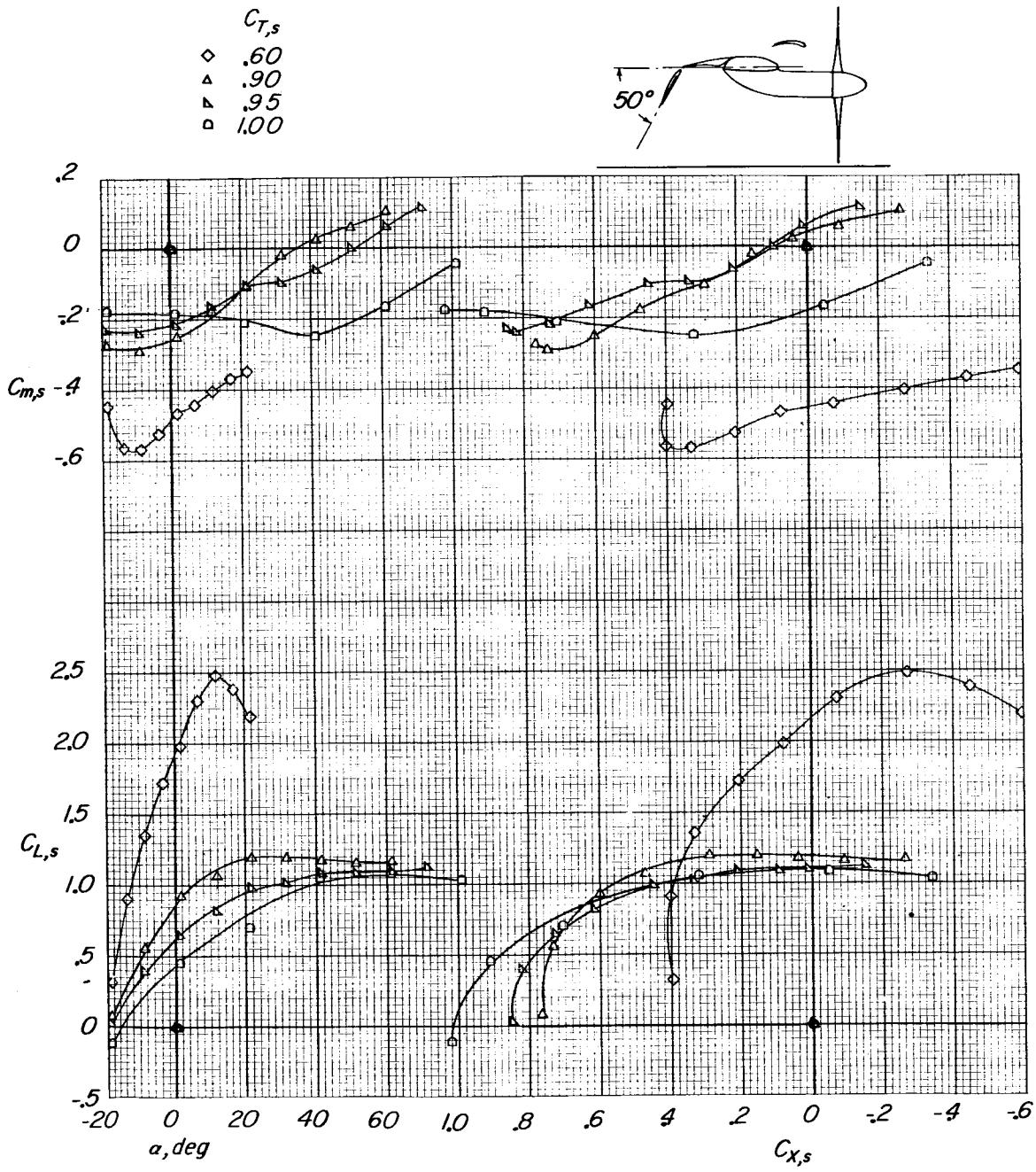

(a) Complete-model data.

Figure 19.- Aerodynamic characteristics of model in region of ground effect. Combination configuration ($\delta_{f,S} = 0^{\circ}$; $\delta_{f,F} = 50^{\circ}$); slat in high position; $\delta_{slat} = 0^{\circ}$; h/D = 0.81.

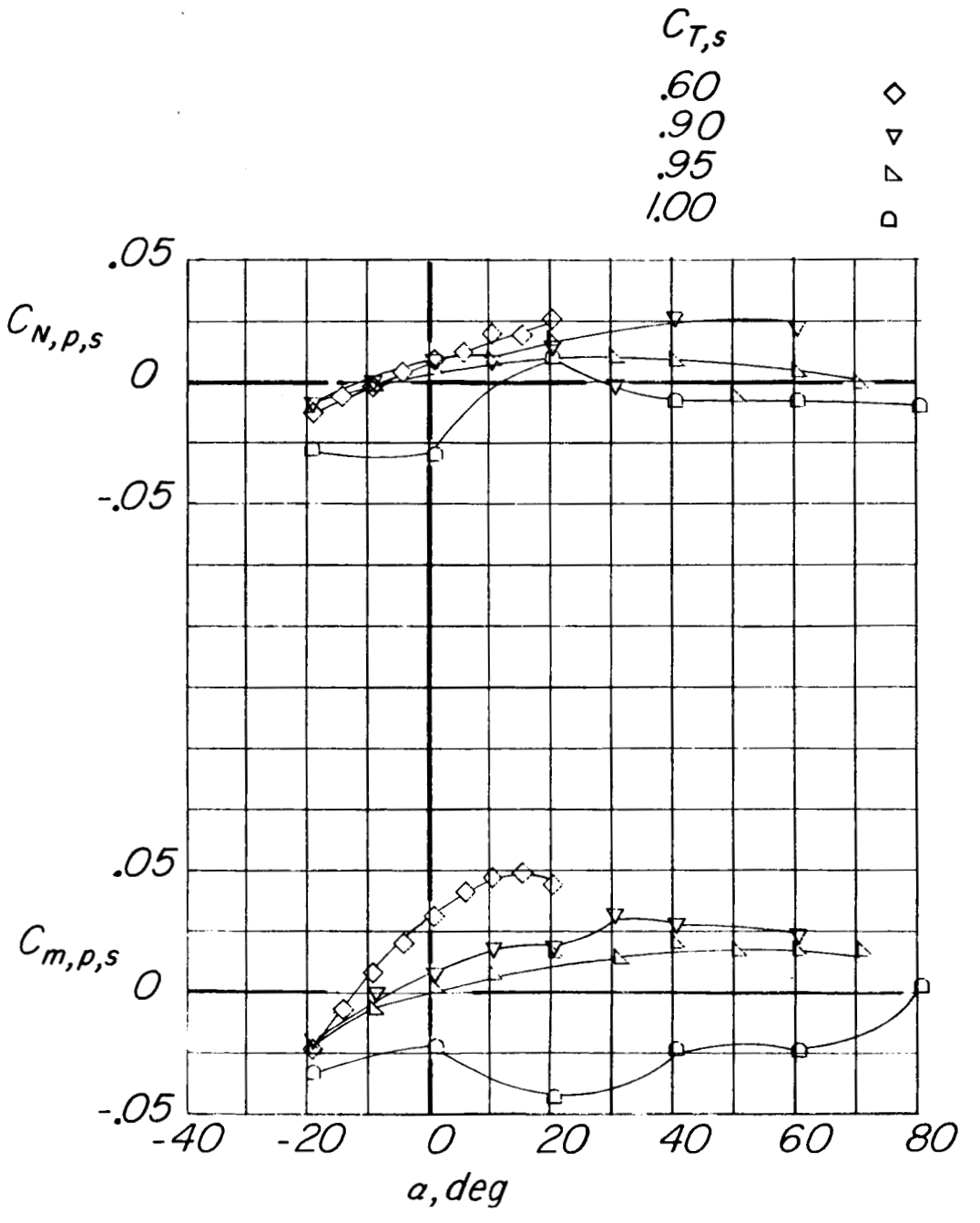

(b) Propeller normal-force and pitching-moment coefficients. Inboard propeller.

Figure 19.- Continued.

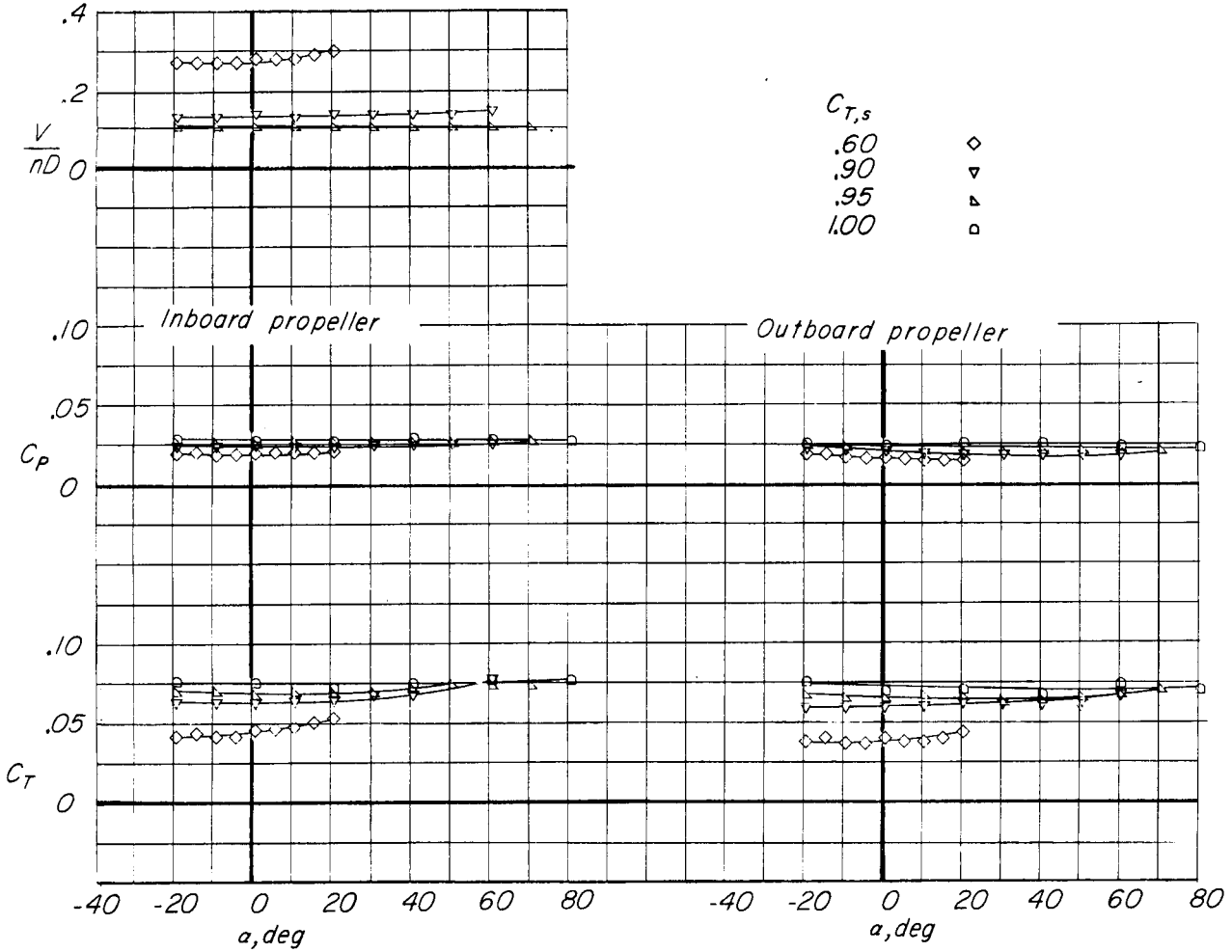

(c) Propeller thrust and power coefficients and advance ratio.

Figure 19.- Continued.

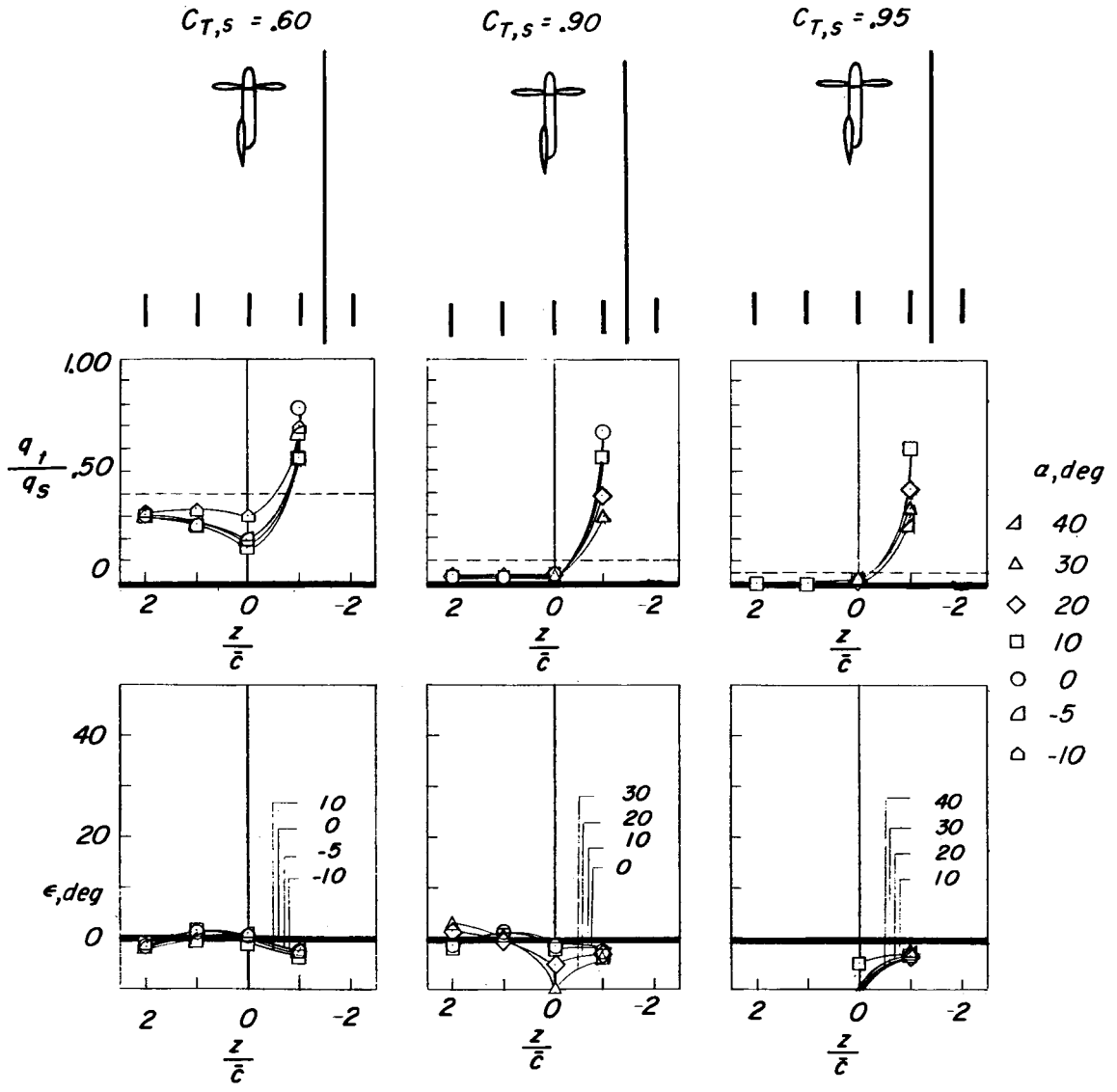

(d) Downwash and dynamic-pressure surveys. Dashed lines indicate level of free-stream dynamic pressure.

Figure 19.- Concluded.

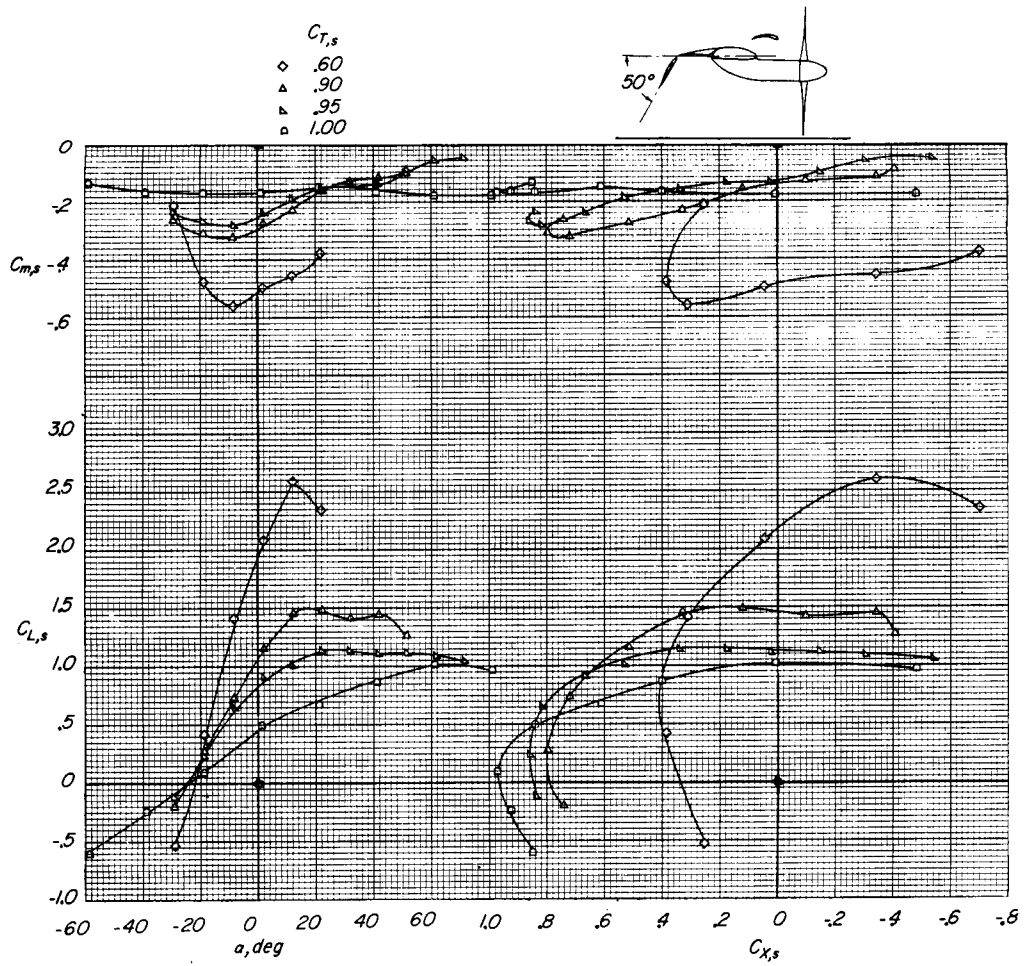

(a) Complete-model data.

Figure 20.- Aerodynamic characteristics of model in region of ground effect. Combination configuration ($\delta_{f,S} = 0^\circ$; $\delta_{f,F} = 50^\circ$); slat in high position; $\delta_{slat} = 0^\circ$; h/D = 1.46.

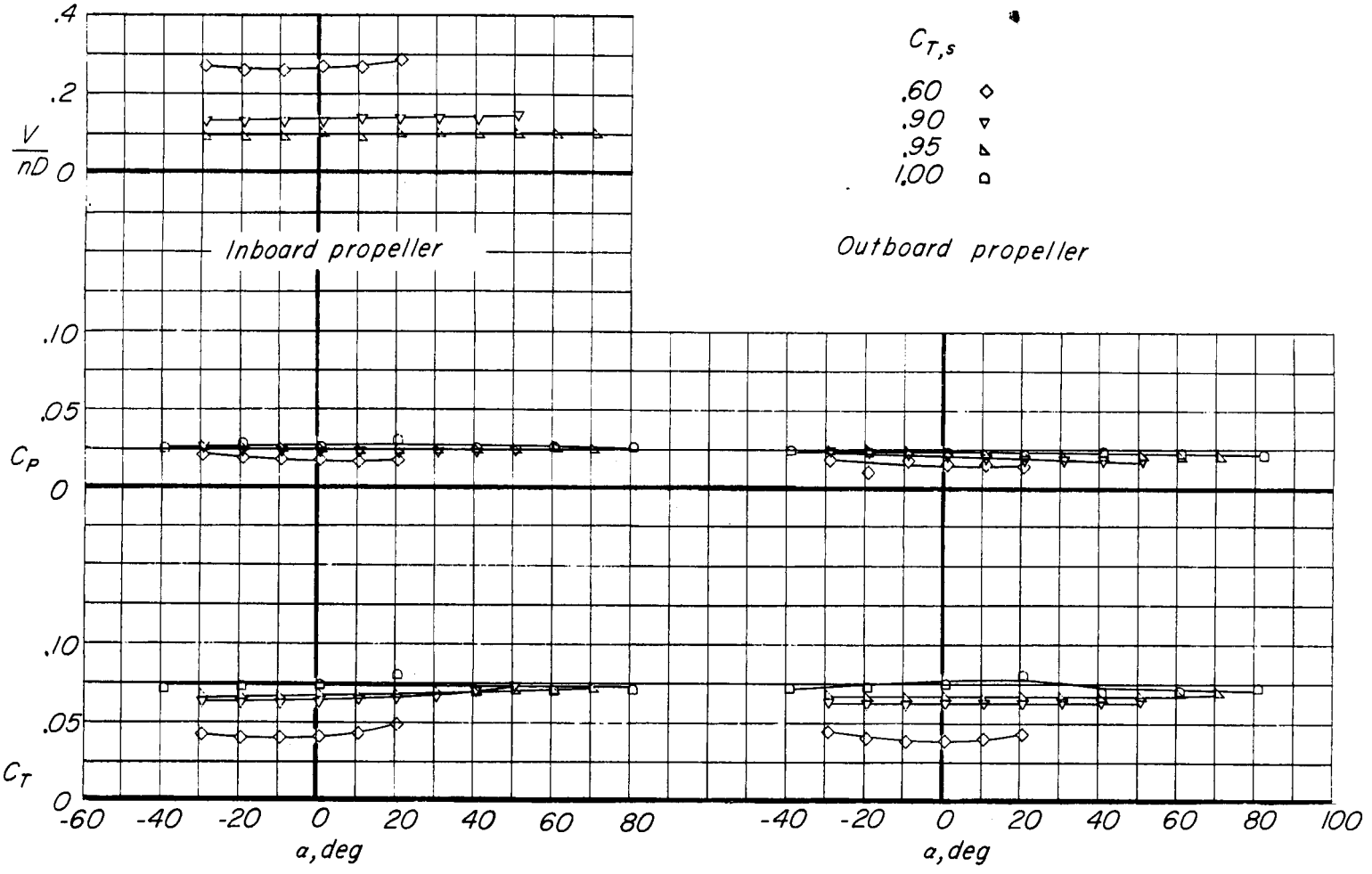

(b) Propeller thrust and power coefficients and advance ratio.

Figure 20.- Concluded.

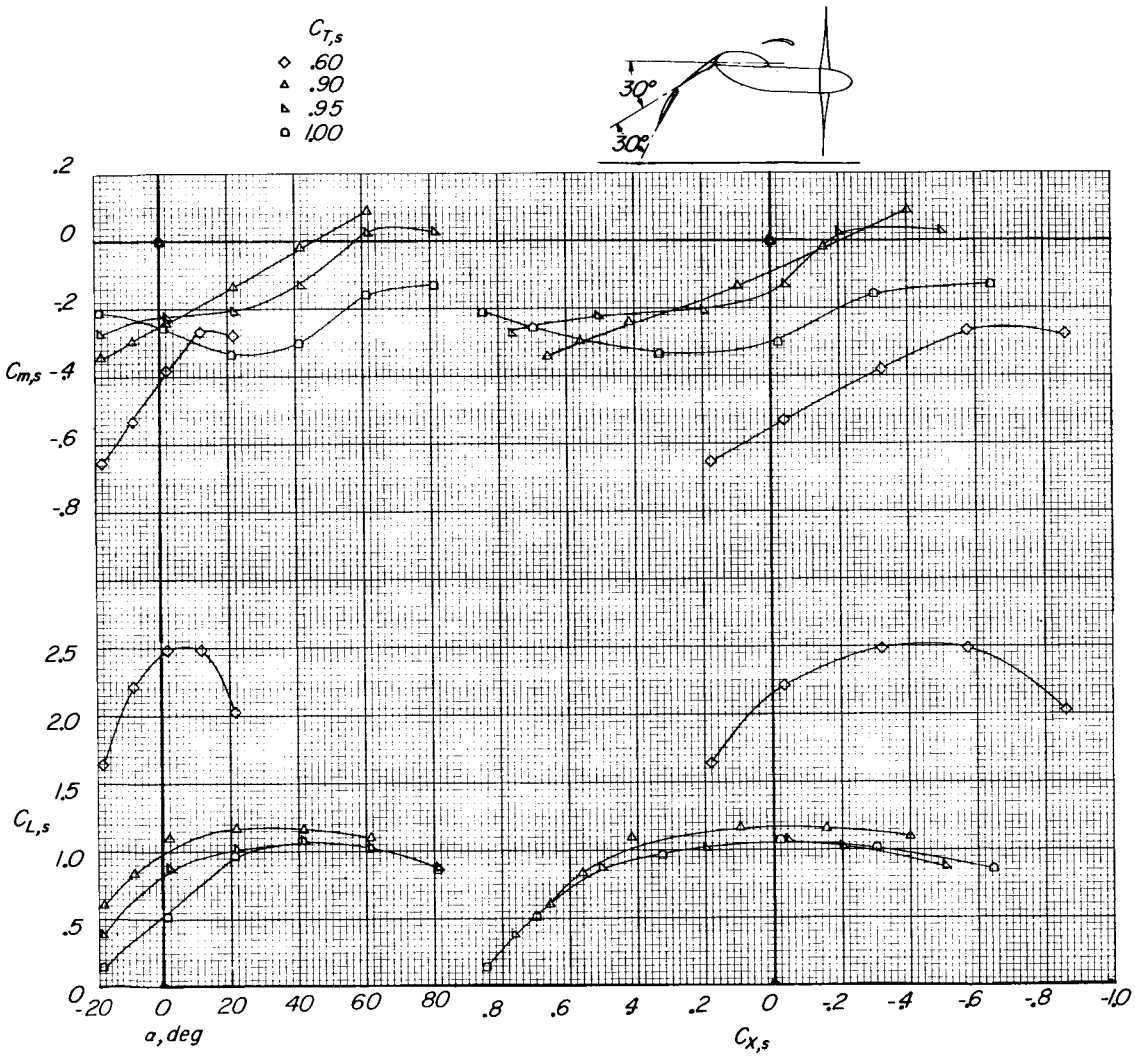

(a) Complete-model data.

Figure 21.- Aerodynamic characteristics of the model in the region of ground effect. Deflected-slipstream configuration ($\delta_{f,S} = 30^{\circ}$; $\delta_{f,F} = 30^{\circ}$); slat in high position; $\delta_{slat} = 0^{\circ}$; h/D = 0.81.

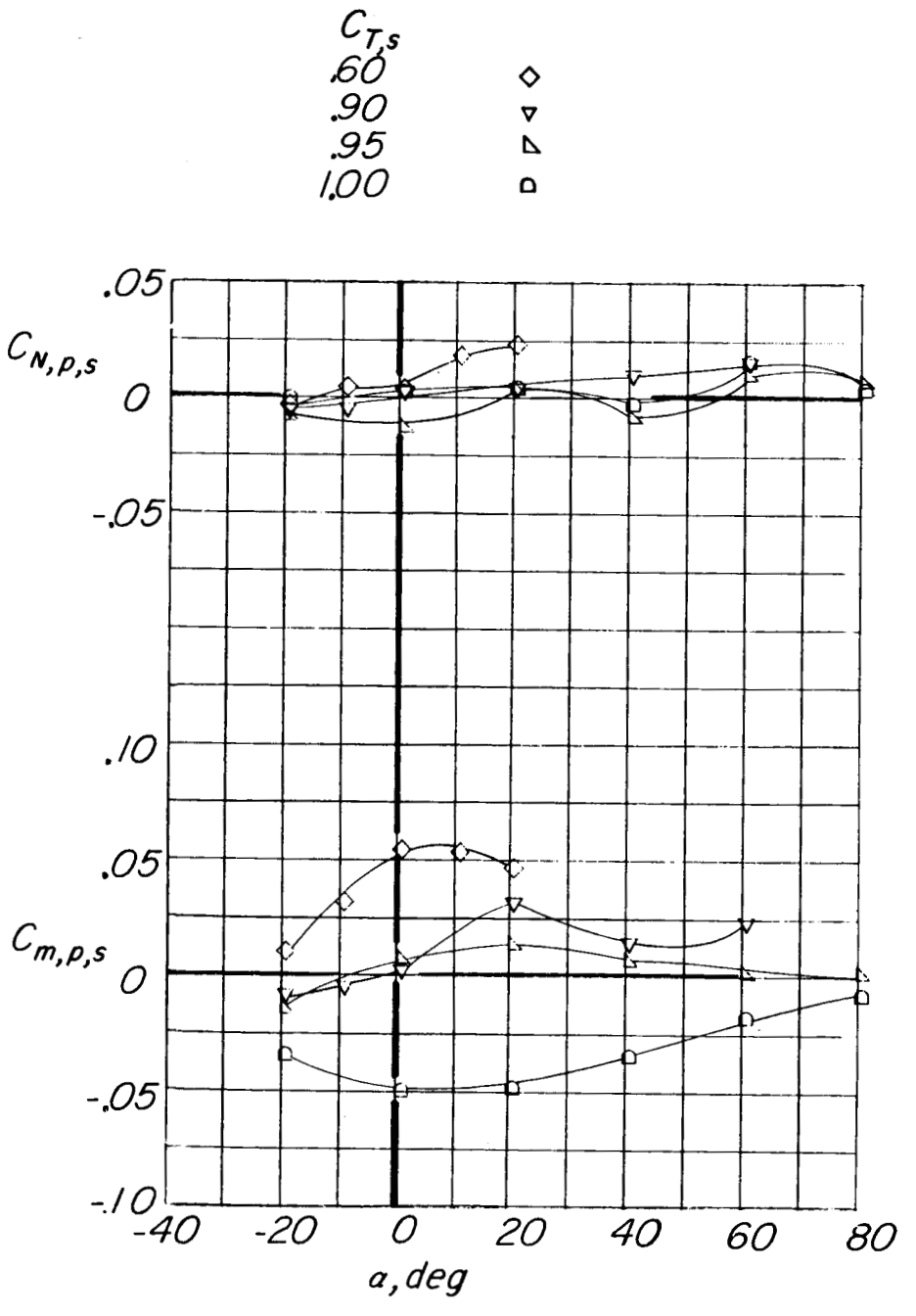

(b) Propeller normal-force and pitching-moment coefficients. Inboard propeller.

Figure 21.- Continued.

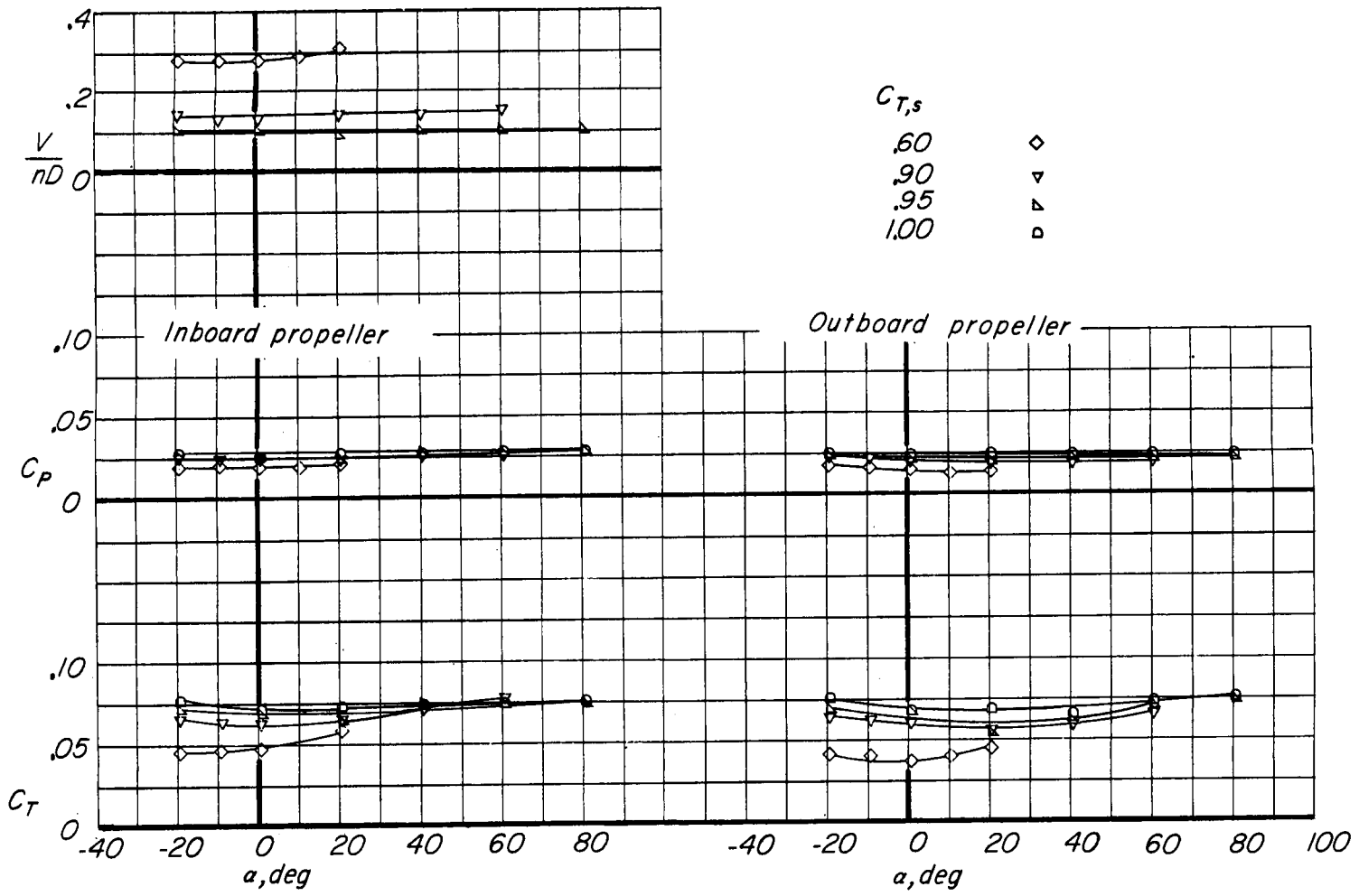

(c) Propeller thrust and power coefficients and advance ratio.

Figure 21.- Continued.

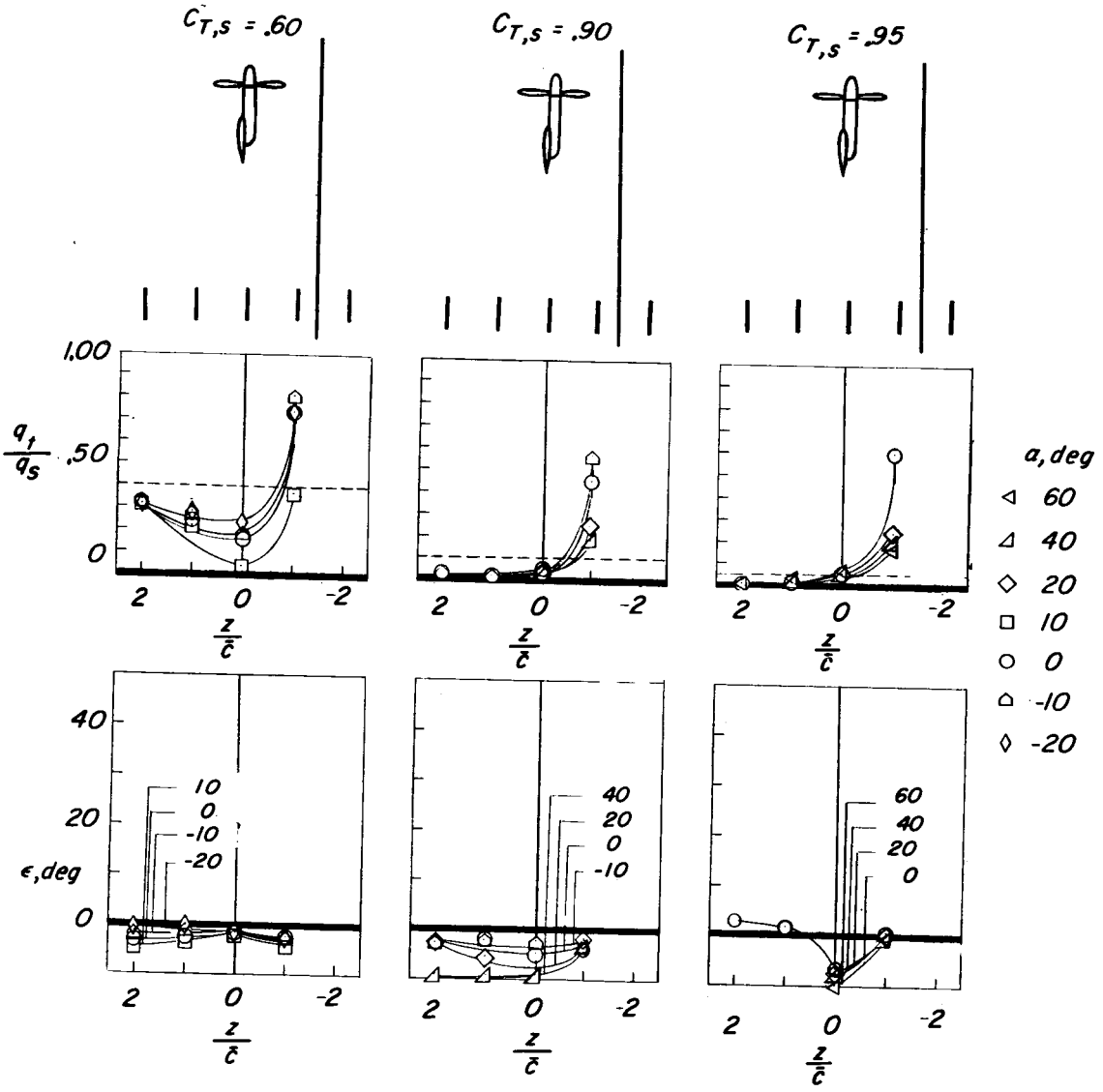

(d) Downwash and dynamic-pressure surveys. Dashed lines indicate level of free-stream dynamic pressure.

Figure 21.- Concluded.

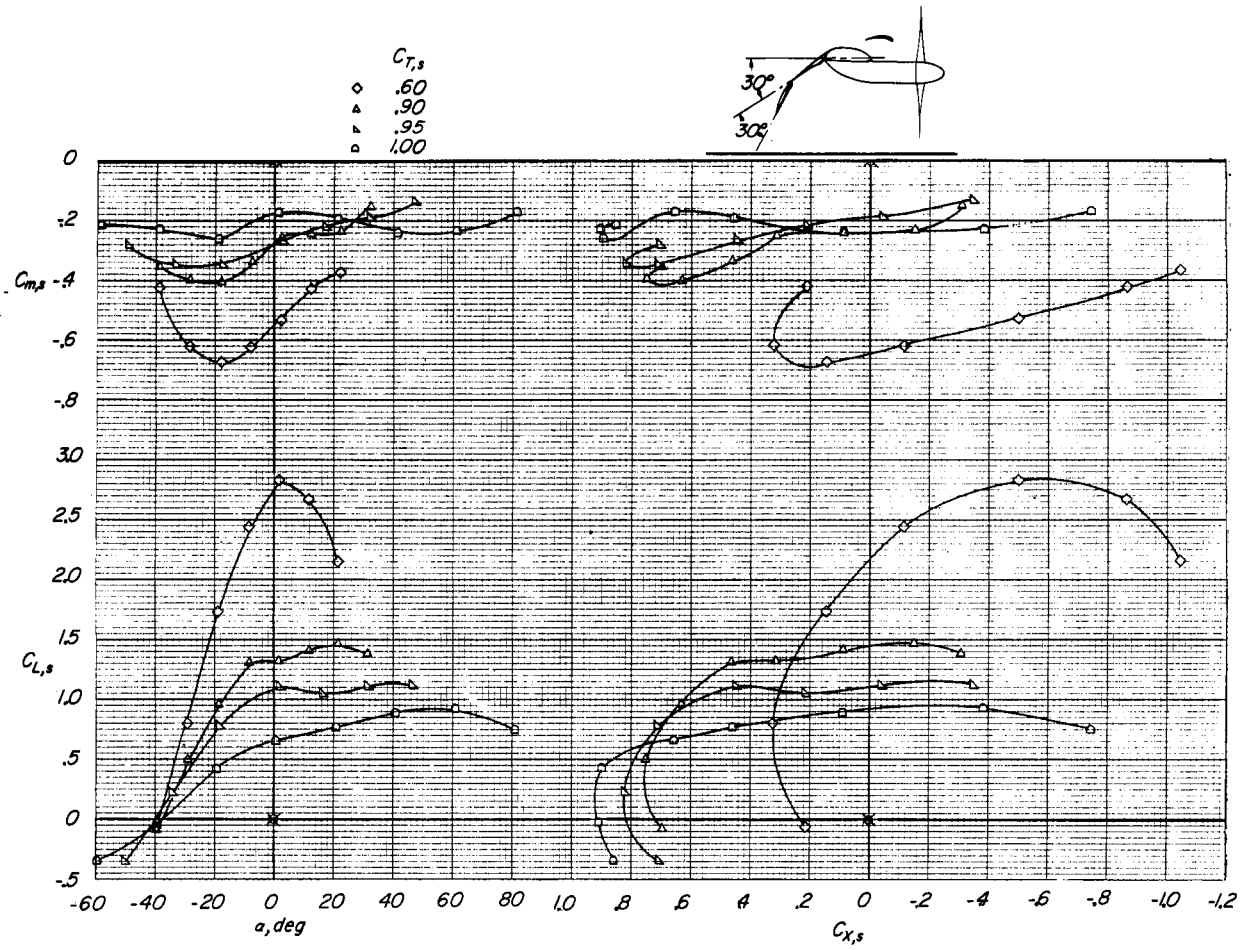

(a) Complete-model data.

Figure 22.- Aerodynamic characteristics of model in region of ground effect. Deflected-slipstream configuration ($\delta_{f,S} = 30°$; $\delta_{f,F} = 30°$); slat in high position; $\delta_{slat} = 0°$; $h/D = 1.46$.

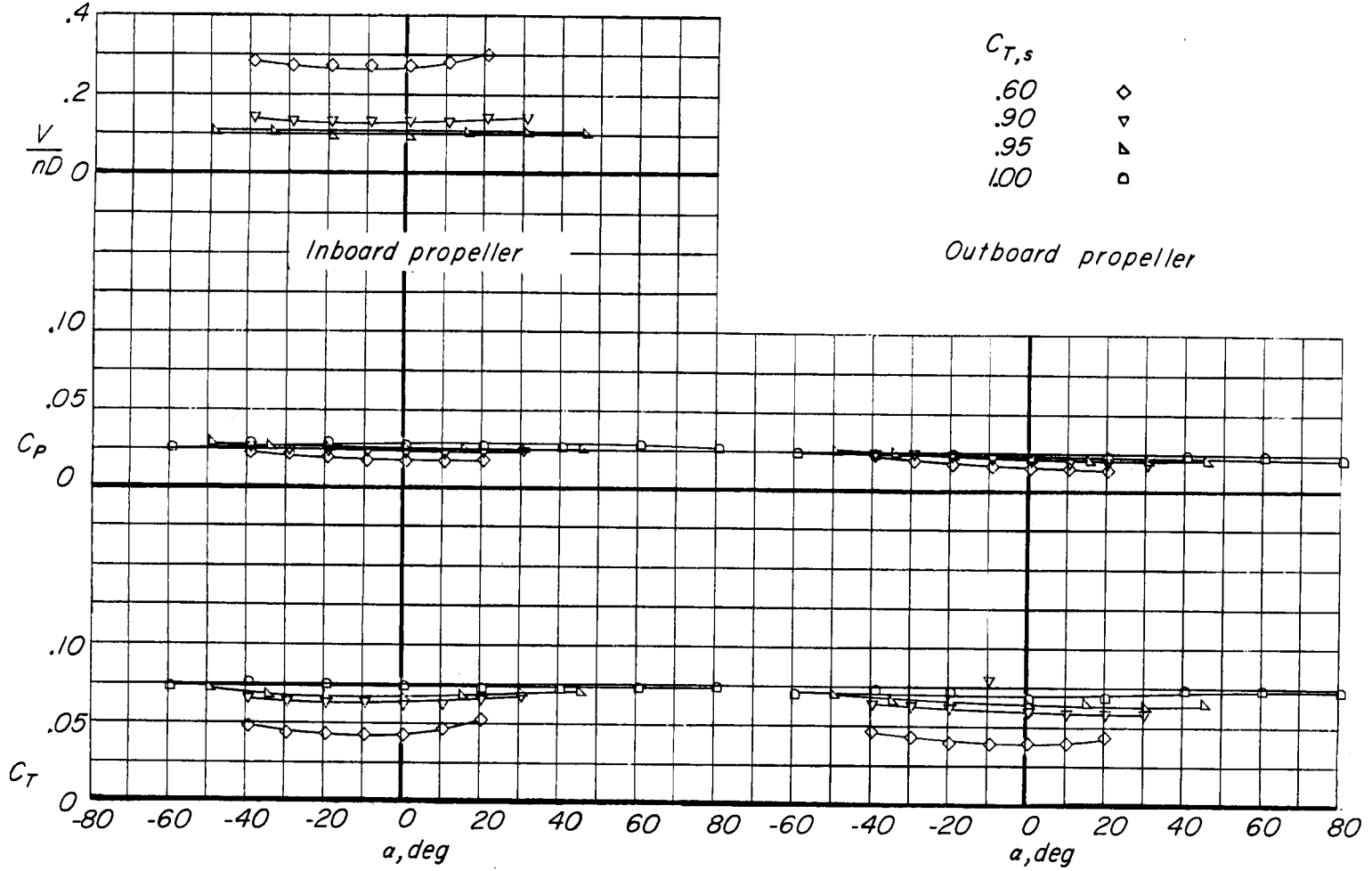

(b) Propeller thrust and power coefficients and advance ratio.

Figure 22.- Concluded.

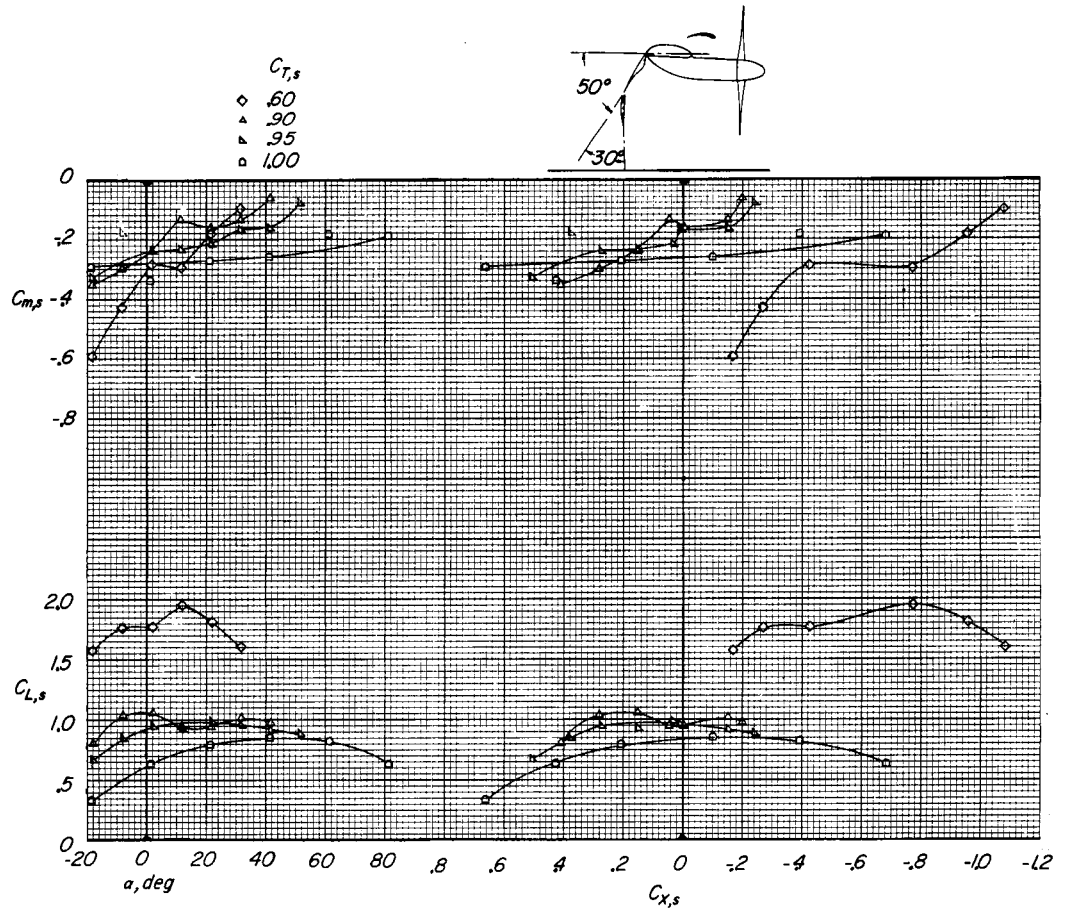

(a) Complete-model data.

Figure 23.- Aerodynamic characteristics of model in region of ground effect. Deflected-slipstream configuration ($\delta_{f,S} = 50°$; $\delta_{f,F} = 30°$); slat in high position; $\delta_{slat} = 0°$; h/D = 0.81.

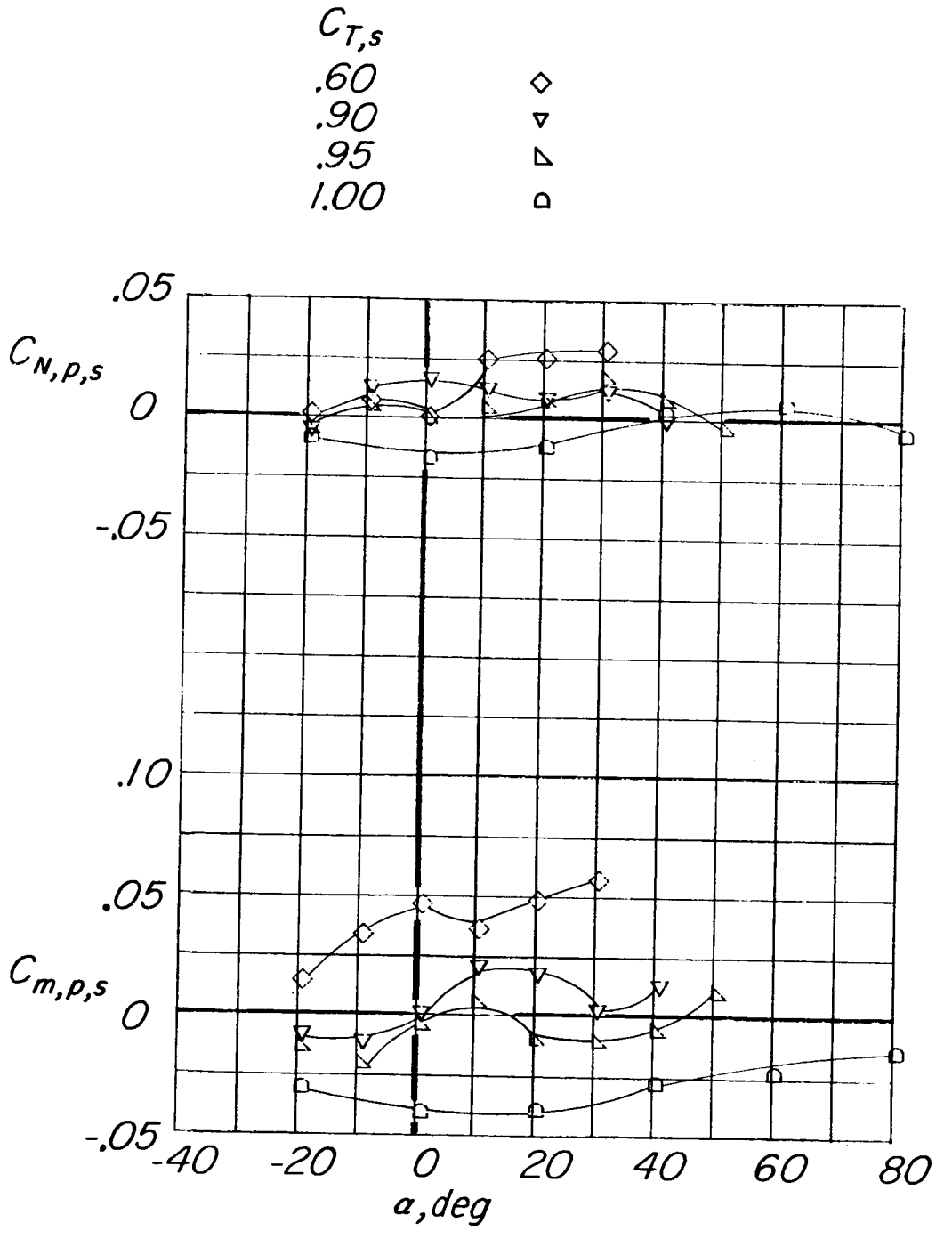

(b) Propeller normal-force and pitching-moment coefficients. Inboard propeller.

Figure 23.- Continued.

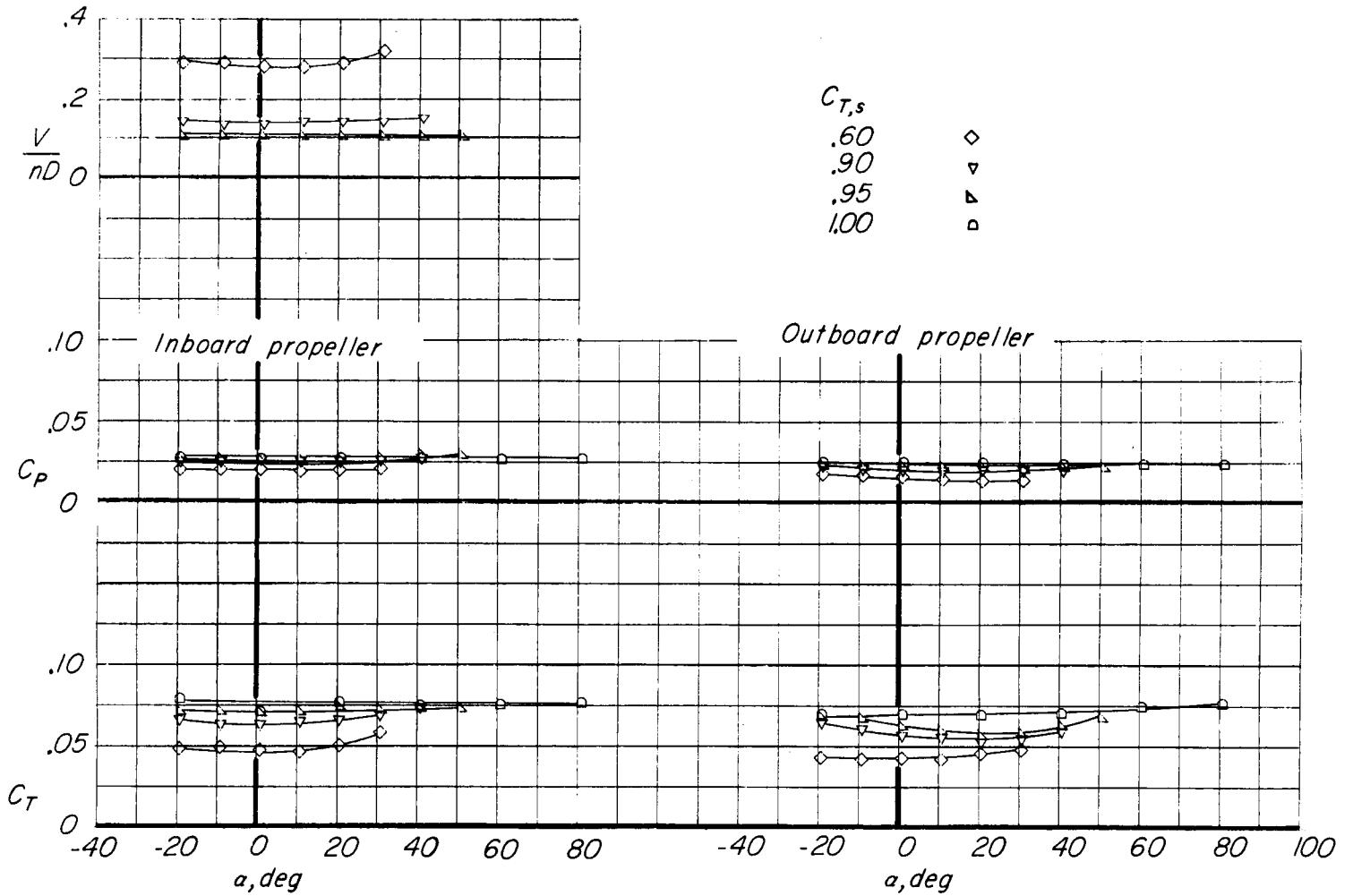

(c) Propeller thrust and power coefficients and advance ratio.

Figure 23.- Continued.

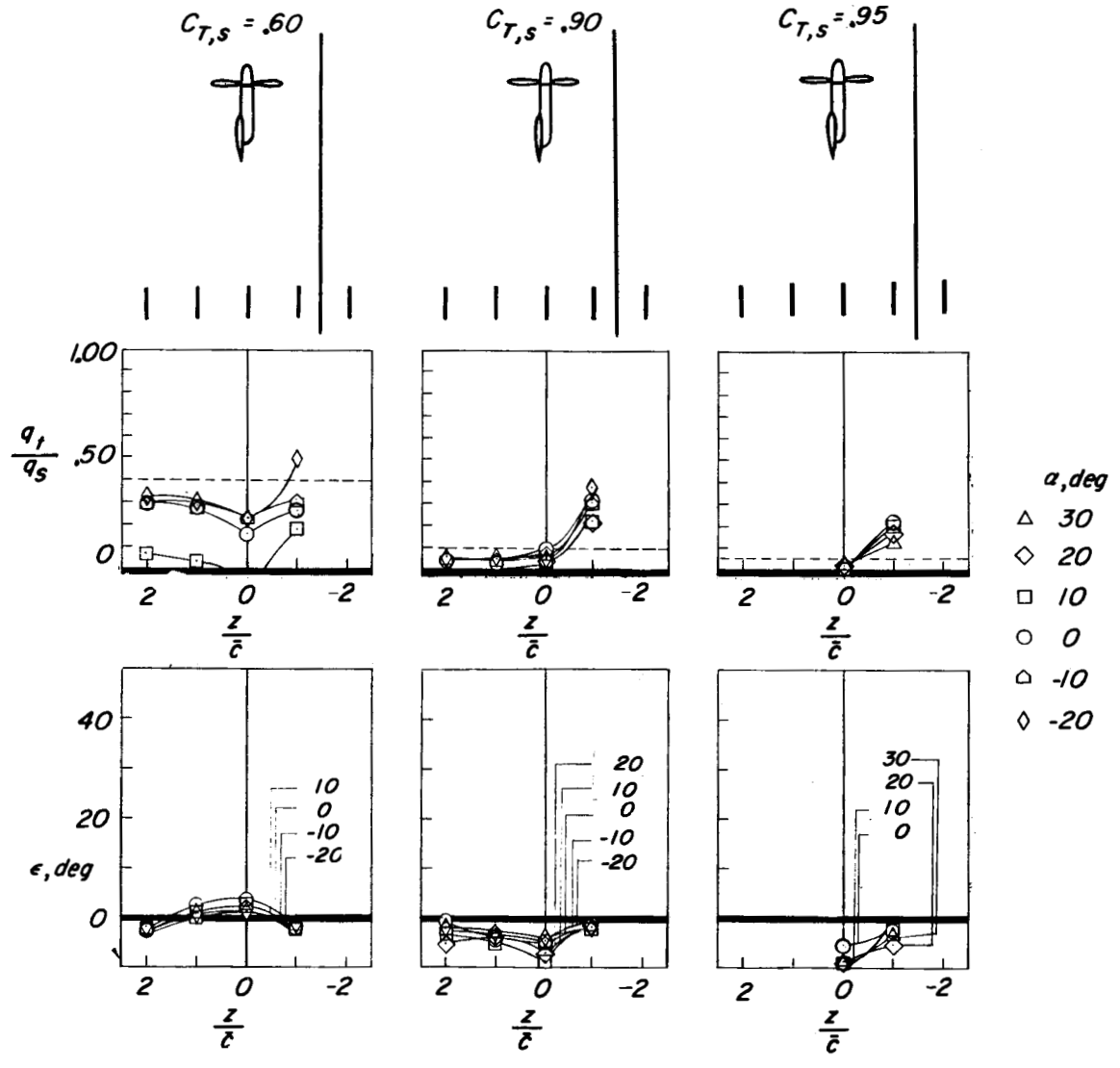

(d) Downwash and dynamic-pressure surveys. Dashed lines indicate level of free-stream dynamic pressure.

Figure 23.- Concluded.

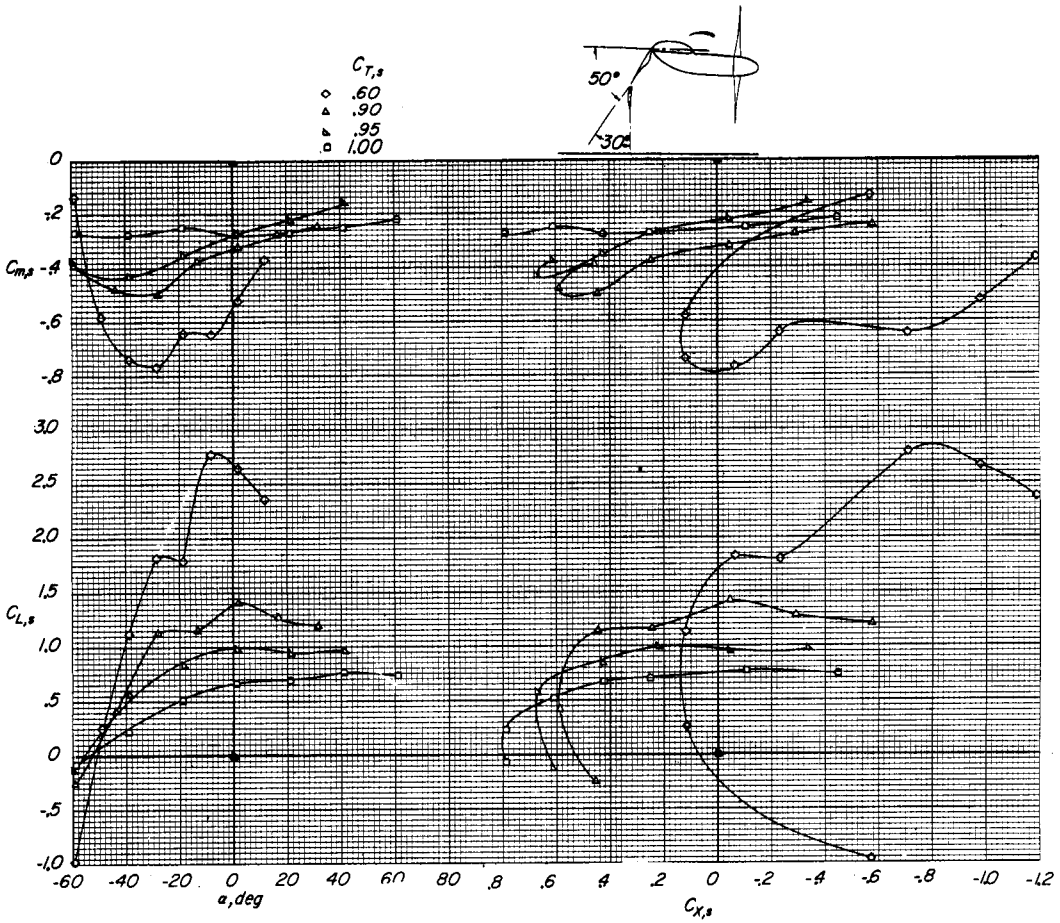

(a) Complete-model data.

Figure 24.- Aerodynamic characteristics of model in region of ground effect. Deflected-slipstream configuration ($\delta_{f,S} = 50^\circ$; $\delta_{f,F} = 30^\circ$); slat in high position; $\delta_{slat} = 0^\circ$; h/D = 1.46.

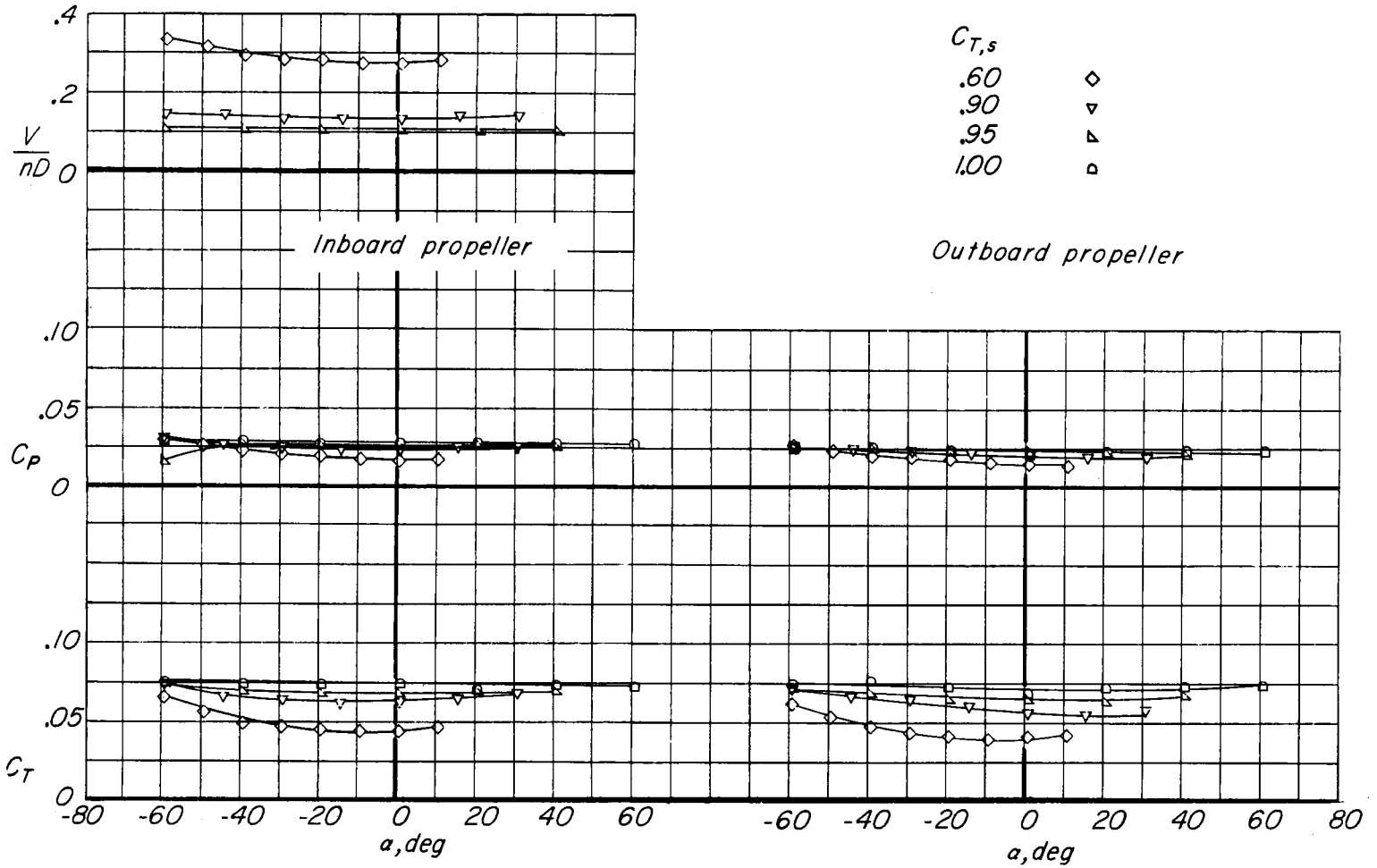

(b) Propeller thrust and power coefficients and advance ratio.

Figure 24.- Concluded.

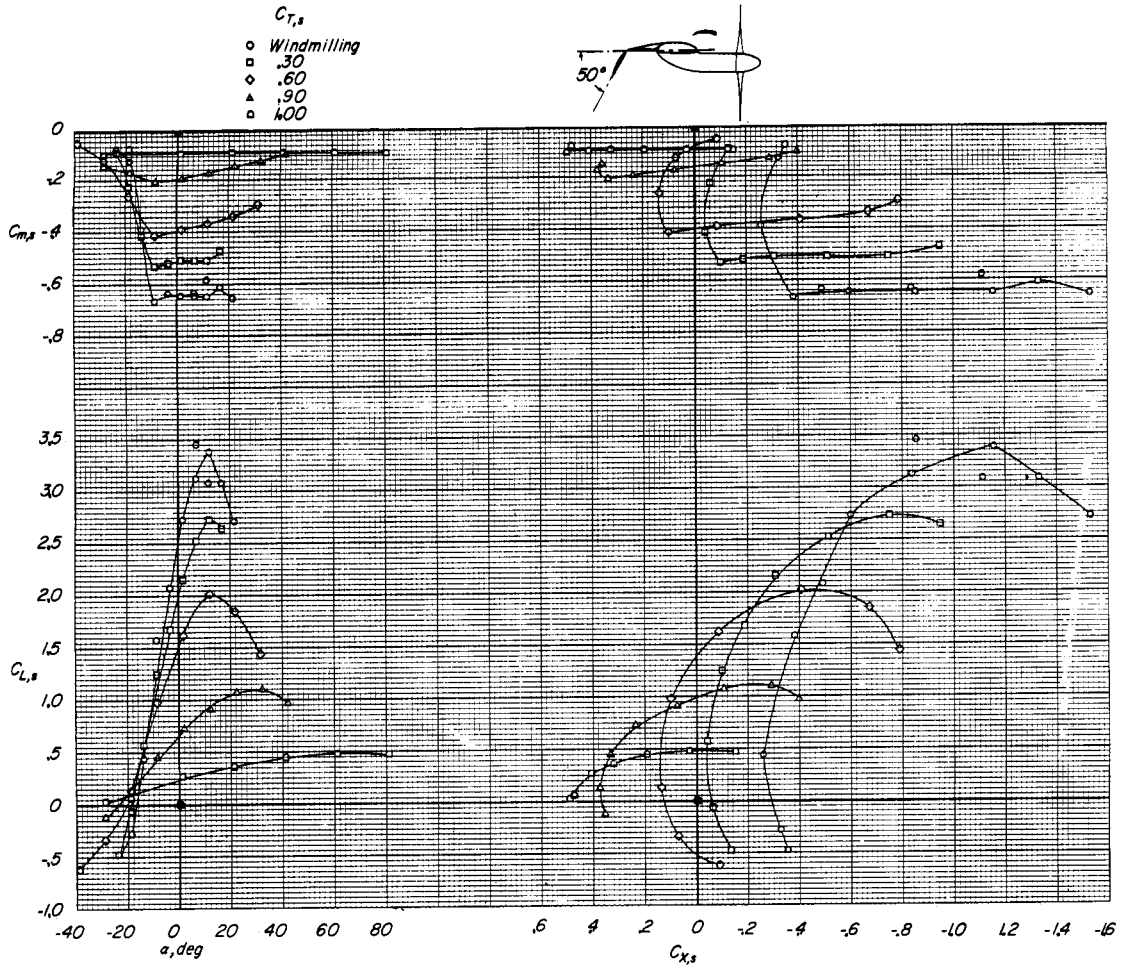

(a) Model data.

Figure 25.- Aerodynamic characteristics of model out of region of ground effect. Combination configuration ($\delta_{f,S} = 0^{\circ}$; $\delta_{f,F} = 50^{\circ}$); single (inboard) propeller operating; slat in high position; $\delta_{slat} = 0^{\circ}$.

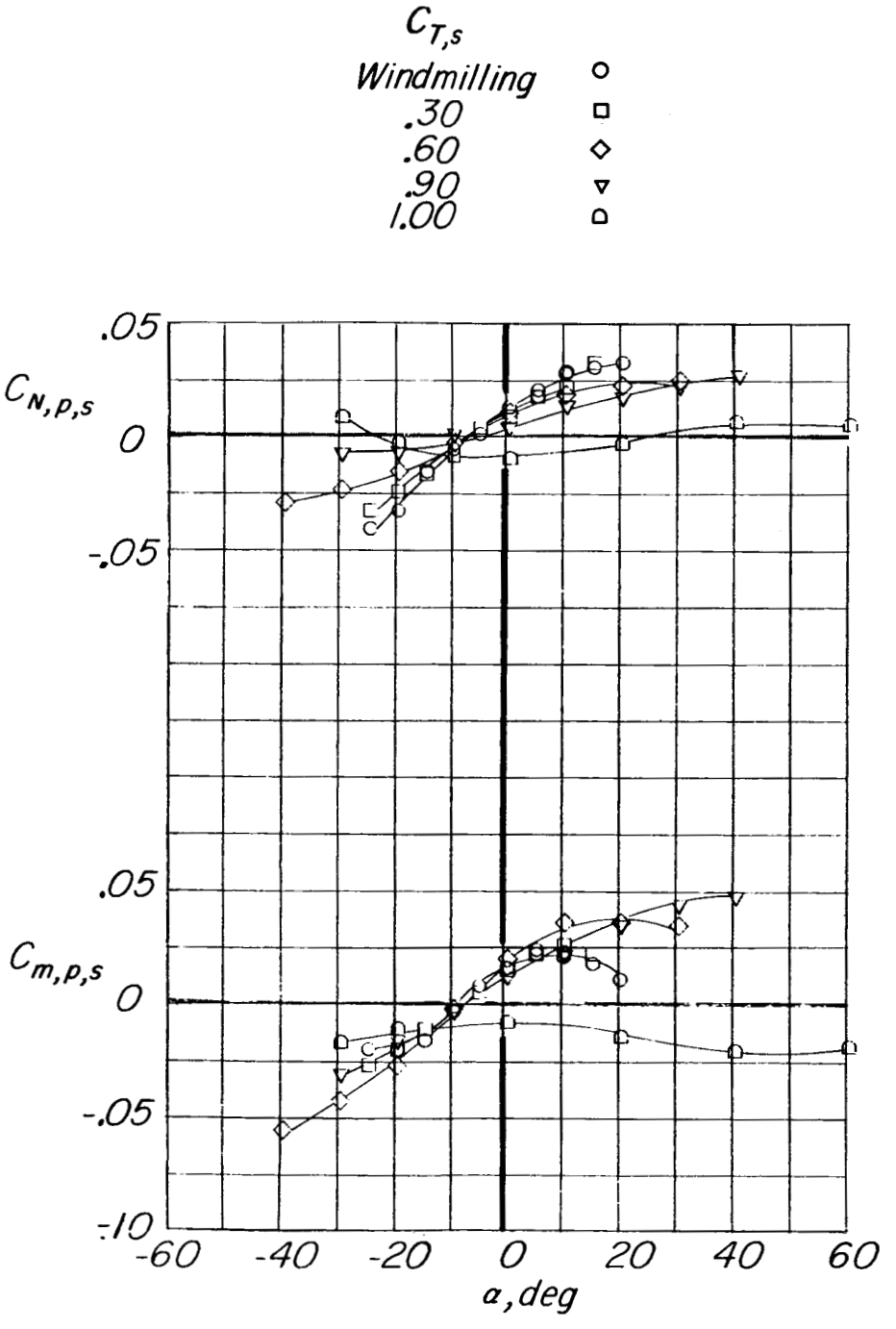

(b) Propeller normal-force and pitching-moment coefficients.

Figure 25.- Continued.

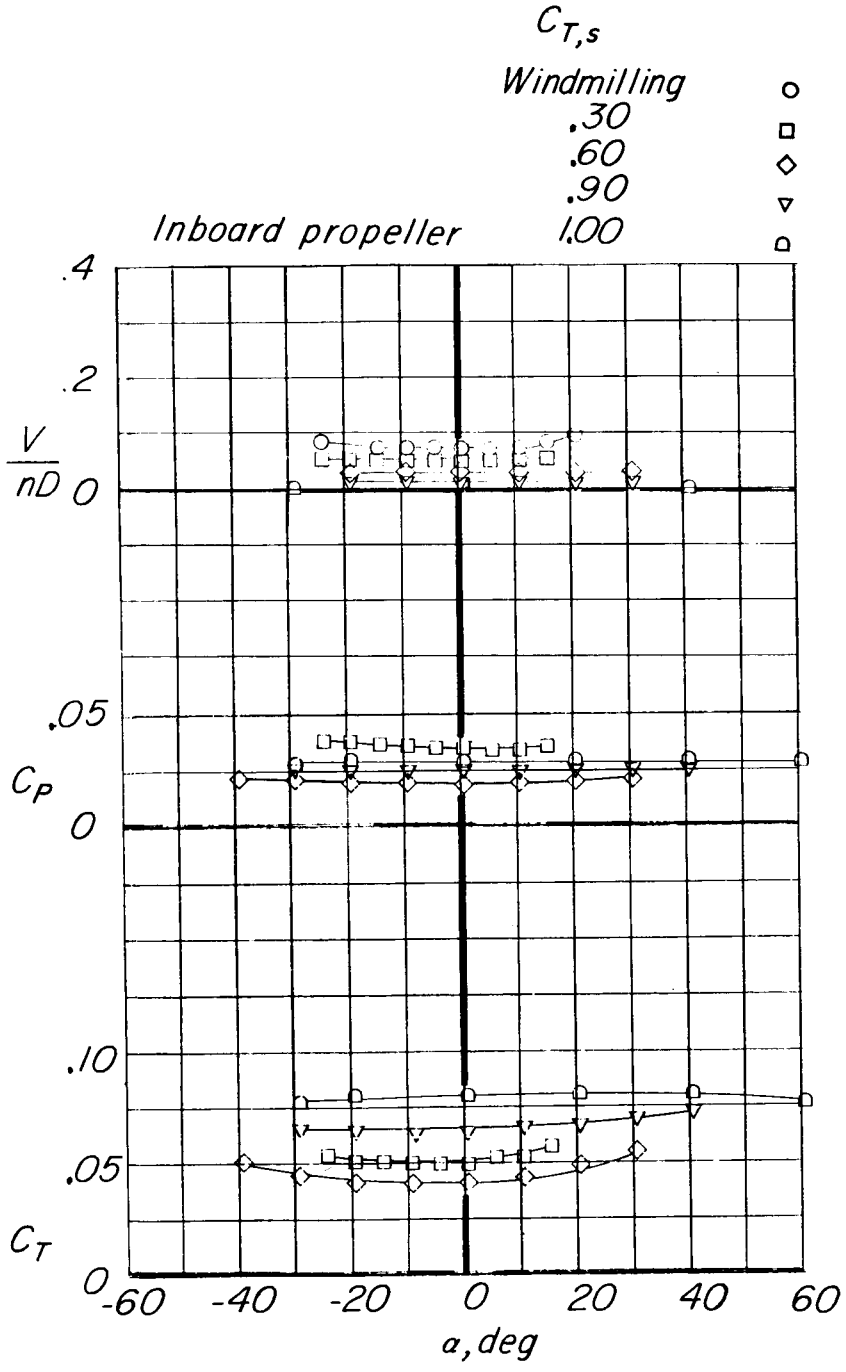

(c) Propeller thrust and power coefficients and advance ratio.

Figure 25.- Continued.

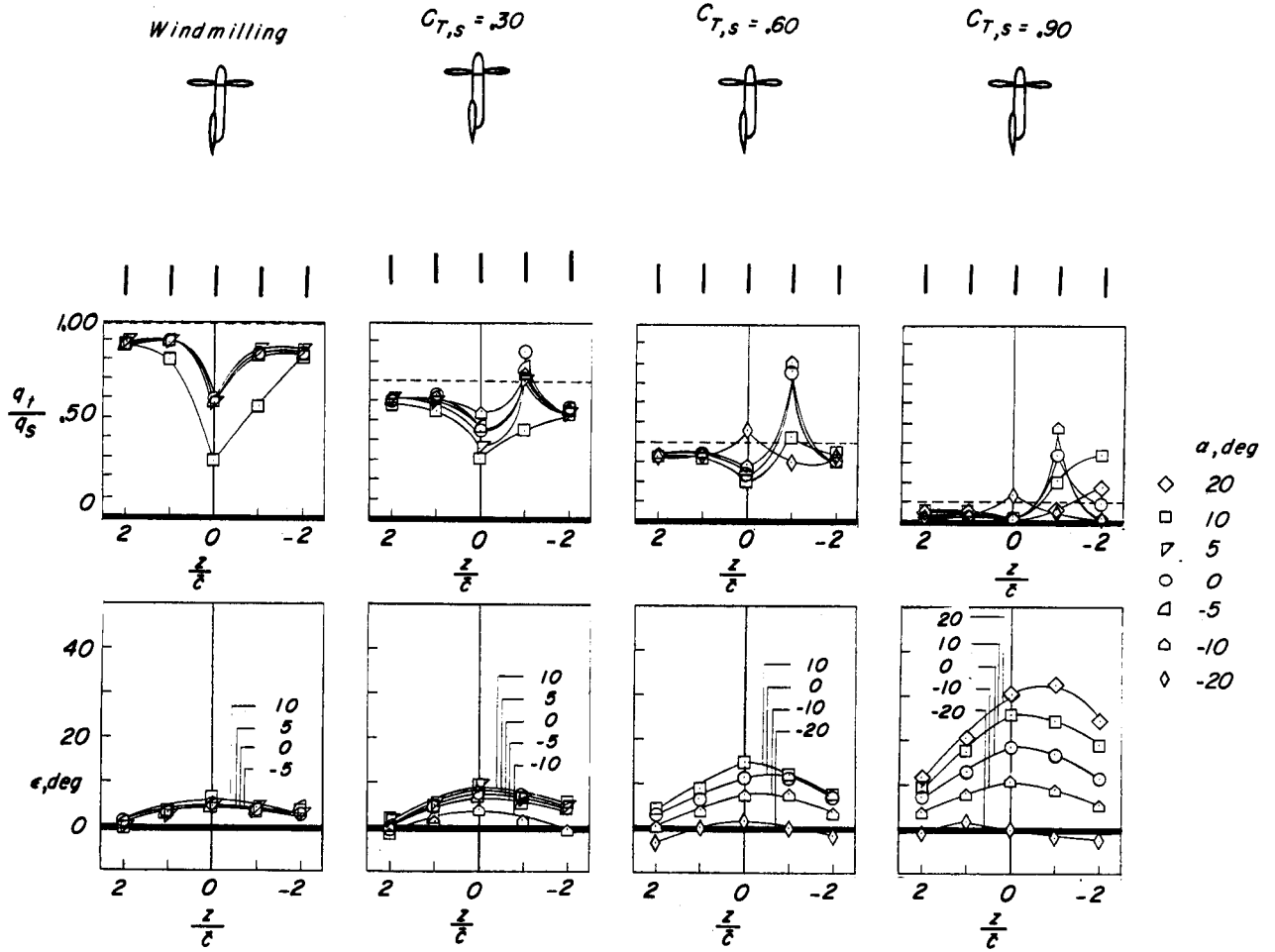

(d) Downwash and dynamic-pressure surveys. Dashed lines indicate level of free-stream dynamic pressure.

Figure 25.- Concluded.

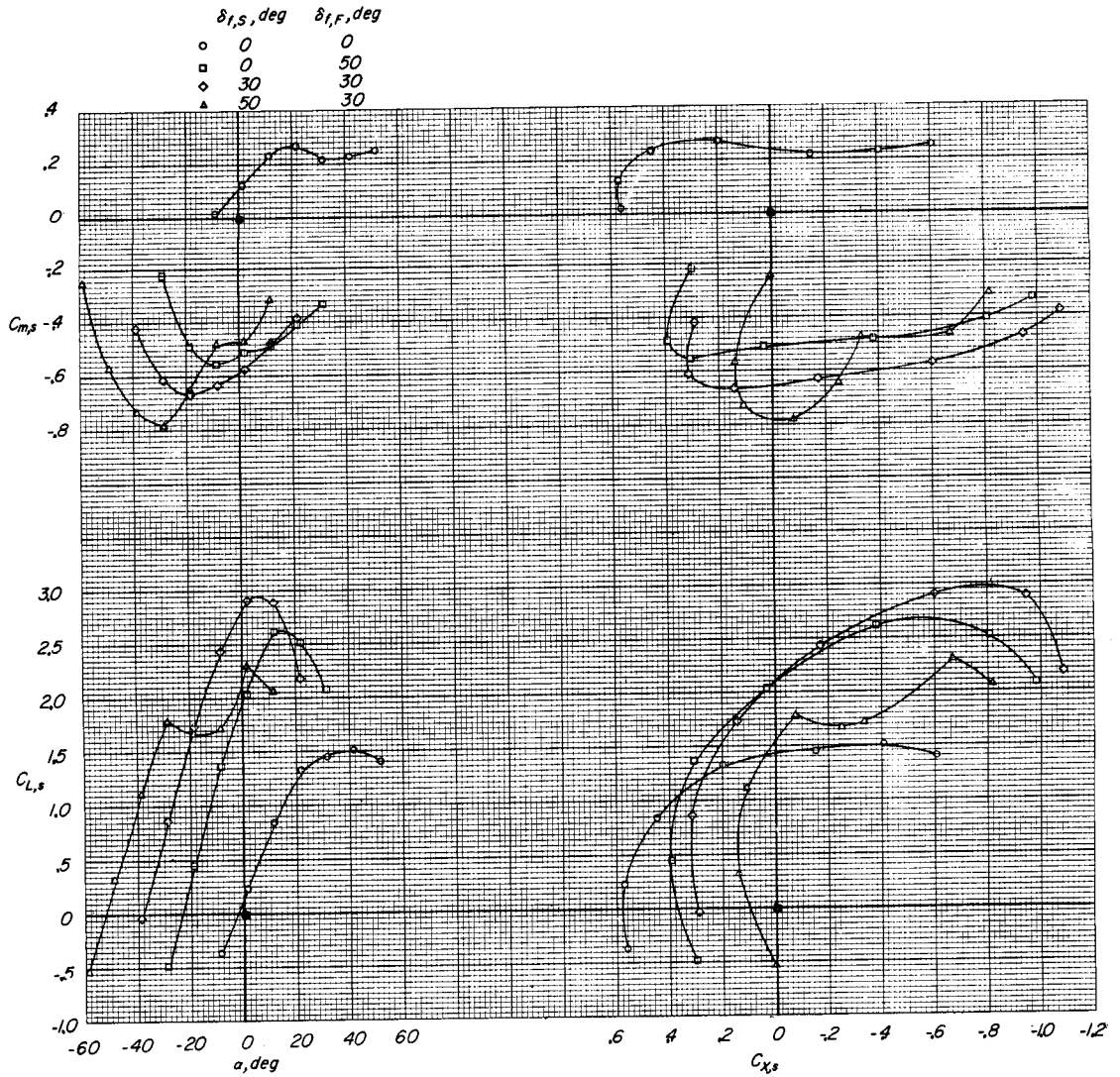

(a) $C_{T,s} = 0.60$.

Figure 26.- Effect of flap deflection at constant thrust coefficient out of region of ground effect. Slat in high position; $\delta_{slat} = 0^{o}$.

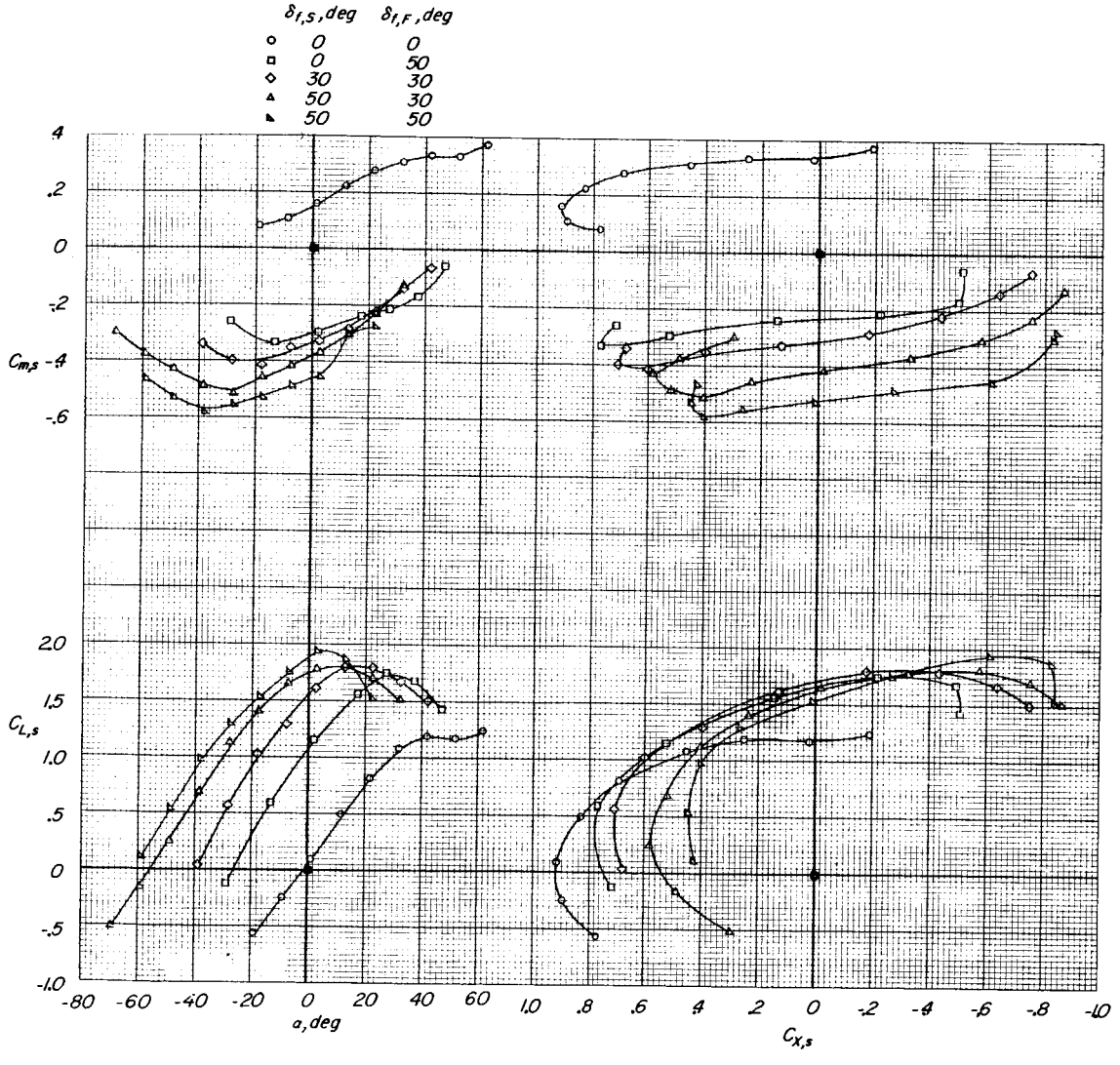

(b) $C_{T,s} = 0.90$.

Figure 26.- Continued.

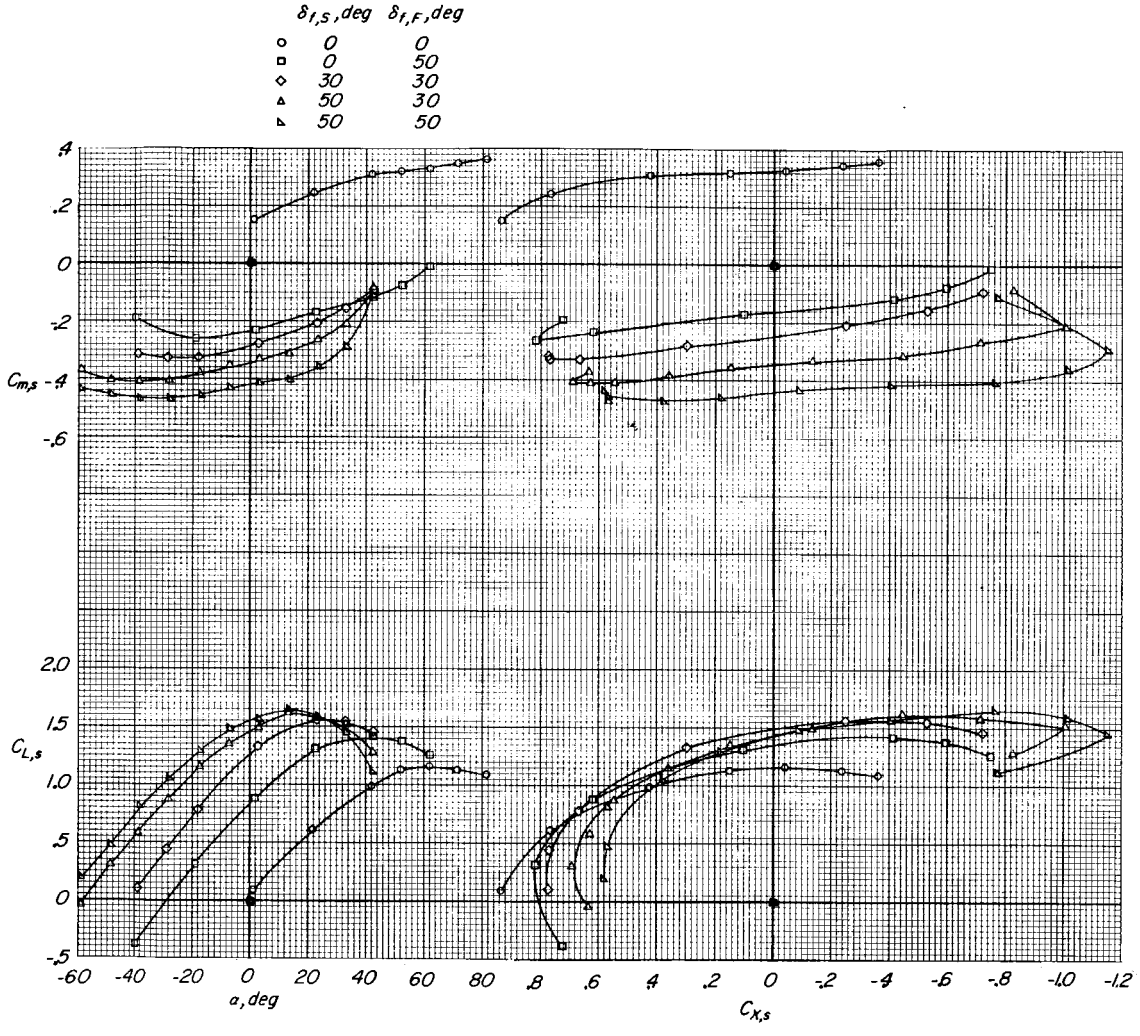

(c) $C_{T,s} = 0.95$.

Figure 26.- Continued.

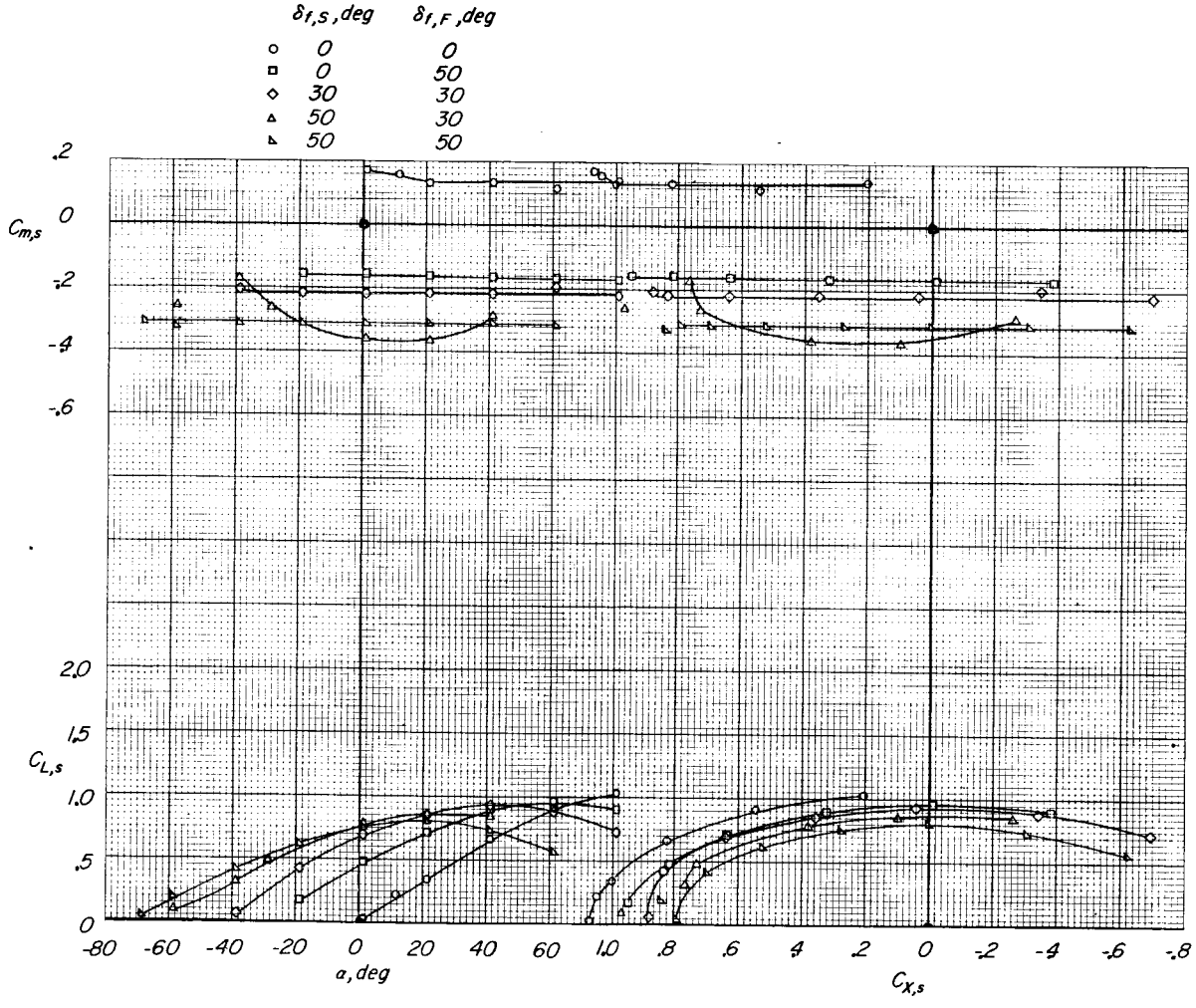

(d) $C_{T,s} = 1.00$.

Figure 26.- Concluded.

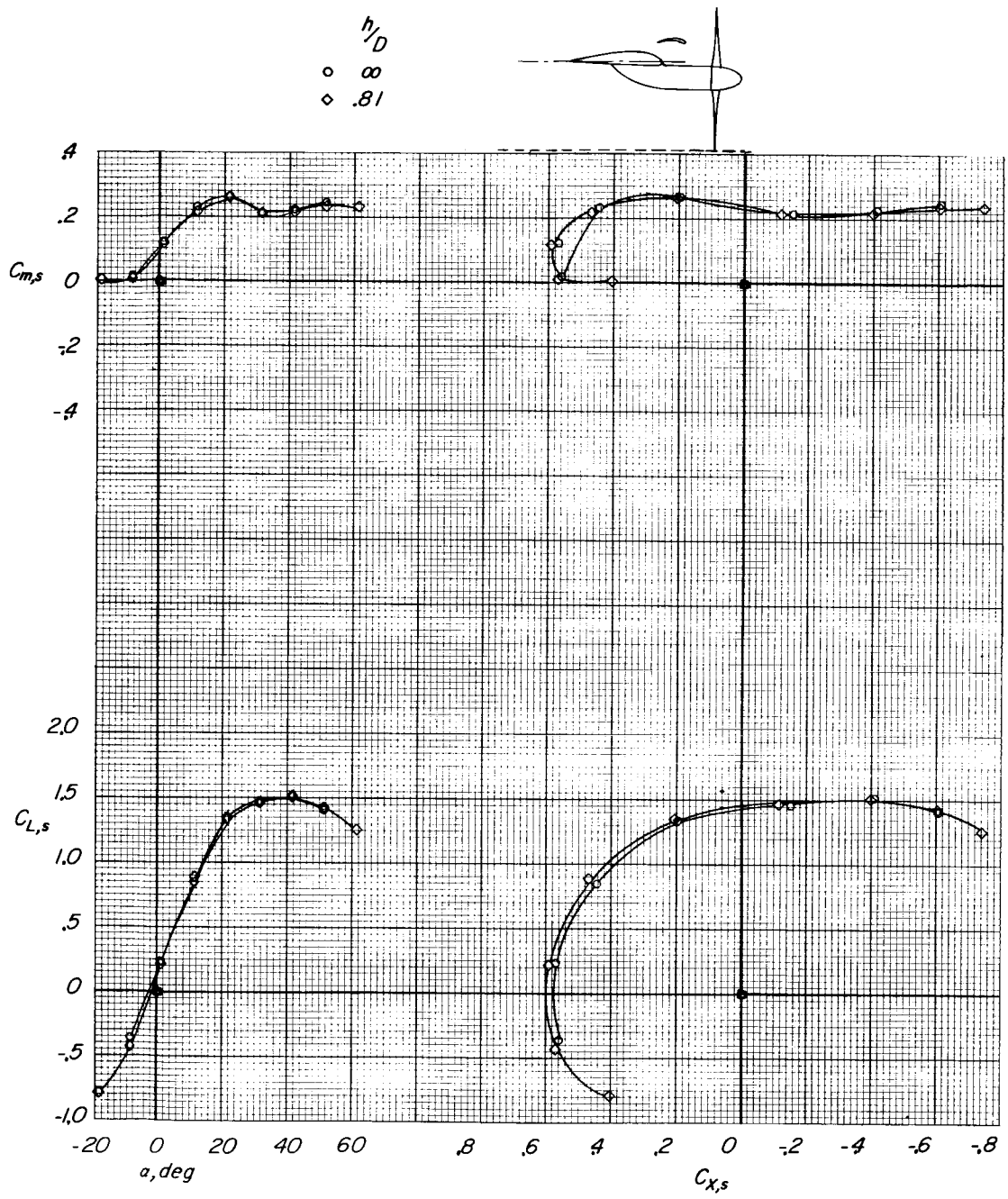

(a) $C_{T,s} = 0.60$.

Figure 27.- Effect of ground proximity. Tilt-wing configuration ($\delta_{f,S} = 0^{o}$; $\delta_{f,F} = 0^{o}$); slat in high position; $\delta_{slat} = 0^{o}$.

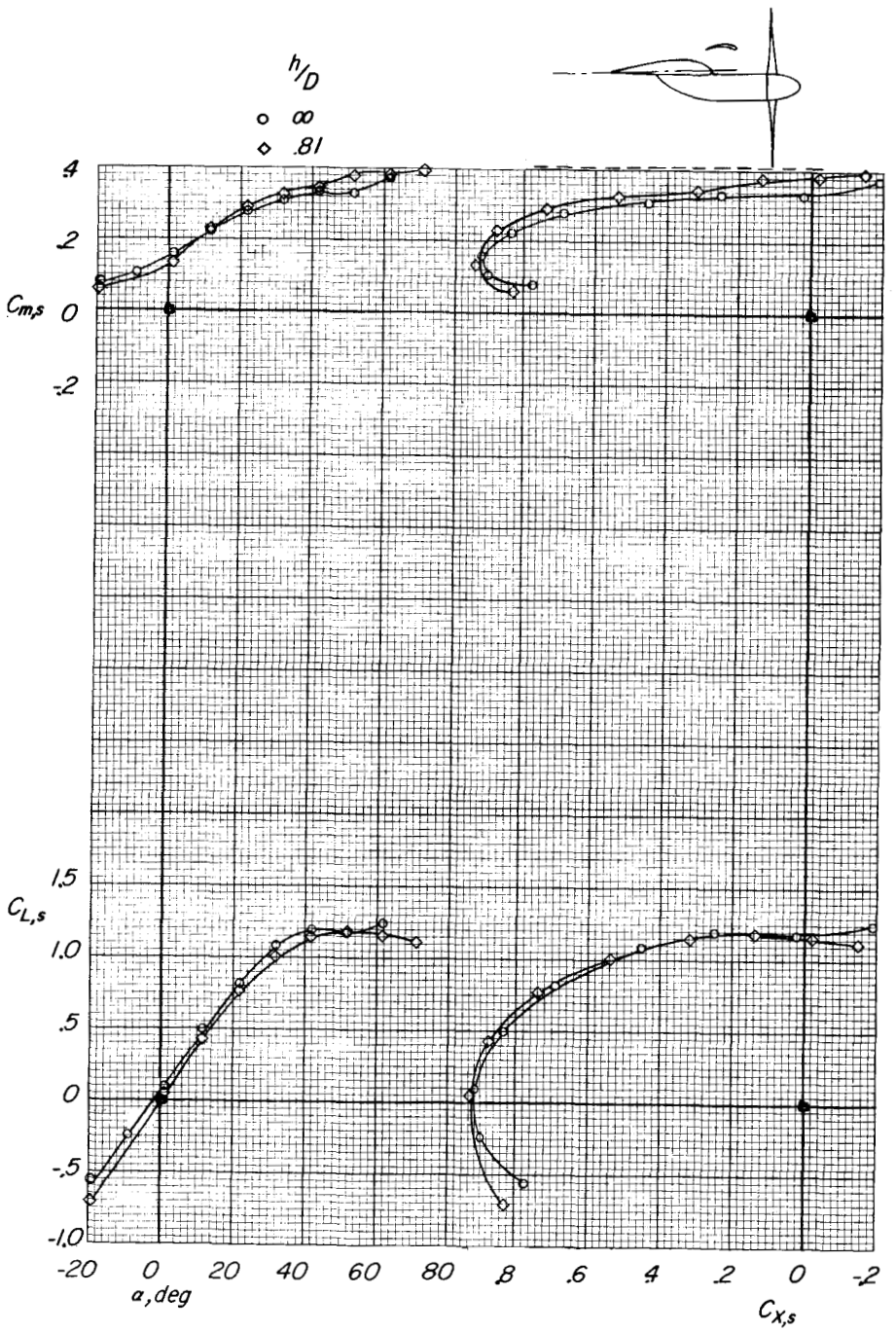

(b) $C_{T,s} = 0.90$.

Figure 27.- Continued.

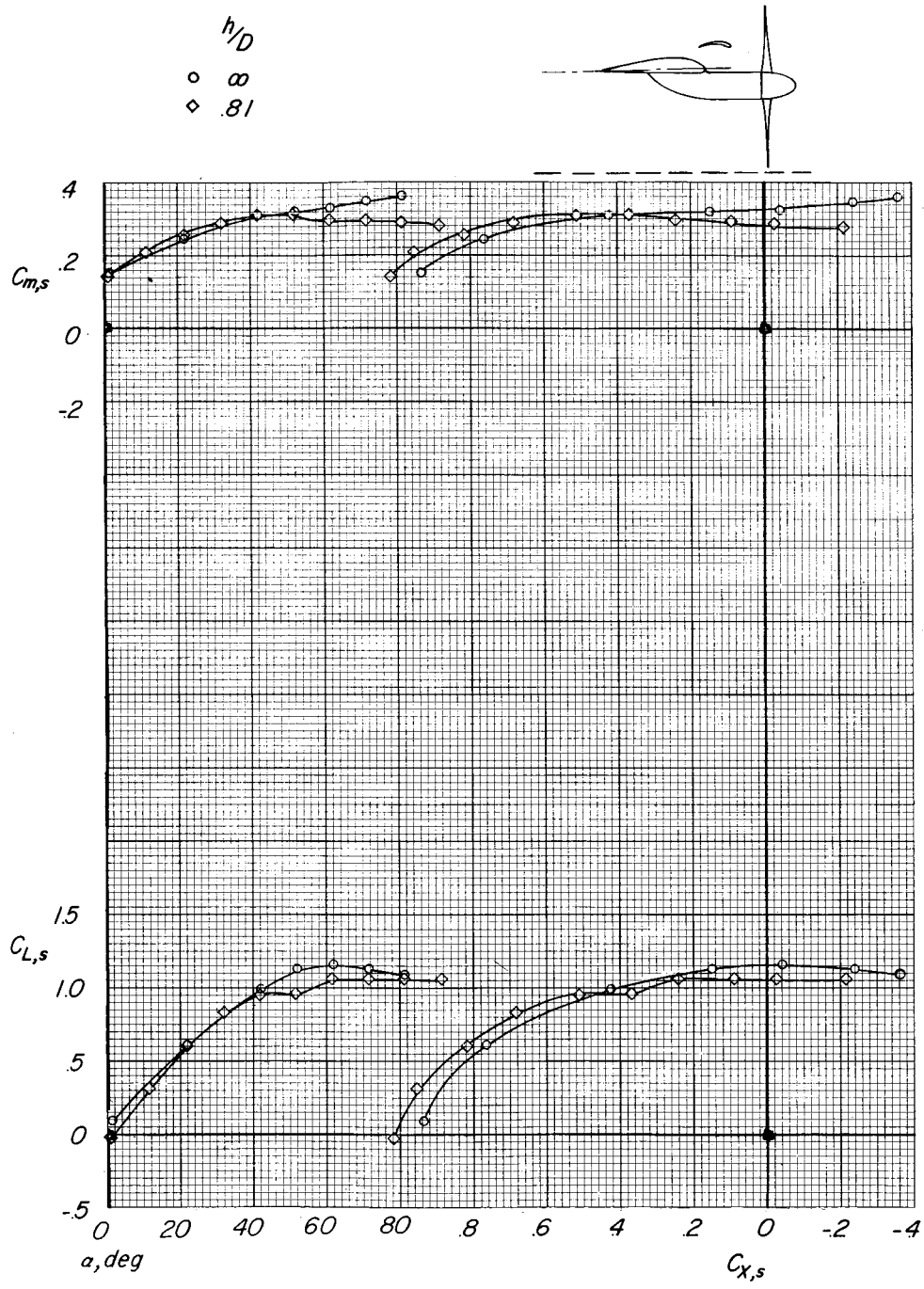

(c) $C_{T,s} = 0.95$.

Figure 27.- Concluded.

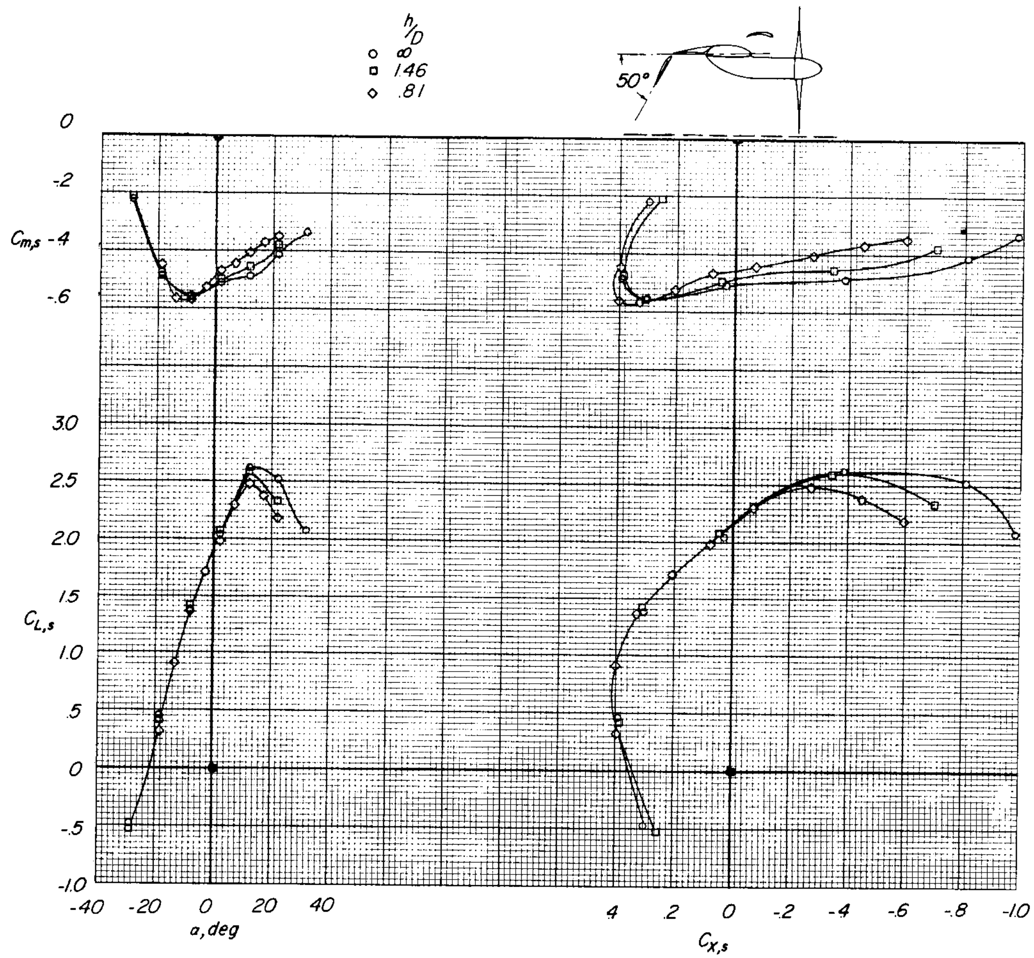

(a) $C_{T,s} = 0.60$.

Figure 28.- Effect of ground proximity. Combination configuration $(\delta_{f,S} = 0^{\circ}; \delta_{f,F} = 50^{\circ})$; slat in high position; $\delta_{slat} = 0^{\circ}$.

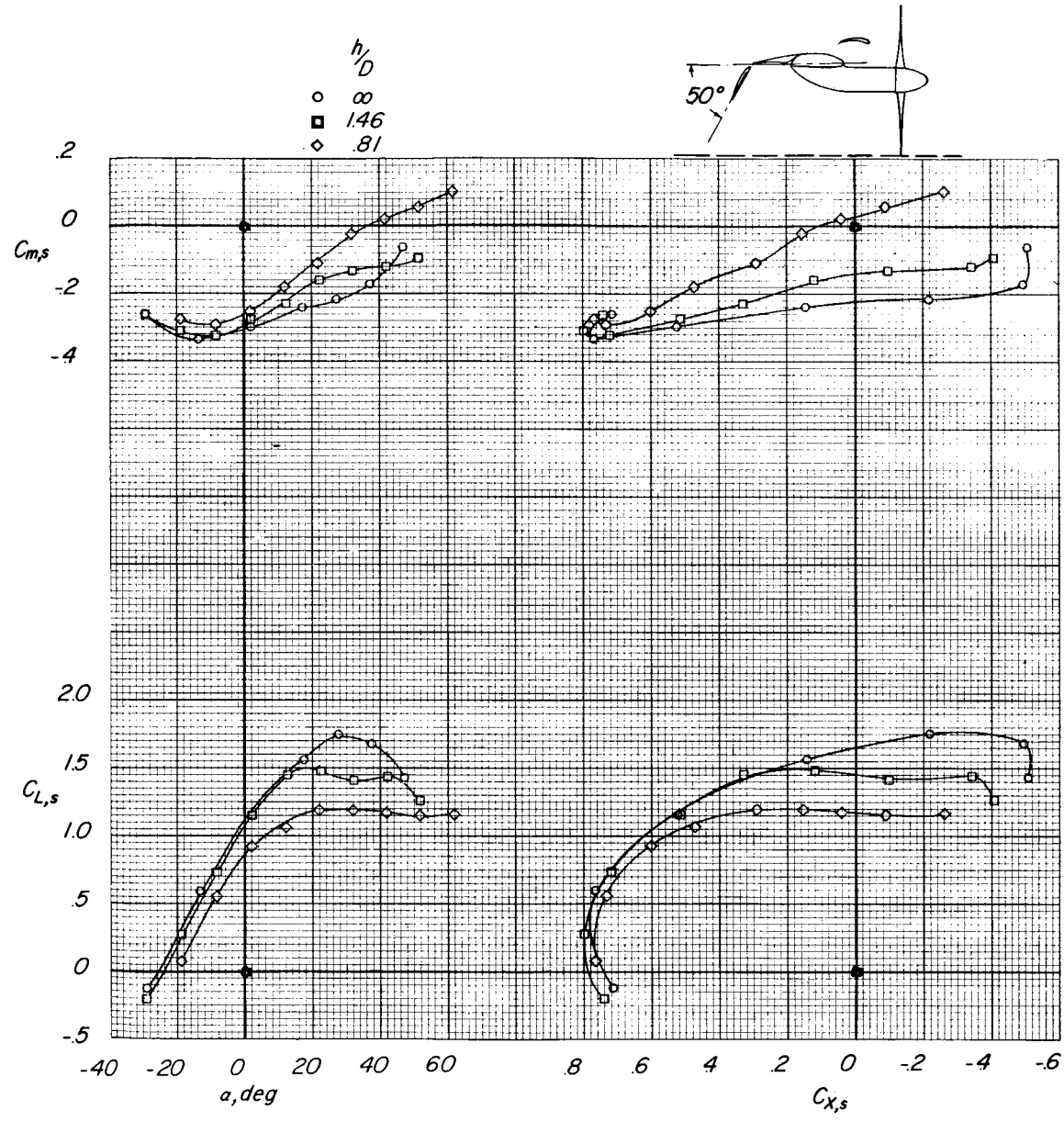

(b) $C_{T,s} = 0.90$.

Figure 28.- Continued.

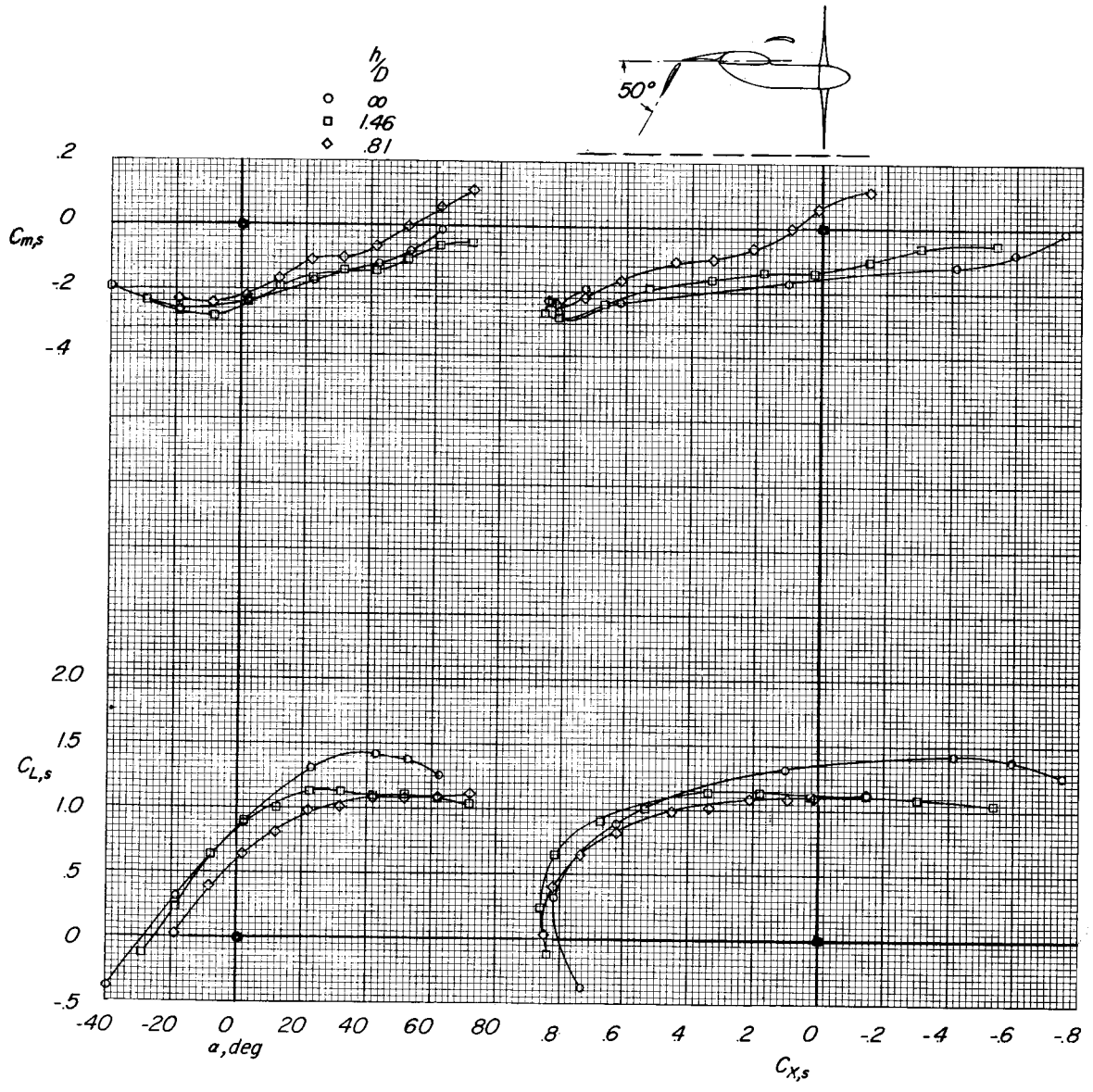

(c) $C_{T,s} = 0.95$.

Figure 28.- Continued.

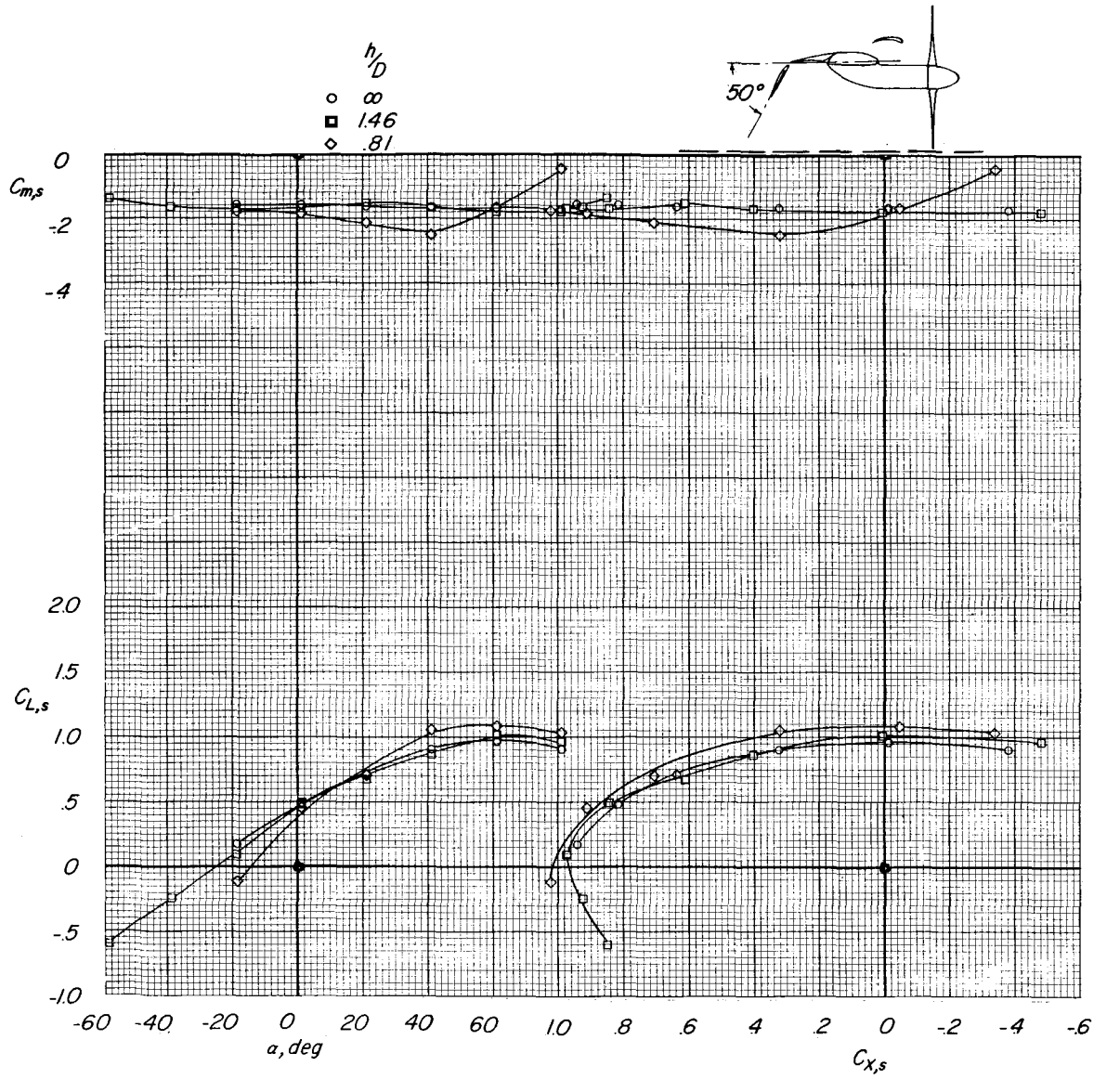

(d) $C_{T,s} = 1.00$.

Figure 28.- Concluded.

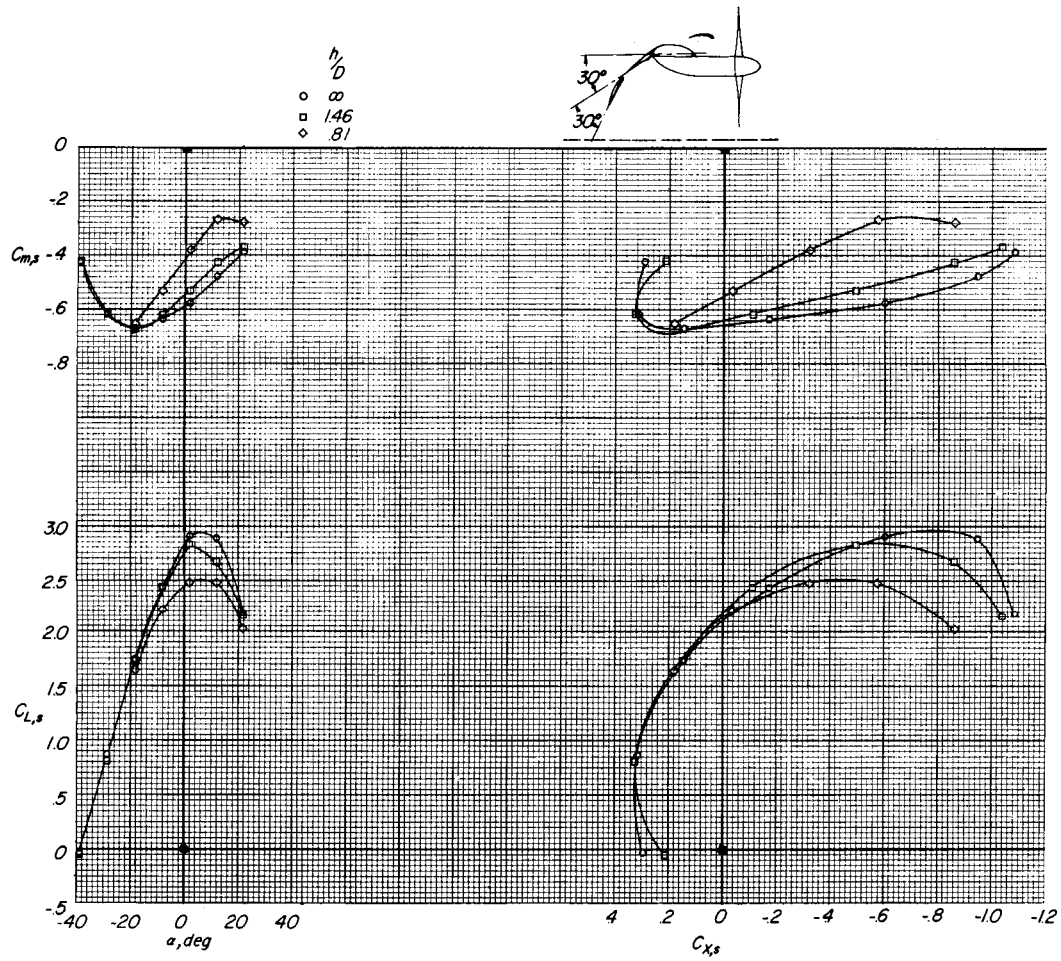

(a) $C_{T,s} = 0.60$.

Figure 29.- Effect of ground proximity. Deflected-slipstream configuration ($\delta_{f,S} = 30^{\circ}$; $\delta_{f,F} = 30^{\circ}$); slat in high position; $\delta_{slat} = 0^{\circ}$.

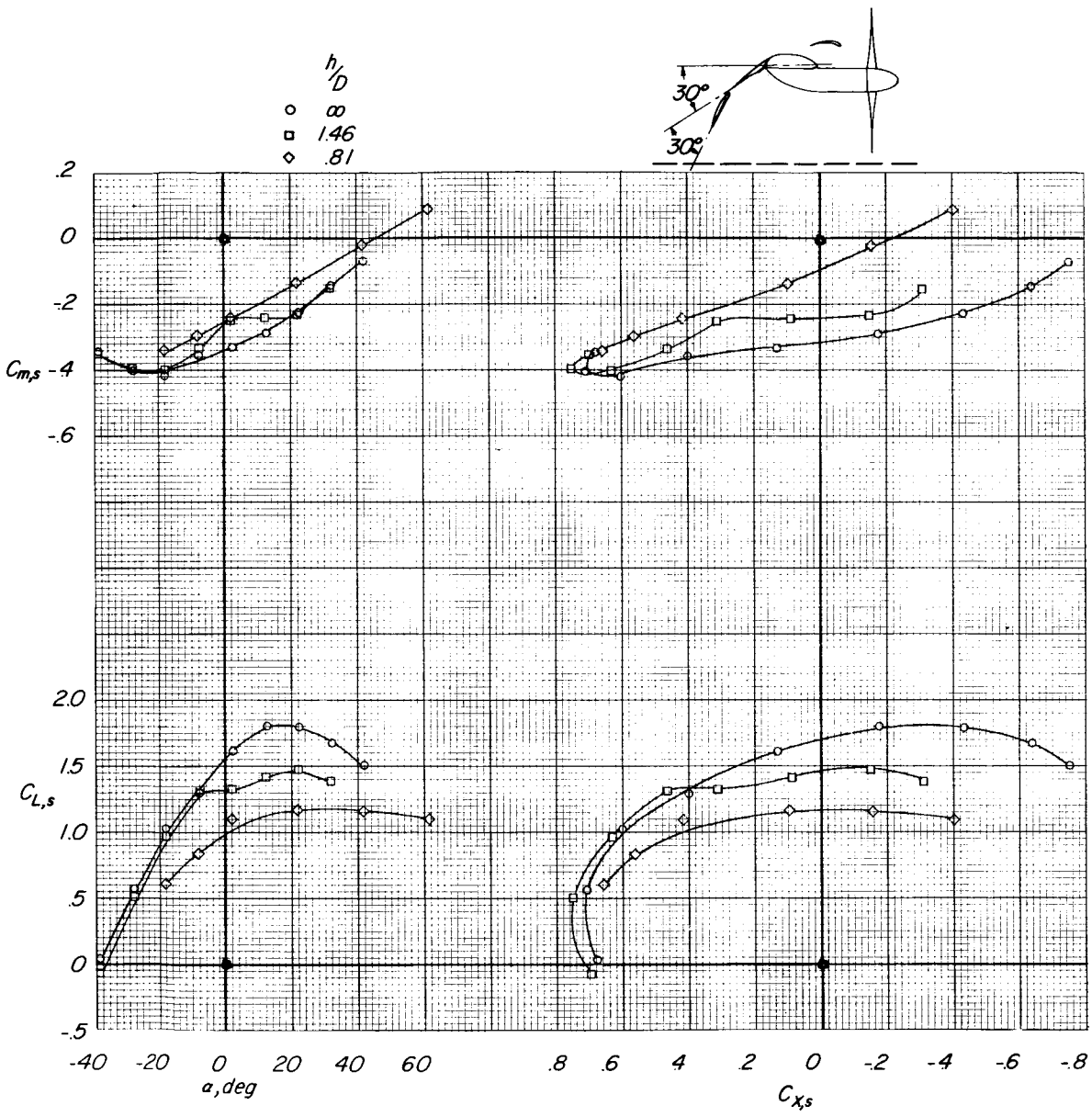

(b) $C_{T,s} = 0.90$.

Figure 29.- Continued.

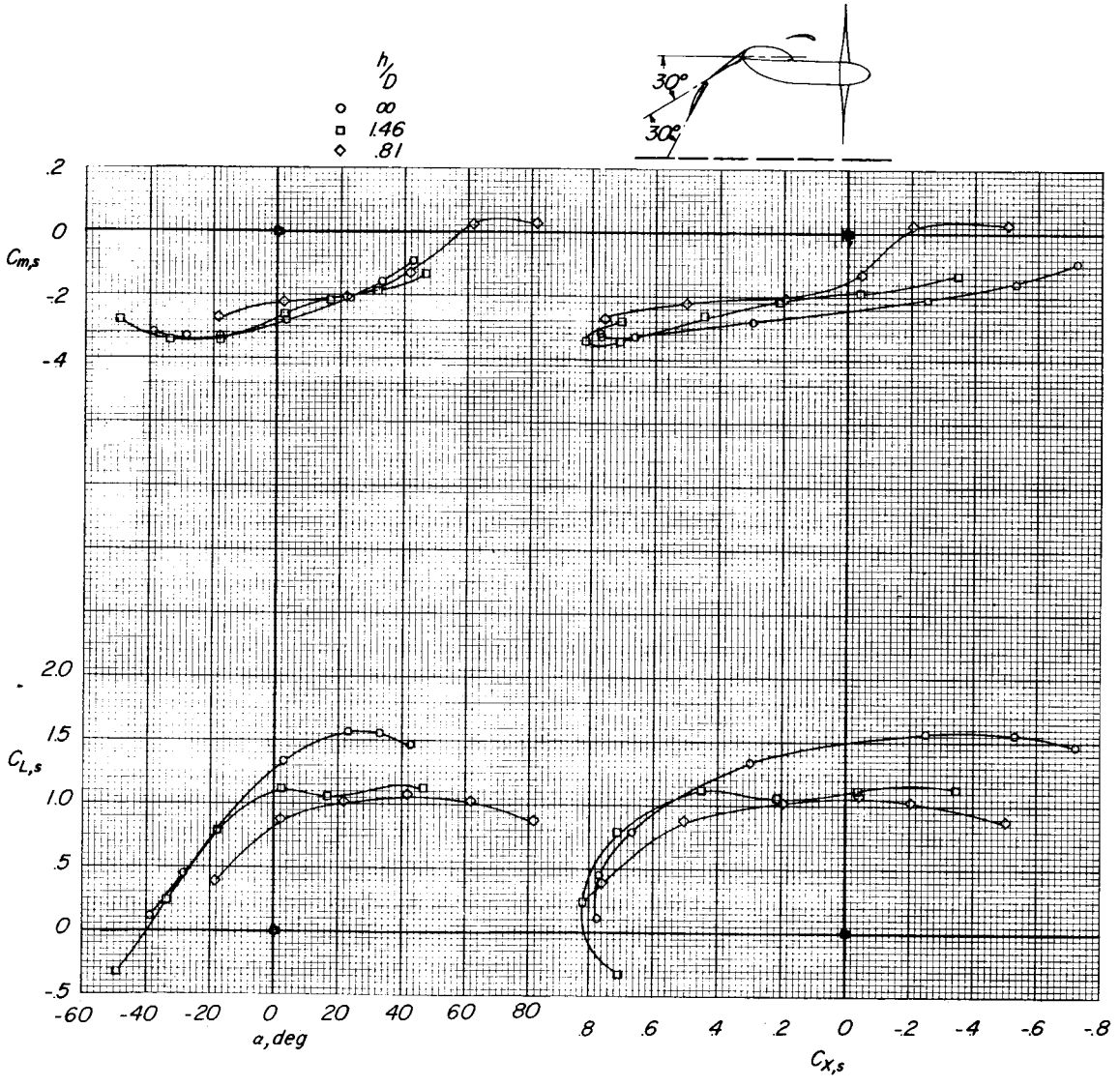

(c) $C_{T,s} = 0.95$.

Figure 29.- Continued.

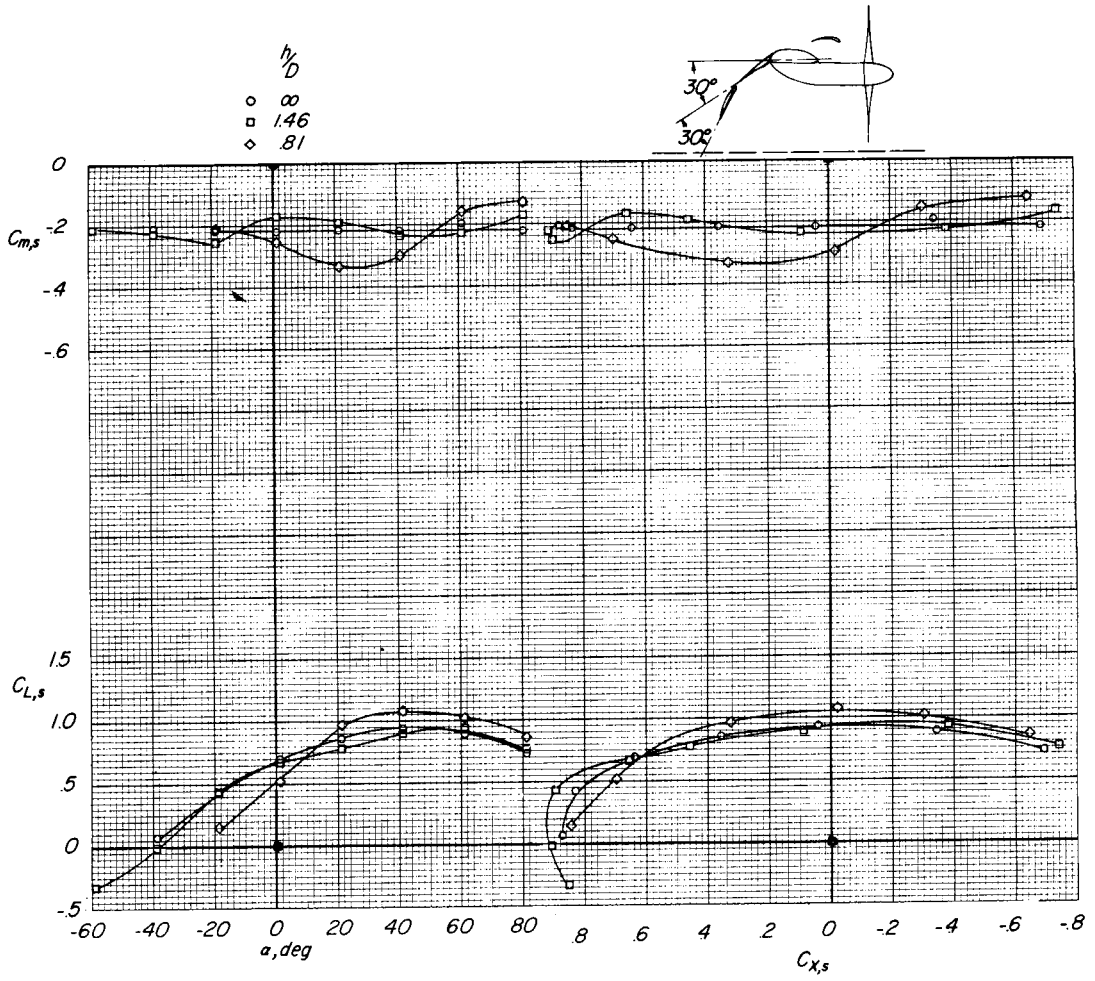

(d) $C_{T,s} = 1.00$.

Figure 29.- Concluded.

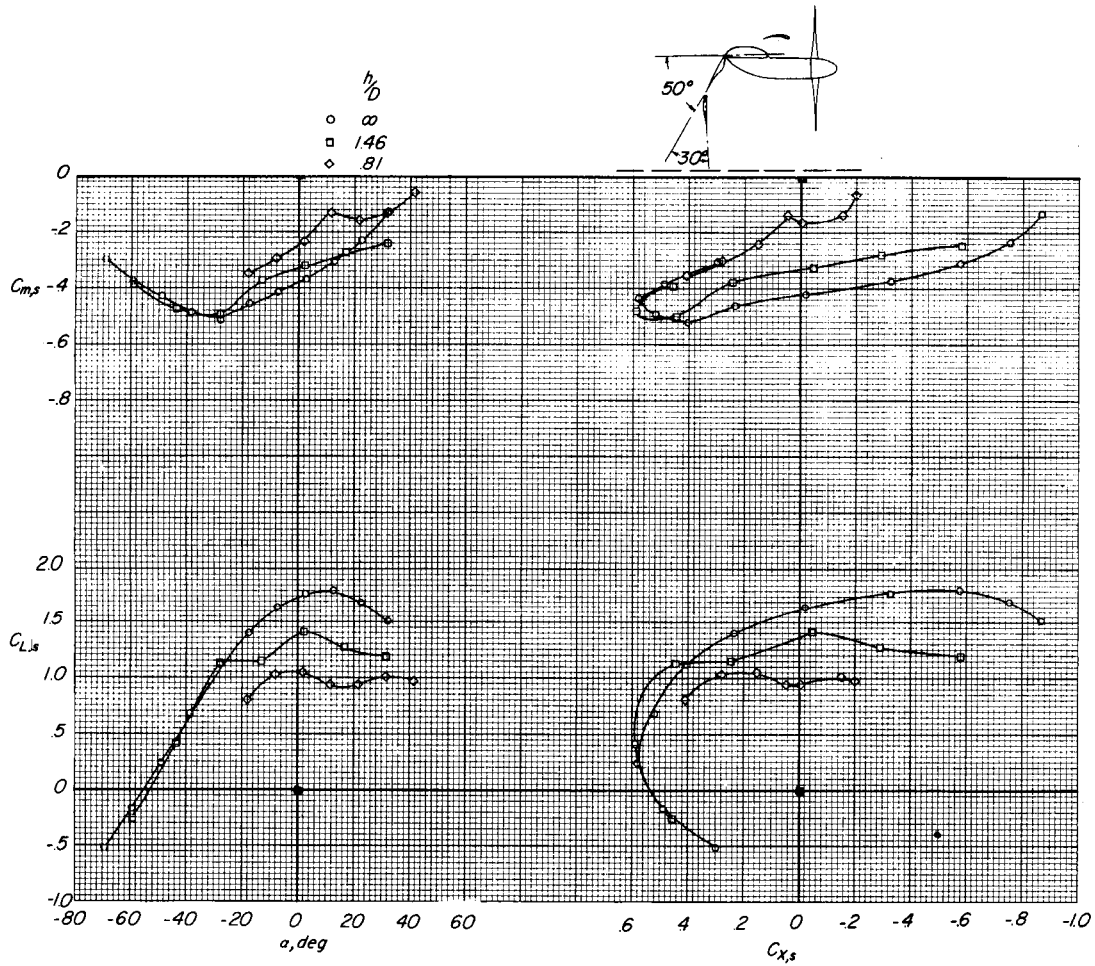

(a) $C_{T,S} = 0.90$.

Figure 30.- Effect of ground proximity. Deflected-slipstream configuration ($\delta_{f,S} = 50^{\circ}$; $\delta_{f,F} = 30^{\circ}$); slat in high position; $\delta_{slat} = 0^{\circ}$.

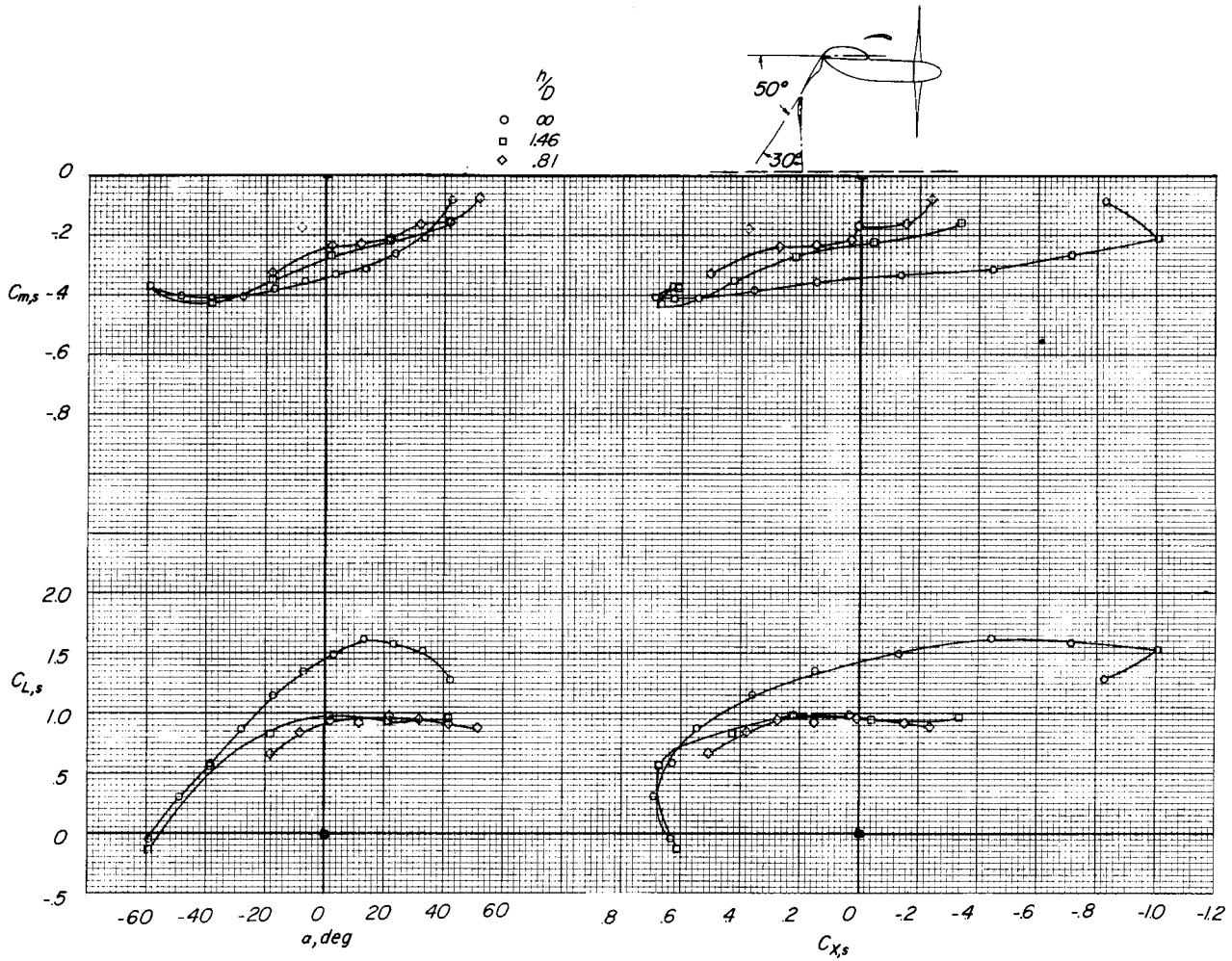

(b) $C_{T,s} = 0.95$.

Figure 30.- Concluded.

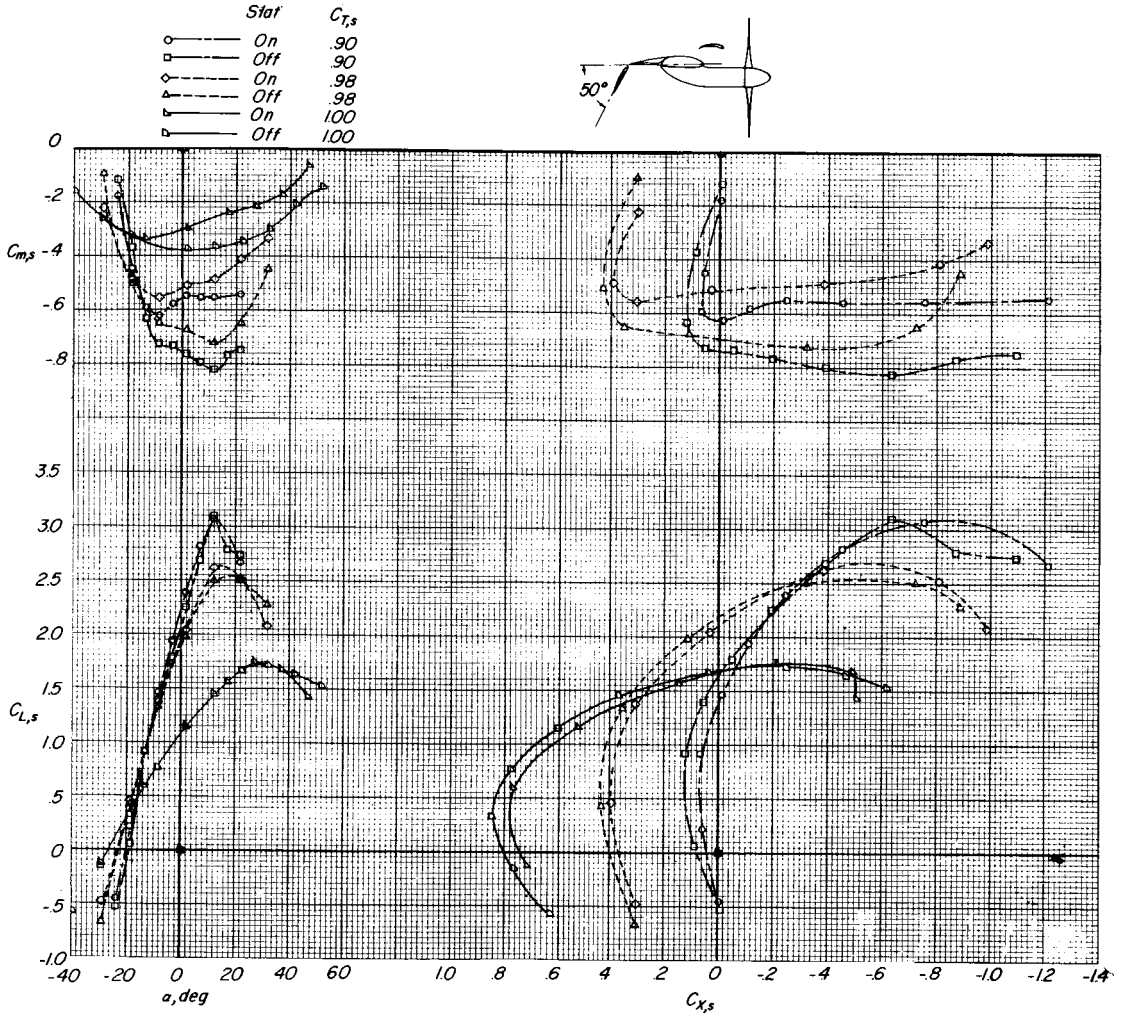

(a) $\delta_{f,S} = 0^{\circ}$; $\delta_{f,F} = 50^{\circ}$.

Figure 31.- Effect of leading-edge slat out of region of ground effect.

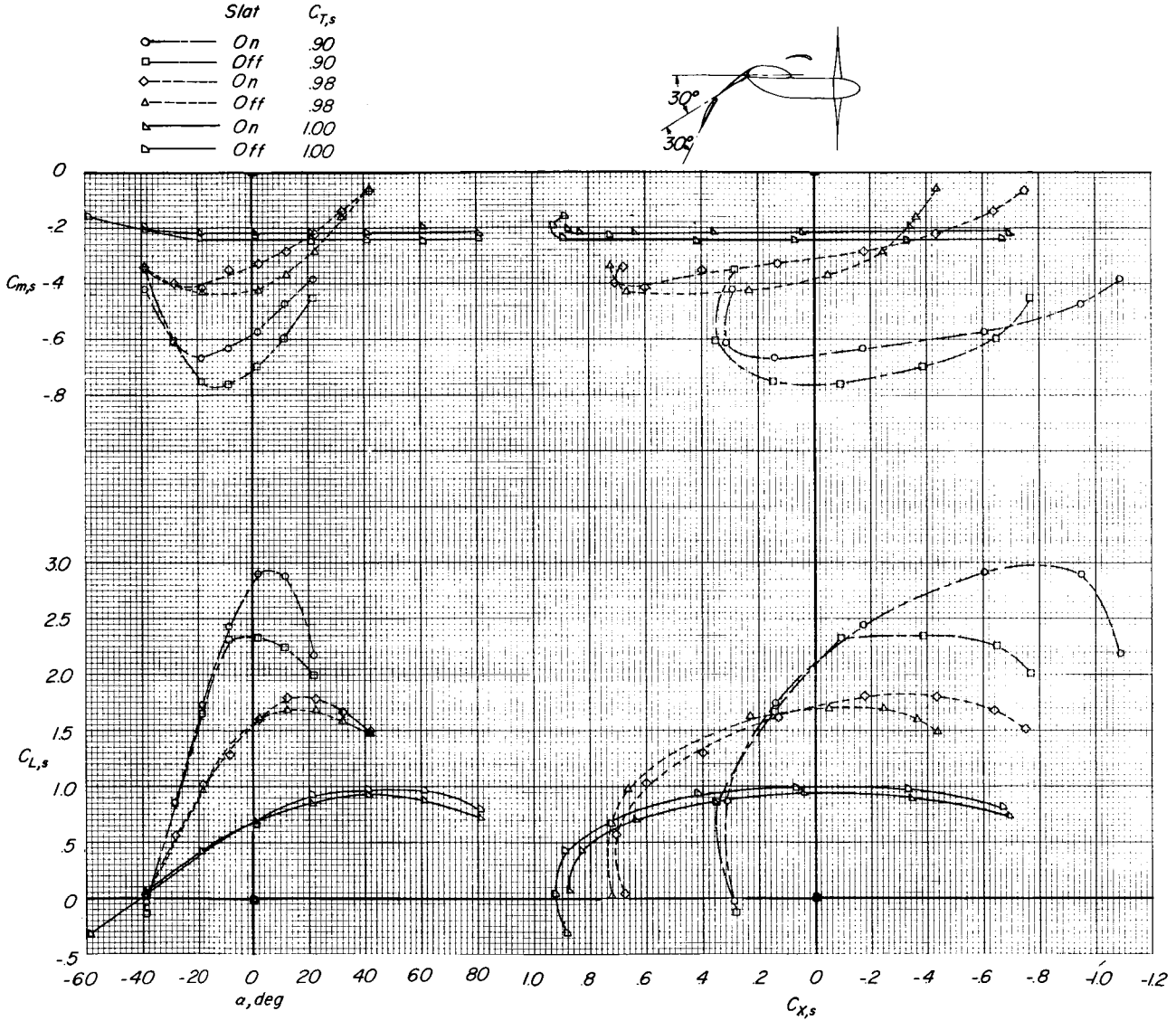

(b) $\delta_{f,S} = 30^{\circ}$; $\delta_{f,F} = 30^{\circ}$.

Figure 31.- Continued.

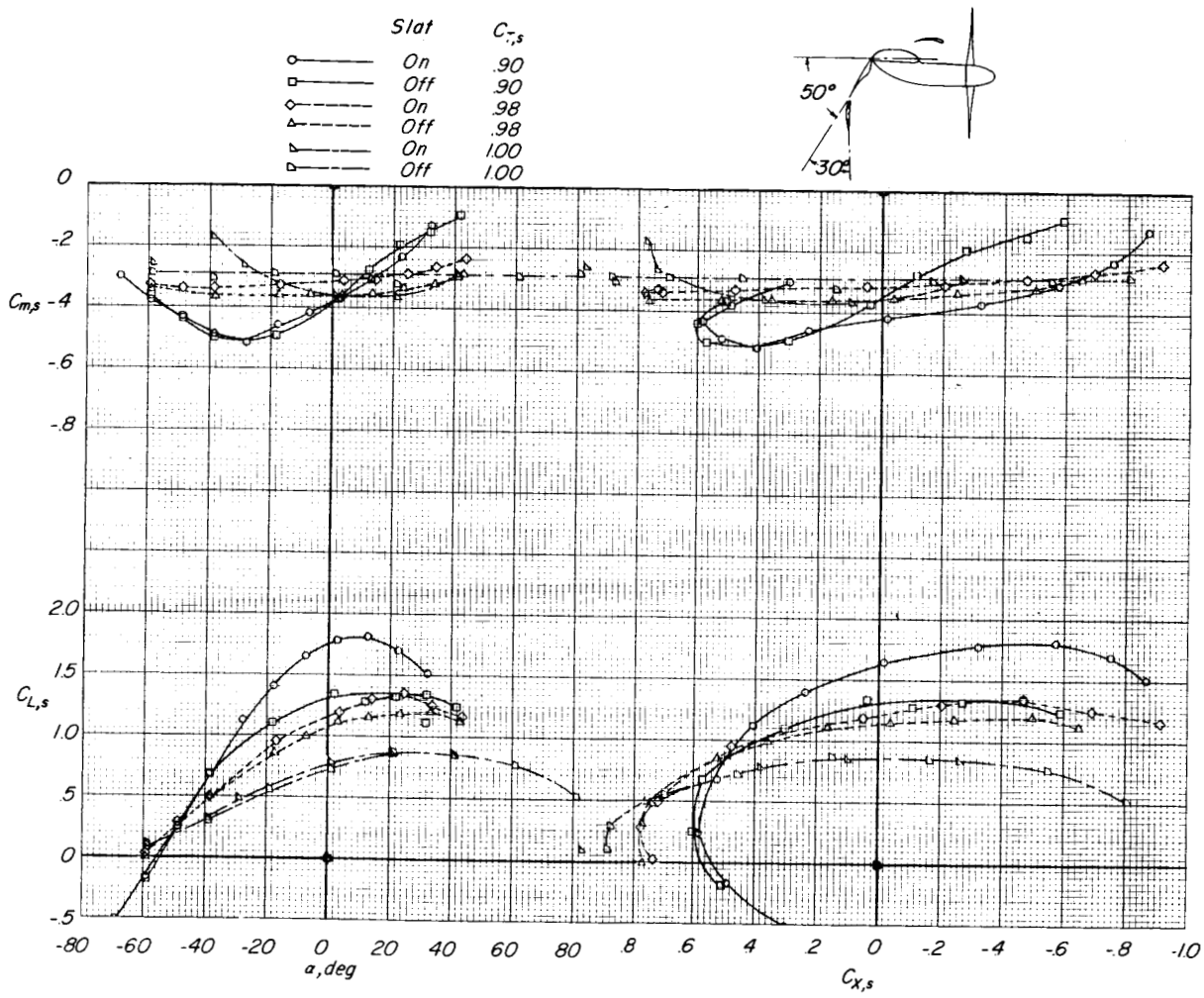

(c) $\delta_{f,S} = 50°$; $\delta_{f,F} = 30°$.

Figure 31.- Concluded.

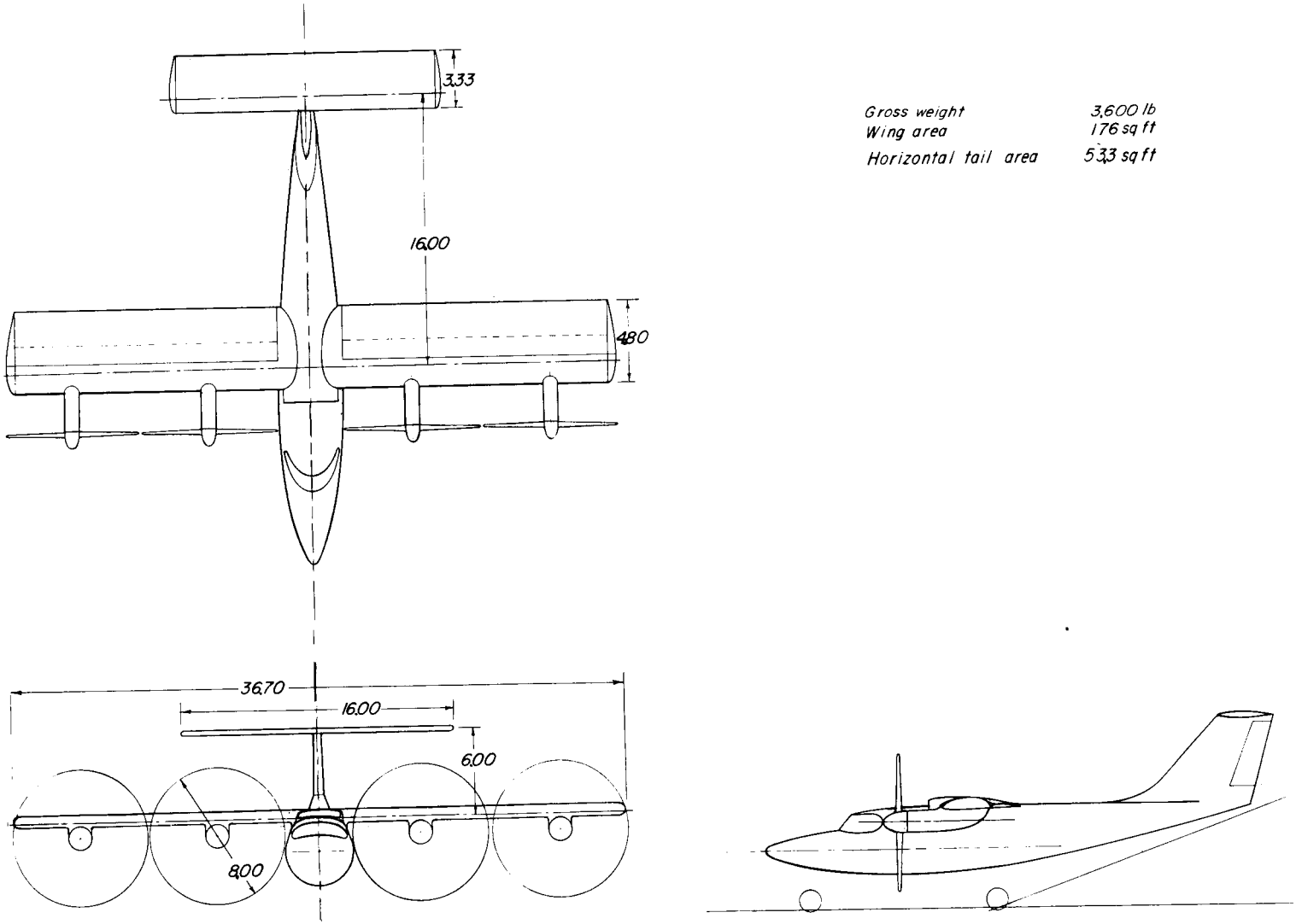

Figure 32.- Sketch of hypothetical VTOL airplane. All dimensions are in feet.

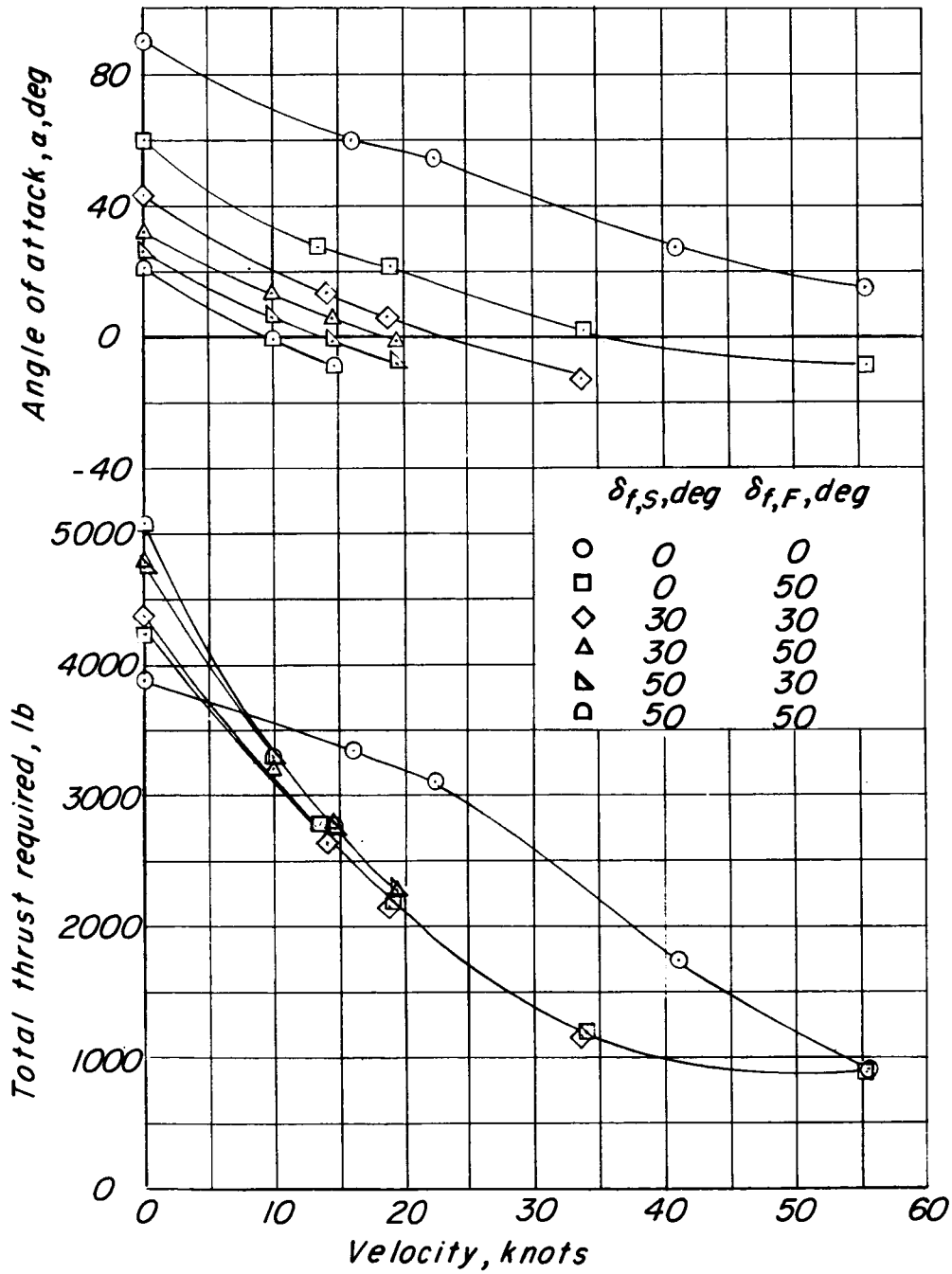

Figure 33.- Effect of flap deflection on angle of attack and calculated thrust required for hypothetical airplane in steady, level transition flight out of region of ground effect. Slat in high position; $\delta_{slat} = 0^{o}$.

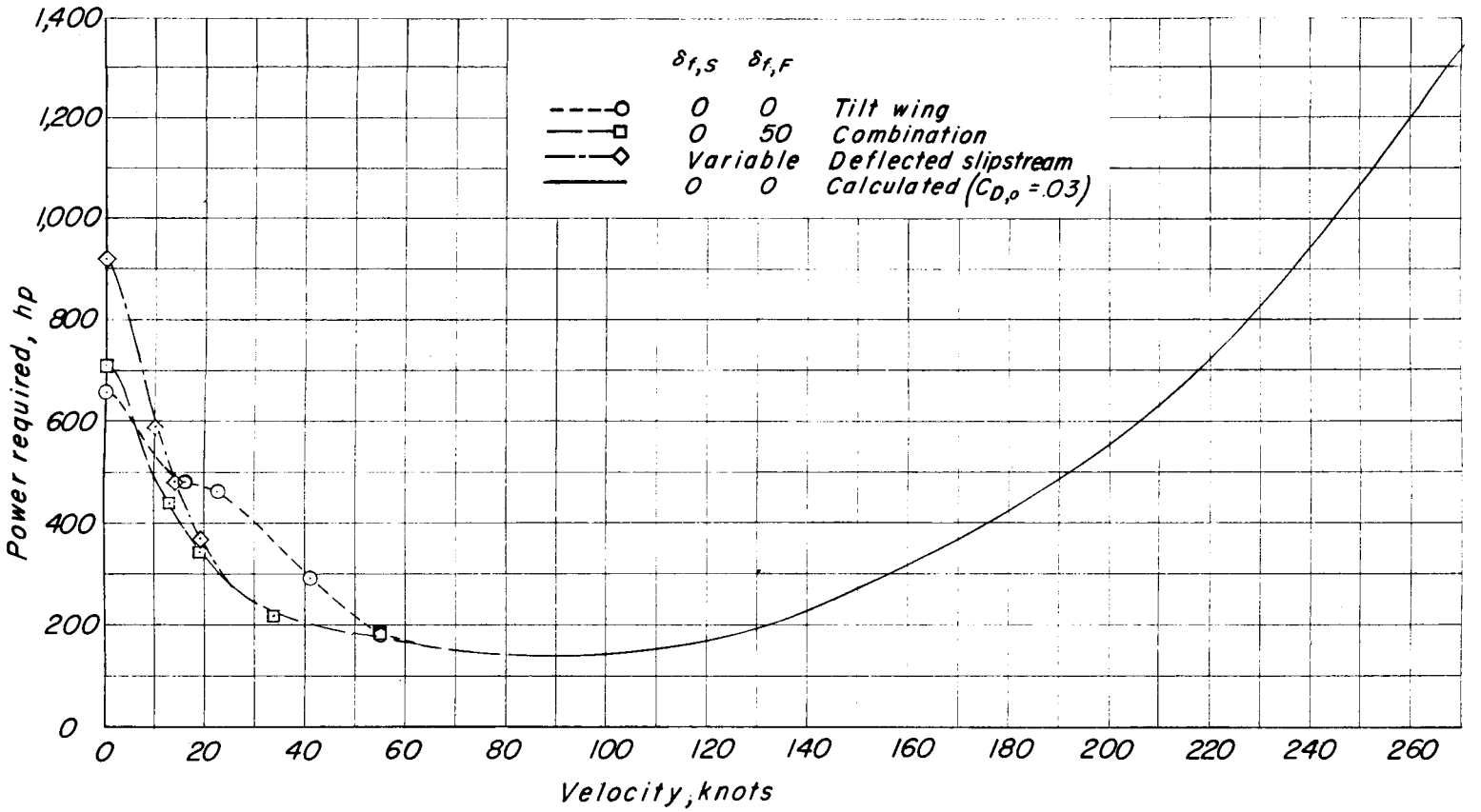

Figure 34.- Comparison of level-flight power requirements for tilt-wing, deflected-slipstream, and combination configurations of the hypothetical airplane in steady, level flight. Slat in high position; $\delta_{slat} = 0^{o}$.

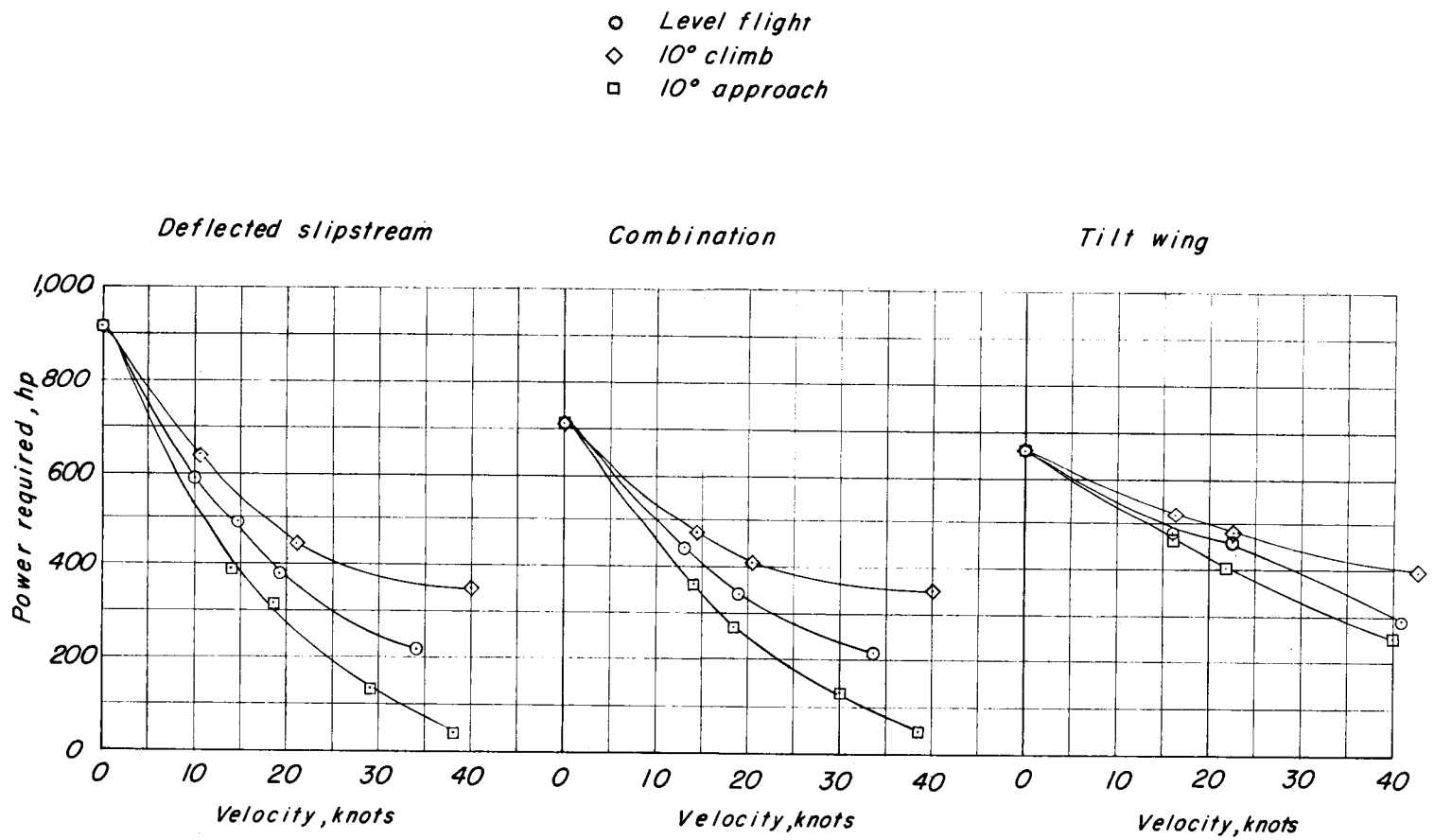

Figure 35.- Comparison of effects of climb and descent on power requirements for tilt-wing, deflected-slipstream, and combination configurations of hypothetical airplane out of region of ground effect. Slat in high position; $\delta_{slat} = 0^{\circ}$.

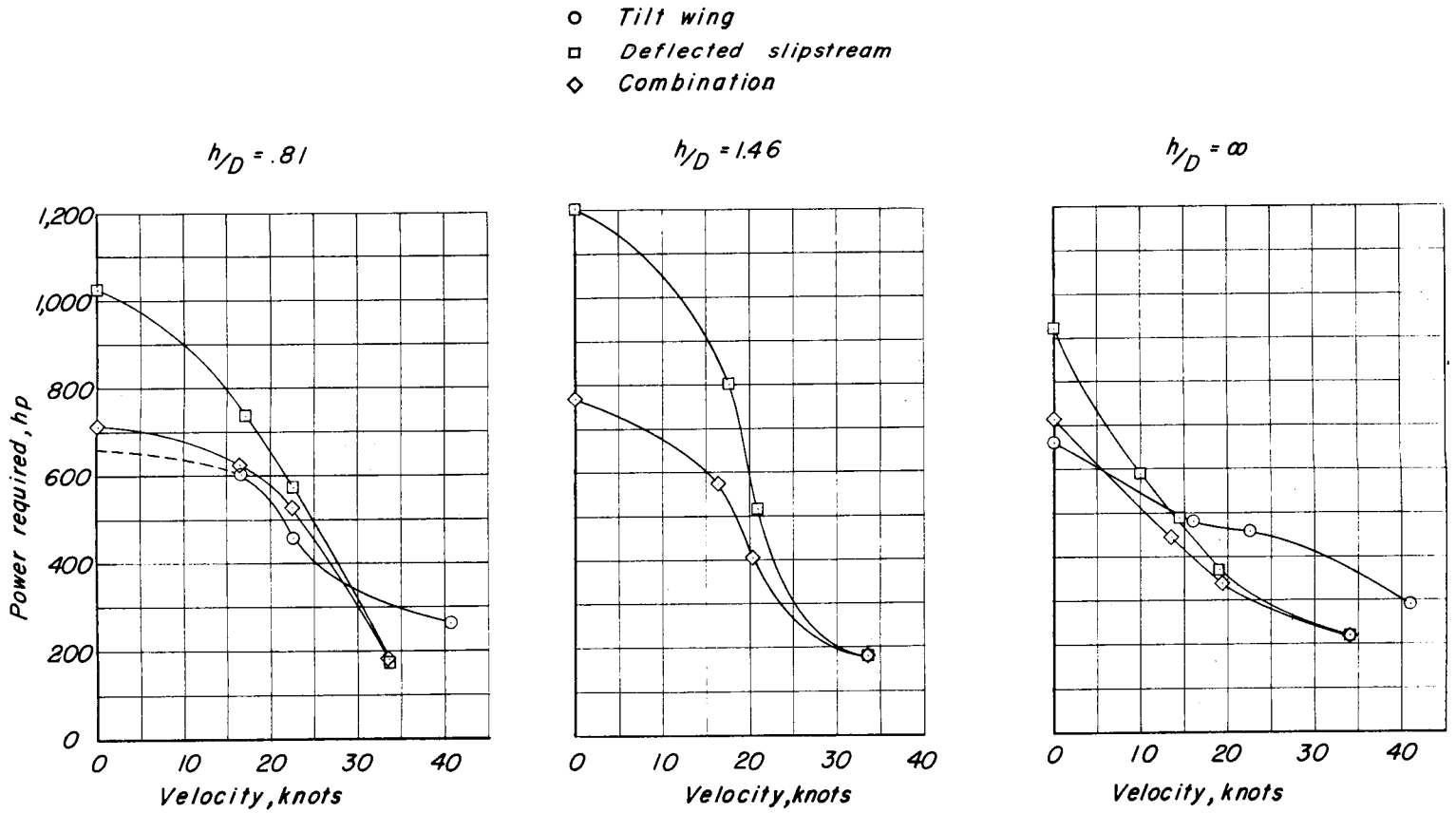

Figure 36.- Effect of ground proximity on power required for level flight of hypothetical airplane. Slat in high position; $\delta_{slat} = 0^{o}$.

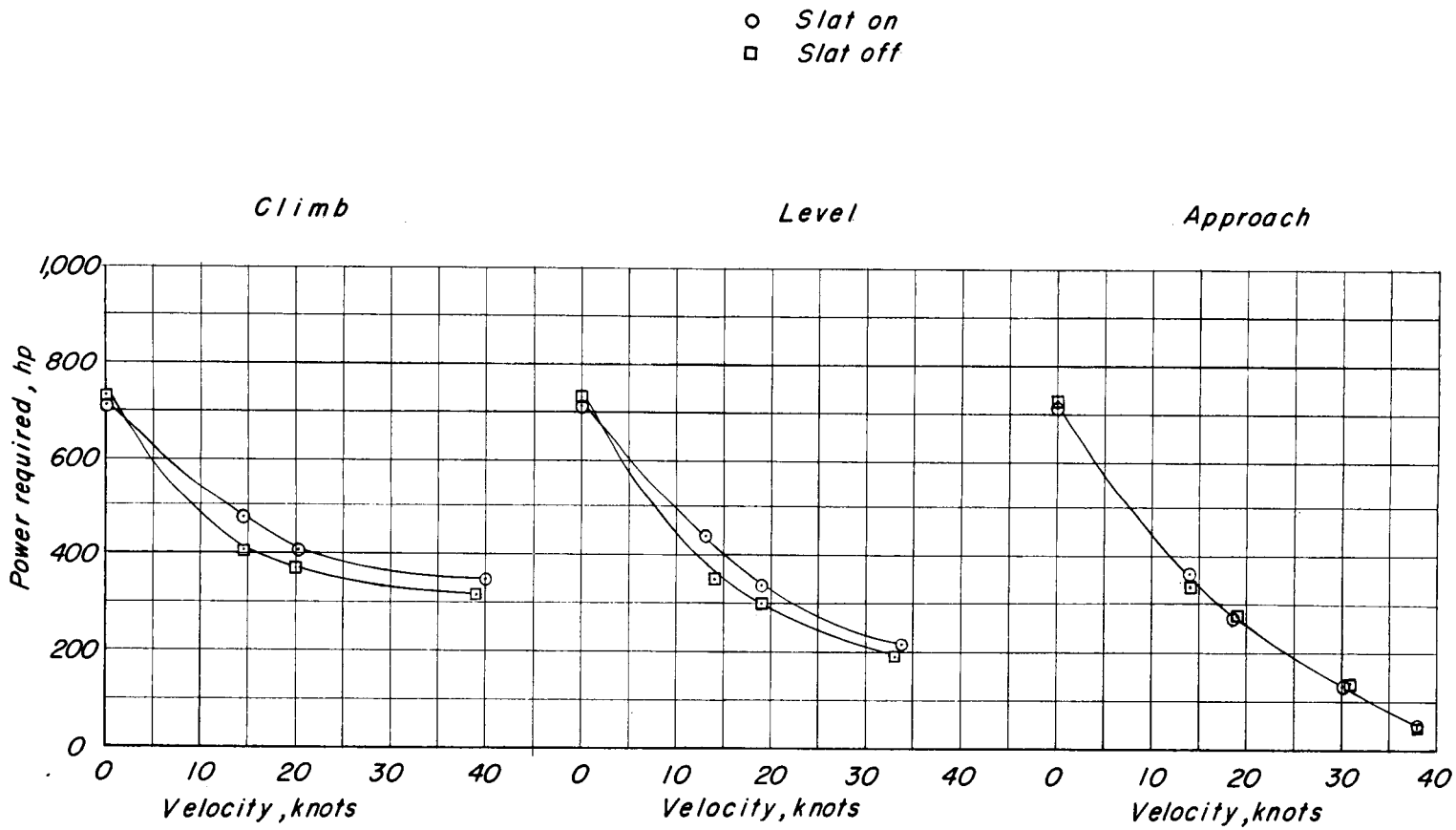

(a) Combination configuration.

Figure 37.- Effect of leading-edge slat on power required for hypothetical airplane out of region of ground effect.

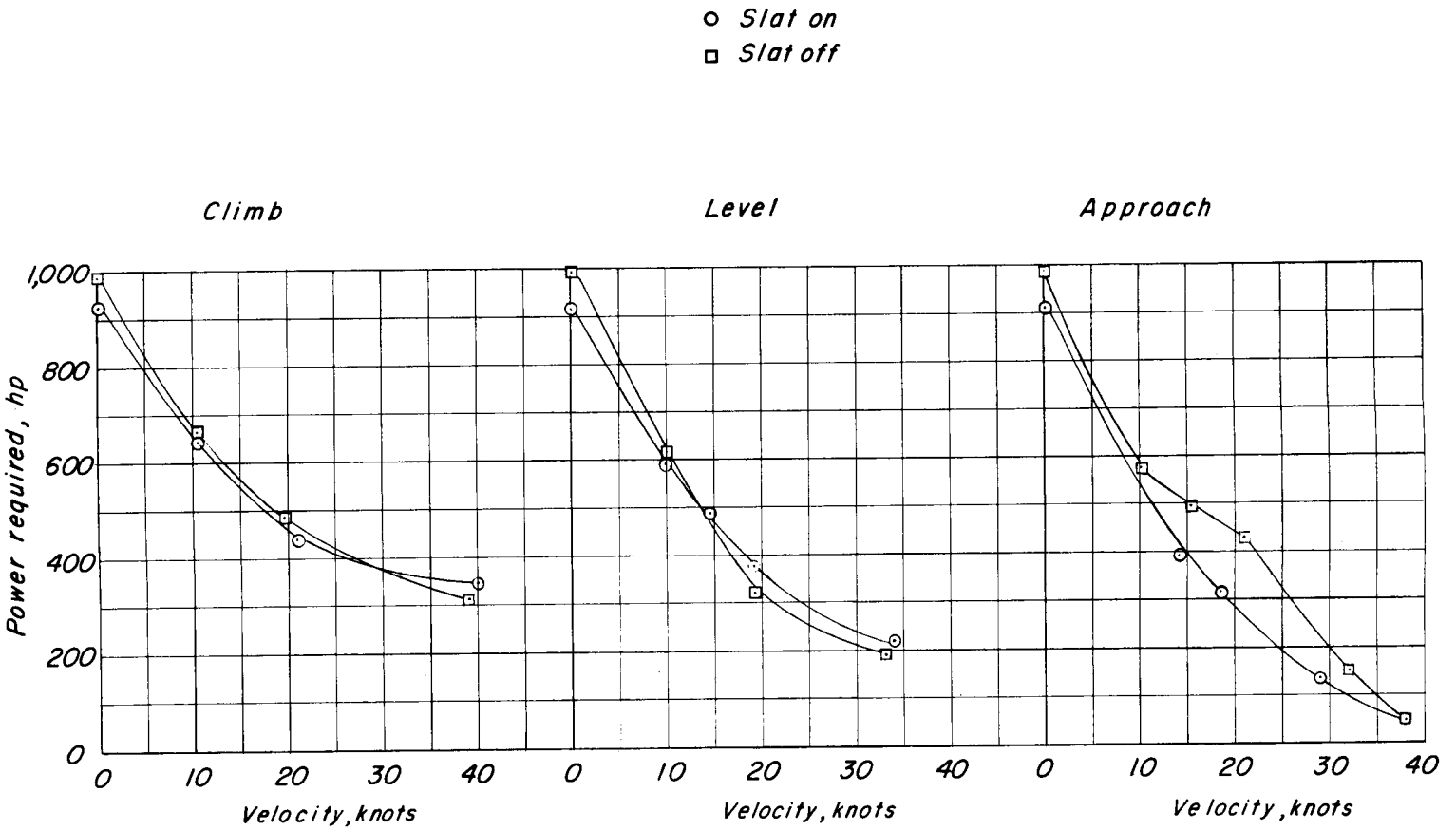

(b) Deflected-slipstream configuration.

Figure 37.- Concluded.

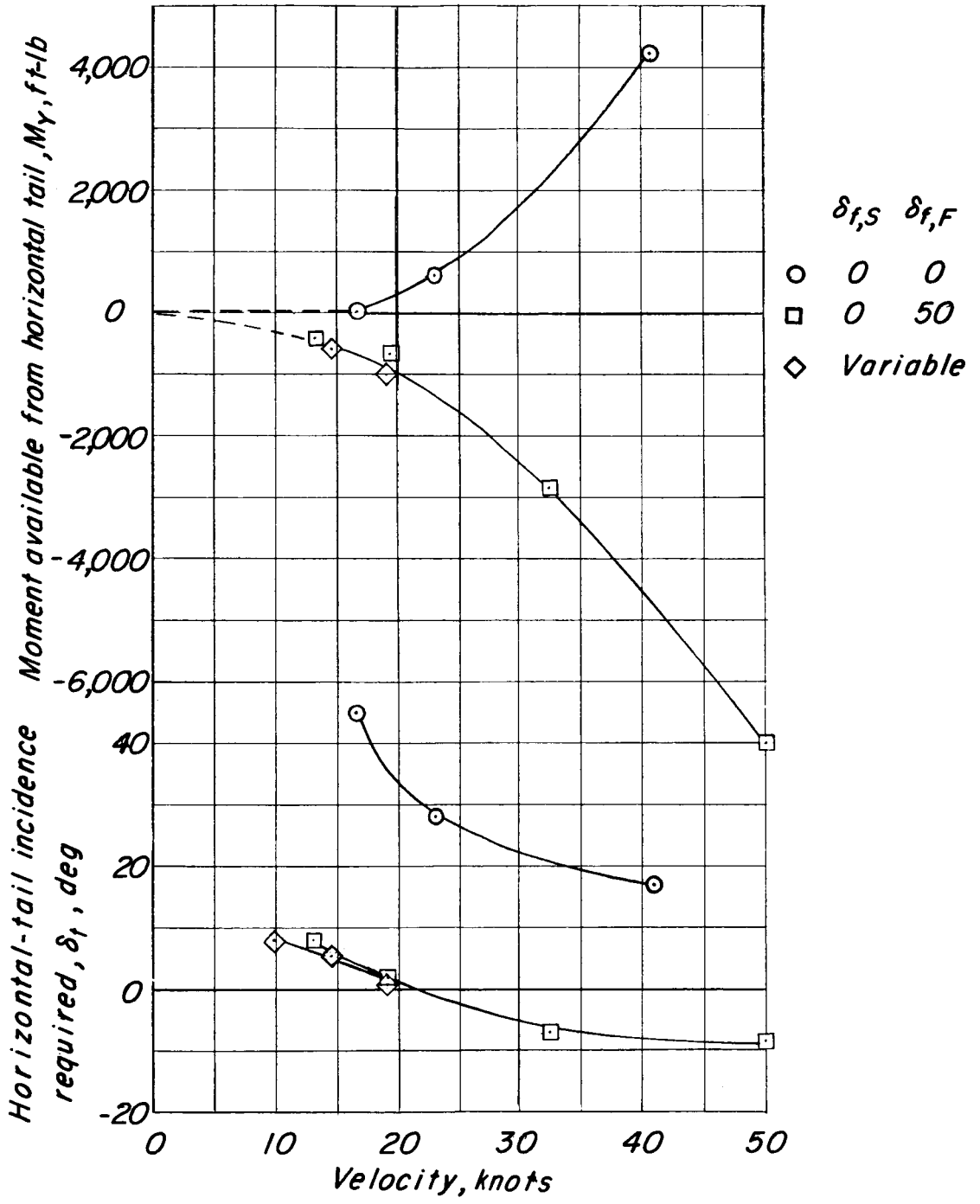

Figure 38.- Trimming moment available with horizontal tail of hypothetical airplane $C_{L,t} = 1.0$ and tail incidence required to produce this moment in transition speed range.

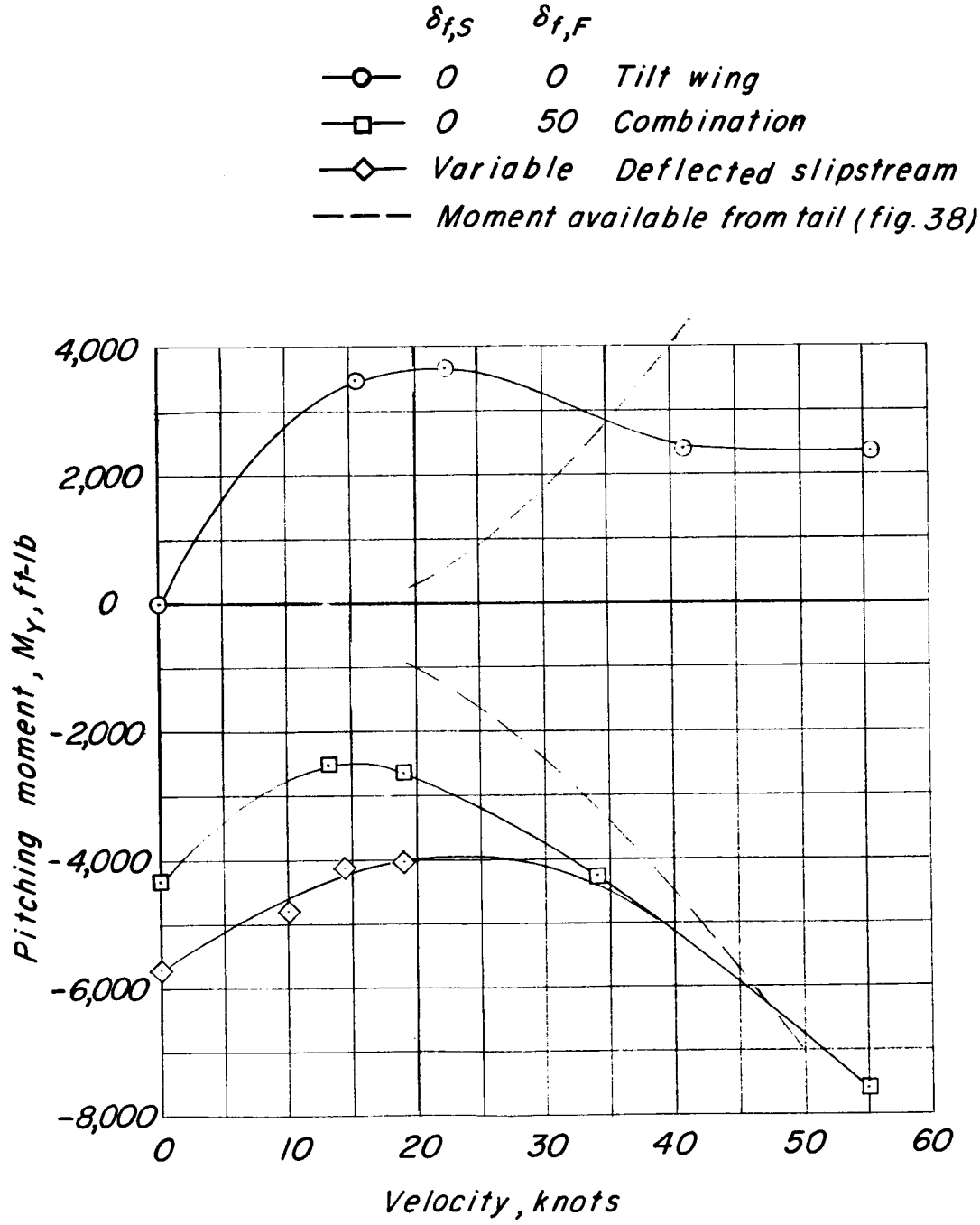

Figure 39.- Variation of untrimmed pitching moment of hypothetical propeller-wing-flap system and trimming moment available with horizontal tail in transition speed range.

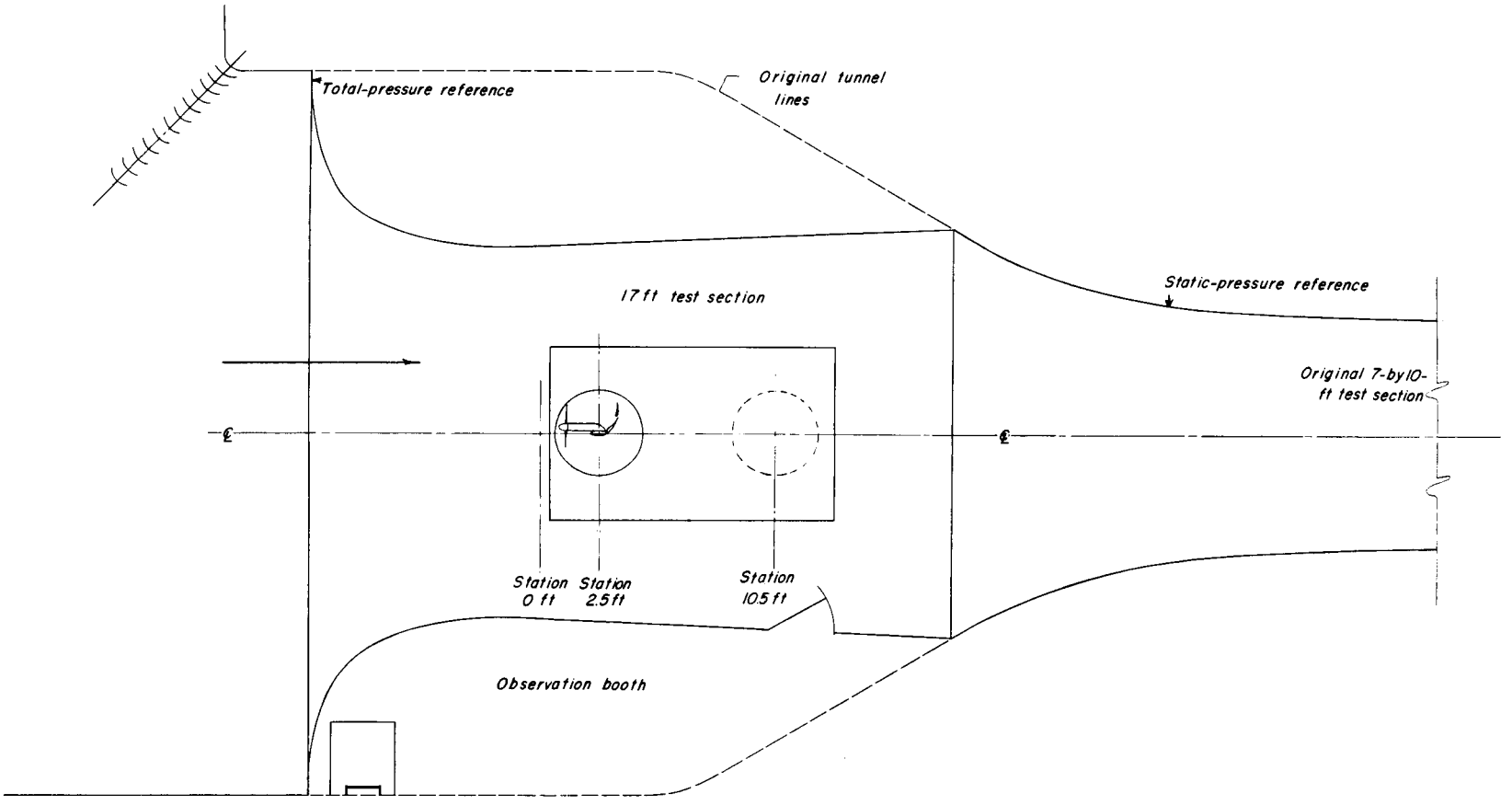

Figure 40.- Plan view of 17-foot test section installed in the Langley 300-MPH 7- by 10-foot tunnel.

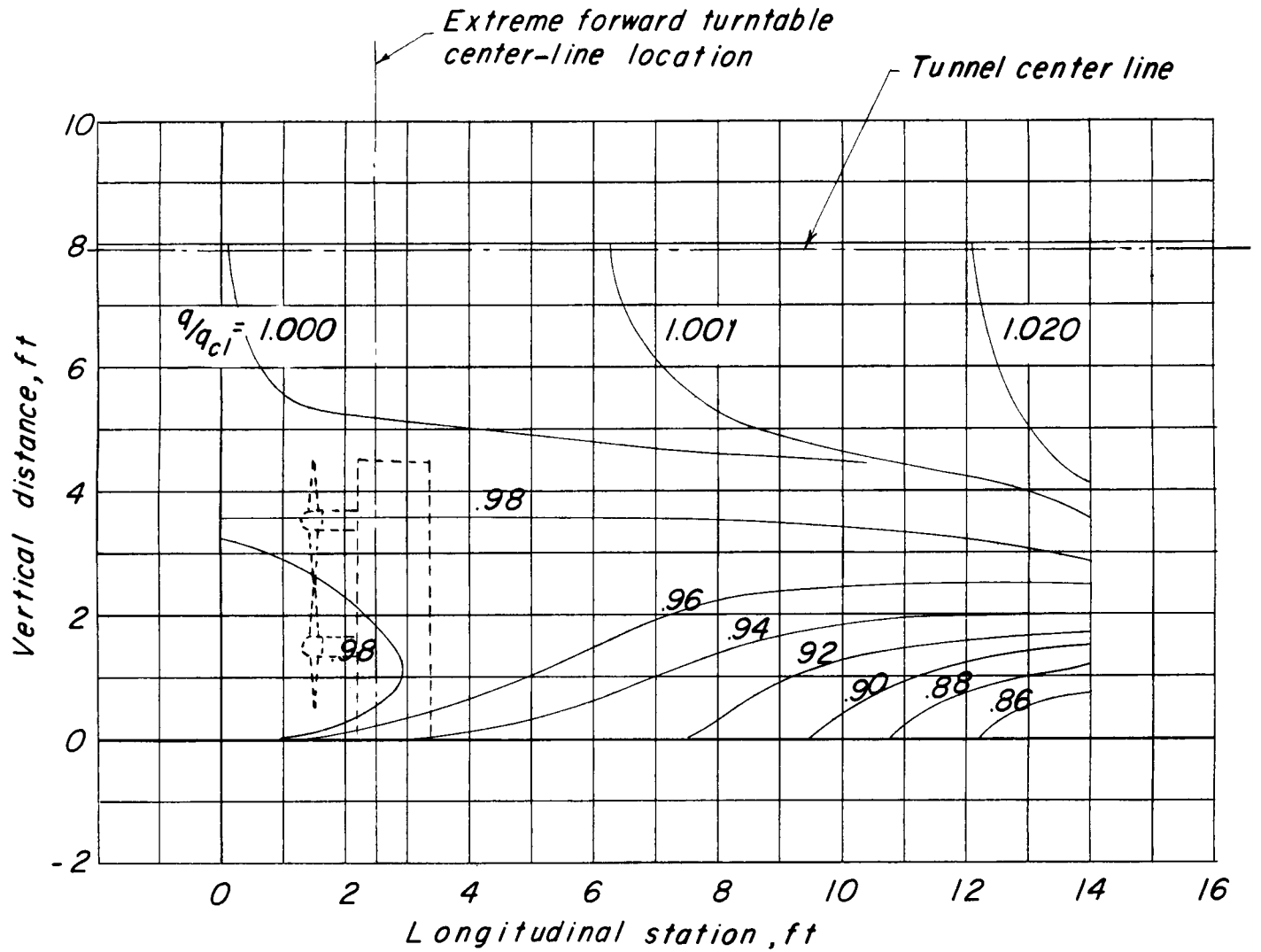

Figure 41.- Dynamic-pressure distribution in vertical plane of 17-foot test section.

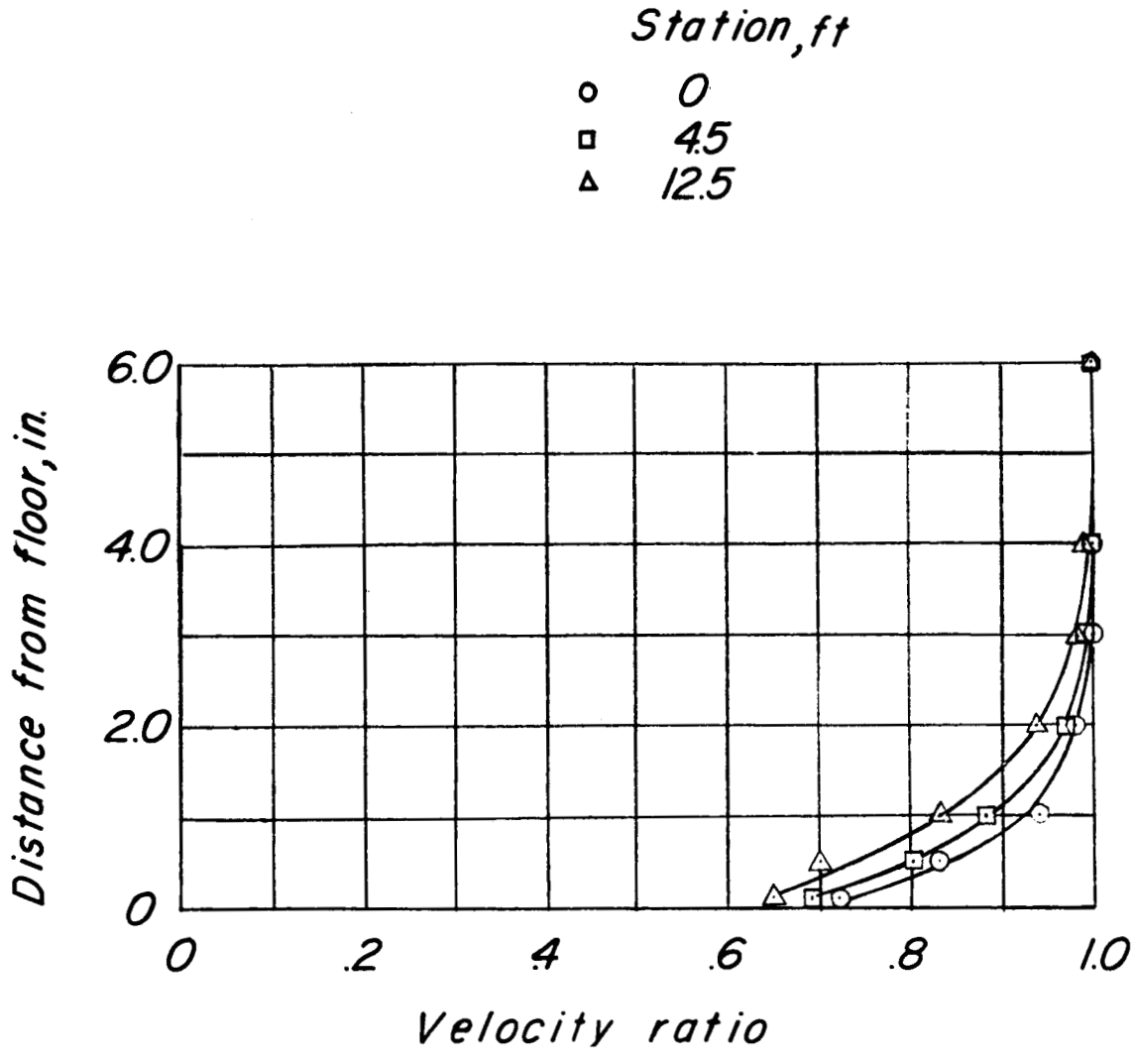

Figure 42.- Boundary-layer profiles at three stations on center line of tunnel floor.

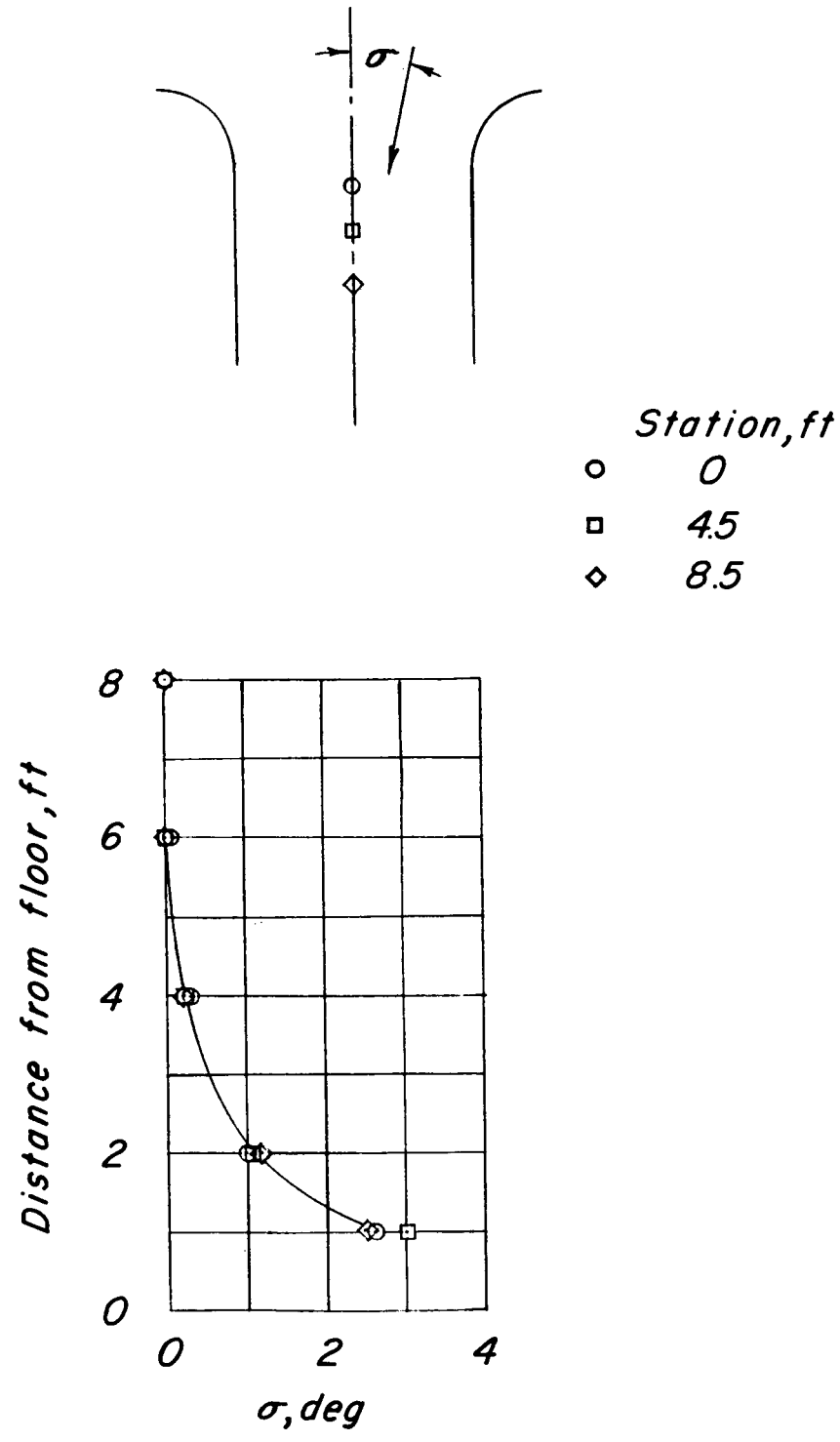

Figure 43.- Sidewash distribution.